

# Atomic Diffusion and Molecular Self-Assembly on Metal Surfaces

---

A dissertation

submitted by

April D. Jewell

In partial fulfillment of the requirements for the degree of

Doctor of Philosophy

in

Chemistry

TUFTS UNIVERSITY

August 2012

Advisor: Professor E. Charles H. Sykes

## Abstract

The research described herein focuses on understanding and exploiting nanometer-scale surface phenomena with respect to surface reactivity and self-assembled systems. Using scanning tunneling microscopy, atoms and small molecules (*i.e.*, fewer than 30 atoms) adsorbed on metal surfaces were studied with the objective being to capture, understand, and manipulate the events occurring at the interface between gases and solid surfaces. The specific approach was to examine a variety of different but related chemical species in order to understand how chemical functionality affects the assembly behavior of technologically important species on metal surfaces. Using this systematic approach, in which, for example, only a single atom (or group of atoms) in the adsorbed species was varied, it was possible to uncover subtle differences in assembly behavior and overlayer stability. These differences are explained in terms of the chemical properties of the differing atom(s), which are based on well-established periodic trends and governed by electrostatics. Similar studies focusing on varying ligand functionality are also presented. Findings from this research add to our understanding of fundamental chemical interactions that govern assembly at the gas/solid interface. Importantly, the work here contributes to the establishment of heuristic rules that, in the future, could help predict assembly behavior. The impact of this research has the potential to transform our approach to sensor technology, heterogeneous catalysis, and other related fields.



## Acknowledgements

What an exciting journey the past five years have been, both professionally and personally. Coming in, I was prepared for graduate school to be one of the most challenging undertakings of my professional life. I was not prepared, however, for how personally rewarding the experience would turn out to be. Many people I have encountered along the way have helped shape my experience in ways I could not have foreseen.

First, I would like to acknowledge my research advisor, Prof. Charles Sykes. When initially choosing a research group, I met with several faculty members, all of whom were doing interesting and impactful science. The meeting with Charlie was special; his vision and enthusiasm for his work was palpable, and his excitement was contagious. When then meeting with his students, it was clear that the entire group shared in Charlie's eagerness to explore. Throughout the past five years, Charlie has been an excellent mentor. His willingness to talk about science and help tackle the problems I have encountered in my research have meant more than I can say. I know that as I move forward in my professional career, I will look to his example as a source of inspiration.

I would also like to thank my thesis committee members. Prof. Elena Rybak-Akimova, whom I met in the *Advanced Inorganic Chemistry* course during my first semester at Tufts: she is an excellent and passionate instructor whose love for chemistry helped to remind me why I was here in the first place. Prof. Albert Robbat, whom I met when first visiting Tufts, and later in *Separation Science*: his no-nonsense approach to teaching, research, and evaluation has shown me that with a

lot of determination (and a little luck) it is possible to actually finish graduate school. Finally, Prof. Karsten Pohl: whom I had the great pleasure of meeting at the regional AVS meeting and again later at the Physical Electronics Conferences: I feel fortunate that our research interests overlapped; even more so that he has agreed to offer his input on my dissertation and make the trip from New Hampshire to participate in my defense.

There are also several individuals whom I met during my career prior to graduate school who instilled in me a love of chemistry and encouraged me to pursue the discipline as a profession. My high school chemistry teacher at Girls Preparatory School, Keith Sanders, made the subject exciting and accessible to my fifteen year-old self. His approach to teaching and passion for chemistry captured my attention. My interest persisted even through the following year when another teacher (name withheld) told me girls could not excel at chemistry. I suppose I owe her a debt of gratitude, as well, for encouraging me to work even harder to prove her wrong. At George Washington University, my undergraduate research advisor, Prof. Houston Miller, took a chance on an inexperienced sophomore and gave me the opportunity to do work in his research lab. Prof. Miller was fun, informative, and a great mentor; I greatly appreciate his guidance and his recommendation to apply for a summer internship at the Jet Propulsion Laboratory, which eventually turned into a job. At JPL I worked with many accomplished scientists and engineers, and many of them directly contributed to my decision to pursue a graduate degree. I would like to thank Dr. Margie Homer, Dr. Shouleh Nikzad, Dr. Margaret Ryan, Dr. Abhijit Shevade, Dr. Lloyd Bell, Dr. Jean-Pierre Fleurial, Dr. Thierry Caillat, Dr. Jeffery Sakamoto and Dr. S.R. Narayanan all for their encouragement.

I feel most fortunate for the personal relationships, new and old, that have helped me through these five years. Graduate school is tough, and I know that I would not have been able to fully (and sanely) appreciate the endeavor without the support system of offered by my loved ones. My co-workers have all helped to make coming into lab an enjoyable experience: Dr. Ashleigh Baber, Dr. Erin Iski, Dr. Heather Tierney, Tim Lawton, Emily Lewis, Matt Boucher, Colin Murphy, Allister McGuire, Prof. George Kyriakou, Dr. Mahnaz El-Kouedi, Darin Bellisario, Mike Mattera, Matt Marcinkowski, Melissa Liriano, Felicia Lucci, and Mishan Blecher. Other friends, both inside and outside the department, have made the hours spent outside of lab exceedingly enjoyable: Kyle McElhoney, Cristy Cella, Naomi Neustadt, Arthur Inasi, Estaban Tapetillo, Heidi Teng, Mollie Hill, Lester, Cherry and Bean.

To my parents, grandparents, brothers, sisters, nieces, nephews, aunts and uncles I owe a great deal of gratitude. They have supported me though thick and thin, always believing in me even when I was unsure of myself. Their confidence in me has been a comfort in times when I was lacking. I especially want to thank Mom and Nic: who have always been there when I needed them. I would also like to make special mention of my grandmother Teena whose love and support were invaluable.

Last, but never least, I want to acknowledge Steven Shafer. Steve and I met during my second year of graduate school, and he has been my rock throughout. From reading my papers to helping me escape work, and everything in between, he has offered his unconditional love and support. As we move forward in our lives together, I do so knowing that our relationship is and will continue to be my greatest accomplishment.

## Table of Contents

Abstract	ii
Acknowledgements	iii
Table of Contents	vi
List of Tables	ix
List of Figures	x
List of STM Movies	xiii
1. Introduction	1
1.1 Scanning Tunneling Microscopy.....	1
1.2 Self-Assembled Monolayers .....	3
1.3 Substrate Structure .....	5
1.4 Molecule-Surface Interactions.....	8
1.5 Molecule Studies.....	11
1.6 Atom Studies.....	15
2 Experimental Methods	18
2.1 Low-Temperature Scanning Tunneling Microscopy .....	18
2.2 Sample Preparation .....	24
2.3 Single-Molecule and Single-Atom Studies.....	28
2.4 Surface Reconstruction Studies.....	32
3 Time-Resolved Studies of Individual Molecular Rotors	39
3.1 Introduction .....	39
3.2 Results and Discussion.....	43
3.3 Conclusions .....	62
3.4 Additional Experimental Details.....	62
4 Adsorption, Assembly and Dynamics of Dibutyl Sulfide on Au(111)	64
4.1 Introduction .....	64
4.2 Results and Discussion.....	65
4.3 Conclusions .....	78
4.4 Additional Experimental Details.....	79
5 Asymmetric Thioethers as Building Blocks for Chiral Monolayers	80
5.1 Introduction .....	80
5.2 Results and Discussion.....	82
5.3 Conclusions .....	98

5.4	Additional Experimental Details.....	99
6	Gently Lifting Gold's Herringbone Reconstruction: Trimethylphosphine on Au(111)	100
6.1	Introduction .....	100
6.2	Results and Discussion.....	101
6.3	Conclusions .....	109
6.4	Additional Experimental Details.....	110
7	Effect of Head Group Chemistry on Surface-Mediated Molecular Self-Assembly	112
7.1	Introduction .....	112
7.2	Results and Discussion.....	114
7.3	Conclusions .....	130
7.4	Additional Experimental Details.....	131
8	Molecular-Scale Surface Chemistry of a Common Metal Nanoparticle Capping Agent: Triphenylphosphine on Au(111)	132
8.1	Introduction .....	132
8.2	Results and Discussion.....	135
8.3	Conclusions .....	144
8.4	Additional Experimental Details.....	145
9	Magic Electret Clusters of 4-Fluorostyrene on Metal Surfaces	146
9.1	Introduction .....	146
9.2	Results and Discussion.....	147
9.3	Conclusions .....	158
9.4	Additional Experimental Details.....	159
10	Palladium Atom Geometries in the 1-10% Pd/Cu(111) Surface Alloy System	161
10.1	Introduction .....	161
10.2	Results and Discussion.....	162
10.3	Conclusions .....	167
10.4	Additional Experimental Details .....	168
11	Self-Assembly of Hydrogen Atoms on Cu(111) <i>via</i> Quantum Tunneling	169
11.1	Introduction .....	169
11.2	Results and Discussion .....	171
11.3	Conclusions.....	182
11.4	Additional Experimental Details .....	182
11.5	Computational Details.....	182

12	Appendices	184
12.1	Appendix to Chapter 4.....	184
12.2	Appendix to Chapter 5.....	185
12.3	Appendix to Chapter 9.....	187
12.4	Appendix to Chapter 11.....	191
13	Bibliography	192

## List of Tables

Table 7.1 Herringbone Disruption as a Function of Adsorption Energy and Footprint .....	130
Table 9.1 The Charge on a 4-Fluorostyrene Molecule Adsorbed on the Cu(111) and Au(111) Surface .....	151
Table 9.2 The dipole moment vector components for 4-FS adsorbed on Cu(111) and Au (111) in Debye .....	152
Table 9.3 Trimer versus Tetramer Stability as a Function of Molecular Charge.....	155
Table 10.1 Pd Deposition Parameters.....	168
Table A.1 Distance Calculations for 4-Fluorostyrene on Cu and Au .....	187

## List of Figures

Figure 1.1 Fun with Scanning Tunneling Microscopy.....	3
Figure 1.2 The Cu(111) Substrate .....	6
Figure 1.3 The Au(111) Substrate.....	7
Figure 2.1 STM Tip Preparation with Omicron Tip Holder.....	21
Figure 2.2 Electron Beam Evaporator .....	26
Figure 2.3 Herringbone Separation on Clean Au(111).....	33
Figure 2.4 Measuring the Herrinbone Spearation using SPIP.....	35
Figure 2.5 Gold Island Area and Coverage Analysis .....	37
Figure 3.1 Thioether Schematic .....	42
Figure 3.2 Isolated Thioether Molecules on Au and Cu.....	44
Figure 3.3 Current <i>versus</i> Time for Dibutyl Sulfide During Rotation.....	45
Figure 3.4 Current <i>versus</i> Time for Butyl Methyl Sulfide During Rotation.....	46
Figure 3.5 Arrhenius Data for Dibutyl Sulfide Rotation on Au .....	51
Figure 3.6 Arrhenius Data for Dibutyl Sulfide Rotation on Au as a Function of Location.....	52
Figure 3.7 Arrhenius Data for Dibutyl Sulfide Rotation on Cu.....	53
Figure 3.8 Arrhenius Data for Butyl Methyl Sulfide Rotation on Cu .....	55
Figure 3.9 Action Spectrum for Dibutyl Sulfide Rotor on <i>for</i> Au.....	59
Figure 3.10 Thermally <i>vs</i> Electrically Excited Rotation.....	60
Figure 3.11 Rotation Rate as a Function of Tunneling Current .....	61
Figure 4.1 Dibutyl Sulfide Assembly on Au at Low Coverage .....	67
Figure 4.2 Dibutyl Sulfide on Au as Dosed .....	69
Figure 4.3 Dibutyl Suldife on Au Following Thermal a Anneal .....	70
Figure 4.4 Monolayer Coverage of Dibutyl Sulfide on Au .....	71
Figure 4.5 Schematic of Dibutyl Sulfide Assembly on Au.....	73
Figure 4.6 Dibutyl Sulfide Assebmly as Influenced by Au's Herringbone Reconstruction.....	74
Figure 4.7 Dibutyl Sulfide Assembly on Au as a Function of Coverage and Temperature.....	76
Figure 4.8 Herringbone Separation of a Function of Dibutyl Sulfide Coverage and Anneal Temperature .....	77
Figure 5.1 Low to High Coverage Butyl Methyl Sulfide on Au.....	82



Figure 5.2 Low to High Coverage 4,4,4-Trifluorobutyl Methyl Sulfide on Au .....	84
Figure 5.3 Unit Cell for Butyl Methyl Sulfide and 4,4,4-Trifluorobutyl Methyl Sulfide on Au .....	85
Figure 5.4 Homochiral Domain Formation.....	87
Figure 5.5 Twelve Degenerate Domains of 4,4,4-Trifluorobutyl Methyl Sulfide on Au .....	88
Figure 5.6 Domain Size Dictated by Herringbone Reconstruction .....	91
Figure 5.7 Herringbone Spacing as a Function of Butyl Methyl Sulfide and 4,4,4- Trifluorobutyl Methyl Sulfide Coverage.....	93
Figure 5.8 Herringbone Separation as a Function of Anneal Temperature.....	94
Figure 5.9 Ejected Au Atoms within the Butyl Methyl Sulfide Monolayer.....	96
Figure 5.10 Step Reorganization on Au in the Presence of Butyl Methyl Sulfide and 4,4,4-Trifluorobutyl Methyl Sulfide.....	97
Figure 6.1 Trimethylphosphine on Au with Island Formation.....	102
Figure 6.2 Monolayer Coverage of Trimethylphosphine on Au.....	103
Figure 6.3 Large Scale Images of Monolayer Coverage Trimethylphosphine on Au .....	104
Figure 6.4 Trimethylphosphine Assembly as a Function of Anneal Temperature ..	105
Figure 6.5 Au Island Coverage and Size as a Function of Trimethylphosphine Coverage .....	107
Figure 6.6 Island Size Histograms .....	109
Figure 7.1 Four Species for Comparison.....	112
Figure 7.2 Monolayer Assemblies for Four Species on Au .....	114
Figure 7.3 Dimethyl Sulfide Assembly Structure on Au .....	115
Figure 7.4 Dibutyl Sulfide and Dibutyl Selenide Assembly Structures on Au.....	117
Figure 7.5 Trimethylphosphine Assembly Structure on Au.....	118
Figure 7.6 Dimethyl Sulfide as a Function of Coverage and Anneal Temperature .	121
Figure 7.7 Dibutyl Sulfide as a Function of Coverage and Anneal Temperature ....	122
Figure 7.8 Dibutyl Selenide as a Function of Coverage and Anneal Temperature	124
Figure 7.9 Trimethylphosphine as a Function of Coverage and Anneal Temperature .....	125
Figure 7.10 Herringbone Separation as a Function of Species, Coverage and Anneal Temperature.....	129
Figure 8.1 Triphenylphosphine on Au.....	135
Figure 8.2 Triphenylphosphine Assembly Structures on Au.....	136
Figure 8.3 Schematic of Triphenylphosphine Arrangements.....	137

Figure 8.4 Triphenylphosphine on Au Following Thermal Anneals .....	138
Figure 8.5 Au Islands Trapped within Triphenylphosphine Monolayer .....	139
Figure 9.1 4-Fluorostyrene Clusters on Cu and Au .....	148
Figure 9.2 4-Fluorostyrene Cluster Arrangements on Cu and Au.....	149
Figure 9.3 Fragment Orbital Analysis and Charge Transfer Calculations for 4- Fluorostyrene on Cu and Au.....	152
Figure 9.4 Dipole Moment Illustrations for Gas-Phase and Adsorbed 4- Fluorostyrene .....	154
Figure 9.5 Relaxed 4-Fluorostyrene Trimer and Tetramer Arrangements.....	157
Figure 10.1 Pd/Cu(111) Alloy and Hydrogen Activation.....	162
Figure 10.2 Pd/Cu(111) Alloy Formation.....	163
Figure 10.3 The Pd/Cu(111) Alloy:.....	164
Figure 10.4 Pd Geometries in the Pd/Cu(111) Alloy.....	165
Figure 10.5 Pd Geometries as a Function of Coverage.....	166
Figure 10.6 Pd Trimer Configurations .....	167
Table 10.1 Pd Deposition Parameters.....	168
Figure 11.1 Hydrogen and Deuterium on Cu(111).....	171
Figure 11.2 Hydrogen Assembly at 5 K.....	173
Figure 11.3 Hydrogen Diffusion on Cu(111) at 5 K .....	174
Figure 11.4 Deuterium Clustering on Cu(111) .....	175
Figure 11.5 Hydrogen Stability on Cu(111) as a Function of Coverage.....	176
Figure 11.6 Hydrogen Pairing Geometry and Stability .....	177
Figure 11.7 Deuterium Hop Distance and Adsorption Site Stability on Cu(111) ...	180
Figure 11.8 Temperature Dependent Behavior for Dueterium on Cu(111).....	181
Appendix Figure 4 Twelve Degenerate Domains of Butyl Methyl Sulfide on Au ..	186
Appendix Figure 5 DFT Optimized Geometries for 4-Fluorostyrene on Cu(111) and Au(111) .....	187
Appendix Figure 6 Relaxed Structures for 4-Fluorostyrene Trimers.....	188
Appendix Figure 7 Relaxed Structures for 4-Fluorostyrene Tetramers.....	189
Appendix Figure 8 DFT Geometries for Neutral 4-Fluorostyrene Trimers with and without Dispersion Corrections .....	190

## List of STM Movies

Movie A1 Molecular Rotation and Translation .....	184
Movie A2 Dimers Rearranging .....	184
Movie A3 Trimer Formation.....	184
Movie A4 Trimer Rearrangement.....	184
Movie A5 Single Molecule Interacting with Molecular Chain .....	184
Movie A6 Enantiospecific Assembly of Butyl Methyl Sulfide Trimer.....	185
Movie A7 Enantiospecific Assembly of Butyl Methyl Sulfide Tetramer.....	185
Movie A8 Butyl Methyl Sulfide Cluster to Chain Rearrangement.....	185
Movie A9 Hydrogen Diffusion on Cu(111).....	191
Movie A10 Deuterium Diffusion on Cu(111) .....	191
Movie A11 Hydrogen Self-Assembly on Cu(111).....	191

## 1. Introduction

### 1.1 Scanning Tunneling Microscopy

Since its invention in 1981,<sup>1</sup> scientists have used scanning tunneling microscopy (STM) to study a myriad of problems in surface chemistry, physics and nanoscience. The atomic-scale resolution offered by STM, coupled with its ability to both track the motion of surface-bound molecules over time and position them accurately, has opened many novel methods with which to study important nanoscale phenomena. STM operates on the principle of quantum mechanical tunneling, in which electrons cross a potential barrier where, according to classical mechanics, no current should flow. During STM operation an atomically sharp tip is brought within a nanometer ( $10^{-9}$  m) of a conducting surface. At this small tip-surface separation, the wave functions of the atoms in the surface and the atom(s) at the end of the tip overlap, and electrons can tunnel across the barrier when a voltage ( $V$ ) is applied between the tip and the surface. The process of electron tunneling gives rise to the tunneling current ( $I$ ) that is exponentially dependent on the tip-surface separation ( $z$ ); thus, small changes in  $z$  give rise to large changes in  $I$ :

$$I \propto e^{-2kz}$$

and

$$k = \sqrt{\frac{2m}{\hbar^2} (V_B - E)}$$

where  $\hbar$  is Planck's constant ( $h$ ) divided by  $2\pi$ ,  $V_B$  is the barrier height, and  $E$  is the energy of the electronic state from which tunneling occurs.

Although STM operation parameters can be tuned in order to perform a variety of spectroscopy measurements - including conductance ( $I/V$ ), differential conductance ( $dI/dV$ ), work function ( $dI/dz$ ) and time-resolved ( $I/t$ ) measurements - it is primarily an imaging technique. Explicit chemical information about a system cannot be gleaned from STM imaging alone, and measurements must be performed in such a way as to avoid ambiguity regarding the identity of the surface and any surface adsorbates. Thus, a clean environment is of the utmost importance, and researchers must take special care to ensure the purity of their samples for each experiment. Also, many processes that occur on surfaces happen relatively quickly at room temperature and cannot be captured with typical STM scan times in which each image requires  $\sim 1$  min. to acquire. These processes can be slowed to an observable rate by cooling the system. In light of these considerations, all of the experimental work described in this thesis was performed at cryogenic temperatures (5 K or 78 K) and in ultra-high vacuum (UHV) conditions. Specific details regarding daily operation of the microscope in the Sykes Lab can be found in Chapter 2. When operated with sufficient care, STM is a very powerful research tool that also offers a fun and exciting platform for more playful endeavors, as shown in Figure 1.1.

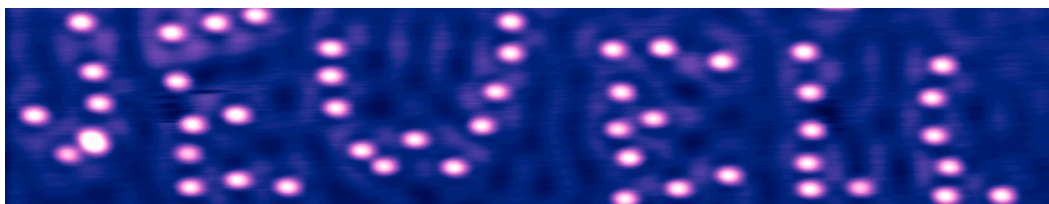


**Figure 1.1 Fun with Scanning Tunneling Microscopy:** STM image showing an area where the I used the STM tip to “write” her family name using individual atoms. In this false color image the bright pink protrusions are Cu atoms on the blue Cu surface. The very bright protrusion in the lower turn of the “J” is a Cu dimer. Image dimensions: 44 nm × 10 nm. Image conditions: 100 pA, -50 mV, 5 K.

## 1.2 Self-Assembled Monolayers

Over the last couple of decades there has been increasing interest in surface-based molecular self-assembly and applications range from sensing to lubrication.<sup>2–10</sup> However, the behavior of molecules on metal surfaces is often difficult to predict and can lead to unexpected self-assembled structures and surface restructuring. On one hand, surface science, compared with well-established fields like organic and inorganic chemistry, is a relatively new area of research that does not yet benefit from a full understanding of fundamental rules, such as those that govern molecular adsorption on and the reconstruction of surfaces. For example, in the field of organic chemistry, one or more synthetic routes to a desired molecule can often be envisioned and created using known methodologies and a vast array of available reagents.<sup>11</sup> Similarly, the spectroscopic properties of inorganic complexes can generally be predicted from a knowledge of their molecular and electronic structures.<sup>12</sup> On the other hand, due to the complexity of the apparatus and time needed to interrogate a single system, the vast majority of studies of molecular self-assembly on surfaces is confined to just one molecule or head group, thus making direct comparison of properties difficult from system to system.

Although direct comparisons of these systems have been difficult, such research on alkane thiol SAMs is growing. Alkane thiol self-assembled monolayers (SAMs) on metal surfaces provide useful structures for many applications, including electrochemical sensing of analytes, lubrication, corrosion resistance, surface patterning, the organization of molecular rotors and switches, and the interfacing of surfaces with macromolecules.<sup>2,3,13–21</sup> SAMs are examined on a variety of substrates, including coinage and platinum group metals. For example, on Cu(111), thiols adsorb *via* an activated cleavage of the S-H bond, and attractive intermolecular interactions lead to well-ordered molecular domains at high adsorbate coverage.<sup>22–24</sup> On Ag(111), tightly packed thiol overlayers were found to be incommensurate with the underlying lattice, and vacancies in the substrate surface lattice were observed post adsorption.<sup>25–28</sup> Williams and co-workers examined the assembly of alkanethiols on Pt films and determined that the molecules formed methyl-terminated, well ordered overlayers with crystalline-like structures.<sup>29</sup> Similar findings were reported by Love *et al.* for thiol assembly on Pd films.<sup>30</sup> The group also suggested that thiols decomposed by cleavage of the S-C bond to form a PdS layer between the SAM and the bulk Pd film.<sup>30</sup> Previous studies of dialkyl sulfide (thioether) SAMs on Cu,<sup>31,32</sup> Au<sup>5,33,34</sup> and highly oriented pyrolytic graphite (HOPG)<sup>35,36</sup> all showed that these molecules adsorb intact (*i.e.* without decomposition of the S-C bond) and that lateral intermolecular interactions lead to well-ordered 2D overlayers.

Additionally, coupling SAMs with other nanoscale systems such as quantum dots and nanorods has led to the design of elaborate, hierarchical structures with applications in a variety of both biological and nanoscience fields.<sup>2,3,37–39</sup> Through the alteration and functionalization of the hydrocarbon backbones, these alkane thiol

systems offer tremendous control over assembly in the dimension perpendicular to the surface.

Despite these successes, however, little influence has been gained over the assembly or chemistry in the plane of the substrate. Also of consequence, thiol-based systems suffer from defects that arise from their strong interaction with gold surfaces (the most common substrate used in SAM studies), which leads to surface restructuring. This process creates vacancies in the surface layer that aggregate into etch pits, which are known to be one of the weakest areas of self-assembled monolayers (SAMs) in terms of attack and degradation by oxidizing species.<sup>40–43</sup> Thus, surface-based systems provide an ideal platform to systematically compare and contrast the surface interaction, self-assembly and surface reconstruction of a variety of molecules with different head group chemistries. Understanding these processes provides insight into the fundamental chemical processes with promise for important practical applications. By relating these results to known trends in, for example, inorganic chemistry, one can generate some useful design rules for surface-based molecular interactions.

### 1.3 Substrate Structure

The work described herein was performed using two different single crystal metal substrates, Cu and Au, both cut to expose the (111) facet. We focus on Cu(111) and Au(111) surfaces as they are the most commonly used in the aforementioned studies due to their commercial availability, ease of preparation and resilience to contamination.<sup>2,44</sup> As shown in the STM image in Figure 1.2, the Cu(111) substrate displays atomically smooth terraces separated by monatomic step



edges 0.21 nm high. The atoms in the surface layer are in a hexagonal close-packed arrangement with an interatomic distance of 0.256 nm.

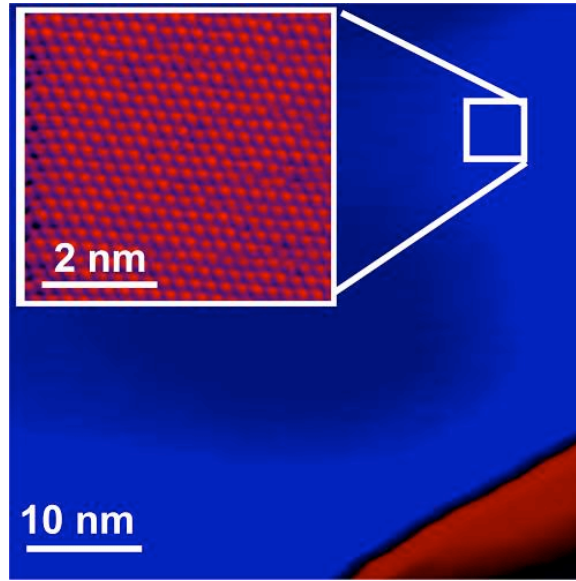


**Figure 1.2 The Cu(111) Substrate:** STM image of a clean Cu(111) substrate in which a monatomic step is visible in the lower right corner. The atomically resolved inset shows the hexagonal atomic lattice. Image conditions: 10 pA, -500 mV (inset 2 nA, 70 mV).

The atoms in the Au(111) surface are also in a hexagonal close-packed arrangement, and the bulk interatomic distance for Au is 0.288 nm. Unlike Cu, clean Au(111) surfaces adopt the  $(22 \times \sqrt{3})$ , or herringbone reconstruction, in order to compensate for the under-coordination of the surface atoms (Figure 1.3).<sup>43,45–49</sup> In this reconstruction, atoms in the surface-most atomic layer contract such that 23 Au atoms are packed into a space equivalent to 22 bulk atoms, leading to local compression in one of the three equivalent close-packed directions ( $[0\bar{1}1]$ ,  $[01\bar{1}]$ , and  $[\bar{1}01]$ ), which is referred to here as the compressed axes (yellow arrows in Figure 1.3); the interatomic spacing along the compressed axis is 0.275 nm. The three equivalent second-nearest-neighbor directions are hereafter referred to as the  $\sqrt{3}$  directions. One of these  $\sqrt{3}$  axes is perpendicular to the compressed axis and is thus

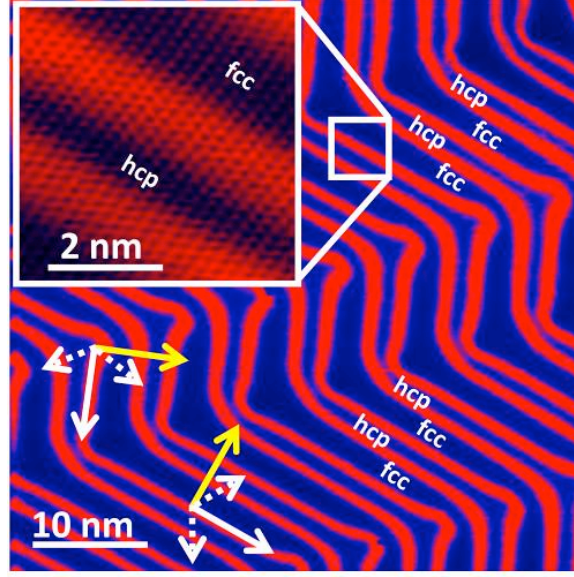


**Figure 1.3 The Au(111) Substrate:** STM image of clean Au(111) in which the herringbone reconstruction is clearly visible. The wide *fcc*-packed regions are separated from narrow *hcp*-packed regions by soliton walls (red). The yellow arrows indicate the compressed axis in each area; the solid (dashed) white arrows show the uncompressed  $\sqrt{3}$  axis (partially compressed  $\sqrt{3}$  axes) in each area. The atomically resolved inset shows the hexagonal atomic lattice. Image conditions: 50 pA, 500 mV (inset 900 pA, 50 mV).

entirely uncompressed (solid white arrows in Figure 1.3). The remaining two  $\sqrt{3}$  axes are at  $30^\circ$  angles to the compressed axis and therefore exhibit only partial compression (dashed white arrows). Because of this surface compression, there is a mismatch between the surface-most Au layer and the bulk crystal, which causes a shift in lattice packing and yields alternating bands of *fcc*- and *hcp*-registered atoms running perpendicular to the compressed axis. Regions termed the “soliton walls,” where atoms in the surface-most layer traverse bridge sites, separate *fcc*- and *hcp*-regions, as shown in Figure 1.3. These soliton walls exist in pairs referred to as herringbones. Unless the surface is artificially strained by external forces,<sup>50</sup> compression is distributed equally in all three high-symmetry directions *via* the inclusion of a secondary surface structure in which the soliton walls bend  $\pm 120^\circ$  every 15-30 nm, as seen in Figure 1.3;<sup>43,44</sup> these bends are referred to as elbows. Due

to an atomic row mismatch, the elbows act as preferential binding sites for adsorbed molecules and atoms.<sup>47,51,52</sup>

## 1.4 Molecule-Surface Interactions

Strong adsorbate-surface interactions are known to perturb the herringbone reconstruction. The expansion or “lifting” of the Au(111) herringbone occurs when the 4.5% excess atoms in the surface are ejected. As these atoms are removed, compression is relieved and the average separation between herringbones increases until the herringbone reconstruction is either partially or completely lifted. Further atom ejection leads to the formation of etch pits or vacancies in the surface. There are several phenomena that lead to lifting of gold’s herringbone reconstruction. It has been shown that applying a high electrical field,<sup>53</sup> mechanical force,<sup>45,54</sup> or even heat<sup>55</sup> to the system will lead to a reorganization, but not lifting, of the native reconstruction. Chemical species can also affect the gold surface reconstruction, but the extent of the reorganization depends entirely on the adsorbate-surface interaction strength. Some chemical species have a strong interaction with gold and, upon adsorption, completely lift the herringbone reconstruction. These strongly interacting species include alkanethiols,<sup>41,56–60</sup> sulfur,<sup>44,61–63</sup> and fullerenes.<sup>64</sup> Others such as styrene,<sup>65,66</sup> benzene,<sup>67,68</sup> and methanol<sup>69,70</sup> have a comparatively weak interaction and do not lift, but may reorganize, the reconstruction. A third class of chemical species was shown to partially lift the herringbone reconstruction, indicating that they have adsorption energies somewhere between the two previously mentioned poles.<sup>71–73</sup>

The herringbone separation can be used as a measure of the number of atoms ejected from the surface using a straightforward mathematical expression. Simply put, the native herringbone spacing of 6.34 nm corresponds to a state of having 0%

of the atoms ejected; if all excess atoms (4.5%) are ejected, the remaining atoms adopt an unreconstructed ( $1 \times 1$ ) arrangement and the herringbone reconstruction would no longer be present (spacing essentially infinite). Thus, the percentage of atoms that have been ejected from the native reconstruction ( $N$ ) can be determined by:

$$N = N_o \left( 1 - \frac{x_o}{x} \right)$$

where  $x_o$  and  $x$  are the native and observed herringbone spacing, respectively, and  $N_o$  is the 4.5% excess atoms in the native Au(111) reconstruction.

Due to the strong interaction between Au and the sulfur atoms in thiols, the herringbone reconstruction is completely lifted during thiol SAM formation.<sup>59,60</sup> Thiols interact so strongly with the resulting ( $1 \times 1$ ) surface that additional Au atoms in the surface layer are ejected, leaving behind etch pits,<sup>2,41,57–59,74–77</sup> which are known to be one of the weakest areas of the SAM films in terms of attack and degradation by oxidizing species.<sup>2,40–43</sup> Very recently, researchers discovered that the structure of the molecule-metal interface in thiol-based SAMs on Au is much more complex than first believed.<sup>41,59,74,78,79</sup> The mechanism by which thiols lift Au's herringbone is still under debate; however, Yates and co-workers showed that dimethyl dithiol SAMs evolve *via* a well-defined “stripe phase” in which the liberated Au adatoms (adsorbed atoms) are each attached to two thiolate species.<sup>41,57,58</sup> The number of Au atoms in the stripe phase is directly correlated with the number of atoms removed from the herringbone reconstruction based on the measured herringbone spacing.<sup>41</sup> Given this bonding scheme, with a 2:1 thiolate to Au adatom ratio, the formation of etch pits is expected as alkane thiol coverage increases to >0.1 monolayer, or more specifically,

when the excess 4.5% atoms in the herringbone have been depleted. Understanding the atomic-scale surface processes that occur when molecules bind to Au(111) is a crucial step towards improving current films and discovering better and more defect-free routes to the self-assembly of a variety of molecules.<sup>61</sup>

A vast number of practical systems utilize alkane thiols supported on gold surfaces. While a strong Au–S bond facilitates self-assembly, the interaction is so strong that the resulting surface overlayers are susceptible to degradation. By adjusting the molecule-surface interaction and using different head group elements, a vast array of new systems with novel properties may be formed. In this document I report on the interaction of a Au(111) surface with several chemical species; each of which was carefully chosen in order to explore how changing chemical functionality (*e.g.* the tail or head groups) affect the dynamics of molecular adsorption, self-assembly and thermal stability in a systematic manner. By performing experiments in ultra-high vacuum, the coverage-dependent behavior and the effect of temperature were studied in a controlled manner. Using STM, each system was examined as a function of molecular coverage and annealing temperature, and subtle differences in adsorption behavior were uncovered. Within this subset of molecules I make direct comparisons to chemical behavior as a function of binding group or ligand identity. The information reported herein is useful, for example, in the field of nanoscale chemical patterning based on soft and hybrid nanolithographies, in which multiple species are patterned on a surface by virtue of their different assembly properties. Microdisplacement printing of multi-component SAMs, as described by Weiss and co-workers,<sup>80</sup> utilizes several different molecules with different interaction strengths. More labile molecules are preassembled on a surface and then displaced in regions

defined by the stamp of a chemical species that assembles in a more dense fashion. My work offers new design options for such systems, as I address two key factors at play: molecule-substrate and molecule-molecule interactions.

## 1.5 Molecule Studies

Thioethers (RSR'), a similar class of molecule to thiols (RSH), remain largely unstudied to date but may offer assembly control parallel to the surface, whereas thiols assemble perpendicularly. The work presented in Chapter 3 examines the behavior of thioether molecules on Au(111) and Cu(111). These initial studies were performed at low molecular coverage in an effort to understand the factors governing adsorption and molecule-substrate interactions. Isolated thioether molecules were previously shown to rotate on surfaces, and their rotation can be switched on/off *via* changes in temperature and proximity to nearby molecules.<sup>81,82</sup> We also demonstrated that it is possible to drive molecular rotation with electrical energy supplied by the STM tip.<sup>83</sup> Thus, thioether molecular rotors show great promise as nanoscale models for exploring the fundamental limits of thermally and electrically driven molecular rotation. By using time-resolved measurements that increase the time resolution of the scanning tunneling microscope it is possible to record the dynamics of individual thioether molecular rotors as a function of surface structure, rotor chemistry, thermal energy and electrical excitation. The results demonstrate that the local surface structure can have a dramatic influence on the energy landscape experienced by the molecular rotors. Time-resolved measurement of electrically excited rotation revealed that vibrational excitation of a C–H bond in the rotor's alkyl tail is an efficient channel with which to excite rotation, and that the excitation is a one-electron process. In terms of rotor structure, altering the length of

the rotor's alkyl tails allowed the origin of the barrier to rotation to be more fully understood.

The low coverage thioether studies were followed up with a rigorous investigation of their monolayer properties. Chapter 4 offers a report of the self-assembly of dibutyl sulfide, a symmetric thioether species, on a Au(111) surface. As with thiols, dibutyl sulfide forms well-ordered monolayers, but due to the slightly weaker molecule-metal bond, the coverage and temperature-dependent behavior is very different than that of alkanethiols. Adsorption is sensitive to the different regions of the Au(111) herringbone reconstruction. Dibutyl sulfide lies parallel to the surface and forms well-ordered chains in domains that preferentially bind first in *fcc*-regions, then *hcp*-areas, and finally on soliton walls. The sulfide-Au interaction is strong enough to disrupt the native herringbone reconstruction of Au; however, unlike thiols, dibutyl sulfide adsorption does not result in etch pit formation. A monolayer of dibutyl sulfide has a very low defect density as compared to thiol SAM-based systems. This low defect density hints at the possibility of using a thioether moiety as a basis for a self-assembled system free of typical defects like etch pits, which allow attack and degradation of the monolayer. Upon annealing the surface with a high molecular coverage to >500 K, dibutyl sulfide desorbs molecularly from the less energetically favorable regions of the surface first. At this reduced coverage, the system returns to an intermediate-coverage structure, thereby demonstrating the reversibility of the assembly. Elevating the temperature further causes the entire monolayer to desorb, and the original herringbone structure of Au returns. We postulate that this reversibility, coupled with the high rate of concerted rearrangements, allows this system to reach a very high level of order.

In Chapter 5, previous work on symmetric thioether (RSR) self-assembly is extended to asymmetric thioethers (RSR'). These monolayers are chiral by virtue of the binding of one of the two pro-chiral lone pairs on the S atom to the Au surface.<sup>84</sup> Well-ordered domains of butyl methyl sulfide form due to van der Waals interactions between molecules, and the self-assembly is almost 100% enantiospecific, leading to the growth of large homochiral domains. There is a growing interest in chirality at surfaces from both a fundamental and an enantioselective reactions/separations viewpoint. With future applications in mind, I also present a study of the partially fluorinated asymmetric thioether 4,4,4-trifluorobutyl methyl sulfide (4TF-BMS) and show that despite this substitution, the same highly enantiospecific assembly leads to similar, well-ordered homochiral domains.

Chapter 6 explores a phosphine (PR<sub>3</sub>)-based system that self-assembles with surface restructuring that is markedly different than that observed with thiols. The results reveal the atomic-scale mechanism by which trimethylphosphine removes gold's native reconstruction but, unlike thiols, stops short of removing further surface atoms. The results also suggest that self-assembly may be controlled and improved by adjusting the molecule-metal bond strength *via* head group substitutions.

Chapter 7 describes a direct comparison of the self-assembly of thioether, selenoether (RSeR') and phosphine species on Au(111). Using gold's herringbone reconstruction as a sensitive readout of molecule-surface interaction strength, it is possible to correlate head group chemistry with monolayer properties. It is demonstrated that the hard/soft rules of inorganic chemistry can be used to rationalize the observed trend of molecular interaction strengths with the soft gold



surface, *i.e.*,  $P > Se > S$ . The structure of the monolayers can be explained by the geometry of the molecules in terms of dipolar, quadrupolar or van der Waals interactions between neighboring species driving the assembly of distinct ordered arrays. As this study directly compares one element with another in simple systems, it may serve as a guide for the design of self-assembled monolayers with novel structures and properties.

In Chapter 8, I examine the triphenylphosphine/Au(111) system. Phosphine-stabilized Au clusters have been extensively studied and are used in various applications due to their unique structural, catalytic and electronic properties. Triphenylphosphine ( $PPh_3$ ) is a key stabilizing ligand in the synthesis of Au nanoclusters. Yet, despite its intense use in nanoparticle synthesis protocols, little is known regarding its surface chemistry, monolayer structure, density and packing arrangement, all of which are important descriptors of functionality. Molecular adsorption of  $PPh_3$  results form very ordered structures on Au(111), and atomic-scale imaging reveals that this formation is accompanied by a partial lifting of the Au(111) surface reconstruction and ejection of extra Au atoms in the surface layer. Interestingly, these ejected atoms are trapped and stabilized as two-dimensional Au nanoislands within the molecular layer. The data illustrates  $PPh_3$ 's milder reactivity and reveals a new picture of its packing structure. These results shed new light on the surface chemistry of this important ligand for organic, organometallic and nanoparticle synthesis.

Chapter 9 describes a combined experimental and theoretical study of the adsorption and assembly of a simple dipolar molecule, 4-fluorostyrene, on both Cu and Au surfaces. Self-assembly occurs in the form of small highly polar electrets with

discrete ('magic') sizes that depend on the surface metal. Charge transfer between the molecule and surface results in a  $\sim 90^\circ$  reorientation of the electric dipole moment as compared to the gas phase molecule and a doubling of its magnitude. The magic size can be understood in terms of a balance between attractive interactions in the form of both directional C-H $\cdots$ F hydrogen bonding and van der Waals interactions as well as repulsive forces from Columbic interaction between the charged molecules. While this work illustrates the importance of interfacial charge transfer in molecular dipole engineering at surfaces, it also offers unique chiral systems that are highly regular and dipolar with which to study and understand charge and spin transfer across metal-organic interfaces.

## 1.6 Atom Studies

In a different but related set of experiments, I have examined the behavior of individual H atoms adsorbed on a Cu(111) surface. Hydrogenation reactions are central to the petrochemical, fine chemical, pharmaceutical, and food industries and are of increasing interest in energy production and storage technologies. The processes of molecular adsorption, dissociation, diffusion, association, and desorption are important surface phenomena in these heterogeneously catalyzed reactions. Given that molecular hydrogen (H<sub>2</sub>) dissociation is often the rate-limiting step for hydrogenation, one strategy to improve and study reactivity is to engineer the minimal catalytic ensemble that will activate H<sub>2</sub> but leave the other reactants untouched. The Pd/Cu(111) surface alloy system described in Chapter 10 offers low dissociation barriers at the Pd sites and weak binding on the Cu terraces. In terms of adsorption, these Pd atoms significantly lower the barrier to H<sub>2</sub> dissociation and

allow the spillover of H atoms onto the Cu surface where they are available for further reaction.<sup>85</sup>

Chapter 10 describes the assembly geometries of Pd atoms in the bimetallic Pd/Cu(111) surface alloy. This system has been extensively studied in the past due to the interesting catalytic properties of the PdCu alloy; however, despite the many reports describing the overall structure, local geometry, and electronic structure of this surface alloy, nearest neighbor Pd-Pd geometries were not observed.<sup>85–90</sup> In fact, some reports explicitly state that nearest neighbor Pd assemblies (*i.e.*, dimers, trimers, etc.) are negligible or simply “do not exist.”<sup>86,89</sup> Chapter 10, demonstrates that Pd-Pd nearest neighbor dimers and trimers do exist, and that their populations become statistically relevant (*i.e.*, >5% abundance) at Pd concentrations as low as 10%. These results are of potential interest for future catalytic studies in which reaction precursors may require specific active site geometry for binding and subsequent reaction.

This system also offers the opportunity to study the diffusion, association, and assembly of large quantities of H and D on the Cu(111) surface, as described in Chapter 11. The diffusion properties of H and D on the Cu surface are explored through careful low-temperature STM tracking experiments. STM and Density Functional Theory (DFT) measurements show that quantum-tunneling effects dominate H(D) diffusion on Cu(111) at 5 K. With this direct visualization and quantification of quantum tunneling effects in adatom diffusion, two types of weak interaction between H adatoms that lead to assembly into small clusters and larger assemblies of small clusters are revealed. The self-assembly of H into large islands is, in fact, a tunneling effect resulting from inter-atom energy being much smaller than

the diffusion barrier. DFT calculations provide estimates for both diffusion and interaction energies; theory also predicts quantum-tunneling probabilities that agree well with experiment. To the best of my knowledge, this finding is the first evidence for tunneling driven assembly.

## 2 Experimental Methods

### 2.1 Low-Temperature Scanning Tunneling Microscopy

#### 2.1.1 Instrumentation

All STM experiments described in this report were performed with a low-temperature scanning tunneling microscope (LT-STM) built by Omicron Nanotechnology.<sup>91</sup> The STM stage is cryogenically cooled using a dual-stage cryostat (static bath), with the temperature determined by the type of coolant used. For operation at 78 K, both dewars are filled with liquid N<sub>2</sub>, while for operation at 5 K, the inner dewar is filled with liquid He and the outer dewar is filled with liquid N<sub>2</sub>. The coolant hold time of the instrument is ~17 hours at 78 K and ~20 hours at 5 K. The STM stage is equipped with a sample heater capable of controlled heating of the sample and tip up to 40 K above the base temperature of 5 K.

The LT-STM is operated in ultra-high vacuum (UHV), and the system that houses the STM includes a preparation (prep) chamber and a low-temperature (LT) chamber. A manual gate valve separates the prep and LT chambers. The chambers are pumped down from atmospheric pressures using a turbo molecular pump backed by a two-stage rotary pump. A pneumatic gate valve separates the turbo pump and the vacuum chamber. The lower limit for the turbo pump is in the 10<sup>-8</sup> mbar range. Typical operating pressure in the prep chamber reaches 10<sup>-9</sup> to 10<sup>-10</sup> mbar and is achieved using an ion getter pump and a titanium sublimation pump (TSP). The pressure in the LT chamber is typically 10<sup>-11</sup> to 10<sup>-12</sup> mbar, also achieved with an ion pump and TSP aided by cryogenic pumping at low temperature. The ion pumps should not be operated unless the pressure is  $<5 \times 10^{-8}$  mbar in order to extend their

lifetime. The TSP should not be operated in the LT chamber while cold to avoid rapid evaporation of the coolant and possible explosion of the dewar. Also, the TSP should not be operated in the prep chamber when a clean sample is present, as titanium could potentially be deposited on the sample. All pressures are read using an ion gauge with a W filament. STM samples and tips are introduced to the vacuum chamber *via* a load-lock attached to the prep chamber; the load-lock is separated from the prep chamber by a manual gate valve and can be independently pumped using the turbo pump. Whenever operating any pump or opening any valve on the STM chamber, common sense should be used to avoid accidental venting of the instrument.

The STM chambers require baking following exposure to atmospheric pressure in order to desorb any unwanted contaminants, including water. Prior to baking out all plastic and electronic cables should be removed from the exterior of the instrument; the ion gauge and TSP cables are both bakeable, as are the black valves attached to vent valves. Also, all windows should be covered with foil. If the entire instrument, *i.e.*, LT and prep chambers, has been vented, the bake-out is performed using the bake-out shields provided from Omicron. The bake-out is typically set to a maximum temperature of 130 °C and continues for at least 48 h. If only the prep chamber has been vented, the prep chamber is evenly wrapped in heating tape and aluminum foil. Thermocouples are attached to several locations on the prep chamber to monitor the bake-out temperature. Variacs are used to control the heating tape power, and the chamber is heated to a maximum temperature of 130 °C; once this temperature is reached, bake-out continues for a minimum of 24 hours. The chambers should cool completely before further experiments are begun.

### 2.1.2 Tip Preparation

STM images were acquired with atomically sharp metal tips, including etched W, etched Ni and cut Pt/Ir (80/20) tips. W tips were purchased from Omicron or Veeco. Omicron tips arrived pre-loaded into Omicron tip-holders compatible with our instrument. Ni and Pt/Ir tips were prepared in house using wire purchased from Goodfellow; procedures for preparing the Ni and Pt/It STM tips have been described in detail elsewhere.<sup>92,93</sup> The “loose” tips were manually loaded into Omicron tip-holders as shown in Figure 2.1. Briefly, while carefully holding the tip, sharp side oriented away from the holder, the researcher lowers the blunt end of the tip into the opening of the tip-column. When the blunt end of the tip is inside the opening, the researcher can release the tweezers so that the tip glides into the column of the holder. If the tip has been cut to the appropriate length, the sharp end should protrude a short distance ( $\sim 1$  mm) above the opening of the tip-column. If the tip is too long, it can be removed with tweezers and trimmed from the blunt end. If the tip is too short, it is best to start with a different tip. When the tip is in place, the researcher should lock its position by crimping the tip-column with wire cutters, being careful not to shear the entire assembly. Once the tip-column is crimped, invert the tip holder and tap it a few times with the tweezers or a gloved finger to ensure that the tip does not fall out. The entire assembly should be rinsed with ethanol prior to being introduced to the vacuum chamber *via* the load-lock. If the sharp end of the tip is touched, dropped, or otherwise compromised, it is advisable to start with a new tip for maximum chance of scanning success.

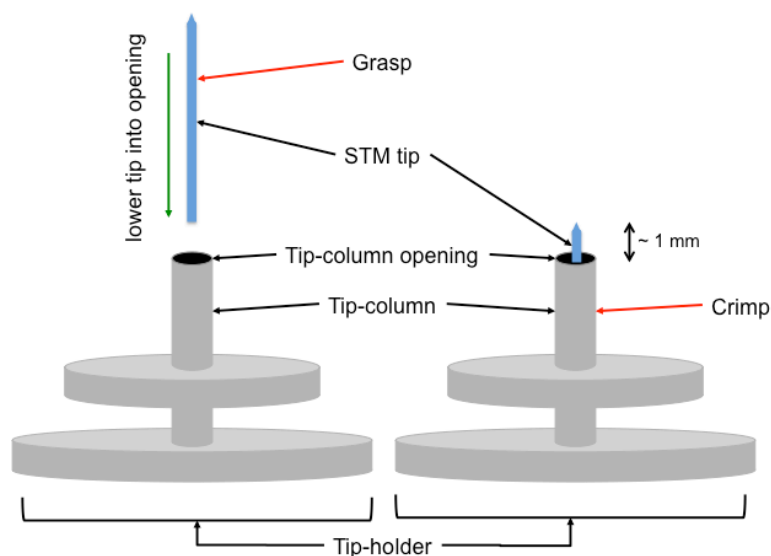


**Figure 2.1 STM Tip Preparation with Omicron Tip Holder:** Schematic showing the procedure for loading an STM tip into an Omicron tip holder. Tweezers should be used to grasp the tip at or below the point indicated, and the tip should be carefully lowered into the tip-column opening. Wire cutters should be used to crimp the tip-column where indicated once the tip is in place. The sharp end of the tip should extend no more than  $\sim 1$  mm above the tip-column opening.

### 2.1.3 STM Imaging

STM images were obtained using the Matrix software package provided by Omicron. This powerful software allows the user to perform imaging, spectroscopy and atomic manipulation all with the click of a button. There are also several built-in tip-conditioning procedures that aid in STM tip preparation as well. The functions of Matrix are described in detail in the software manual, and will not be elaborated upon here.

STM imaging with Matrix is designed to operate well when paired with most Omicron instruments. Upon loading Matrix, the user must select the appropriate instrument type and coolant variant. The instrument is capable of scanning in the  $+10$  to  $-10$  V range; however, depending on project goals, the voltage range can be set to  $\pm 10$  V or  $\pm 1$  V. For example, if the project involves investigating the



geometry or electronic properties of a metal alloy system (case 1), low voltages are often required to access electronic states near the Fermi Level. In this case, the  $\pm 1$  V range should be used so that the instrument is not at the extreme end of the set point limits. If the project involves scanning molecular overlayers (case 2), it is sometimes desired to scan at higher voltages to access different molecular states, and the  $\pm 10$  V range can be used. The tunneling current range can also be toggled between 1 pA – 3.3 nA versus 1-333 nA. For case 1 above, either current range can be employed; if atomic resolution is the goal, the higher current range offers more signal and a better opportunity for success. For case 2 above, low currents are preferred. As the current increases, the tip approaches the surface; if the tip gets too close, molecules may interact or be picked up by the tip, making imaging difficult. Again, the range setting should be toggled so that the instrument is not scanning at extreme limits. For example, asking for  $I_t = 5$  pA in the 1-333 nA range may result in a fuzzy, unusable image, but, it is more likely that the tip would not be able to detect this low setpoint and would not approach the sample properly.

The most common problem that arose during STM imaging was in the form of elevated noise levels within the image that made data analysis difficult. Noise typically was caused by mechanical vibrations due to physical contact between the STM stage and the surrounding instrument. The tunneling current is proportional to  $\exp(-2kz)$ , where  $z$  is the tip-surface separation, and  $k$  is a constant. Thus, any mechanical vibrations that changes  $z$  also causes a change in the tunneling current ( $I_t$ ), as outlined in equation below, and may have a detrimental effect on image quality.

$$dI_t \propto I_t \times dz$$

A quick test to identify mechanical noise is to compare the noise peak-to-peak amplitude at different scanning currents; if the mechanical coupling of vibrations is the culprit, the noise amplitude will be proportional to the current setpoint. Repositioning the port-aligners on the tower above the STM stage or the air legs that lift the table often solves this problem. A note for new users: it is important that when the stage is dropped into tunneling position that it appears to hang freely on the springs without resting against the interior wall in order to reduce the chance for vibrational/mechanical noise. As the tip is moved back and forth within the scan area, the sample should appear to glide in the opposite direction as the center of gravity of the stage assembly shifts. If the sample does not appear to move freely, further adjustments may be required.

Electrical noise is more difficult to diagnose and its source often remains a mystery. The most frequently encountered source of electronic noise in the Sykes Lab arises from problems with connections on the airside of the instrument. For example, the tunneling ( $I_t$ ) wire that carries the tip voltage and tunneling current between the STM tip and the exterior electronics box is shielded by the  $I_0$  wire. If one of these wires is severed or shorted, data collection can be compromised or completely halted. Such problems can be quickly fixed either by in-house repair or part substitution if they originate outside of the instrument. However, wiring problems inside the instrument must be handled Omicron service personnel. If not readily resolved within 1-2 days, electronic noise issues should be tackled by STM users in conjunction with Omicron technicians. Any changes to the STM electronics

box or cables should be discussed with Omicron technicians in order to avoid any unforeseen incompatibilities.

## 2.2 Sample Preparation

### 2.2.1 *Preparing Single-Crystal Metal Surfaces*

As these experiments are highly dependent on surface cleanliness, a reliable preparation of the metal crystals prior to each experiment was necessary. For the purpose of sample cleaning the prep chamber is equipped with an ISE 5 Ion Source, operated by the NG ISE 5 Control Unit, as well as resistive heating of the sample using a power supply by Delta Elektronika. The operation and maintenance of these devices has been described in detail elsewhere.<sup>94</sup> The most common problems associated with the cleaning peripherals arise from user error (*i.e.*, wiring not properly connected) and periodic failure of the ion source due to metallization of the insulating ceramics within the device. The Au(111) and Cu(111) samples purchased from MaTeck were prepared under vacuum by cycles of Ar<sup>+</sup> sputtering (1.0 keV/15  $\mu$ A) and annealing to  $\sim$ 1000 K. Between each STM experiment the crystals were prepared by two sputter/anneal cycles. After the final anneal, the crystals were transferred to the LT chamber within 5 min. to the pre-cooled STM stage. The sample cooled from room temperature to 78 K or 5 K within  $\sim$ 1 hour. Sample cleanliness was confirmed by STM imaging.

### 2.2.2 *Molecular Dosing*

The majority of the work described herein required the deposition of chemical species from solid, liquid or gas phase onto a metal sample. The species examined were deposited onto the cold sample (78 K or 5 K) *via* a collimated doser attached to

a precision leak valve. The dose amounts were calculated in Langmuir (L,  $10^{-6}$  Torr·s), and were calibrated using the ionization cross-section of the analyte in use and the ion gauge sensitivity.

Annealing treatments below 300 K were performed in the LT chamber by removing the sample from the cold STM stage and placing it into a room temperature sample holder at the edge of the chamber. The temperatures attained using this procedure were determined by the total anneal time and were calculated from thermal diffusion studies of dimethyl sulfide on Cu(111).<sup>32</sup> Annealing treatments above 300 K were performed in the prep chamber by resistively heating the sample to the target temperature.

### *2.2.3 Metal Deposition*

Chapter 10 describes a detailed investigation of the atomic scale geometry of the Pd/Cu(111) surface alloys. The alloys were prepared in the prep chamber using an Omicron Focus EFM 3 (EFM3) electron beam evaporator (Figure 2.2), controlled by the EVC 300 power supply. The EFM3 employs a Th/W (5/95) filament (W can be used if the alloy is not available), which is resistively heated to induce atomization (evaporation) of a nearby deposition source. The source material is connected to the high voltage ( $HV$ ) feed through, and its lateral position with respect to the filament can be controlled using a bellowed connector with a range of  $\sim 25$  mm. Water cooling during sample preparation helps to ensure low background pressure (typically in the  $10^{-10}$  mbar range) during evaporation, which helps to safeguard against contamination. In the Sykes Lab, the EFM3 is always set up with the shutter open to avoid breaking the shutter mechanism from overuse, and each evaporant is

connected to the  $HV$  feed through using a Mo barrel connector purchased separately from Omicron (part number B001259-S).

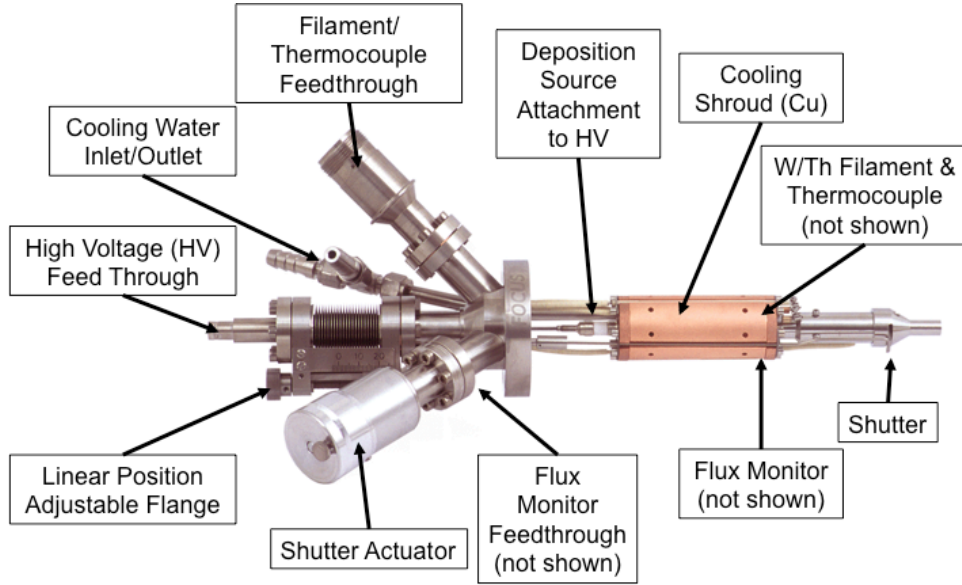


**Figure 2.2 Electron Beam Evaporator:** Schematic of the Focus EFM3 electron beam evaporator from Omicron NanoTechnology.<sup>95</sup>

Upon installation, and after venting or baking the prep chamber, it was necessary to degas the EFM3 and the evaporant itself; this procedure helped ensure clean (*i.e.*, high purity) depositions and low background pressures. Prior to degassing the EFM3, the user should turn on the turbo pump, but leave the pneumatic valve closed. Degasing the EFM3 assembly can be done using filament heating or evaporant heating, and should be performed without water-cooling so that the entire instrument is allowed to reach high temperatures (200-300 °C) and contaminants, such as water, will desorb. For filament heating, the  $HV$  remains at 0 V, and the filament current ( $I_{FIL}$ ) is increased to 2.1 A. For evaporant heating,  $HV$  is set to 200 V, and  $I_{FIL}$  is increased until the emission current ( $I_{EIS}$ ) reaches 5 mA (emission power  $\sim 1$  W). It is important that the chamber pressure not exceed  $10^{-6}$  mbar during the degas procedure and that the EFM3 temperature not exceed 300 °C. If the

pressure exceeds  $10^{-9}$  mbar during the degas procedure, pumping should be switched from the ion pump to the turbo pump by powering down the ion pump and then opening the pneumatic gate valve. Degassing of the EFM3 should be performed for a minimum of 3 h.

The Pd evaporant (Goodfellow, 99.95%) used in these experiments is a metal rod, 2 mm in diameter and cut to 45 mm in order to fit within the EFM3 without hitting the filament. Degassing the evaporant was done following the same procedure as for deposition (described below), but without the Cu sample in the beam path. For Pd degassing,  $HV$  was set to 920 V and  $I_{FIL}$  increased until  $I_{EMIS}$  reached  $\sim 13$  mA; these conditions were maintained until the target flux current ( $I_F$ ) stabilized.

The following describes Pd/Cu(111) sample preparation. Prior to Pd deposition, the Cu crystal was prepared as previously described and transferred to the cooled STM stage for pre-characterization. Typically, the prep chamber was allowed to pump down overnight in order to ensure that the base pressure was  $< 5 \times 10^{-10}$  mbar prior to deposition of the active metal (Pd). The clean Cu sample was transferred to the pre-deposition position in the prep chamber and heated to a sample temperature ( $T_s$ ) of  $\sim 600$  K in order to desorb any unwanted adsorbates. While the sample was heating, evaporation was started using the EFM3 with a target  $I_F = 10.4$  nA ( $\sim 0.05$  monolayers/min). Typical settings were  $HV = 920$  V,  $I_{FIL} \sim 2.02$  A, and  $I_{EMIS} \sim 13$  mA. Once the target  $I_F$  was reached, it was maintained by pressing the “AUTO” button on the EVC 300; the power supply then automatically maintained a constant  $I_F$  by varying  $HV$ . When  $T_s = 10.0$  mV, the sample heater was turned off and the sample moved to deposition position with  $\theta = 356^\circ$ , and when  $T_s = 6.8$  mV, the

sample was turned to face the EFM3 ( $\theta = 225^\circ$ ), and Pd was deposited for 125 s. During heating and evaporation, the background pressure in the preparation chamber remained in the  $10^{-10}$  mbar range and typically increased by only  $\sim 2 \times 10^{-10}$  mbar. The procedure described above yields a Pd coverage of  $\sim 10\%$ , which could be varied by adjusting the  $I_F$  and/or deposition time (preferred), as described in Chapter 10. The sample was then transferred to the pre-cooled STM stage where Pd coverage was quantified using atomically resolved STM images as described in Chapter 10.

If, over time, the  $I_{FIL}$  required to achieve  $I_F = 10.4$  nA or  $I_{EMIS}$  deviated significantly from 2.0 A, it was necessary to reposition the evaporant using the linear adjustor to move the sample evaporant closer to the filament or to replace the evaporant for a new source entirely. Other problems that may lead to difficulties evaporating (*i.e.*, broken filament) were uncommon; refer to the EFM3 User Manual for instructions on resolving these types of issues.

## 2.3 Single-Molecule and Single-Atom Studies

### 2.3.1 *Single Molecule Rotation*

#### 2.3.1.1 Time-Resolved Measurements

Chapter 3 describes a study in which the rotation of single molecules is investigated. In order to characterize the rotation rates of single thioether molecules, tunneling current *versus* time ( $I$  *vs*  $t$ ) experiments were performed. The feedback loop (which adjusts the STM tip-sample distance to maintain a constant tunneling current during imaging) was turned off during the  $I$  *vs*  $t$  measurements. As the molecules rotated, the alkyl tails passed under the STM tip causing changes in the tunneling current. If the tip was placed just to the side of one of the six lobes of the hexagonal

shape of the spinning molecule, the tunneling current was observed to fluctuate between three discrete values.<sup>81</sup>

By using  $I$  vs  $t$  spectroscopy the rate and directionality of molecular rotations can be obtained on a time-scale  $> 1,000$  Hz. This allows for the characterization of molecular rotation with a resolution beyond what is achievable using STM imaging alone. Providing that one is consistent with the assignment of current levels to specific orientations of the molecule under investigation, it is possible to determine which way the molecule is rotating. In order to characterize the overall directionality of rotation, switches were labeled as positive (+) or negative (-), depending on the sequence of current levels. For example, a switch from orientation  $a$  to orientation  $b$  would be labeled as (+) and a  $b \rightarrow a$  switch as (-). The relative abundance (+) and (-) switches indicated the degree to which rotation was unidirectional (*i.e.*, more clockwise or anti-clockwise) within a particular data set. This approach of characterizing molecular rotation has its flaws, which will not be discussed here, and has since been modified as described by Tierney *et al.*<sup>96</sup>

#### 2.3.1.2 Automated Switch Counting

The  $I$  vs  $t$  curves generated with the feedback loop disabled often contained thousands of data points and hundreds to thousands of tunneling current changes, each representing a molecular reorientation, or “switch.” For a graduate student collecting statistical data for many different molecules, counting these switches by hand would be a time consuming and daunting task. To that end, a computer program was developed that quantifies the number of switches in each  $I$  vs  $t$  data set based on a set of user defined inputs for the tunneling current range of each



molecular orientation (or “state”). Each curve was initially examined by lab-personnel and a current range (“bin”) for each state was defined and added to the program which then counted the number of switches within the curve. The program interrogated each point within the curve to determine if it fit within one of the defined bins, and if not, the point was excluded from the data set. The program then compared consecutive points, ignoring excluded points; if consecutive points did not fall within the same bin, the computer recorded a switch. For example, if there were two bins defined as  $a$  and  $b$ , consecutive points ( $a-a-a$ ) or ( $b-b-b$ ) would not be counted as a switch, nor would points with the same bin assignment separated by an excluded point(s) ( $a-null-a$ ). However, ( $a-a-b$ ) would be counted as one switch, and ( $a-b-a$ ) would be counted as two switches.

The computer program also labeled each switch as positive (+) or negative (-) depending on the user defined sequence of orientational switches. Each  $I$  vs  $t$  curve was assessed and its output reported the total number of (+) and (-) switches which could be equated to rotations in opposite directions (*i.e.*, clockwise or anti-clockwise). A more sophisticated program, which will not be discussed in this document, has since replaced the automated switch-counting program described above.

### 2.3.1.3 Arrhenius Data

In order to investigate the energetic barriers for individual molecular rotors Arrhenius experiments were performed. The rates of rotation for individual rotors as a function of temperature were obtained by performing  $I$  vs  $t$  experiments at a variety of temperatures. In order to determine a rate of rotation at each temperature for the Arrhenius plots presented Chapter 3, the number of changes in tunneling current

were counted within the  $I$  vs  $t$  curves by hand and the number of “switches” was divided by the total time.

### 2.3.2 *Single Atom Diffusion*

Chapter 10 describes the assembly and diffusion of H and D atoms on Cu(111); diffusion data were obtained exclusively from STM images. These measurements presented unique challenges due to (1) the fast diffusion rate of isolated H atoms and (2) the short hop distance between neighboring lattice sites. Thus, it became increasingly important to maximize the spatial and temporal resolution of the instrument. The data acquisition software, Matrix, allows these parameters to be controlled through a set of defined inputs. The spatial resolution ( $Q$ ) of STM images is determined using the equation  $Q = s/(lp)$ , where  $s$  is the scan area,  $l$  is the number of lines recorded, and  $p$  is the number of pixels recorded per line. The time resolution is determined by the parameter “T-raster” (raster time), which controls the time lapse between points. The time per line ( $T_L$ ) is calculated by  $T_L = T_R p$ , where  $T_R$  is the raster time. Under typical scanning conditions, the instrument records data as the tip moves “forward and backward” (x-direction) and “up and down” (y-direction) across the area of interest. As such, each data file contains four images: Up Trace, Up Retrace, Down Trace and Down Retrace, where “Trace” is the forward scan and “Retrace” is the backward scan. The total time required for a complete data scan ( $T_S$ ) consisting of four images can be calculated by  $T_S = 4T_R p l$ .

The lowest energy adsorption site for H(D) on Cu(111) is in a three-fold hollow, and the shortest diffusion distance is to a neighboring three-fold hollow site, or 0.148 nm. Deuterium atoms diffused relatively slowly, and it was possible to characterize

the distance moved for >100 diffusion events. In order to capture these short-length diffusion events, the scan size was set to  $7 \times 7 \text{ nm}^2$  or smaller, and the number of points and lines were each set to 400, giving a spatial resolution of  $\leq 0.0003 \text{ nm}^2$ . Conversely, isolated hydrogen atoms diffused rapidly and appeared in STM images as streaks. Even with very fast scanning rates (*i.e.*, 7 s/image) it was not possible to capture an image of a complete H atom before it moved on the surface; however, it was possible to determine the residence time ( $\tau$ ) of the atom before it moved by  $\tau = (2n-1)pT_R$ , where  $n$  is the number of lines over which the atom was stationary. The rate of diffusion ( $r$ ) can then be calculated by fitting the residence time data to an exponential,  $y = \alpha \exp(-rt)$ , where  $y$  is the number of events in a given time bin and  $\alpha$  is a pre-factor that depends on the number of points and the chosen time bin. The results of these measurements are summarized in Chapter 11.

## 2.4 Surface Reconstruction Studies

### 2.4.1 Herringbone Separation Characterization

As previously described in the Introduction (Chapter 1), the clean Au(111) substrate exhibits the unique  $22 \times \sqrt{3}$  or “herringbone” unit cell. This surface reconstruction presents as a highly regular, periodic array of stacking faults with areas of *fcc*- and *hcp*-packed atoms separated by atoms traversing bridge sites in the layer beneath. The bridge site atoms comprise the “soliton walls” which are topographically higher than surrounding atoms by  $\sim 20 \text{ pm}$ , and appear as bright lines in STM images (Figure 2.3). Chapter 1 also described the process whereby the herringbone separation can be lifted, and Chapters 4-8 describe the behavior of several molecular systems on Au(111) as a function of coverage and anneal

temperature. In the studies presented, the herringbone separation is used as a sensitive readout of the molecule-surface interaction strength. The herringbone separations reported in these studies correspond to the average measured spacing between herringbone pairs in the compressed, close-packed  $[\bar{1}\bar{1}0]$  direction, perpendicular to the soliton wall, which runs along the uncompressed  $[\bar{1}\bar{1}\bar{2}]$  direction.

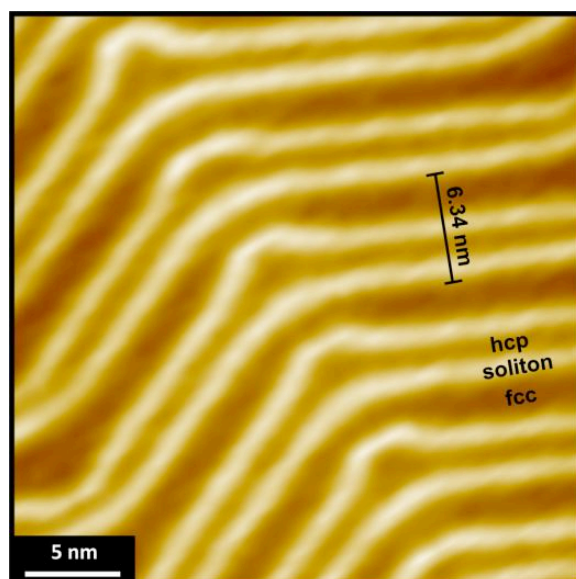


**Figure 2.3 Herringbone Separation on Clean Au(111):** Clean Au(111) with different stacking configurations identified. The native herringbone spacing is 6.34 nm, as indicated. Image conditions: 78 K, 1.5 nA, 0.1 V.

The average herringbone separation in a given system can be determined using the Scanning Probe Image Processor (SPIP) software package from Image Metrology. This program is the primary software used in the Sykes Lab for data processing. The procedure described below is meant for a moderately experienced user, familiar with basic SPIP operations. An image is loaded into the program and plane flattened as usual. The image gain correction factors should be applied to the image using the “Properties” dialog. Using the “Angle Tool” on the “Markers

'Toolbar' align one leg parallel to the soliton wall, and determine the normal ( $90^\circ$ ) direction with the other leg; this line corresponds to the compressed, close-packed direction. Then place a line scan with the "Single Line Profiling Tool" from the "Markers Toolbar" to bring up a topographic line scan. Figure 2.4 shows two STM images in which butyl methyl sulfide is adsorbed on a Au(111) surface at different coverages. In Figure 2.4A, the soliton walls are free of molecules and thus appear topographically lower than the surrounding area, while in Figure 2.4B the soliton walls are covered by the molecular domain and appear as protrusions. The blue and red lines in Figure 2.4A and B, respectively, run along the close-packed direction perpendicular to the soliton walls; the topography along the two lines are shown in Figure 2.4C and D, respectively. The green arrows in A and B, and the green circles in C and D, indicate the points where the herringbone measurements were made. For the image in Figure 2.4A, the measured distances are 23.42 nm, 10.84 nm, and 10.15 nm, for an average separation of 14.8 nm; the measured distances for the image in Figure 2.4B are 8.85 nm and 8.75 nm, for an average of 8.80 nm. For an accurate determination of the herringbone separation in a given system, these measurements should be made over several images and in each of the three close-packed directions, where appropriate.

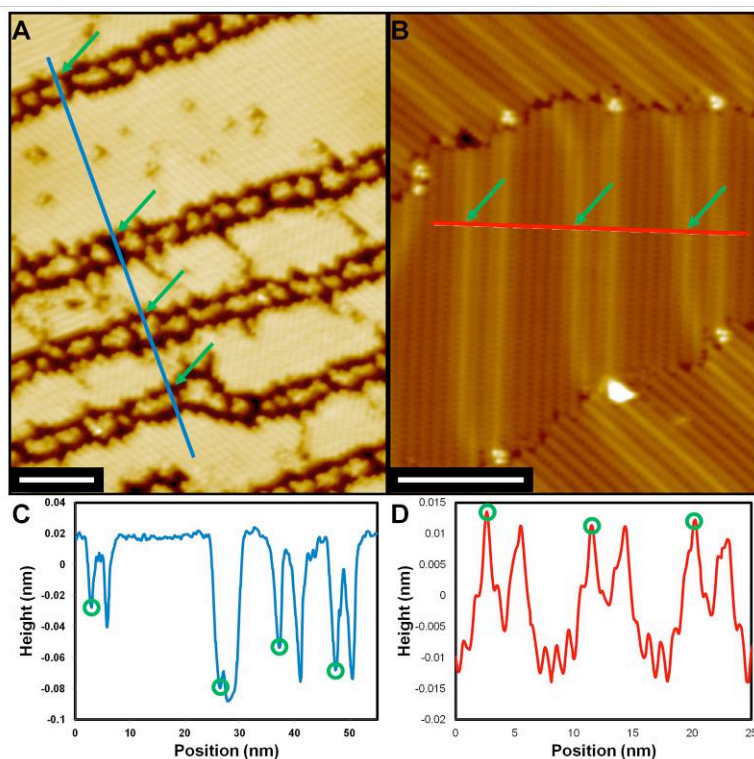


**Figure 2.4 Measuring the Herringbone Separation using SPIP:** STM images of butyl methyl sulfide on Au(111) at (A) near and (B) full monolayer coverage. These images can be used to measure the herringbone separation in these systems. The topographic line scans in (C) and (D) are from the indicated portions of (A) and (B), respectively. Scale bars = 10 nm. Image Conditions: 78 K, 50 pA, 100 mV.

#### 2.4.2 Gold Island Characterization

The expansion of Au's herringbone reconstruction occurs concomitantly with ejection of Au atoms from the surface layer (see Chapter 1). As will be shown in subsequent chapters, the process of atom ejection is activated and depends on temperature and molecular coverage. Depending on overlayer density, the ejected atoms can either be trapped as isolated adatoms, diffuse to coalesce into islands on terraces, or migrate to nearby step-edges where they are indistinguishable from the original step in STM images. In the same way that the herringbone separation can be used to quantify the percentage of atoms that were removed from the surface ( $N$ ), if islands are present, the island coverage in a system can be used as a partial measure

of  $N$ , especially when one desires to determine the fate of expelled atoms (*i.e.*, did atoms all go into islands, or have some diffused to steps, etc.?).

The Au island coverage and individual island sizes can also be determined using SPIP. An image is loaded into the program and plane flattened as usual. The image gain correction factors should be applied to the image using the “Properties” dialog. It is best to use images with no steps so that island will be easier for SPIP to identify. The image in Figure 2.5A has been cropped from a larger image and features several Au islands in the trimethylphosphine/Au system (described in detail in Chapter 6). The island size and coverage can be analyzed within SPIP by two different methods, the “Circle Measurement Method” (Circle) in Figure 2.5B and C, and the “Grain Analysis Method” (Grain) in Figure 2.5D-F. The Circle method uses the “Ellipse/Circle Measure Tool” on the “Measure Toolbar”. The user chooses the tool and then circles the islands on the image itself (Figure 2.5B), manually determining the island perimeter and boundary. This action will open a “Measure Result” window where the user can choose and view the parameters to be displayed (Figure 2.5C). The output data can be directly copied and pasted from the Measure Results window into another document or can be saved in a SPIP specific format to be opened later within SPIP. For the Grain Method, the user chooses “Activate the Grain Analysis

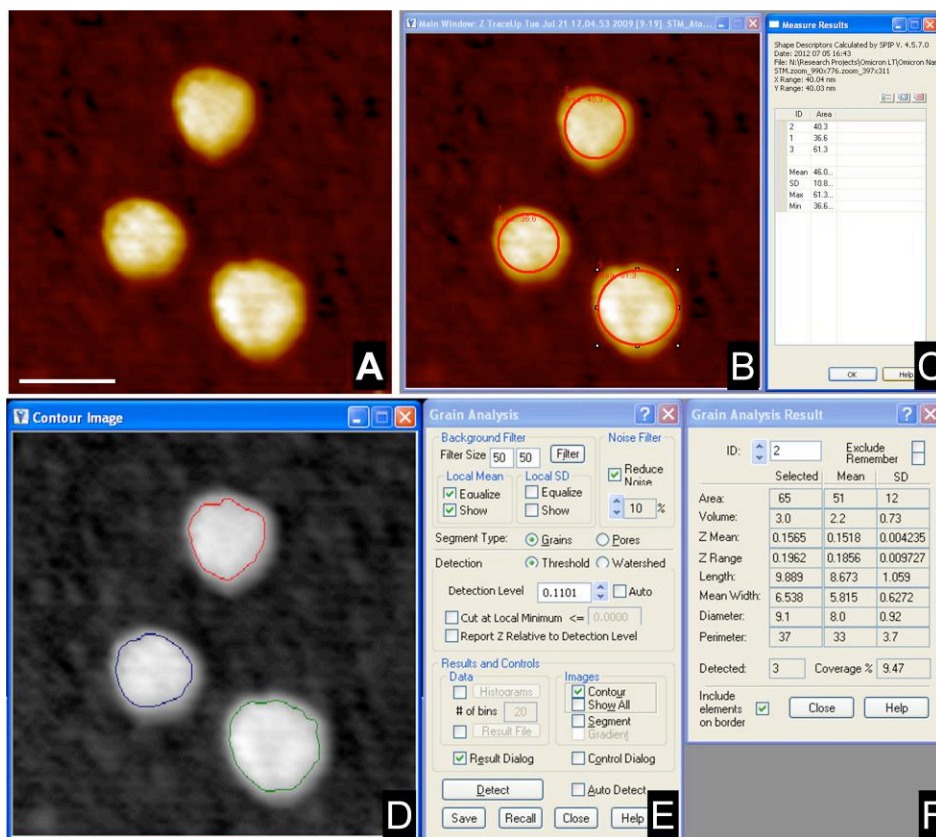


**Figure 2.5 Gold Island Area and Coverage Analysis:** (A) STM image of Au islands in the trimethylphosphine/Au system. The Circle Analysis Method for determining island sizes and island coverage is shown in (B) and (C) and the Grain Analysis Method is shown in (D-F). Scale Bar = 10 nm. Image conditions: 300 pA, 200 mV.

Dialog” on the “Analysis Toolbar”. The program will automatically detect a “threshold” value based on the current image; the threshold is a topographic height (z-value) used as a cutoff parameter for island detection. SPM will display a new image with the detected island features outlined (Figure 2.5D). The user can also manually input a threshold value by un-clicking the “Auto” toggle box next to “Detection Limit” within the Grain Analysis dialog (Figure 2.5E). The user should click the “Result Dialog” toggle box to open the “Grain Analysis Report” window (Figure 2.5F). In the Grain Analysis dialog window the user can also choose to have a result file generated in which feature dimensions are reported. To view the options



for the result file click the check box next to the “Result File” button under “Results and Controls > Data” in the Grain Analysis dialog box. This action will open a new window where you can choose and view the parameters to be saved.

For the image in Figure 2.5A, the Circle Method yields an island coverage of 8.6%, while the Grain Method gives 9.5%. Note that this image was chosen to illustrate the procedure and does not reflect the true island coverage for this system. To get an accurate measure of average island size and island coverage one must consider many images, including areas free of islands, and choose a threshold detection limit (and island boundary) that best matches the tip shape and image resolution. Having this process automated as in the Grain Method typically results in more reliable results.

### 3 Time-Resolved Studies of Individual Molecular Rotors

#### 3.1 Introduction

Since its invention in 1981, the scanning tunneling microscope (STM) has been used to study a myriad of problems in surface chemistry, physics and nanoscience. The STM's atomic-scale resolution coupled with its ability to both track the motion of surface-bound molecules over time and position them accurately has opened many novel methods with which to study important nanoscale phenomena. One major limitation of STM imaging is the time resolution; conventional STMs record images over a period of a couple of minutes, giving a time resolution of  $\sim 0.01$  Hz. This is due to the limited bandwidth of the preamplifier that amplifies the tunneling current and enables the feedback loop to prevent the STM tip from crashing into the surface. The ability to image and record the progression of events on a surface in real time would provide unprecedented insight into the fundamental mechanisms of many important surface processes from nanoscience to catalysis. However, often the phenomena which interest surface scientists (*i.e.*, diffusion, nucleation, reaction and surface reconstruction) occur on much faster timescales than conventional STM imaging can record.<sup>97</sup>

Recent advances in fast-scanning STM technology, including the construction of very small STM heads using stiff materials with high resonant frequencies, have allowed for an increase in image acquisition rate up to  $\sim 100$  Hz.<sup>98–101</sup> A second option for tracking the dynamics of fast processes, pioneered by Don Eigler, involves lowering the sample temperature so that the processes being studied occur at a much lower rate. For example, a process that occurs at  $10^{10}$  Hz at room

temperature would take place less than once per minute if the system was cooled to 5 K. While low- and variable-temperature approaches have been very successful over the last 15 years, they are based on the assumption that molecular dynamics and surface structure are identical at the high and low temperatures.

Another option for increasing the time resolution of the STM involves direct measurement of the tunneling current with the feedback loop turned off. With this approach, changes in tunneling current can be correlated to conformational or positional changes of the molecule directly below (or in proximity to) the STM tip. The approach of measuring the tunneling current over time, allows the dynamics of single molecules to be tracked with sub-nanometer precision and with a time resolution  $>1,000$  Hz. Researchers have used this approach to measure processes as fast as 20,000 Hz.<sup>81,102–120</sup> Our group has successfully exploited this fast measurement technique to study and characterize the dynamics of single molecule rotors.

Our research in this field is aimed at uncovering the fundamental workings of surface-bound molecular rotors and investigating methods for directing their motion. In nature, molecular motors perform tasks such as powering the motion of individual cells (*i.e.*, the bacterial flagellar motor), organizing the cellular cytoplasm by vesicle transport (*i.e.*, kinesin or dynein), and even driving whole body locomotion *via* muscle contraction.<sup>121</sup> With the exception of liquid crystals, mankind has been unsuccessful in taking advantage of nanoscale molecular motion in designing and building devices. This is due in part to a gap in the understanding of how individual molecular components behave in the face of opposing forces such as friction, thermal fluctuations, coupling to neighbors and lack of inertia.

Organic chemists have been able to design and synthesize molecules in which rotation can be measured, turned on and off and even driven unidirectionally in solution using either photons or chemical power.<sup>122–124</sup> Very recently molecular rotors have even been used to measure microviscosity in living cells, a property linked to disease and malfunction.<sup>125–127</sup> However, much of the chemistry to date has focused on the synthesis of rotor molecules that, on paper, look similar to their macroscopic counterparts. This approach has provided many surprises: molecules with molecular structures that appear sterically restricted rotate freely, while others that look free have larger barriers to motion.<sup>128</sup>

Understanding and actuating the rotation of individual molecules on surfaces is a crucial step towards the development of nanoscale devices such as fluid pumps, sensors, delay lines and microwave signaling applications.<sup>122</sup> Recent research in our group has employed low-temperature STM experiments performed on a stable and robust system of thioether (RSR') molecular rotors bound to metal surfaces.<sup>31,32</sup> This system serves as a platform for characterizing the dynamics of individual molecular rotors as a function of temperature, rotor length, proximity of neighboring molecules and electrical excitation.<sup>81,83,129,130</sup>

### 3.1.1 Thioether Molecular Rotors

Recently a series of symmetric thioethers  $[C_nH_{2n+1}SC_nH_{2n+1}]$ , with  $n = 1, 2, 4$  and  $6$ , were studied on a Au(111) surface.<sup>81</sup> In these simple systems, thioether (RSR') molecules bind to the metal surfaces through a central S atom (the axle) and the alkyl tails (rotor) interact weakly with the surface, allowing the molecule to rotate if excited thermally. Figure 3.1 shows a simple model of a static and a spinning dibutyl sulfide

molecule (DBS).<sup>81,83,129,130</sup> Au(111) was chosen as the first support for these molecules due to its inertness and binding strength to S-containing molecules. The investigation revealed that dimethyl sulfide (DMS) had a very low barrier to rotation (*i.e.*, rotated at all accessible temperatures as low as 5 K), but the molecules with  $n > 1$  had higher barriers. Unexpectedly, the larger molecules ( $n = 2, 4$ , and 6) all had roughly the same barrier to rotation. We initially hypothesized that the barrier to rotation was related to the interaction between the surface and the second ( $\beta$ )  $\text{CH}_2$  group from the sulfur atom and that increasing the length of the alkyl tail would not significantly affect the torsional barrier.<sup>81</sup>

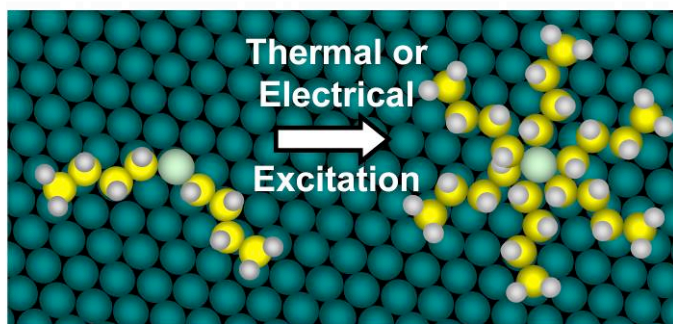


**Figure 3.1 Thioether Schematic:** Model of individual static and spinning dibutyl sulfide thioether molecular rotors.

The results of recent molecular dynamics (MD) simulations performed for several symmetric RSR molecules have demonstrated that the mechanism for rotation is more complex than our initial hypothesis suggested.<sup>130</sup> Calculations indicated that as the alkyl chain lengths increased, the van der Waals interactions with the metal surface increased, thereby driving the rotational barrier up. However, due to the flexibility of the alkyl tails, the number of atoms that strongly interact with the surface below did not change appreciably with an increased number of atoms. These

two factors effectively cancel one another out; thus, the rotational barrier does not increase as the alkyl tails get longer in the range  $n = 2-6$ . As there is very little interaction of the alkyl tails of  $\text{Me}_2\text{S}$  with the surface, it is expected that this molecule would have a very low barrier to rotation as our experiments have shown.<sup>84</sup> In this paper we describe recent experimental work aimed at elucidating the factors that control the dynamics of both symmetric and asymmetric thioether molecular rotors. The two molecular rotors of interest are DBS and butyl methyl sulfide (BMS). In order to investigate the effect of surface composition and structure we have performed time resolved dynamics experiments on both Au(111) and Cu(111) surfaces as shown in Figure 3.2.

Au(111) has a unique *herringbone*, or technically, the  $22 \times \sqrt{3}$  reconstruction.<sup>43,45-49</sup> Cu(111) on the other hand is much simpler with flat (111) terraces, all of which are *fcc* in structure. While Au(111) is an ideal substrate for anchoring S-containing molecules, the heterogeneity in its surface structure means that measuring and understanding the dynamics of adsorbed species is a more complex task. This point will be discussed in detail later in the chapter.

### 3.2 Results and Discussion

Figure 3.2 shows STM images of individual thioether molecular rotors on both Au(111) and Cu(111) surfaces. The top row shows molecules on Au(111), and the bottom row shows molecules on Cu(111). The left block shows DBS molecules, and the right block shows BMS molecules. When imaging under non-perturbative scanning conditions and at temperatures  $\leq 7$  K, both molecules are static and appear in STM images as crescent-shaped protrusions as shown in the left column of each

block of Figure 3.2. The right column in each block of Figure 3.2 shows images of molecular rotors at temperatures  $>7$  K (see Figure 3.2 caption for the temperature of each image). At elevated temperatures the molecules rotate *via* fast interconversion between six, equivalent orientations dictated by the high symmetry directions of the (111) surfaces. The molecular rotation occurs much faster than the timescale of STM imaging (ca. 1 min per image) thus; the molecules appear as hexagons due to the time averaged appearance of all six orientations.<sup>58,131</sup>

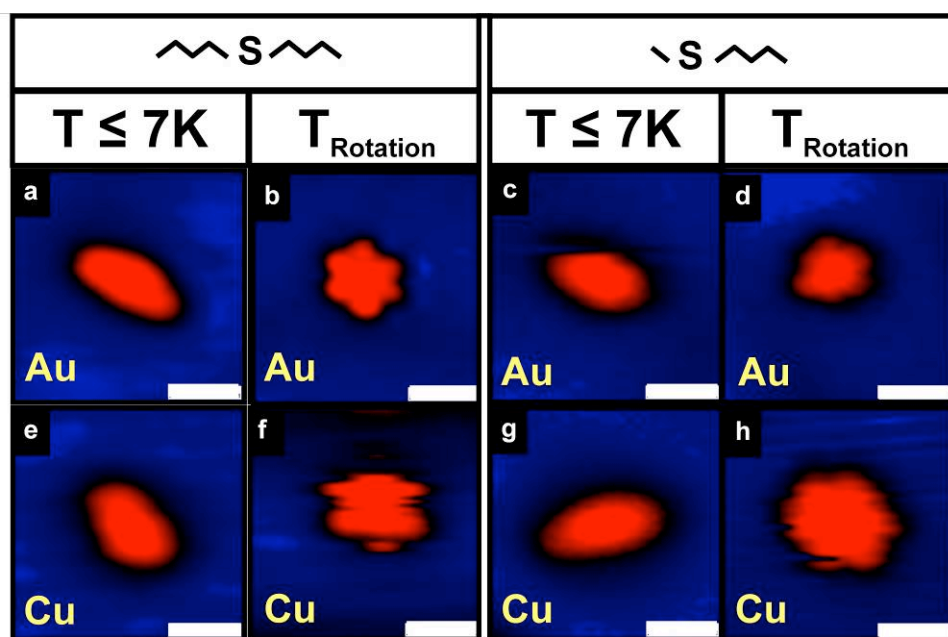


**Figure 3.2 Isolated Thioether Molecules on Au and Cu:** STM images showing thermal activation of dibutyl sulfide and butyl methyl sulfide molecular rotors on Au(111) (top row) and Cu(111) (bottom row) surfaces. Molecules a, c, g and e appear as roughly linear protrusions because they are stationary, while molecules b, d, f and h appear hexagonal in shape because they are rotating faster than the time-scale of STM imaging. Scale bar = 1 nm. Image conditions: 5-10 pA,  $\pm$  50-300 mV a) 7 K; b) 35 K; c) 7 K; d) 22 K; e) 7 K; f) 9 K; g) 5 K; h) 8 K.

### 3.2.1 Time-Resolved Measurements

In order to characterize the rotation rates of single RSR' molecules, tunneling current versus time (*I vs t*) experiments were performed. The feedback loop (which

adjusts the STM tip-sample distance to maintain a constant tunneling current during imaging) was turned off during the *I vs t* measurements. As the thioether molecule rotated, the alkyl tails passed under the STM tip causing changes in the tunneling current. If the tip was placed just to the side of one of the six lobes of the hexagonal shape of the spinning molecule, as described previously for dibutyl sulfide, the tunneling current was observed to fluctuate between three discrete values.<sup>81</sup> We report here that the asymmetry of BMS leads to the appearance of six discrete values of the tunneling current during *I vs t* measurements (see Figure 3.3 and Figure 3.4 for a comparison of the molecules). These discrete tunneling current levels correspond to the three inequivalent orientations of DBS (or six for BMS) with respect to the STM tip. The hexagonal arrangement of (111) surfaces imposes a hexagonal (or six-fold) symmetry on the preferred orientations of thioether molecular rotors.<sup>81,83,129,130</sup>

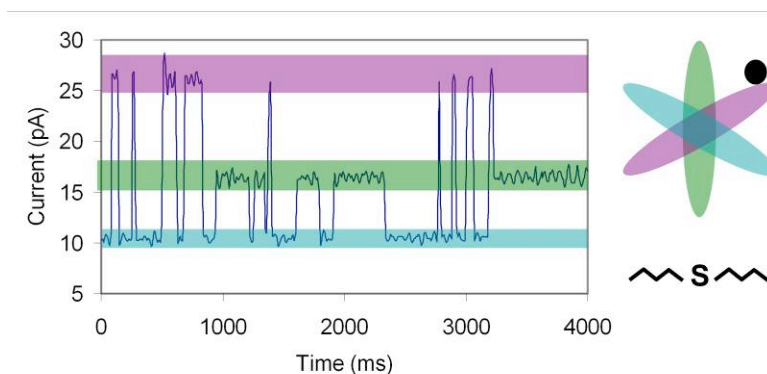


**Figure 3.3 Current *versus* Time for Dibutyl Sulfide During Rotation:** Tunneling current as a function of time (*I vs t*) curves for dibutyl sulfide on Cu(111) reveal three levels of tunneling current that correspond to the three inequivalent orientations of the molecule (purple, green and light blue) with respect to the STM tip position (black dot). Measurement conditions: 10 pA, 0.2 V, 11 K.



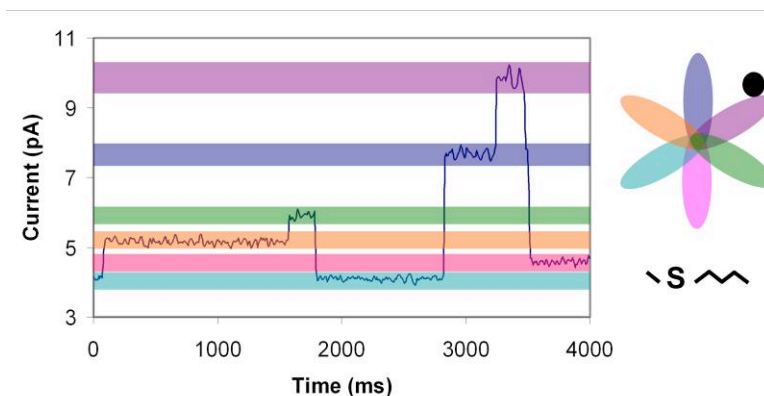


**Figure 3.4 Current *versus* Time for Butyl Methyl Sulfide During Rotation:** Tunneling current as a function of time ( $I$  *vs*  $t$ ) plots for butyl methyl sulfide on Cu(111) reveal six levels of tunneling current that correspond to the six inequivalent orientations of the molecule's butyl tail (purple, blue, green, orange, pink and light blue) with respect to the STM tip (black dot). Measurement conditions: 5 pA, 0.2 V, 5 K.

The three orientations of DBS (as shown in Figure 3.3) could be distinguished based on the different levels of tunneling current that arose depending on the position of the molecule with respect to the STM tip. The highest tunneling current corresponds to the orientation of the molecule (shaded purple) almost directly under the tip (shown as a black dot). The next highest tunneling current corresponds to the molecule orientation shaded in green, and the lowest current arises from the orientation shaded in light blue.

Since BMS is an asymmetric molecule, if the STM tip was carefully placed just to the side of one of the six lobes for  $I$  *vs*  $t$  spectroscopy measurements, the six states could be distinguished (as shown in Figure 3.4). Assigning the tunneling current levels to specific molecular orientations is not as straightforward for BMS as it was for DBS. To first approximation, as the tip is always positioned toward the edge of the molecule, the butyl tail contributes the majority of the tunneling current. Therefore, the highest tunneling current would correspond to the molecular orientation shaded purple and successively lower tunneling currents correspond to

the butyl tail located farther from the STM tip location (Figure 3.4). In this simplified explanation, due to the asymmetry of the alkyl tail the light blue lobe directly across from the purple lobe is no longer equivalent, and if the molecule rotated  $180^\circ$ , this would correspond to the lowest tunneling current. The remaining tunneling current levels are shaded according to the schematic in Figure 3.4. In reality, the position of the methyl tail may have somewhat unpredictable contributions to the tunneling current. Therefore, the lowest tunneling current levels may not be assigned correctly due to a contribution from the methyl group. However, in terms of tracking the dynamics of motion, and in particular detecting directional motion, knowledge of the progression of a set of discrete levels is almost as valuable as an absolute assignment of the progression of orientation states. In simpler terms, directional motion would lead to a periodic, reproducible series of discrete current states, whereas random motion would yield a random progression.

It is interesting to note the relative magnitudes of the discrete tunneling current levels in Figure 3.3 and Figure 3.4. The separation of a particular current state and the state immediately below it decreases as the magnitude of the state decreases. Due to the exponential dependence of tunneling current on the tunneling gap width, as the molecule rotates away from the STM tip, the tunneling current will drop off in a pseudo-exponential fashion as is observed experimentally.

By using *I vs t* spectroscopy the rate and directionality of molecular rotations can be obtained on a time-scale  $> 1,000$  Hz. This allows for the characterization of molecular rotation with a resolution beyond what is achievable using STM imaging alone. Providing that one is consistent with the assignment of current levels to specific orientations of the molecule under investigation, it is possible to determine

which way the molecule is rotating. In the case of DBS, a current change or “switch” from the high (purple) current state to the low (light blue) current state would signify a clockwise rotation, while a switch from the high (purple) current state to the intermediate (green) current state would signify an anti-clockwise rotation. Using a similar approach, the rotations of the asymmetric molecule (BMS) can be characterized as clockwise or anti-clockwise. As discussed, the exact assignment of states is not necessary to monitor the progression through consecutive states with this technique as long as one is consistent with the assignments of current levels and molecular orientation.

In order to characterize the overall directionality of rotation, switches were labeled as positive (+) or negative (-), depending on the sequence of current levels. For example, a switch from orientation  $a \rightarrow$  orientation  $b$  would be labeled as (+) and a  $b \rightarrow a$  switch as (-). When the collection of switch assignments was examined for a particular data set, the degree to which rotation was unidirectional (*i.e.*, more clockwise or anti-clockwise) would be indicated by the relative abundance of (+) and (-) switches. Approximately 13,000 thermally-induced switches have been analyzed initially by hand for BMS on Cu(111) and the +/- ratio was determined to be 49.8/50.2 (essentially 50/50). This ratio is expected as, according to the Second Law of Thermodynamics, it is not possible to get useful work from a system at thermal equilibrium.<sup>132</sup> Occasionally the change in tunneling current indicated a 180° rotation, making the +/- assignment ambiguous. In these events the user would assign the rotation direction based on the sequence of current levels (*e.g.* low to high versus high to low) taking care to be consistent with any previous similar events. Analysis

indicates that the predominant rotation steps are single  $60^\circ$  ones with  $120^\circ$  accounting for less than 35% and  $180^\circ$  less than 9% of rotations. Therefore, this approach can identify directionality associated with all but a few of the rotational events considered. While this presents a small problem in overall direction assignment, ultimately, any type of directional motion would lead to a periodic, reproducible series of discrete current states, whereas random motion would yield a random progression.

### *3.2.2 Automated Switch Counting*

The  $I$  vs  $t$  curves generated with the feedback loop disabled often contained thousands of data points and hundreds to thousands of tunneling current changes, each representing a molecular reorientation, or “switch”. The process whereby this data was analyzed is described in detail in Chapter 2. The program was used to characterize thermally-induced rotation of BMS on Cu(111), and the ratio of +/- switches was determined to be 49.1/50.9 which indicates a slight preference for one direction. As mentioned, thermally-driven rotation would always be expected to show no net directionality. The results from the automated analysis indicate a slight bias for rotation in one direction, which suggests that there may be a small error in the program itself. When  $I$  vs  $t$  curves from the same system were analyzed by hand the results indicated equal amounts of rotation in both directions. The bias in the automated analysis may indicate a limitation of the measurement itself, but it is likely that this represents an inherent limitation of the STM preamplifier’s bandwidth and the computer’s processing capabilities. Specifically, when rotational switching begins to occur faster than the response time of the tunneling current preamplifier, the  $I$  vs  $t$

curves no longer register a series of well-defined discrete tunneling currents connected by very steep changes in current. Instead, there is a lag time between discrete current states, and the computer program will erroneously identify switches that are not real. If the response times from higher to lower states and vice versa are different, then a non-existent state will be added to the curves in a regular fashion (*i.e.*, *a-b-c* instead of *a-c*) and lead to an apparent bias in one rotational direction. While this effect is always present when assigning the direction of rotation of individual molecular rotors, we have never observed an associated error larger than 6%.

### 3.2.3 Arrhenius Data

In order to investigate the energetic barriers for individual molecular rotors Arrhenius experiments were performed. The rates of rotation for individual rotors as a function of temperature were obtained by performing *I vs t* experiments at a variety of temperatures. Measurements were made for the rotation of DBS molecules adsorbed on the *fcc*-regions, *hcp*-regions and the soliton walls of the Au(111) surface. Arrhenius plots for DBS molecules in the three regions are shown in Figure 3.5a. The plots represent data taken for the molecules highlighted in Figure 3.5b. It is immediately evident from the graph that there is fair degree of scatter and a variability of the Arrhenius parameters for each molecule depending on where they reside. This is somewhat expected as the corrugation of the Au(111) surface gives rise to different electronic properties, and local strain within the surface itself that changes on a length scale of nanometers.<sup>43,45–49</sup> This leads to different binding properties for molecules depending on which part of the surface they are

adsorbed.<sup>66,133–135</sup> From these Arrhenius measurements we found the average rotational barrier ( $E$ ) of DBS in the *fcc*-region was  $1.2 \pm 0.1$  kJ/mol with an attempt frequency ( $\mathcal{A}$ ) of  $7 \times 10^{7 \pm 0.3}$  Hz, while in the *hcp*-region  $E = 0.8 \pm 0.1$  kJ/mol and  $\mathcal{A} = 1 \times 10^{6 \pm 0.5}$  Hz, and for a molecule adsorbed on the soliton wall  $E = 2.0 \pm 0.8$  kJ/mol and  $\mathcal{A} = 1 \times 10^{12 \pm 4}$  Hz.

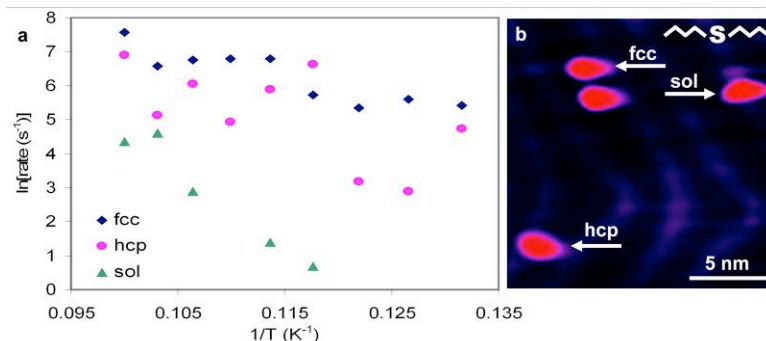


**Figure 3.5 Arrhenius Data for Dibutyl Sulfide Rotation on Au:** (a) Arrhenius plot for the rotation of individual dibutyl sulfide molecular rotors on the three different regions of the Au(111)  $22 \times \sqrt{3}$  surface and (b) an STM image indicating the positions of three molecules interrogated. Rotation rates are obtained at each temperature from switching events in  $I$  vs  $t$  curves under nonperturbative measurement conditions (5 pA and 0.2 V). Image conditions: 5 pA, 0.2 V, 7 K.

It is well known that the different regions of the Au(111)  $22 \times \sqrt{3}$  surface gives rise to different electronic properties as well as different local structural properties (strain) within the surface itself, which changes on a length scale of nanometers. This has been shown to lead to different binding properties for molecules depending on which part of the surface they are adsorbed. It is however not usually possible to decouple the effect of strain from the electronic structure of the surface as both change in concert. While other studies have discussed adsorption effects in terms of electronics we do not believe that we can explicitly attribute the rotor energetics solely to surface strain or electronic effects.

These data reveal that the rotational energetics are strongly coupled with the molecule's exact position on the herringbone surface reconstruction of Au(111). In order to uncover the degree of variability arising from the Au reconstruction, Arrhenius

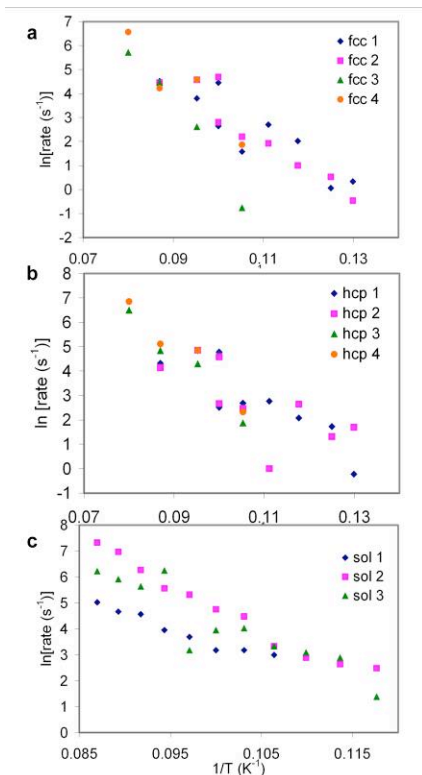


**Figure 3.6 Arrhenius Data for Dibutyl Sulfide Rotation on Au as a Function of Location:** Arrhenius plots for several dibutyl sulfide molecules on the (a) *fcc*, (b) *hcp* and (c) soliton wall regions of Au(111)  $22 \times \sqrt{3}$ . All data was taken using nonperturbative measurement conditions: 5 pA and 0.2 V.

data for several molecules in each area were recorded. Figure 3.6 shows Arrhenius plots for several individual molecules each adsorbed within one of the three regions (*fcc*, *hcp* and soliton wall) of the herringbone reconstruction. It can be seen from these plots that there is a great deal of variation, even for molecules within the same region of the surface. As the unit cell of the reconstruction is only 6.3 nm in width, moving a rotor laterally across the surface by only 0.1 nm changes the position of the

molecule with respect to the different *hcp*, *fcc* and soliton regions significantly. As a result, the underlying surface properties change, as does the molecule's rotation rate. Therefore, it is expected that we observe such large variations within the Au(111) data set. While much of the preliminary work for this study was performed using Au as a substrate, these results demonstrate that care must be taken in comparing the dynamics of molecular rotors on different areas of this surface.

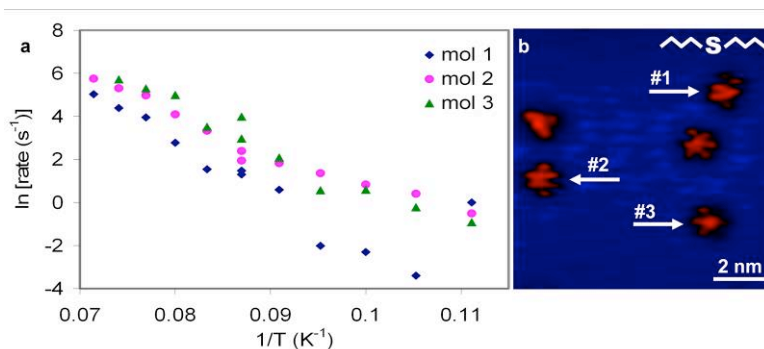


**Figure 3.7 Arrhenius Data for Dibutyl Sulfide Rotation on Cu:** Arrhenius plots (a) for the rotation of three individual dibutyl sulfide molecules (mol 1, 2 & 3) on a Cu(111) surface. Rates of rotation for each temperature are obtained at nonperturbative tunneling conditions (10 pA and 0.2 V). (b) An STM image showing the molecules interrogated, the molecules appear to rotate because they are electrically excited at these image conditions: 100 pA, 0.2 V, 5 K.

In order to circumvent the variability introduced by the Au(111) surface structure itself, the rotational dynamics of DBS molecules were also studied on a Cu(111) surface. The Cu(111) surface offers the same hexagonal symmetry as Au(111), but without the complexity arising from the surface reconstruction (see Figure 1.2). It is expected that a homogeneous surface structure would lead to less variability in the rotational dynamics data as, unlike on Au, the relative position of the rotor molecule in its equilibrium adsorption site on the Cu surface should not influence its barrier to rotation. Arrhenius data were obtained as before for several individual DBS rotor molecules on Cu(111). The plots are shown in Figure 3.7a



along with STM images (Figure 3.7b) which indicate the molecules interrogated. The molecules in Figure 3.7b are electrically excited at the imaging conditions used; thus they appear to spin. As expected, the data obtained for molecules on the Cu surface showed much less variability. These measurements yielded an average rotational barrier ( $E$ ) of  $1.48 \pm 0.02$  kJ/mol and an attempt frequency ( $\mathcal{A}$ ) of  $8 \times 10^{7 \pm 0.8}$  Hz for DBS on Cu(111).

Our previous work on the rotation of thioether molecular rotors on Au(111) showed that dimethyl sulfide ( $\text{Me}_2\text{S}$ ) has a very low barrier to rotation, while larger symmetric thioethers (diethyl-, dibutyl- and dihexyl-sulfide) have roughly the same barrier ( $\sim 1.2$  kJ/mol).<sup>81,84</sup> The results from the experiments reported herein suggest that DBS has a slightly higher rotational barrier on Cu(111) than it does on Au(111). This is an interesting result given that the phonon energy also differs between Cu and Au surfaces (Cu = 2.1 kJ/mol,  $\text{Au}_{fcc,hcp} = 1.0$  kJ/mol and  $\text{Au}_{sol} = 1.8$  kJ/mol).<sup>136</sup> One would naively expect that the energy of the surface phonons being excited during heating would directly map to the onset of excitation of molecular rotation. There is a weak correlation between the lower phonon energies of the *hcp* and *fcc* areas of Au and the higher phonon energies of Cu and the solution walls of Au and their respective torsional barriers ( $0.8 \pm 0.1$  kJ/mol,  $1.2 \pm 0.1$  kJ/mol,  $1.48 \pm 0.02$  kJ/mol, and  $2.0 \pm 0.8$  kJ/mol). However, the fact that the correlation of torsional barrier with phonon energy is somewhat weak is not entirely unexpected given that the molecule-substrate interactions also change between Cu and Au. Our earlier molecular dynamics work also demonstrated that in addition to the rotor tail-substrate interaction, the S-metal bond strength also affects the rotational barrier.<sup>126</sup>

Therefore, while this trend is obeyed qualitatively, phonon energies are not the only factor in determining molecular rotor energetics.

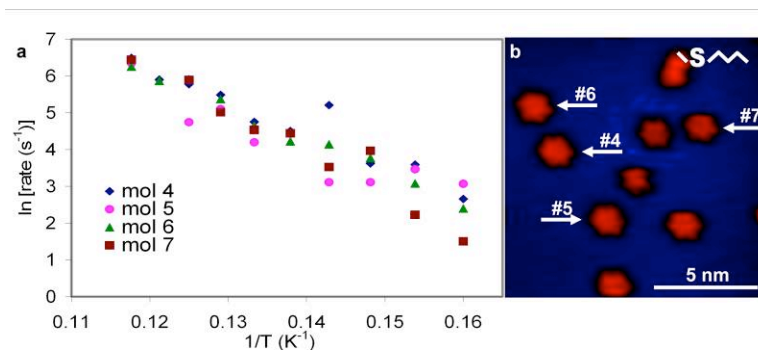


**Figure 3.8 Arrhenius Data for Butyl Methyl Sulfide Rotation on Cu:** Arrhenius plots (a) for the rotation of four individual butyl methyl sulfide molecules (mol 4, 5, 6 & 7) on a Cu(111) surface. Rates of rotation are obtained for each temperature at nonperturbative tunneling conditions (10 pA and 0.2 V). (b) An STM image of the molecules interrogated; the molecules appear to rotate due to tip proximity effects at these image conditions: 400 pA, 0.5 V, 5 K.

According to MD simulations, the rotational barrier for BMS should lie between that of  $\text{Me}_2\text{S}$  and DBS.<sup>130</sup> An Arrhenius plot for several BMS molecules on Cu(111) is shown in Figure 3.8a, along with an STM image (Figure 3.8b) indicating the molecules interrogated. The molecules in Figure 3.8b appear to rotate due to effects arising from the relatively high voltage and current conditions. Once again, the data show reasonably good reproducibility from molecule to molecule due to the homogeneity of the local Cu(111) surface structure. These measurements yielded an average activation barrier ( $E$ ) of  $740 \pm 60 \text{ J/mol}$  and an attempt frequency ( $\mathcal{A}$ ) of  $2 \times 10^{7 \pm 0.4} \text{ Hz}$  for BMS. The barrier to rotation at  $\sim 0.7 \text{ kJ/mol}$  for BMS on Cu(111) lies at an intermediate level between  $\text{Me}_2\text{S}$  and DBS. This indicates that, to first approximation, the rotational barrier of thioether molecular rotors is a linear combination of each alkyl tail's barrier to rotation.  $\text{Me}_2\text{S}$  has a very low (unmeasurable) barrier, DBS has a barrier  $\sim 1.5 \text{ kJ/mol}$ , therefore by this logic, BMS

would be expected to have a rotational barrier of intermediate magnitude as is observed experimentally.

It is important to note that the attempt frequencies quoted for DBS molecules on Cu(111) (Figure 3.7) and on the *fcc*- and *hcp*-regions of Au(111) (Figure 3.6) differ by several orders of magnitude from the expected range ( $10^{10}$  -  $10^{15}$  Hz).<sup>137</sup> The value of  $\mathcal{A}$  for BMS on Cu(111) is also unexpectedly low at  $\sim 10^7$  Hz. Our initial hypothesis was that the butyl tails have many degrees of freedom, only a few of which have low rotational barriers. We investigated BMS with the expectation that its attempt frequency would be closer to the expected range, however, the results shown here indicate that even with one long tail removed, the rotors still have low attempt frequencies. Lyo and co-workers also recently reported a very low attempt frequency ( $\sim 10^2$  Hz) for the chemisorption of ethylene on Si(001)c-( $4 \times 2$ ); they attributed the low  $\mathcal{A}$  value to entropic effects of the transition state.<sup>138</sup> This effect could be at play in our system if the rotor molecule becomes “stiffer” as it transitions between its preferred rotational orientations. Further experiments are required in order to understand the low attempt frequencies observed experimentally.

For the Arrhenius plots presented in this chapter, rates of rotation were obtained by counting the number of changes in tunneling current within the  $I$  vs  $t$  curves by hand and dividing the number of “switches” by the total time in order to determine a rate of rotation at each temperature. An alternative method for determining a rate involves fitting the distribution of lifetime intervals of a particular state to an exponential and getting the rate directly from the inverse of the decay constant. This method has been employed to characterize a variety of systems with successful results but requires a lot more raw data in order to obtain reasonable

exponential fits for each temperature.<sup>117,118</sup> Our goal is to study the Arrhenius behavior of a wide variety of molecular rotors on different surfaces and to make relative comparisons of the systems. As such, we have found that good rate data can be obtained from counting raw numbers of events as described earlier and that smaller data sets can yield good fits.

### 3.2.4 *Electrically Inducing Molecular Rotation*

The results discussed thus far demonstrate that relatively small amounts of thermal energy can induce the rotation of a variety of both symmetric and asymmetric thioether rotors. However, as previously stated, useful work cannot be derived from a purely isothermal process. In order to extract useful function from molecular rotors, methods for coupling them with external sources of energy to initiate rotation and eventually drive unidirectional rotation must be sought.<sup>111,117,118,122,132,139–156</sup> Our experiments demonstrated that at temperatures below 8 K, larger ( $n > 1$ ), symmetric thioether molecules were static and could be imaged stably for many hours at tunneling voltages less than  $\pm 0.35$  V (non-perturbative conditions). However, either imaging or positioning the STM tip over the molecules at biases greater than  $\pm 0.35$  V caused the molecules to rotate.<sup>81</sup> In order to elucidate the mechanism of this electrically-excited rotation we performed Action Spectroscopy.<sup>111,117,118,130,139–145,157</sup> This time-resolved technique correlates a molecular action (*i.e.*, rotation) to the energy of electrons needed to induce the process. The action spectrum (linear plot of rotation rate *vs* tunneling electron energy) for a DBS molecule on the *fcc*-region of Au(111) is shown in Figure 3.9. Such data characterizing the rotation of electrically-excited DBS molecules in different areas of

the Au(111) surface showed marked increase in the rotational rate when tunneling electrons energies above  $375 \pm 5$  meV were injected into the molecule.

The energy onset was found to be independent of the direction of the tunneling electrons indicating an inelastic electron excitation of a molecular vibration. Furthermore, this onset energy range corresponds to a C–H stretching mode, which occurs at  $\sim 360$  meV.<sup>116,158,159</sup> Further experiments were performed using both DBS and fully deuterated-DBS (d-DBS) on Au(111) and the action spectra showed a distinct difference in the energy of the rotation onset.<sup>83</sup> For d-DBS the onset energy shifted to  $285 \pm 5$  meV, which is indicative of an isotope shift of  $\sim 1/\sqrt{2}$  in the C–D stretch frequency.<sup>116,158,159</sup> These findings support the hypothesis that rotation of the molecule occurs *via* the excitation of a high-energy C–H or C–D stretch which then decays into different stretches, bends, and hindered rotations of the molecule and ultimately into rotation of the molecule as a whole. A finite amount of rotation was also observed at very low voltages ( $< \pm 0.05$  V) as shown in Figure 3.9. At these tunneling conditions the STM tip is very close to the molecule and can interact with it in a manner similar to the atomic manipulation mode.<sup>104</sup> We postulate that this low-voltage effect arises not through any type of electronic excitation, but rather at close distances the tip forms a weak bond to the molecule, which decreases its interaction with the surface, thereby lowering its barrier to rotation.

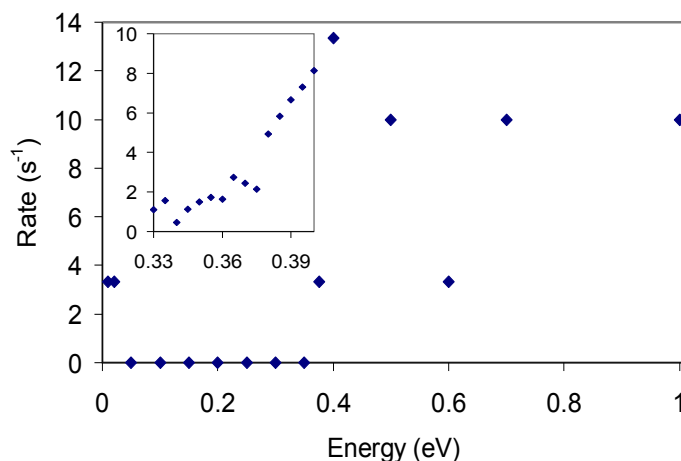


**Figure 3.9 Action Spectrum for Dibutyl Sulfide Rotor on *fcc* Au:** At electron energies approaching 0.4 eV a marked increase in rotation rate is observed. The inset shows higher resolution data from the 0.33 – 0.4 eV range that reveals that the onset of rotation occurs at an electron energy  $\sim 375$  meV, which correlates with a C-H stretch excitation. At very low voltages ( $<0.05$  V) the tip-molecule distance is small, the barrier to rotation is lowered and a finite amount of rotation is observed. Conditions: 5 pA and 7 K.

### 3.2.5 Thermal versus Electrical Rotation

Figure 3.10 shows a representative plot of two  $I$  vs  $t$  curves for (a) thermally- and (b) electrically-induced rotation. These time-resolved plots illustrate that the lifetimes of the different rotational orientation states are affected by the mode of excitation. Visual inspection of the thermal plot reveals that the rotational orientations are all populated approximately equally. In the case of electrically-excited rotation, the molecule spends more time in the states that receive lower tunneling currents and considerably less time in the higher tunneling current states. When rotation is induced with thermal energy alone (*i.e.*, with minimal perturbation by the STM tip), all rotational orientations with respect to the STM tip are populated to an equivalent degree. However, when rotation is induced with energetic electrons from the STM tip, the high current states (*i.e.*, states in which the rotor is closest to the tip and therefore receiving the highest flux of tunneling electrons) have the shortest

lifetimes. This phenomenon arises because in the electrical excitation case, the electrons themselves are exciting the rotation of the molecule; the higher tunneling current orientations of the molecule receive a higher flux of electrons that excites rotation to other states. Therefore, the molecule exists in the high tunneling current states for the shortest period of time.

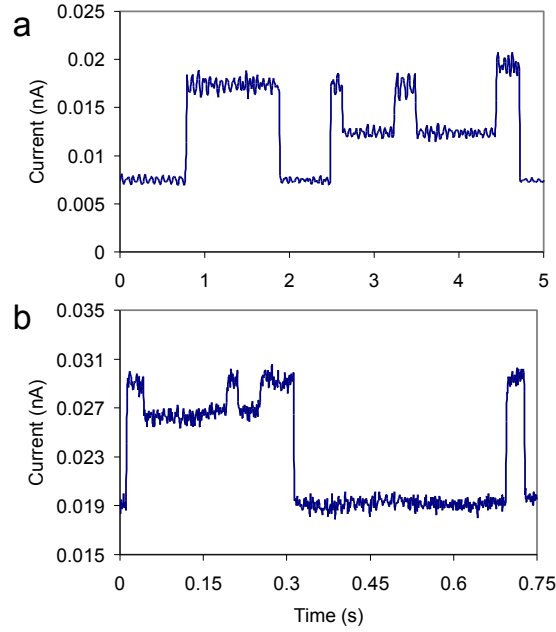


**Figure 3.10 Thermally *vs* Electrically Excited Rotation:** a) Thermal *vs* b) Electrical  $I$  *vs*  $t$  curves for DBS on Cu(111). Thermal excitation populates all three rotational states equally whereas electrical excitation leads to shorter lifetimes of the orientations in which the molecule receives a higher flux of tunneling electrons. Conditions: a) 8.5 K, 0.2 V, 10 pA and b) 7 K, 0.37 V, 10 pA.

Each orientation state lifetime of the molecular rotors can be analyzed in order to deduce more about the mechanism of electrically excited rotation. In a tunneling electron induced process the rate of an event  $k$  is proportional to tunneling current  $I$  to the power  $n$ :

$$k \propto I^n$$

The value of  $n$  indicates the number of electrons that are involved in the process. As the lifetime of a particular state  $\tau$  is inversely proportional to the rate ( $k$ ) of leaving the state:

$$\tau \propto \frac{1}{I^n}$$

Therefore, high current states should have shorter lifetimes and low current states should have long lifetimes as is observed experimentally. Using the automated computer program the lifetimes of each state could be quantified and a rate of leaving each state calculated. Figure 3.11 shows a graph relating the rate of leaving each of the three states to the tunneling current the DBS molecule receives in each state. On this  $\ln$ - $\ln$  plot the gradient gives the  $n$  value and hence the order of the process. From inspection of Figure 3.11 it appears that electrically driven rotation of DBS on Cu(111) is a one-electron process. This result is consistent with a one-electron excitation of a C-H stretch at an energy of 0.37 eV that in turn leads to rotation of the whole molecule.

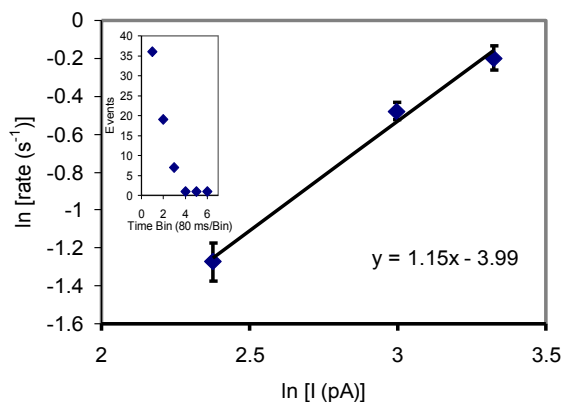


**Figure 3.11 Rotation Rate as a Function of Tunneling Current:** Plot of the rate of rotation of DBS on Cu(111) as a function of tunneling electron current for electrically driven rotation with an electron energy of 370 meV. Inset shows a typical exponential lifetime distribution, in this case for the highest current state. The gradient of 1.15 indicates that electrical excitation occurs *via* a one-electron process. Conditions: 370 mV, 10 pA, and 7 K.



### 3.3 Conclusions

In summary, we have shown here the great utility of time-resolved measurements in obtaining quantifiable data on the dynamics and hence the energetics of molecular rotors on an individual molecule basis. *I vs t* curves allow a lot of rotational events to be captured in a short time period. By correlating changes in the magnitude of the tunneling current to the position of the molecule with respect to the STM tip one can derive the direction of rotation of the rotor. The rate data from *I vs t* curves allows the effect of both thermal- and electrical-excitation to be studied in a quantitative manner. We find that surface structure and molecular chemistry have a great influence on the energetics of molecular rotation and that these effects can be used to uncover some of the fundamental mechanisms behind molecular rotation. Ultimately, in order for molecular rotors to do useful work they must be coupled to an external energy source. We show here that the STM tip can act as a source of electrons that excite molecular rotation as well as monitor the rotation rate of the molecule being excited. These measurements reveal that molecular rotation can be driven electrically *via* excitation of a C-H stretch and that the electrical excitation is a one-electron process. Due to its relative ease of use and versatility this relatively new type of single-molecule time-resolved measurement will continue be a crucial tool in the quest to create nanoscale motors and devices.

### 3.4 Additional Experimental Details

Thioethers (between 99.9 and 99.95% purity) were obtained from Sigma Aldrich and were further purified by freeze/pump/thaw cycles prior to introduction to the STM chamber through a collimated molecular doser. The STM stage was

equipped with a sample heater capable of controllably heating the sample and tip up to 50 K above the base temperature.

## 4 Adsorption, Assembly and Dynamics of Dibutyl Sulfide on Au(111)

### 4.1 Introduction

Thioethers (RSR') may be preferable to thiol SAMs for many uses because they are more resistant to oxidation. Early investigations of thioether SAMs predicted an upright geometry of the alkyl tails, similar to thiols.<sup>33,160</sup> More recent studies, however, have conclusively shown that thioethers with tails up to 18 carbons in length adsorb with their alkyl tails parallel to the surface.<sup>31,32,35,36,81,83,130,161</sup> As such, adjusting side chain length may enable control over lateral spacing. It has been debated whether thioether species dissociate upon adsorption *via* cleavage of a S-C bond,<sup>162</sup> but it is now accepted that these species adsorb intact.<sup>31,35,163</sup>

The literature is teeming with information about thiol self-assembly on metal surfaces; however, despite their potential advantages, only a handful of papers discuss the nanoscale assembly of thioethers on metals.<sup>31–33,35,36,81,161,164–166</sup> Adsorption of thioethers on graphite has been studied, where the molecules formed well-ordered domains with their alkyl tails aligned parallel to one another, held together by van der Waals interactions.<sup>35,36,167,168</sup> These findings were supported by further reports of thioether SAM formation on metal surfaces, including Au and Cu.<sup>31,32,35,36,81</sup> Previous nanoscale investigations have suggested that thioether SAMs are less ordered than thiol SAMs, primarily due to thioethers' relatively weak interaction with the substrate.<sup>35,169</sup> Hara and co-workers investigated the self-assembly of both dioctadecyl sulfide and tetrahydrothiophene on Au(111), and reported that the molecules adsorb intact and that the strength of the molecule-substrate interaction greatly depends on

the identity of the side chains.<sup>36,161</sup> Additionally, studies by this group have shown that adsorbed thioether molecules lie flat with their alkyl tails aligned parallel to one another to increase van der Waals interactions.<sup>31,81</sup>

In this chapter the assembly of a thioether species, dibutyl sulfide (DBS), on a Au(111) surface has been explored using scanning tunneling microscopy (STM). The energetics of the DBS-Au(111) interaction have been previously studied using helium beam reflectivity and temperature-programmed desorption, and the adsorption energy was found to be  $\sim 90$  kJ/mol.<sup>5</sup> Here we present an atomic-scale investigation of this system.

In this chapter we use the unit cell of the herringbone reconstruction (or more simply the herringbone spacing parallel to the compressed axis) to determine whether the DBS-Au interaction was strong enough to remove or “lift” the reconstruction from its ideal spacing of 6.34 nm. At 78 K and low coverage we observed that the molecules did not order beyond the formation of short-chain aggregates. After the system was provided with more thermal energy, the molecules formed well-ordered layers and the herringbone reconstruction was partially lifted. We find that the extent to which the herringbone was lifted depended on the molecular coverage and temperature treatment. However, the herringbone reconstruction was never completely lifted, and etch pits were not observed at any temperature regime examined in this study of DBS on Au(111).

## 4.2 Results and Discussion

When adsorbed on the Au(111) surface, DBS exhibited a high degree of order on molecular, nanometer, and micrometer length scales. Figure 4.1 shows STM images and schematics of the nanoscale behavior of individual DBS molecules and

aggregates. The molecules appeared structurally preserved, with their alkyl tails oriented near the plane of the surface. As reported in previous work by this group and in Chapter 3, isolated DBS molecules behave as molecular rotors on Au(111).<sup>81-83,130,170</sup> The central sulfur atom acts as an anchor and the alkyl tails rotate between six equivalent orientations; at 78 K the rotation is significantly faster than the STM imaging rate ( $\sim 2$  min per image), and the molecules appear hexagonal in shape, as depicted in Figure 4.1A. Furthermore, the molecules rotate at a rate significantly greater than that of translational motion, as evidenced by STM movies acquired at 78 K, in which rotating molecules did not diffuse more than a few lattice spacings throughout the movie taken over several hours (see Appendix).

When in the vicinity of other molecules, DBS molecules assembled with their alkyl tails and sulfur centers aligned adjacent to their neighbors' (Figure 4.1B and C). This behavior hindered rotation and resulted in the formation of long chains of DBS molecules (Figure 4.1C) with an average intermolecular spacing of  $0.50 \pm 0.05$  nm. The adsorbates assembled in this manner to optimize van der Waals forces between adjacent alkyl tails,<sup>31,35,36</sup> analogous to the tilting observed for thiol SAMs.<sup>41,160</sup> The proposed aggregate structure is similar to that observed for DBS on Cu(111), which had a spacing of  $0.39 \pm 0.03$  nm.<sup>31</sup>

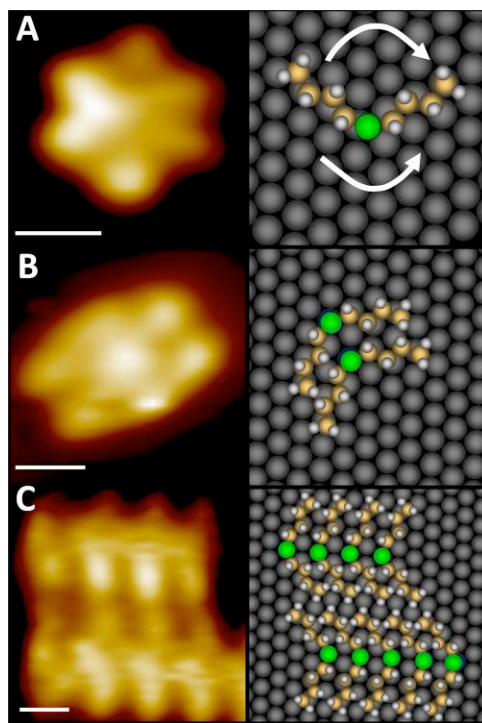


**Figure 4.1 Dibutyl Sulfide Assembly on Au at Low Coverage:** STM images (left) and corresponding schematics (right) of A) one, B) two and C) nine DBS molecules on Au(111). In the schematics sulfur atoms are green, carbon is yellow, hydrogen is white, and Au is gray. A) Isolated molecules behaved as rotors with the alkyl tails rotating around the central sulfur atom. The direction of rotation is random, as indicated by double-headed arrows. B) Pairs of molecules stacked parallel to one another, stabilized by van der Waals interactions between adjacent alkyl tails. C) This stacking behavior was observed with larger aggregates that formed adjacent DBS chains, which aligned along the  $\sqrt{3}$  axes of the surface. Some of the self-assembly steps that led to these aggregates can be visualized in STM movies (see Appendix). Scale bars = 0.5 nm. Image conditions: 78 K, 10 pA, 0.1 V.

Figure 4.1C illustrates that the alkyl tails of DBS tilted both to the right and to the left of the molecular row. The gas-phase DBS species has two lone pairs of electrons, one of which interacts with the surface upon adsorption. Thus, surface-adsorbed DBS are expected to have a near tetrahedral geometry around the S atom, which leads to the “crescent” shape of the individual molecules.<sup>84</sup> At 78 K adjacent chains adopted opposite tail orientations as seen in Figure 4.1C. This phenomenon, along with the regular spacing between chains ( $1.4 \pm 0.1$  nm), suggests significant chain-to-chain interactions. Furthermore, at full monolayer coverage the alternating

tail orientation from chain to chain was preserved rigidly across entire domains many tens of nm in width.

Because the chains were linear, their direction relative to the substrate could be assigned. The chains oriented along one of the three  $\sqrt{3}$  directions, and intermolecular spacings within the chains were regular and corresponded to  $\sqrt{3}d_{\text{Au}}$  (where  $d_{\text{Au}}$  is the diameter of an uncompressed Au atom, 0.288 nm), suggesting that the assembly was commensurate with the underlying Au lattice. Beyond the short-range interactions and behavior of DBS on Au(111), it was possible to examine large-scale system trends. At low coverage DBS existed as single rotating species and short chain aggregates, but no long-range ordering was observed to take place when the molecules were dosed and imaged at 78 K, as shown in Figure 4.2. While chains did orient along the  $\sqrt{3}$  axes of the surface, the rotors were randomly dispersed. Furthermore, neither chains nor rotors showed a preference for the compressed or uncompressed axes or for the *hcp*, *fcc*, or soliton wall regions of the herringbone reconstructions was observed. As the coverage of DBS was increased to  $>0.3$  ML, no ordering or assembly beyond the formation of short chains emerged. Only an increase in aggregation was noted, which one might predict purely from the rise in adsorbate-adsorbate interactions that comes with an increase in population.

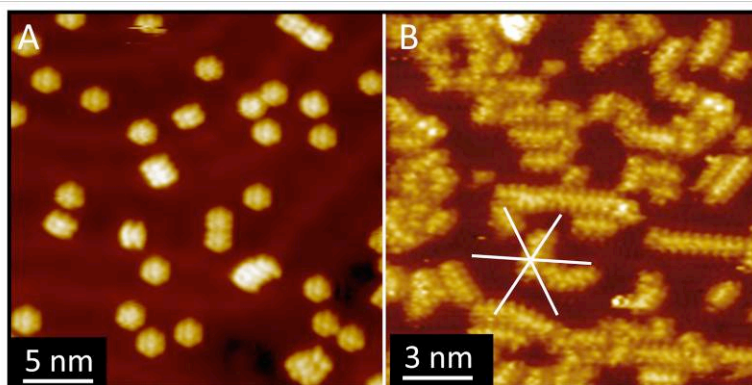


**Figure 4.2 Dibutyl Sulfide on Au as Dosed:** STM images of A) 0.06 ML and B) 0.33 ML of DBS on Au(111) at 78 K. Chains appeared to align along the  $\sqrt{3}$  axes of the underlying Au surface (indicated by white lines), but no global ordered assembly or preferred adsorption region was observed. Image conditions: 78 K, 5-10 pA, -0.01 V.

When the molecular coverage was increased and the system was annealed to 120 K, the randomly distributed molecules and aggregates organized to form large-scale self-assembled arrays with regular geometries, as shown in Figure 4.3. The appearance of order indicates that the disordered state of the pre-annealed system (Figure 4.2) was a kinetic effect in which molecules could not diffuse far enough to form large ordered domains. Various processes, including dimer rearrangement, trimer formation and reorientation, and the interaction between a single molecule and a five-molecule DBS chain are observed in STM movies obtained at 78 K (see Appendix). These STM movies, acquired over several hours and before the system was annealed, contained on the order of a hundred diffusion events and showed some self-assembly events, but did not run long enough to show the emergence of long-range ordering (see Appendix).

After deposition of 0.62 ML and annealing to 120 K the herringbone unit cell dimensions increased only slightly to  $6.6 \pm 0.7$  nm. The increase in the herringbone spacing suggests that Au atoms may have been released from the surface, as previously discussed; however this value is still very close to the herringbone spacing



of native Au (6.34 nm), so it is possible that the herringbone's were not lifted at this coverage and anneal temperature.

In annealed systems between 0.4 and 0.8 ML DBS on Au(111), a self-assembled system formed wherein molecular chains stacked adjacently within the *fcc* and *hcp* regions of the herringbone reconstruction. The chains exhibited sensitivity to these two regions, and showed a great preference for the *fcc* regions of the surface, as depicted in Figure 4.3. Nucleation of the DBS chains began in the *fcc* regions of the herringbone and continued there until the *fcc* regions were saturated. As the coverage was further increased, DBS chains began to populate the *hcp* regions. Such region-selective, well-ordered systems as seen in Figure 4.3 did not emerge until the sample was annealed to 120 K, indicating that multiple diffusion events are needed to assemble these complex patterns.

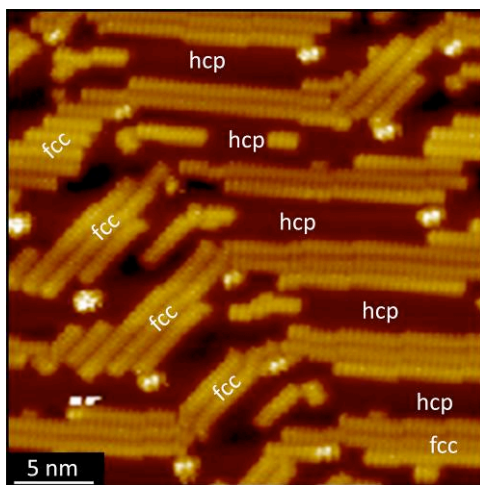


**Figure 4.3 Dibutyl Sulfide on Au Following Thermal Anneal:** STM image of 0.62 ML of DBS on Au(111). DBS preferentially adsorbed in the *fcc* regions of the herringbone reconstruction, resulting in the initial saturation of the *fcc* areas and subsequent filling of the *hcp* bands. Image conditions: 78 K, 30 pA, -0.3 V.

The strong region specificity of DBS is likely due to the regional variations in electron density or packing geometry of Au's herringbone reconstruction.<sup>171,172</sup> The

order of stability suggests a preference for adsorption in areas of low electron binding energy.<sup>66,133,134,171,172</sup> In this system the orientation of the chains in each domain was directed by the geometry of the herringbones reconstruction, which has been seen previously for methane thiol self-assembly on Au(111).<sup>57,59</sup> The domains were often oriented such that the chain length was maximized and continued uninterrupted parallel to the straight portion of a soliton wall until an elbow was encountered. The DBS molecules that terminate a chain have only one nearest neighbor, which makes them less coordinated and therefore less stable than the molecules within the chain. Thus, a given population of DBS species favors the formation of the longest chains possible, minimizing the number of chain termini.

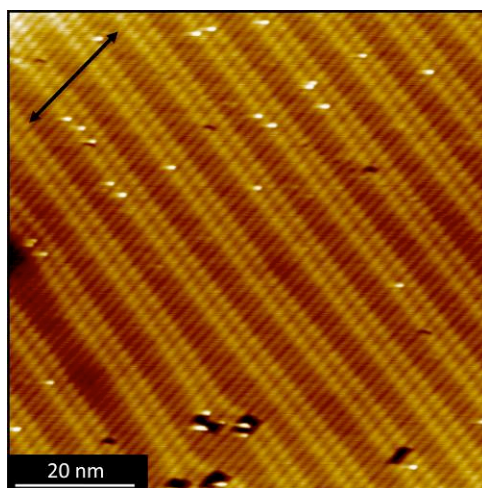


**Figure 4.4 Monolayer Coverage of Dibutyl Sulfide on Au:** STM image of 0.97 ML of DBS on Au(111) after annealing to 120 K. The black arrow indicates the DBS chain direction, which runs at a 60° angle with respect to the herringbones (visible through the SAM). The herringbones have a spacing of  $7.6 \pm 0.5$  nm at this coverage and temperature treatment. Image conditions: 78 K, 5 pA, -0.4 V.

As the coverage of DBS was increased to near-monolayer populations, the domains that were previously segregated into the herringbone *fcc* and *hcp* regions coalesced into large unidirectional domains, seen in Figure 4.4. These unidirectional, single domain structures have been observed to occupy regions larger than 10,000

nm<sup>2</sup> with few defects. These domains traversed the *fcc*, *hcp*, and soliton wall regions of the herringbone reconstruction and had a proposed unit cell of ( $\sqrt{3} \times 10$ ). As the molecules point in opposite directions in neighboring chains the unit cell spans two molecular rows and hence 10 Au atoms. The herringbone spacing for this high coverage system was  $7.6 \pm 0.5$  nm, indicating that the herringbone reconstruction was being partially lifted at this coverage and temperature treatment. The observation that the reorganization of the Au surface happens at such low temperatures (*i.e.*, 120 K) indicates that it is an extremely rapid process.<sup>6</sup> Furthermore, DBS adsorption and subsequent annealing resulted in a straightening of the herringbone reconstruction, thus reducing the number of 120° bends in some areas. This phenomenon has been observed by Friend and co-workers for oxygen adsorbed on Au(111),<sup>44</sup> and indicates that the molecular layer stabilizes the surface and effectively reduces strain, thus negating the need for the formation of a secondary structure (*i.e.*, elbows) for strain relief. The fact that the primary structures (*i.e.*, the soliton walls) remain provides evidence that the molecule-Au interaction for DBS is weaker than for thiols, which completely lift the herringbone reconstruction.

Unlike the lower coverage system, the chains in this SAM adopted a dominant directionality that did not rigorously follow the herringbone reconstruction. There was a correlation between the molecular domain direction and the herringbone reconstruction, as only 6% of observed domains ran in the uncompressed  $\sqrt{3}$  direction, while the vast majority of the domains (94%) ran in the two partially compressed  $\sqrt{3}$  directions, as shown in the high resolution STM image and accompanying model in Figure 4.5. Figure 4.5 shows the alkyl tails on neighboring molecular rows aligned in opposite directions, as seen in the short chain aggregates at

lower coverage and temperature treatments (Figure 4.1). The fact that the rows ran predominantly along compressed directions suggests that the large domains were more stable with slightly closer molecule-molecule spacing than offered by the uncompressed  $\sqrt{3}$  direction (0.482 nm versus 0.499 nm).

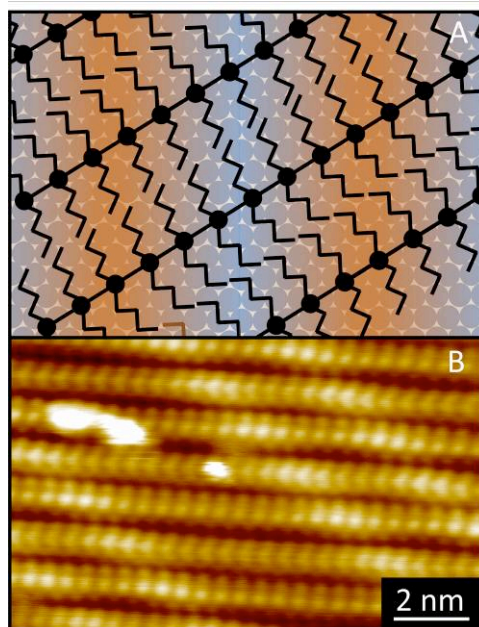


**Figure 4.5 Schematic of Dibutyl Sulfide Assembly on Au:** A) Schematic and B) high-resolution STM image of a monolayer of DBS. In A, the hexagonal array of blue circles represents the Au surface atoms and the orange bands indicate the position of the soliton walls. The adsorption site of the DBS molecules (black) is arbitrary in A, but their positions relative to one another are exact. It also is clear from figure B that the alkyl tails of the molecules orient in opposite directions in adjacent rows. Image conditions: 78 K, -0.4 V, and 5 pA.

At high coverages, the domains often spanned micron-sized areas of the surface, but were sporadically broken by small vacancies in the molecular layer as seen in Figure 4.6. These vacancies did not form randomly, but rather served to stabilize the SAM as a whole by appearing in three distinct locations: near elbows, at domain boundaries, and over portions of the substrate in which the domain ran in the unfavorable uncompressed  $\sqrt{3}$  direction. Vacancy formation around the herringbone elbows may be driven by the surface compression that occurs at there, which is

slightly different than over the rest of the surface.<sup>43,46</sup> In some instances the herringbones changed direction for only a relatively brief span as seen in the bottom right portion of Figure 4.6. In these instances the high-coverage DBS domains traversed unfavorably oriented herringbones (regions where the chains were aligned along the uncompressed axis of the surface). Vacancies in these regions may relieve the stress to the overall monolayer caused by the changes in packing. Vacancies also formed in the uncompressed region and preferentially in the *hcp* bands of the uncompressed region. This reflects and further verifies the greater stability of DBS adsorption in the *fcc* versus the *hcp* regions of the Au(111) surface. The population of vacancies decreased with increasing coverage to the point that there are no such defects at full monolayer coverage, suggesting that, while vacancy location is driven by the optimization of the SAM structure, vacancy formation is not required to stabilize the system.

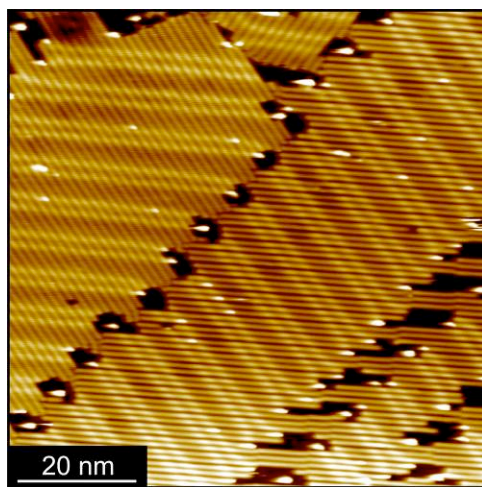


**Figure 4.6 Dibutyl Sulfide Assembly as Influenced by Au's Herringbone Reconstruction:** STM image of 0.97 ML DBS on Au(111). The location of vacancies in the structure is dictated by the absence of molecules in the least favorable adsorption sites such as *hcp* regions, herringbone elbow regions and regions in which the domains run along an uncompressed  $\sqrt{3}$  axis. Image conditions: 78 K, 5 pA and -0.4 V.

The structurally unique medium and high coverage systems were thermodynamically stable up to desorption temperatures (575 K) and a coverage-dependent equilibrium therefore existed between the two. After increasing the coverage from intermediate to high and annealing to 120 K, the moderate coverage SAM was replaced entirely by the high coverage SAM structure (Figure 4.7A versus B). The high coverage system was then annealed to 300 K, and little difference from the 120 K annealed system was observed other than an increase in the herringbone spacing to  $11 \pm 1$  nm (Figure 4.7B versus C). This marked increase provides further evidence that more Au atoms are being released from the surface at elevated temperatures. Upon annealing the high coverage system to 575 K for two minutes, some of the DBS molecules desorbed, thereby decreasing the coverage to 0.67 ML. Upon depositing more DBS onto this SAM system at 78 K, it was necessary to again anneal the system to reach thermodynamic equilibrium because additional DBS added at low temperature formed disordered clumps on top of the pre-existing SAM and substrate.

Greater adsorbate stability in the *fcc* region is also supported by these coverage and temperature dependent studies. Heating the high coverage system to 575 K caused *hcp*-bound DBS molecules to desorb, while molecules occupying the *fcc* regions remained. In this manner a SAM could be generated in which only the *fcc* regions of the Au(111) surface were masked. At this reduced coverage the system returned to the intermediate-coverage SAM structure and the herringbone spacing was  $9.8 \pm 0.6$  nm, similar to that of the 300 K annealed system, indicating that the herringbones did not fully reappear upon DBS desorption. Additionally, the



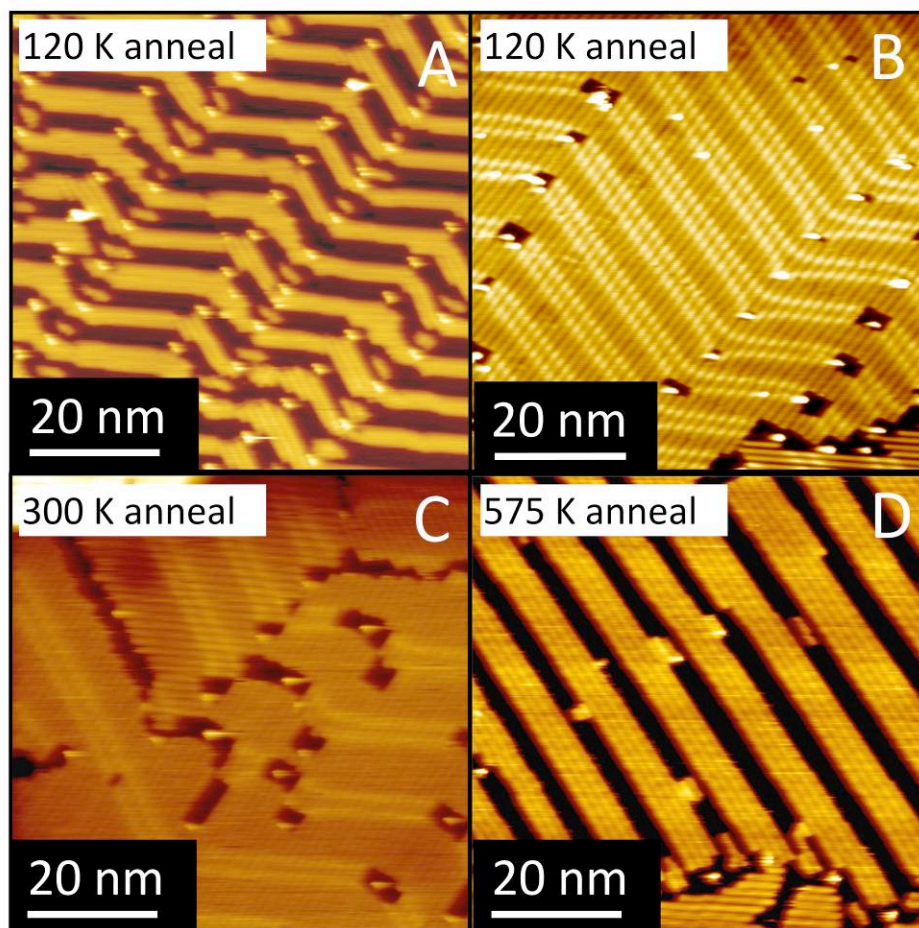


**Figure 4.7 Dibutyl Sulfide Assembly on Au as a Function of Coverage and Temperature:** STM images exhibiting the reversibility of intermediate and high coverage SAM formation. A) Intermediate DBS coverage ( $0.4 \text{ ML} < \theta < 0.8 \text{ ML}$ ) annealed to 120 K exhibited a SAM with domains segregated into the *hcp* and *fcc* herringbone bands. B) Higher coverage systems annealed to 120 K yielded large, single domains. C) Annealing to 300 K had little effect on coverage, as very few molecules desorbed, but the herringbone spacing did increase. D) After a brief anneal at 575 K, partial desorption lead to a system similar to the intermediate coverage assembly. Image conditions: 78 K, 5 pA (A, C, D) -0.2 V, and (B) -0.3 V.

herringbones straightened, which indicates that the thioether layer stabilizes the surface and reduces strain, as mentioned earlier.

The evolution of the herringbone spacing as a function of temperature ( $T$ ) and coverage ( $\theta$ ) is plotted in Figure 4.8. At low  $\theta$  and low  $T$  (120 K), the herringbone spacing was the same as that of native Au, within error. When  $\theta$  was increased to

high coverage, the herringbone spacing increased only slightly after a low T anneal; however, a moderate T (300 K) anneal of the same system caused a marked increase in the herringbone spacing. The observation that higher  $\theta$  caused the herringbone to be lifted more than the lower  $\theta$  suggests that the molecular layer stabilized the Au(111) ( $1 \times 1$ ) surface. Furthermore, the fact that the higher T anneal of the high  $\theta$  caused a more dramatic lifting of the herringbone indicates that the restructuring of the Au(111) surface is a kinetically limited process. Finally, the high T treatment (575 K) caused some of the molecules to desorb, resulting in a low  $\theta$  system and the herringbones began to return. Even though the final system had roughly the same  $\theta$  as the first and the herringbones began to return, the surface did not fully revert to its previous state. The plot in Figure 4.8 demonstrates the reversibility of the restructuring of the system, but also shows that there was some hysteresis as the herringbones were lifted and then returned.

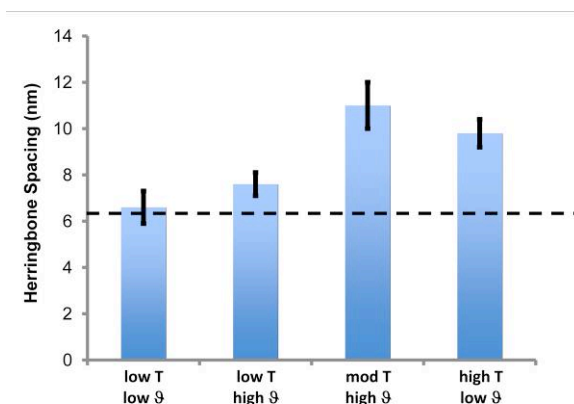


**Figure 4.8 Herringbone Separation of a Function of Dibutyl Sulfide Coverage and Anneal Temperature:** Plot showing the evolution of the herringbone spacing as a function of temperature treatment (T) and molecular coverage ( $\theta$ ). Low, mod and high T refer to 120 K, 300 K, and 575 K, respectively. Low  $\theta$  refers to 0.4 – 0.8 ML and high  $\theta$  refers to near monolayer coverage. The dashed line indicates the native Au(111) ( $22 \times \sqrt{3}$ ) herringbone spacing at 6.34 nm.



### 4.3 Conclusions

This investigation has revealed that DBS, much like alkane thiols, spontaneously forms highly ordered structures on the Au(111) surface. The herringbone reconstruction of the substrate has a significant influence on the assembly process. The fundamental interactions driving the organization are similar to thiol SAMs on Au; strong Au-S interactions and dispersive forces between adjoining alkyl tails stabilize the monolayer. Nevertheless, several unique properties of this system provide opportunities for further research and development. Furthermore, work by Noh *et al.* on dioctadecyl sulfide suggests that these structural qualities are not limited to dibutyl sulfide, but may be true of other thioether species, which have the potential to form stable assemblies under ambient conditions.<sup>35</sup>

This work revealed that the native herringbone reconstruction of Au was partially lifted during DBS SAM formation, even at temperatures as low as 120 K. This change indicates that the strength of the molecule-Au interaction is strong enough to physically remove Au atoms from the substrate's surface, but not so strong that the herringbone reconstruction is completely lifted, as is the case with thiols, which remove atoms beyond the herringbone reconstruction to form etch pits. Higher temperature treatments (300 K) provided more thermal energy to the system allowing the surface to equilibrate even further and yielded a dramatic increase the herringbone separation. Ther herringbones were not completely lifted in any of the systems examined, but we did note a disappearance of the secondary elbow structure, indicating that the SAM relieves some of the inherent strain of the substrate reconstruction.

The most significant deviation from the assembly of alkane thiol species was the orientation of the alkyl tails. Because the tails remain near the plane of the surface, potential exists for control of surface plane structure and chemistry *via* their modification. This control could, for example, enable the formation of highly ordered polymers from pre-assembled reactants if unsaturated alkyl tails are used. As with alkane thiols, it could also permit the tuning of interfacial properties on macroscopic and molecular scales, with the added element of an exposed sulfur atom. Additionally, the sensitivity of the SAM to surface inhomogeneities (due to the herringbone reconstruction) holds possibilities for creating molecular templates structured at the nanoscale with open regions that are many tens of nanometers long but only  $\sim 4$  nm wide. This may permit regionally selective masking of the Au(111) surface for multi-component SAM design *via* coadsorption with regular, nanometer-scale features derived from the native herringbone reconstruction of Au(111).

#### 4.4 Additional Experimental Details

Dibutyl Sulfide (99.9% purity) was obtained from Sigma Aldrich and further purified by freeze/pump/thaw cycles. DBS was deposited onto the cold sample in the STM with a collimated molecular doser. All STM images were recorded at 78 K with etched W tips. All voltages refer to the sample bias. Full monolayer (ML) coverage refers to a complete molecular layer exhibiting a  $(\sqrt{3} \times 10)$  unit cell. Herringbone spacings were measured using line scans set perpendicular to the soliton wall (or parallel to the compressed axis).

## 5 Asymmetric Thioethers as Building Blocks for Chiral Monolayers

### 5.1 Introduction

In the mid-19th century, Louis Pasteur performed the first experiments that provided direct evidence of chirality on the molecular scale.<sup>173</sup> Since then, researchers have taken advantage of molecular chirality in a variety of fields and applications. Self-assembled monolayers of chiral molecules have proven to be very useful systems for the study of two-dimensional chiral interactions, separations, templating, and amplification. In the arena of chiral assembly, tartaric acid,<sup>174–182</sup> cinchona alkaloids<sup>183–185</sup> and heptahelicene<sup>186–188</sup> are among the most commonly studied molecules. Several reports in the literature have revealed that chiral adlayers on achiral surfaces exhibit enantiospecific interactions with chiral probe molecules.<sup>189–192</sup> For example, (S)-propylene oxide exhibits a preference to adsorb on a Pt(111) surface modified with (S)-butoxide over an identical surface modified with (R)-butoxide, with the former system adsorbing 35% more of the probe molecule than the latter.<sup>190</sup>

Applications of self-assembled monolayers (SAMs) often take advantage of tunable chemical functionality and shape. For example, the most common type of SAM involves thiol species (HSR) and utilizes a strong sulfur-metal interaction to form the layers.<sup>5,58,59,78,193</sup> The thiols can be functionalized with groups that are polar, aromatic, etc. Typically, the formation of chiral adlayers has relied on the self-assembly of species that are chiral in the gas phase<sup>174–176,189,190,192,194,195</sup> or that organize into rigid structures *via* hydrogen-bonding interactions.<sup>7,196–206</sup> However, some molecules that are achiral in the gas phase can exhibit a surface-bound chirality due

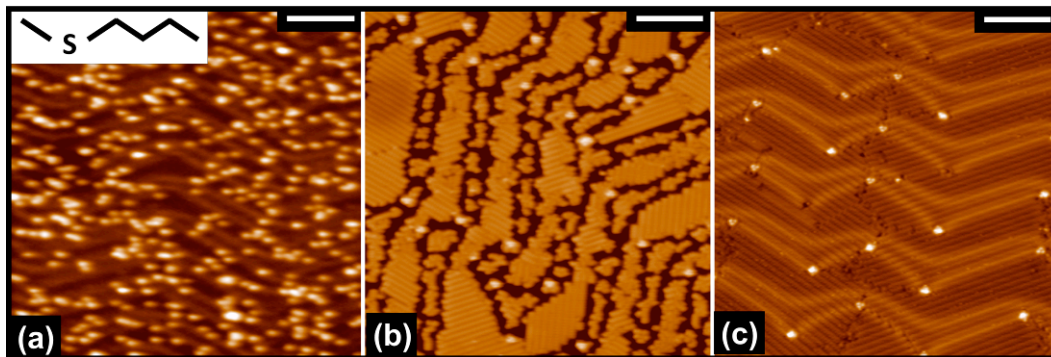
to the removal of mirror symmetry.<sup>111,197,202</sup> The adlayers formed from such prochiral species are necessarily racemic in nature. However, Ernst and Raval have demonstrated that the use of a chiral perturbation, or a small percentage of a "seed molecule", can flip the chirality of the adsorbed molecules, thus creating an overall single-handed organization.<sup>181,182,186,207</sup>

In this chapter, previous work on symmetric thioether (RSR) self-assembly<sup>31,32,208</sup> is extended to asymmetric thioethers (RSR'), and I show that these monolayers are chiral by virtue of the binding of one of the two pro-chiral lone pairs on the S atom to the Au surface.<sup>84</sup> Well-ordered domains of butyl methyl sulfide (BMS) and 4,4,4-trifluorobutyl methyl sulfide (4TF-BMS) form due to van der Waals interactions between molecules, and the self-assembly is almost 100% enantiospecific, leading to the growth of large homochiral domains. With future applications in mind, a study of a partially fluorinated asymmetric thioether is also presented, where, despite this substitution, the same highly enantiospecific assembly leads to similar, well-ordered homochiral domains. The hope is to eventually use these chiral, dipolar layers for studies of spin-polarized electron transmission through organic layers. Also, the fact that asymmetric thioethers are pro-chiral in the gas phase but form enantiomorphic domains when surface-adsorbed offers possibilities for the interrogation of chirality at surfaces. Such experiments might involve symmetry breaking, in which small amounts of a chiral "seed" species are introduced to amplify the global single-handed organization of the molecules.

## 5.2 Results and Discussion

### 5.2.1 Self-Assembly of Asymmetric Thioethers

Previous reports have shown that symmetric thioethers (RSR) adsorbed intact on a Au(111) surface with their alkyl tails parallel or nearly-parallel to the substrate.<sup>31,35,36,81,129,170,208,209</sup> The molecules bonded through one of the two lone pairs on the central S atom and maintained their tetrahedral geometry in the adsorbed state.<sup>84</sup> Furthermore, as shown in the previous chapter RSR species formed well ordered arrays built of rows of molecules with their S atoms aligned and alkyl tails parallel to one another, held together by van der Waals interactions between the alkyl tails.<sup>31,35,36,208,209</sup>



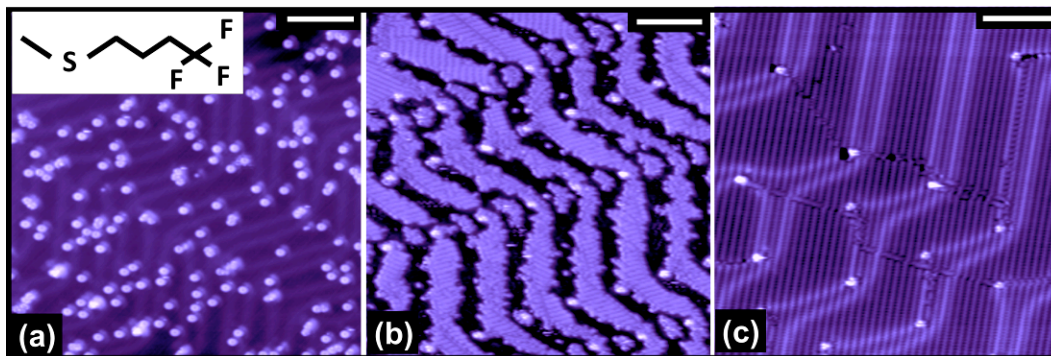
**Figure 5.1 Low to High Coverage Butyl Methyl Sulfide on Au:** STM images showing (a) 0.19 ML, (b) 0.67 ML and (c) 0.99 ML BMS on Au(111). The low-coverage system in (a) was imaged as dosed at 78 K, while the medium and high systems in (b) and (c), respectively, were annealed to 120 K prior to imaging at 78 K. Scale bars = 10 nm. Image Conditions: 78 K; (a) and (b) 10 pA, 100 mV and (c) 200 pA, 200 mV.

Figure 5.1 shows the nanometer-scale characteristics for the long-range self-assembly of butyl methyl sulfide (BMS) on Au(111). BMS is an asymmetric thioether species (see schematic in Figure 5.1a). When adsorbed on Au(111), BMS forms self-assembled systems that vary as a function of coverage. At low coverage ( $< 0.3$  monolayers (ML)), BMS molecules show no preference for any region of the Au

surface and essentially stick where they land as shown in Figure 5.1a. Upon further adsorption, BMS exhibits no long-range ordering at 78 K. The system was then annealed to 120 K, after which the molecules aggregate into well-ordered rows. This observation suggests that long range ordering is a kinetically-limited process that requires thermal diffusion of the molecules.<sup>208</sup> At medium coverage (0.3 ML to 0.8 ML), after annealing to 120 K, BMS forms small domains of ordered rows of molecules. A representative image of BMS at medium coverage is shown in Figure 5.1b. The size and shapes of the molecular domains are dictated by the soliton walls of gold's reconstruction, which separate *fcc* and *hcp* stacked regions of the surface and appear as pairs of lines running along the surface. The molecules exhibit different binding preferences for the different regions of the Au surface, with molecules aggregating first in the wider *fcc*-packed regions, then the narrower *hcp*-packed regions, and finally the soliton regions of the surface reconstruction. This variation in stability within the different regions of the surface suggests a preference for adsorption in *fcc* areas either due to the atomic spacing or local electronic structure.<sup>66,134,171,172,210</sup> At high coverage (>0.9 ML), the molecules form large continuous domains that span all regions of the herringbone reconstruction.

4TF-BMS was designed and synthesized to be a highly dipolar analog of BMS, with three fluorine atoms at the end of the butyl tail (see schematic in Figure 5.2a). Even with this added functionality, 4TF-BMS shows similar self-assembly properties to BMS at low, medium, and high coverage (Figure 5.2). The medium- and high-coverage systems of 4TF-BMS were also annealed to 120 K to promote long-range molecular assembly before imaging at 78 K. Furthermore, the 4TF-BMS shows the

same regional preferences as its non-fluorinated counterpart, being most likely to aggregate in the *fcc*-, then *hcp*-, then soliton regions of the Au surface.



**Figure 5.2 Low to High Coverage 4,4,4-Trifluorobutyl Methyl Sulfide on Au:** STM images showing (a) 0.18 ML, (b) 0.63 ML, and (c) 0.99 ML 4FT-BMS on Au(111). The low-coverage system in (a) was imaged as dosed at 78 K, while the medium- and high-coverage systems in (b) and (c), respectively, were annealed to 120 K prior to imaging at 78 K. Scale bars = 10 nm. Image conditions: 78 K; (a) 100 pA, -300 mV, (b) 100 pA, 600 mV, and (c) 500 pA, -500 mV.

Higher-resolution, molecularly resolved STM images allowed for the determination of local molecular packing. The images in Figure 5.3 reveal that both BMS and 4TF-BMS adsorb intact with their alkyl tails parallel or nearly parallel with the Au substrate, and both species exhibit a  $(\sqrt{13} \times \sqrt{3})R13.9^\circ$  unit cell. The herringbone reconstruction is removed with increasing molecular coverage and temperature treatments (this phenomenon will be explored in detail in Section 3.3 of this chapter). As such, the majority of the molecular domains reside on  $(1 \times 1)$ , unreconstructed Au(111). Therefore, the  $(\sqrt{13} \times \sqrt{3})$  unit cell describes the periodicity of the molecular overlayer with respect to the ideal (*i.e.*, unreconstructed) Au(111) surface with a Au-Au spacing of 0.288 nm.

Our previous studies examining dimethyl sulfide (DMS) and dibutyl sulfide (DBS) on Cu(111) and Au(111) offer evidence that van der Waals attractions play an important role in the assembly of the longer tailed species.<sup>31,32,208,211</sup> DMS arranges in

a perpendicular (or “herringbone”) packing arrangement, which is typical of quadrupolar molecules.<sup>32,211</sup> However, DBS, which is very chemically similar to DMS,

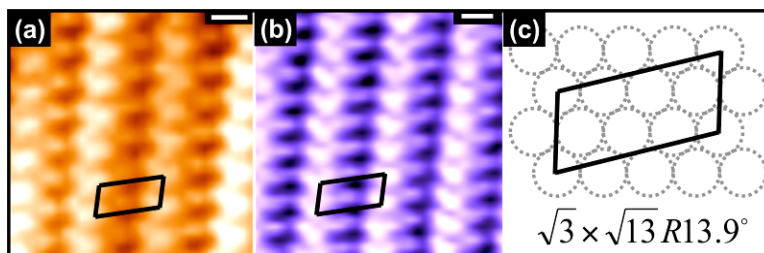


**Figure 5.3 Unit Cell for Butyl Methyl Sulfide and 4,4,4-Trifluorobutyl Methyl Sulfide on Au:** Molecularly-resolved STM images showing the unit cell packing structure of (a) BMS and (b) 4TF-BMS on Au(111). The schematic in (c) shows the unit cell dimensions with respect to the underlying atomic lattice. Scale bars = 0.5 nm. Image Conditions: 78 K; (a) 200pA, 200 mV and (b) 300 pA, -600 mV.

packs in linear rows.<sup>31,208</sup> The difference in packing structure of the two molecules is due to the competition between intermolecular quadrupole-quadrupole and van der Waals interactions. DMS has short alkyl chains, and quadrupole-quadrupole interactions dominate the packing energetics leading to a herringbone packing structure. DBS, however, has larger alkyl chains that contribute to increased van der Waals interactions. This interaction is larger than the quadrupole-quadrupole energy and forces the molecules to arrange in linear chains that maximize van der Waals interactions.

Additionally, Density Functional Theory (DFT) charge calculations for the adsorption of BMS on Au show that upon adsorption, a charge of  $0.11 e^-$  is transferred to the surface from the S atom of the molecule.<sup>82</sup> Thus, there is a partial positive charge on the S atom, and a corresponding partial negative charge on the metal surface beneath. From the perspective of electrostatics, it would be unfavorable for the S atoms to align in straight rows; however, this behavior is observed. It is likely that the same competing quadrupole-quadrupole and van der



Waals interactions discussed above are at play in determining the packing structure for BMS and 4FT-BMS.

The fact that BMS and 4FT-BMS self-assemble on Au(111) in a similar manner indicates that substitution of three H atoms for F atoms does not significantly alter the molecular packing structure. The difference between the van der Waals radii of the C-H and C-F bond is  $\sim 0.02$  nm, or 4% of the average thioether-thioether molecule spacing of 0.5 nm.<sup>212</sup> This means that in steric terms the BMS and 4FT-BMS molecules are almost identical. Also, our previous work exploring DBS SAM formation on Au(111) revealed that the majority of the molecular rows (94%) ran predominantly in the two partially compressed  $\sqrt{3}$  directions.<sup>208</sup> These findings suggest that the DBS molecules are electrostatically stable even with the slightly closer separation (0.482 nm *vs* 0.499 nm) exhibited by this lattice direction. Furthermore, the monolayer structure of BMS is in part driven by van der Waals interactions. Due to electron pair donation to the surface, the S atom of each molecule has a partial positive charge.<sup>82</sup> The F atoms at the end of each butyl tail in 4FT-BMS are strongly electron withdrawing, resulting in a partial negative charge. As such, we can describe the 4FT-BMS molecular rows as being a series of nested dipolar molecules. Therefore, from both a size and electrostatics perspective BMS and 4TF-BMS are most stable in the same molecular arrangements.

### 5.2.2 Homochiral Domain Formation

Within the islands of self-assembled BMS and 4TF-BMS that form at medium to high coverage, there are a few domain boundaries. Figure 5.4 shows a high-resolution image of 0.83 ML of 4TF-BMS; upon close inspection, it is clear that

boundaries separate homochiral domains of the molecules. When these molecules (which are achiral in the gas-phase) adsorb on a surface, bonding occurs through only one of the two pro-chiral lone pairs on the S atom.<sup>82,84</sup> The alkyl tails align parallel to the surface; thus, the thioether molecules essentially retain their tetrahedral geometry upon adsorption.<sup>84</sup> This bonding behavior leads to two surface-bound enantiomers depending on which of the lone pairs bonded to the surface (see Figure 5.4 for schematic).<sup>82</sup> In STM images, the adsorbed molecules appear as "V-shaped" protrusions, with one leg of the V shorter than the other corresponding to the methyl group. Thus, the chirality of the adsorbed molecules can be inferred based on their appearance in STM images.

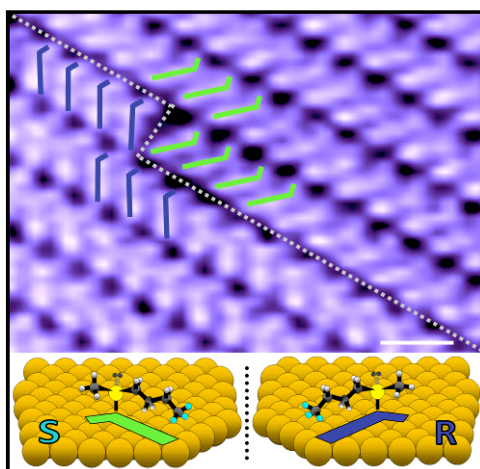


**Figure 5.4 Homochiral Domain Formation:** STM image (top) showing the boundary between two homochiral domains in a 4TF-BMS system. These molecules are achiral in the gas-phase, but become chiral when adsorbed on a surface. The schematics in the lower portion of the figure show the mirror-symmetry of two adsorbed asymmetric thioether species. The handedness (R *vs* S) of the surface-bound molecule is determined by which lone-pair interacts with the surface. In the schematic, the surface is comprised of Au (gold) atoms; S is yellow, C is black, H is white, and F is cyan. Scale bar = 1 nm. Image conditions: 78 K, 300 pA, 600 mV.

Due to the three-fold symmetry of the hexagonally packed Au(111) surface and the asymmetry of the molecules, the molecular domains can adopt one of twelve orientations (see Figure 5.5 for schematic). Due to a 180° rotation about each close-

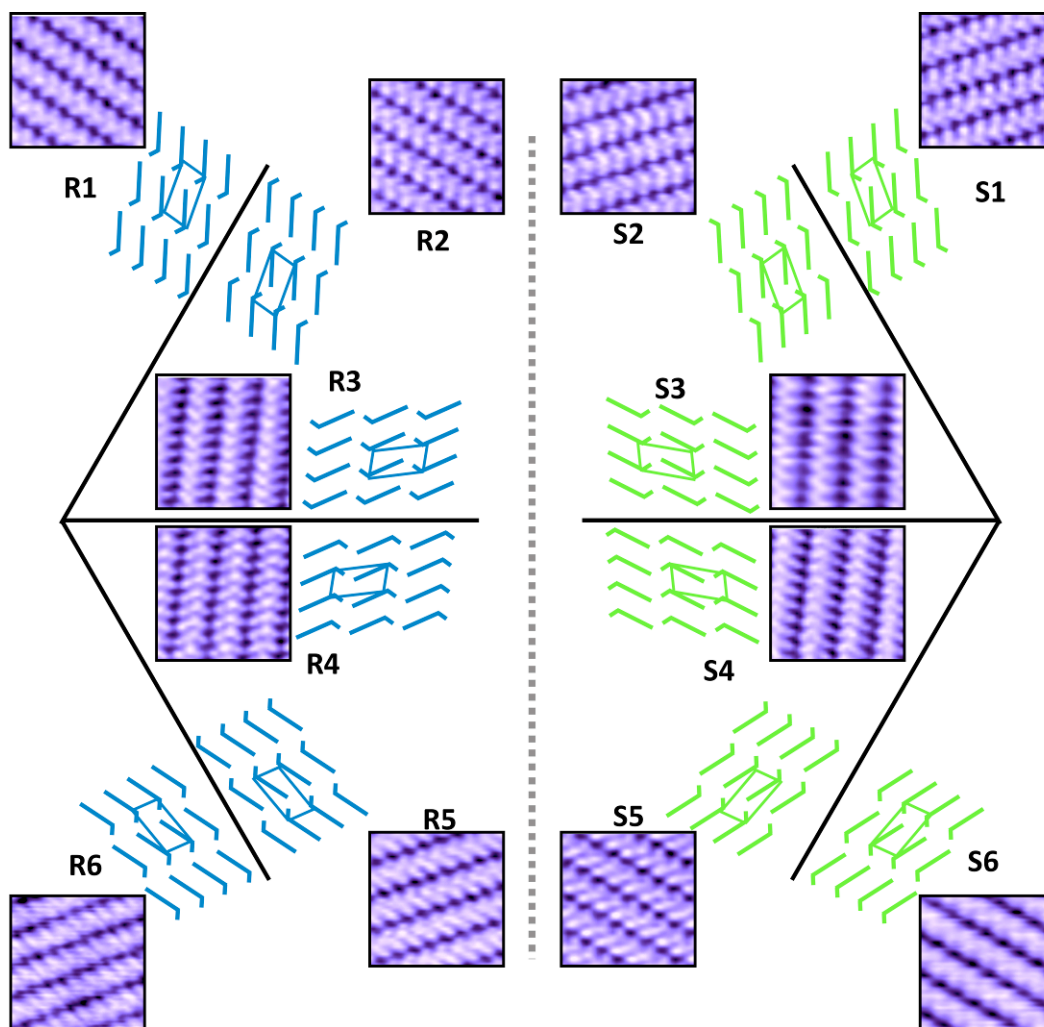


**Figure 5.5 Twelve Degenerate Domains of 4,4,4-Trifluorobutyl Methyl Sulfide on Au:** STM images and schematics showing the twelve molecular packing structures for 4TF-BMS on Au(111). Six of the orientations arise for each of the molecule's two enantiomers due to the three-fold symmetry of the (111) surface lattice. All twelve structures are related by either rotational or mirror symmetry. S/R labels refer to the different rotational domains for the packing of the two enantiomers. All images are  $\sim 4 \text{ nm} \times 4 \text{ nm}$  in dimension. Image conditions: 78 K, 10-500 pA,  $\pm(100-600) \text{ mV}$ .

packed lattice direction, each row of molecules can orient with its tails pointing up or down relative to each atomic row. Therefore, six different rotational positions can exist for molecular rows of a single enantiomer.<sup>81,83,84,130,170,213</sup> As there are two enantiomers, there is the possibility for the assembly of twelve monolayer structures on the surface, each related by rotational or mirror symmetry. Each of these twelve

structures had the same ( $\sqrt{13} \times \sqrt{3}$ ) unit cell rotated  $\pm 13.9^\circ$  from the close-packed direction. Thus, the images and schematic in Figure 5.3 show domains and the unit cells of R enantiomers for both BMS and 4TF-BMS. Figure 5.5 shows STM images of 4TF-BMS with corresponding unit cell schematics for each of the twelve possible orientations. All twelve of these domains were found on self-assembled monolayers of both BMS and 4TF-BMS. See the Appendix for a similar figure for BMS.

Our previous study using DFT calculations showed that the R and S surface-bound enantiomers of BMS are equivalent in energy, as would be expected.<sup>82</sup> Thus, there is no preference for adsorption in either configuration. DFT also revealed that the barrier to invert from one enantiomer to the other, which requires switching the lone pair bound to the surface, is on the order of 0.24 eV.<sup>82</sup> Assuming the inversion exhibits Arrhenius-type behavior with a typical pre-factor  $\sim 10^{12}$ , at 78 K (the sample temperature during deposition) the molecules invert chirality at a rate of  $\sim 0.0002$  Hz. At 120 K (the annealing temperature that led to the formation of large homochiral domains), the inversion rate would be  $\sim 80$  Hz.

Previous reports of the self-assembly of dibutyl sulfide (DBS) on Au(111) showed that symmetric thioether molecules diffused on the surface at a rate that increased with temperature.<sup>208</sup> When the molecules diffused to within a nanometer of each other, they interacted to form chains.<sup>208</sup> A similar process of diffusion and self-assembly likely occurs in the asymmetric thioether systems as well. The equal and random distribution of R and S enantiomers coupled with the rapid inversion of chirality at elevated temperatures ( $\sim 80$  Hz at 120 K) dictate that the number of (R-R), (S-S), and (R-S) collisions are nearly equivalent. If all molecule-molecule interactions were also equivalent, then one would expect to see a predominance of

disordered, heterochiral domains. The fact that we observe ordered, homochiral domains almost exclusively suggests that (R-R) and (S-S) molecular interactions are energetically favorable compared to (R-S) interactions. This result is consistent with the fact that van der Waals interactions between the alkyl tails stabilize the layers; the nested butyl-butyl/methyl-methyl interaction in homochiral pairs is more stable than the butyl-methyl/methyl-butyl interaction of heterochiral (R-S) pairs.

At 120 K (the lowest anneal temperature used in this investigation), molecules on the surface diffuse and invert their chirality rapidly. The process of homochiral domain formation can occur *via* two routes. When similar enantiomers (R-R or S-S) collide, the chains formed would be relatively stable. However, if dissimilar enantiomers (R-S) collide, the resultant chains would be less stable. In the first proposed mechanism, the dissimilar enantiomers stay together for only a short time before separating and diffusing to find like molecules with which to interact. In the second mechanism, the two dissimilar enantiomers undergo rapid inversion until their chiralities match, stabilizing the resulting chain. Assuming that both processes occur on similar timescales, it is likely that both mechanisms contribute to the process of homochiral domain formation. STM movies showing the enantiospecific assembly of BMS are provided in the Appendix. These movies also show BMS inversion events that occur at a rate that agrees well with that predicted by theory and lead to homochiral assembly.

At this point, it is important to mention the effect of the gold substrate's native reconstruction on molecular assembly. At medium coverage, the boundaries of the molecular domains are determined by the directionality of the herringbone reconstruction. At near monolayer coverage, however, the molecular layer crosses

the soliton walls of the herringbone reconstruction, creating large homochiral domains that are seemingly unaffected by the gold surface. Both of these effects can be seen in Figure 5.1 and Figure 5.2. While equivalent numbers of each enantiomeric domain are found, each of the homochiral domains can span areas on the order of  $10^3$ - $10^4$  nm<sup>2</sup> (see Figure 5.6 for comparisons). Thus, this system provides control over the size of enantiopure domains based solely on the coverage of the system.

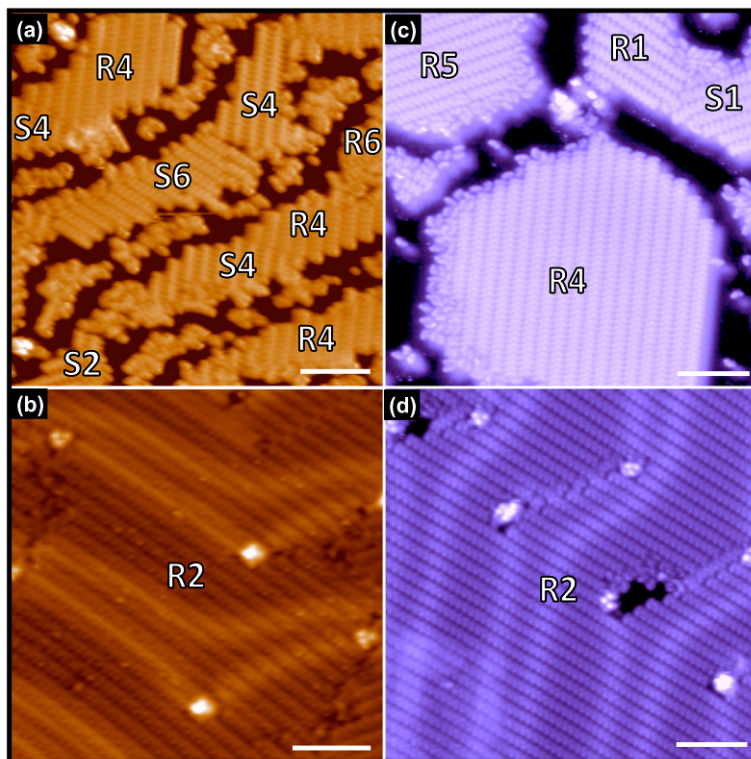


**Figure 5.6 Domain Size Dictated by Herringbone Reconstruction:** STM images of medium (top) and high (bottom) coverage BMS (left) and 4TF-BMS (right) on Au(111). At medium coverage, small homochiral domains are formed in both systems. The domains are primarily confined to the *fcc*-regions of the Au surface. At high coverage, homochiral domains span across the herringbones to form large ( $>10^3$  nm<sup>2</sup>) domains. Scale bars = 5 nm. Image conditions: 78 K; (a) and (b) 200 pA, 200 mV, (c) 300 pA, -600 mV, and (d) 500 pA, -500 mV.

Although there are large homochiral domains in our systems, the overall architecture is racemic in nature. This global achirality is similar to that observed for 50:50 (R,R)-tartaric acid: (S,S)-tartaric acid adsorbed on Cu(110).<sup>174</sup> Subsequent

experiments with tartaric acid have shown that using slight enantiomeric excess can lead to systems displaying a predominance of single-handed organization. In these non-racemic tartaric acid systems, the minor component often displayed a tendency to remain disordered on the surface.<sup>174</sup>

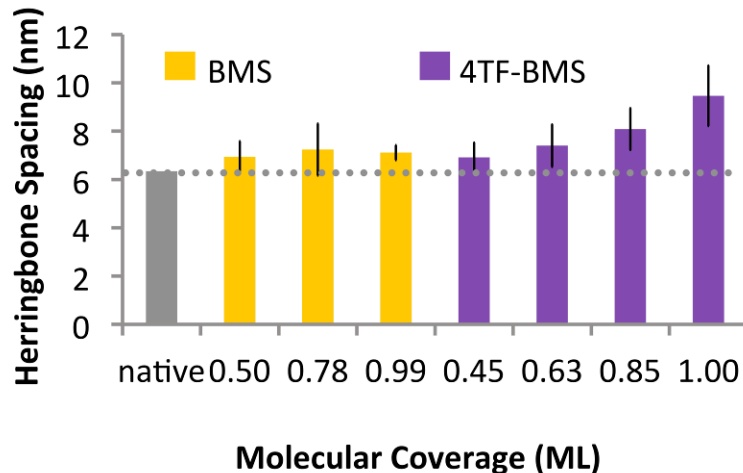
Given that the molecules used in this study are achiral in the gas phase, it is not feasible to break symmetry by introducing initial enantiomeric excess. However, it might be possible to take advantage of the molecules' ability to interconvert between its two energetically equivalent enantiomers. Future plans include using the approach of finding appropriate seed molecules for these thioether systems.<sup>181,182,186</sup>

### 5.2.3 Surface Interaction: Lifting Gold's Herringbone Reconstruction

Adsorbates with a weak interaction with Au(111), such as styrene ( $\sim 60$  kJ/mol), do not lift the herringbone reconstruction.<sup>67</sup> However, adsorbates with a stronger interaction with Au(111), such as thiols ( $\sim 130$  kJ/mol), fully lift the herringbone reconstruction to form  $(1 \times 1)$  Au.<sup>5,41,58,59,78,172</sup> The work presented in Chapter 4 showed that the adsorption of the symmetric thioether species DBS caused gold's native herringbone reconstruction to be *partially* lifted, even at temperatures as low as 120 K.<sup>208</sup> Temperature programmed desorption experiments have indicated that the DBS gold interaction is  $\sim 90$  kJ/mol.<sup>5</sup> As a measure of the interaction strength of thioethers with Au surfaces, we use the spacing of the herringbone reconstruction.<sup>214</sup> A weakly interacting molecule does not alter the surface, and hence the spacing remains at 6.3 nm, the unit cell of clean Au ( $22 \times \sqrt{3}$ ). Slightly stronger interacting adsorbates remove a few atoms from the surface, therefore annihilating some of the herringbones and making their separation appear larger. After the extra 4.5% surface

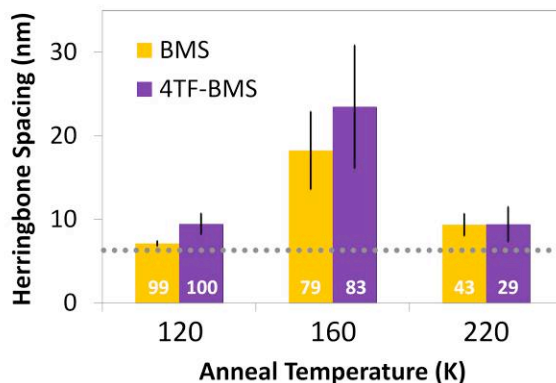
Au atoms are removed, the herringbones disappear completely and their spacing is infinite. As herringbone spacing can be easily measured from STM images, this approach provides an accurate measure of the interaction strength of adsorbates as a function of coverage and molecular chemistry.<sup>208,214</sup>

Figure 5.7 shows the herringbone spacing as a function of BMS and 4TF-BMS coverage. These systems were annealed to 120 K following each subsequent dose. As the BMS coverage increases (orange), the herringbone spacing remains relatively unchanged; however, as 4TF-BMS coverage increases (purple), the herringbone spacing increases slightly. The data therefore suggest a slightly stronger interaction between Au and the partially fluorinated thioether than with the unfluorinated analog. The variability in the herringbone spacing as a function of molecular coverage can be seen in the STM images in Figure 5.1, Figure 5.2, and Figure 5.6.



**Figure 5.7 Herringbone Spacing as a Function of Butyl Methyl Sulfide and 4,4,4-Trifluorobutyl Methyl Sulfide Coverage:** Plot showing the average herringbone separation for native gold (grey) as a function of coverage for BMS (orange) and 4TF-BMS (purple). Each system was annealed to 120 K. The data suggests that the fluorinated species has a slightly stronger interaction with the Au surface as evidenced by the wider herringbone separations at high coverage.





**Figure 5.8 Herringbone Separation as a Function of Anneal Temperature:** Plot showing the average herringbone separation as a function of anneal temperature for BMS (orange) and 4TF-BMS (purple) on Au(111) ( $22 \times \sqrt{3}$ ). The dotted grey line indicates the native herringbone reconstruction spacing. The initial high coverage systems (120 K) were subsequently annealed to 160 K and 220 K. Annealing led to molecular desorption, and molecular coverage (% ML) is indicated by the white numbers for each data set. The data from the 120 K and 160 K anneals suggest that the lifting of the herringbone reconstruction is a kinetically-limited process, which is aided by an increase in thermal energy. The data from the 220 K anneal reveal that upon desorption of the molecular layer, the Au native reconstruction begins to return.

The full coverage BMS and 4TF-BMS systems (shown in Figure 5.1(c) and Figure 5.2(c), respectively) were also annealed to successively higher temperatures from 120 K to 220 K. The herringbone spacing is presented as a function of annealing temperature in Figure 5.8. As the temperature increases, some of the molecules desorb, leading to lower coverage as indicated by the numbers (% of ML) on the bars in Fig. 8. The data reveal that 120 K is sufficiently hot enough to promote a restructuring of the Au surface, as indicated by the slight increase in the herringbone separation. A subsequent anneal at 160 K is enough to promote a marked increase in the herringbone separation, indicating a significant restructuring of the Au surface. Further annealing to 220 K leads to significant molecular desorption in both systems, and the herringbone reconstruction begins to return. These observations indicate that the restructuring of the Au surface is a kinetically-

limited process, which is accelerated by an increase in thermal energy. These findings are further supported by previous work examining DBS on Au(111), in which the reversible lifting of the herringbone reconstruction showed a similar temperature dependence.<sup>208</sup>

The coverage and temperature-dependent behavior observed in the BMS and 4TF-BMS systems is analogous to that previously reported for DBS on Au(111).<sup>208</sup> The maximum herringbone separation measured for the system DBS was  $11 \pm 1$  nm (measured for 97% coverage after annealing at 300 K).<sup>208</sup> We therefore conclude that BMS and 4TF-BMS have a stronger interaction with the Au substrate than DBS, as indicated by the greater degree of surface reorganization exhibited in these systems. A possible rationalization for the observed difference is that the "footprints" for BMS and 4TF-BMS are smaller than that for DBS; consequently, the adsorption of BMS and 4TF-BMS leads to more S-Au bonds per unit area than with DBS and hence more Au surface reorganization. Conversely, both BMS and 4TF-BMS layers are almost fully desorbed after being annealed to 300 K; while DBS was stable with respect to desorption at 300 K. In fact, DBS was present on the surface at a coverage of 0.67 ML even after being annealed to  $>500$  K.<sup>208</sup> The length of the alkyl tails clearly affects the stability of the system. It is likely that longer tails stabilize the molecular layer due to van der Waals interactions between the tails in neighboring molecules, as described previously, and between individual molecules and the Au surface. Interestingly, our results indicate that functionalization of the butyl tail does not appear to affect the stability of the molecular layer, as BMS and 4TF-BMS exhibit similar temperature-dependent desorption behavior.

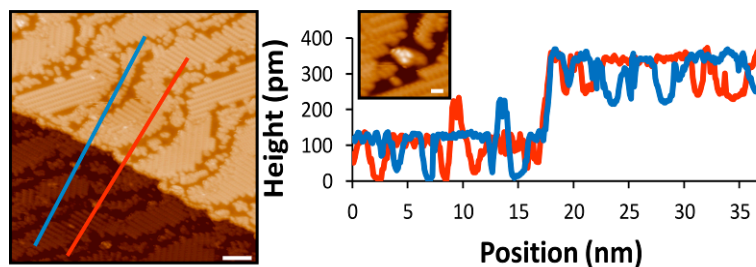


**Figure 5.9 Ejected Au Atoms within the Butyl Methyl Sulfide Monolayer:** STM image (left) showing 0.73 ML BMS on Au(111) at 78 K after annealing at 120 K. The inset shows a zoomed-in image at an elbow in which three bright lobes are clearly visible. Line scans over the lobes and a step show that they are the same height, suggesting that the lobes are Au atoms. In this system, the herringbone reconstruction is partially lifted; as Au atoms are ejected from the surface, some are trapped at the herringbone elbows. Scale bar = 5 nm (inset scale bar = 1 nm). Imaging conditions: 78 K, 200 pA, 200 mV.

The native herringbone structure of gold is lifted as Au atoms are ejected from the surface layer, and this process often occurs in conjunction with molecular adsorption.<sup>41,44,59,215</sup> If adsorbed species are deposited quickly, the ejected Au adatoms can be trapped near the ejection point.<sup>6,214</sup> If the molecular layer is not dense, the ejected adatoms can diffuse and incorporate into nearby defects and step edges.<sup>62</sup> Figure 5.9 shows an STM image taken near a step edge in the medium-coverage BMS system. At this coverage, the herringbone is partially lifted, and most of the Au adatoms diffuse to nearby steps. The low molecular coverage and increased anneal temperature (120 K) provide sufficient space and thermal energy, respectively, for the steps to reorganize (*i.e.*, minimal faceting occurred). However, a small number of Au adatoms are trapped at each elbow and appear as the three-lobed structures in Figure 5.9 (see the inset for a more detailed image of the three-lobed feature). The edge dislocations at the herringbone elbows serve as the ejection site for Au atoms leaving the surface.<sup>216</sup> Height measurements over step edges and these three lobed structures confirm that they are the same height as a Au step and are most likely Au atoms (see plot in Figure 5.9). We postulate that these three adatoms are complexed

with a number of thioether molecules, which stabilize their presence and hinder their diffusion to more stable sites such as step edges.

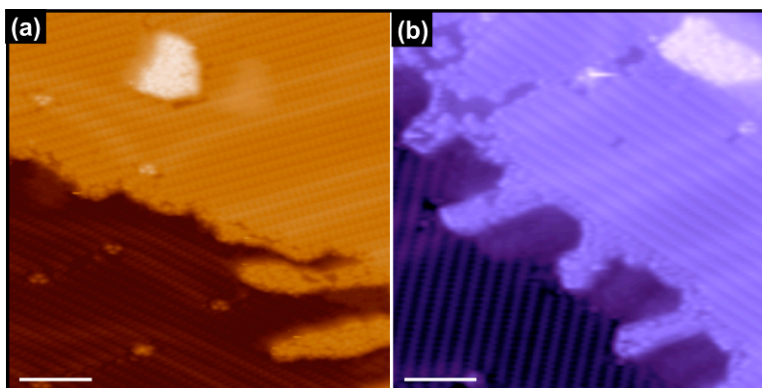


**Figure 5.10 Step Reorganization on Au in the Presence of Butyl Methyl Sulfide and 4,4,4-Trifluorobutyl Methyl Sulfide:** STM images of (a) 0.99 ML BMS and (b) 0.99 ML 4TF-BMS on Au(111), both systems have been annealed to 120 K. In these systems, the herringbone reconstruction is partially lifted. Some of the Au atoms ejected from the surface are free to diffuse. These atoms form small islands or combin with step-edges to form finger-like extensions. Further reorganization of the surface (*i.e.*, smoothing of the step-edge) is hindered due to the dense molecular layer. Other ejected atoms are trapped at elbows (see three-lobed structures) as in the medium-coverage systems. Scale bars = 5 nm. Imaging conditions: 78 K, (a) 50 pA, 100 mV and (b) 500 pA, -500 mV.

The phenomenon of Au atom ejection and incorporation at step edges can also be observed in Figure 5.10, which shows STM images taken at step edges of the full coverage BMS and 4TF-BMS systems. These systems differ from that shown in Figure 5.9 only in the initial dose, which was higher for those shown in Figure 5.10. The full coverage systems contain islands on the terraces and finger-like growths at the step edges, which arise from Au adatoms diffusing to and aggregating with one another at the step edges. The dense molecular layer hinders reorganization of the steps, which leads to the finger-like islands growing from the steps in each system.<sup>217</sup> Also visible are three bright protrusions at the herringbone elbows, which may correspond to Au adatoms trapped within the dense molecular layer. These observations support our hypothesis that the lifting of the herringbone

reconstruction and Au adatom diffusion is a kinetically-limited process that depends on molecular coverage and temperature.

### 5.3 Conclusions

In this Chapter, the behavior of two asymmetric thioether species adsorbed on Au(111) surfaces was examined as a function of coverage and temperature. Both BMS and 4TF-BMS are achiral in the gas phase, but exhibit chirality upon adsorption to the surface of gold. Even though fluorination introduces a significant dipole moment, both molecules exhibit similar self-assembly to form well-ordered homochiral domains of the same unit cell, which vary in size depending on molecular coverage. At medium coverage, the domains are small, and their boundaries are constrained by the soliton walls of Au's herringbone reconstruction. At high coverage, however, the domains span large areas of the surface and are unaffected by the reconstruction. The fact that the introduction of fluorine fails to perturb the overall assembly scheme suggests that other types of functionalization might also have a minimal impact on domain formation. The ability to fine-tune these overlayers for a specific chemical function will open up new possibilities for the chiral templating of surfaces.

The herringbone reconstruction of the Au substrate also evolves as a function of molecular coverage and temperature. Experiments reveal that both species only partially lift the herringbone reconstruction, indicating intermediate interaction strengths for thioethers on gold, less than that of alkanethiols. The degree of surface reorganization increases with coverage. Furthermore, adding energy to the system in the form of heat has a marked affect on the herringbone separation, indicating that

the lifting of the herringbone reconstruction is a kinetically-limited process at low temperatures.

## 5.4 Additional Experimental Details

### 5.4.1 *Low-Temperature Scanning Tunneling Microscopy*

For both species under investigation, molecular coverage values were calculated from molecularly resolved STM images; one monolayer (ML) refers to full coverage with a  $(\sqrt{13} \times \sqrt{3})R13.9^\circ$  unit cell.

### 5.4.2 *Butyl Methyl Sulfide Preparation*

Butyl methyl sulfide (BMS) was obtained from the rare chemical library of Sigma Aldrich and was further purified by cycles of freeze/pump/thaw prior to introduction to the STM chamber *via* a precision leak valve. The purity of the BMS sample has been previously determined by experiment to be >99% from both high-resolution STM and mass spectrometry data.<sup>213</sup> BMS was deposited from the liquid state onto the cold sample (78 K) by a collimated molecular doser.

### 5.4.3 *4,4,4-Trifluorobutyl Methyl Sulfide Synthesis and Preparation*

4,4,4-Trifluorobutyl methyl sulfide (4FT-BMS) is not commercially available, and was prepared *via* a novel synthetic approach by collaborators at the University of Houston. The synthesis procedure has been published elsewhere.<sup>218</sup>

## 6 Gently Lifting Gold's Herringbone Reconstruction: Trimethylphosphine on Au(111)

### 6.1 Introduction

The interaction and assembly of trimethylphosphine (TMP) on Au(111) was examined in an effort to weaken the molecule-metal interaction strength and prevent the formation of etch pits. Early macroscopic investigations of trialkylphosphines ( $\text{PR}_3$ ) indicate that they form strongly-bound layers on Au(111),<sup>219–223</sup> and that the bond enthalpy of the  $\text{PR}_3$  layer on Au is  $\sim 120$  kJ/mol, which is slightly weaker than that of an adsorbed thiol layer (130 to 170 kJ/mol).<sup>5,219</sup> The  $\text{PR}_3$  molecules bind *via* the lone electron pair on the phosphorous atoms and their alkyl tails point away from the surface.<sup>219</sup>  $\text{PR}_3$  species are widely used in organic synthesis (for C-C bond formation)<sup>224</sup> and as surfactants in the formation of metal nanoparticles,<sup>225</sup> so understanding their interaction with metal substrates on the atomic scale is critical to improving such processes.

Coverage dependant behavior and the effect of temperature were studied in a controlled manner. To our knowledge, this report is the first atomic-scale characterization of any trialkylphosphine species adsorbed on a metal surface. The TMP molecules bind strongly to the surface, dramatically changing the surface reconstruction and creating kinetically-trapped Au nanoislands. I propose a mechanism by which the Au surface is reorganized, and have found that the degree of surface reorganization can be controlled as a function of coverage and temperature. These films form well-ordered monolayers which are stable at room temperature and desorb molecularly at  $T > 500$  K. Importantly from a self-assembly

point of view, no etch pits are formed when TMP adsorbs on Au(111), even at full monolayer coverage.

## 6.2 Results and Discussion

### 6.2.1 *Lifting the Herringbone and the Formation of Gold Nano-Islands*

Figure 6.1a shows an STM image of 0.62 ML TMP on Au(111) that has been annealed to 220 K. At this coverage the molecular density was  $1.2 \pm 0.1$  molecules/nm<sup>2</sup> and the characteristic herringbones of the Au(111) surface were not visible. This observation suggests that the adsorbed molecular layer relieved the inherent strain of the native surface<sup>44</sup> ejecting Au atoms from the herringbone and leading to a  $(1 \times 1)$  surface configuration. The ejected adatoms formed islands, which were themselves covered with molecules and comprised  $0.9 \pm 0.4$  % of the surface. Line scans over islands, such as those shown in Figure 6.1b, yielded a measured height of  $0.25 \pm 0.05$  nm, which is comparable to the height of a monatomic Au step of 0.24 nm. These two observations, coupled with the notable lack of etch pit formation, affirms that the islands were comprised of Au adatoms, which came directly from the extra atoms released from the herringbone reconstruction.

In this first experiment, the disappearance of the herringbone reconstruction was concerted with the appearance of Au islands. In order to investigate in detail how the reconstruction lifted, we imaged molecular coverages and annealing temperatures that yielded some Au islands but retained a portion of the herringbone surface reconstruction. This set of experiments allowed us to elucidate the mechanism by which TMP lifted Au's reconstruction by spatially correlating the



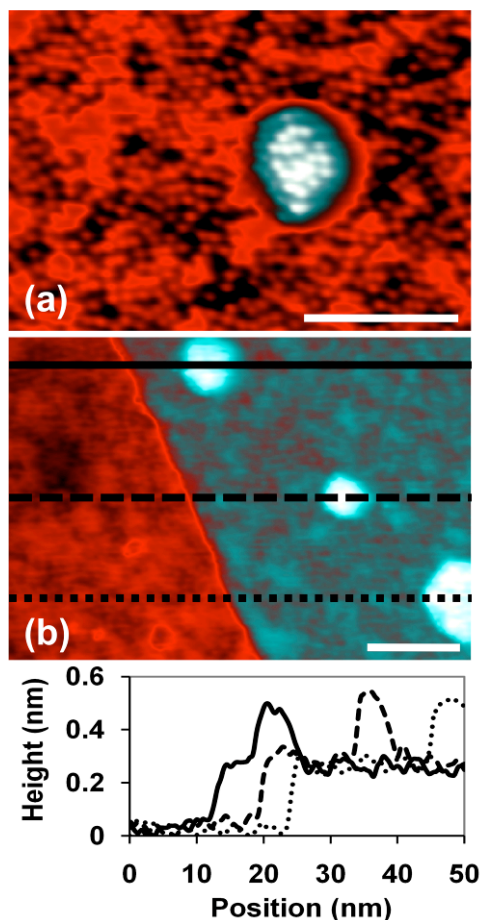


**Figure 6.1 Trimethylphosphine on Au with Island Formation:** STM images showing 0.62 ML TMP on Au(111); the system has been annealed to 220 K. Line scans, each traversing a single island and a monatomic step edge, indicate that the islands are one gold atom high. Scale bars = 10 nm. Image conditions: 78 K, (a) 500 pA, 500 mV and (b) 300 pA, 200 mV.

position of the Au island arrays with that of the Au herringbones. Figure 6.2 and Figure 6.3 show STM images of 1.0 ML TMP on a Au(111) surface, after annealing to 220 K. The surface topographies of bare Au and the 1.0 ML TMP systems are compared in Figure 6.2. The plots indicate that the Au surface topography (*i.e.*, the height of the soliton walls) is not affected by the TMP molecules, however, it is more difficult to resolve due to the corrugation of the adsorbed molecular layer. At full coverage TMP formed a nearly perfect overlayer, which exhibited hexagonal packing

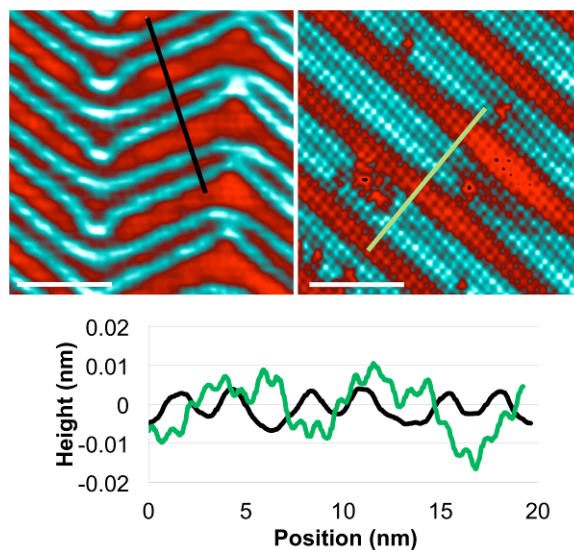


**Figure 6.2 Monolayer Coverage of Trimethylphosphine on Au:** Images of clean Au (top left) and 1.0 ML trimethylphosphine on Au annealed to 220 K (top right), and accompanying line scans (bottom). The plot shows line scans taken over the indicated portion indicated on both the unmodified (black) and modified (green) surfaces. Both plots show the corrugation of Au's herringbone reconstruction, in which the soliton walls are slightly higher than the rest of the surface. The plot from the modified surface also shows the corrugation due to the molecular layer which dominates the z scale making the topographic height modulation due to the soliton walls harder to see in the line scan. Scale bars = 10 nm. Image conditions: 78 K, (left) 2 nA, 50 mV and (right) 300 pA, 200 mV.

with a close-packed distance of  $0.76 \pm 0.06$  nm and a density of  $2.0 \pm 0.1$  molecules/nm<sup>2</sup>. The unit cell was calculated to be  $(\sqrt{7} \times \sqrt{7})R19^\circ$  using molecular row spacing and angle measurements taken from high resolution images such as those in Figure 6.3. The unit cell dimensions were confirmed with 2D Fourier transform analysis. Several small islands were present, covering  $2.4 \pm 0.7$  % of the surface, and were relatively monodisperse in size:  $5 \pm 2$  nm<sup>2</sup>. The herringbones were still visible, but with an increased unit cell dimension of  $11.2 \pm 0.9$  nm. Finally, there was no evidence for further disruption of the Au surface in the form of vacancies left by ejected atoms (etch pits) in this system. The dark areas in the images shown are vacancies in the adsorbed molecular layer rather than the underlying surface.

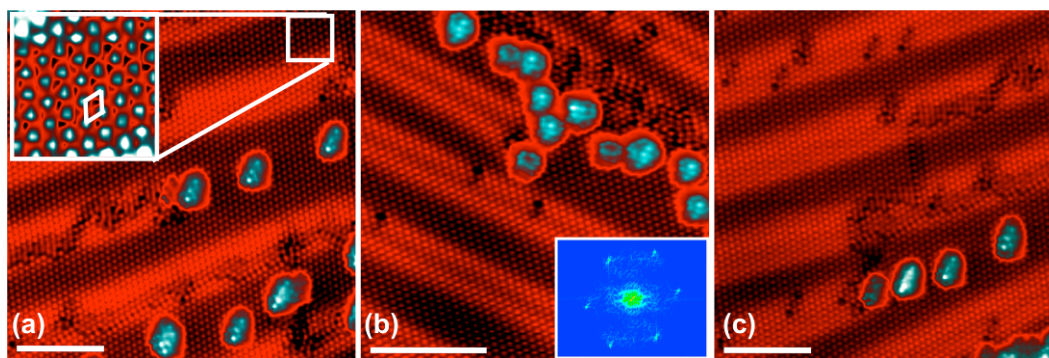


**Figure 6.3 Large Scale Images of Monolayer Coverage Trimethylphosphine on Au:** Several STM images showing 1.0 ML TMP on Au(111); the system has been annealed to 220 K. The molecules form a dense, hexagonally-packed layer with a  $(\sqrt{7} \times \sqrt{7})R \pm 19^\circ$  unit cell, as shown in the high-resolution inset in (a). 2D Fourier transform analysis – image inset in (b) – supports this unit cell assignment. These large-scale images reveal that the unit cell of the herringbone reconstruction is larger than on clean Au(111) and that Au islands appear at the positions once occupied by *hcp* domains. Scale bars = 10 nm. Imaging conditions: 78 K, 300 pA and 200 mV.

Images like those shown in Figure 6.3 revealed that at full monolayer coverage the herringbones were fewer in number than on clean Au and that the ejected atoms formed rows of islands parallel to the reconstruction itself. Close inspection of these images suggested that the lifting mechanism involved atoms being ejected from the *hcp* regions between soliton walls to leave rows of Au atoms in the form of small islands. The middle right side of Figure 6.3(a) shows a soliton wall loop that terminates with an ejected Au atom island. This loop marks an area where there is an edge dislocation in the underlying Au surface arising from a mismatch in the atomic rows between the *fcc*- and *hcp*-stacked regions.<sup>226</sup> The under-coordination of Au atoms at edge dislocations leads to a perturbed electron density which allows these areas to act as preferential binding sites for adatoms and other adsorbates.<sup>47,51,52</sup> Edge dislocations can also behave as ideal sites through which adatoms can enter and exit the surface layer.<sup>216</sup> As the herringbone was lifted upon TMP adsorption, it is likely that the atoms were ejected at edge dislocations sites like the one shown in Figure

6.3(a). Figure 6.3(b) and (c) show a similar arrangement in which edge dislocations have retreated, leaving behind rows of Au islands on top of *fcc*-packed Au. From an energetic standpoint, these atoms would have ideally migrated to a nearby step edge,<sup>62</sup> but they were trapped by the dense TMP layer, had a limited diffusion length, and coalesced into small islands ( $5 \pm 2$  nm<sup>2</sup>). The fact that the Au adatoms formed rows of small islands that closely followed the herringbone strongly suggests that they are kinetically-trapped by the surrounding TMP layer, similar to the NO<sub>2</sub>/Au(111) system examined by King and co-workers.<sup>6</sup>

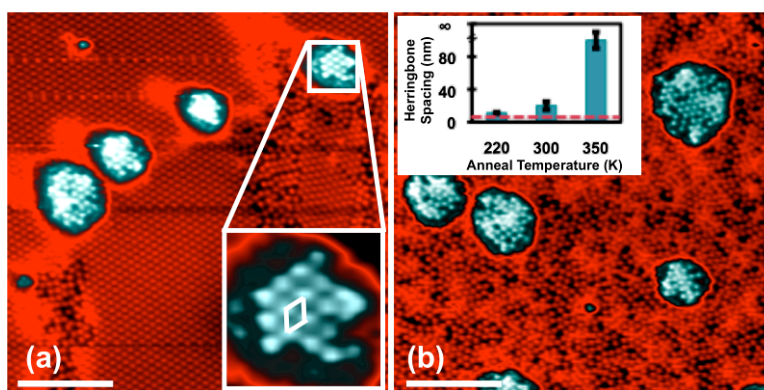


**Figure 6.4 Trimethylphosphine Assembly as a Function of Anneal Temperature:** STM images showing TMP on Au(111). The initial coverage system (Fig. 3) was annealed to (a) 300 K and (b) 350 K, resulting in 0.90 ML and 0.88 ML coverage, respectively. In the systems, the Au adatoms originating from the herringbone have a longer diffusion path and coalesce to form large islands. The plot inset in (b) shows the evolution of the herringbone spacing as a function of anneal temperature; the dashed line indicates Au's native herringbone spacing of 6.34 nm. Scale bars = 10 nm. Image conditions: 78 K, (a) 300 pA and 200 mV, and (b) 200 pA, and 200 mV.

The full coverage system shown in Figure 6.3 was exposed to a series of controlled annealing treatments, which allowed us to examine the effects of coverage and temperature on the evolution of the TMP-Au system. Figure 6.4 shows STM images of TMP on Au(111) annealed to (a) 300 K and (b) 350 K; these annealing treatments resulted in systems with similar molecular coverage, but with very different molecular packing structures. In the 300 K annealed system, some

molecules desorbed, which resulted in an increase in the number of vacancies in the molecular layer. The molecular density dropped slightly to  $1.8 \pm 0.2$  molecules/nm<sup>2</sup> and the herringbone spacing increased to  $20 \pm 5$  nm. The molecule's preference for the *fcc* region is evident in images like the one shown in Figure 6.4(a), where the density of molecules is much higher in the *fcc* than in the *hcp* region ( $2.0 \pm 0.1$  versus  $1.6 \pm 0.1$  molecules/nm<sup>2</sup>). Molecules in the densely packed *fcc* regions maintained the  $(\sqrt{7} \times \sqrt{7})R \pm 19^\circ$  unit cell. The Au islands were larger and with a wider size distribution ( $7 \pm 6$  nm<sup>2</sup>) unlike in the previous system, and covered  $2.1 \pm 0.9$  % of the surface. When the same system was further annealed to 350 K, more molecules desorbed and the herringbones were no longer visible, suggesting that the substrate surface had globally adopted a  $(1 \times 1)$  arrangement. The molecular density of this system was  $1.8 \pm 0.1$  molecules/nm<sup>2</sup>; however, regions of densely packed molecules were no longer observed. Au islands covered  $2 \pm 1$  % of the surface and their placement no longer followed the herringbone reconstruction and appeared to be random. Furthermore, the average island size increased dramatically to  $20 \pm 10$  nm<sup>2</sup>. These observations suggest that island formation and growth is a kinetically-limited process at high molecular density. The lower molecular density of the annealed systems allowed the ejected Au adatoms to migrate farther and coalesce to form larger islands as the Au surface globally adopted a  $(1 \times 1)$  *fcc*-configuration.

The herringbone spacing of the high coverage system evolved as a function of annealing temperature, as shown in Figure 6.4(c). The full coverage system, which resulted from dosing molecules at 78 K and then annealing to 220 K, exhibited a herringbone spacing of  $11 \pm 1$  nm, almost twice that of native Au (6.34 nm). Upon annealing this system to 300 K, the herringbone was lifted even further ( $20 \pm 4$  nm),

and the herringbones fully disappeared after the 350 K anneal. These data support the hypothesis that the restructuring of Au surface is a kinetically-limited process that requires vacant surface sites to induce Au atom ejection. These sites become available as a result of molecular desorption upon annealing the system. A similar lifting of the herringbone reconstruction has been reported for the comparatively large aromatic thiol species Azure A (3-amino-7-(dimethylamino)phenothiazine-5-ium chloride) adsorbed on Au(111).<sup>71</sup> Azure A adsorption resulted in a maximum increase of 22% in the herringbone spacing (up to 7.7 nm), indicating that it has a weaker interaction with Au than TMP.

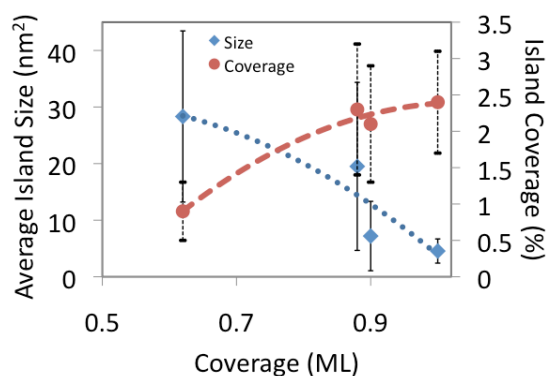


**Figure 6.5 Au Island Coverage and Size as a Function of Trimethylphosphine Coverage:** Plot showing percent Au island coverage (red circles) and average island size (blue diamonds) as a function of molecular coverage. As molecular coverage increases, the island coverage increases but the island size decreases. This data indicates that island growth is a kinetically-limited process dictated by molecular coverage.

Figure 6.5 illustrates the relationship between molecular coverage and Au island coverage (red circles), as well as average Au island size (blue diamonds). As the molecular coverage increased, the total island coverage increased, while the average island size decreased. These observations provide further evidence that the processes under investigation are kinetically-limited. At high molecular coverage, ejected Au

atoms were trapped among densely packed molecules and unable to form large islands. Island growth was hindered by the short diffusion lengths afforded by the dense molecular layer. This phenomenon can be clearly seen in the evolution of island growth resulting from annealing the full coverage (1.0 ML) system to 300 K and 350 K. Annealing the system caused molecules to desorb leading to lower coverage systems (0.90 ML and 0.88 ML, respectively). In these systems, Au adatoms diffused rapidly and coalesced into nearby islands, defects, and step edges. The process of molecular desorption led to vacancies in the molecular layer. This process opened surface sites allowing even more atoms to be ejected, and eventually fully lifted the herringbone (as shown in Figure 6.4(b)); the resulting islands were larger than in the high-coverage systems. The largest islands were observed for the 0.62 ML system, which is entirely expected in light the proposed mechanism.

There was no step restructuring, or “faceting”, observed in the systems examined, which is expected given the proposed mechanism of surface reorganization. At full monolayer coverage, Au adatom diffusion distances were limited due to high molecular density. As such, Au adatoms did not migrate to the step-edges and faceting did not occur. In all other systems studied, the molecular density was low enough the adatoms migrated to nearby step-edges. However, in each case the temperature was high enough that atoms along the steps could reorganize and did not appear faceted.

### *6.2.2 Error analysis*

The error margins associated with island measurements are relatively large and overlap in the case of measurements performed on the same initial coverage



annealed to three different temperatures. The complexity and inhomogeneities present in these systems make them somewhat difficult to characterize. The broad distributions in island sizes (shown in the histograms provided in Figure 6.6) and local island density are the main factors contributing to the difficulty in making precise measurements for percent island coverage. The added process of Au atom diffusion to nearby step edges and defects further complicates the system. Thus, the error bar reported does not reflect an error in the experimental measurement itself, rather the complex and inhomogeneous nature of the system as a whole.

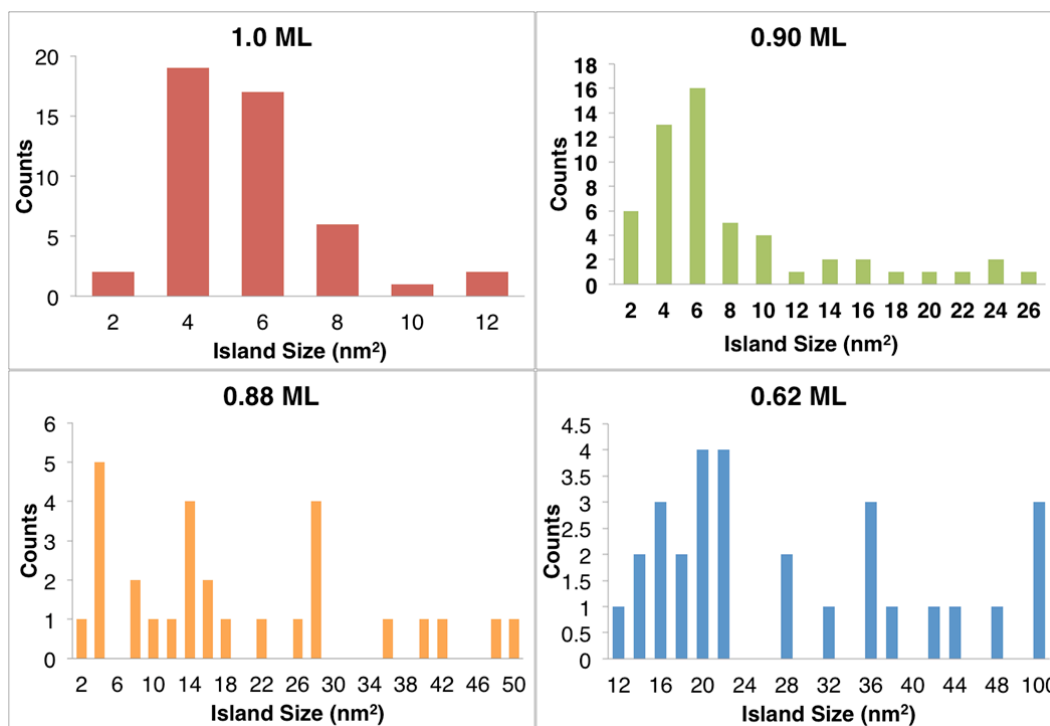


**Figure 6.6 Island Size Histograms:** Histograms of Au adatom islands sizes for each of the four trimethylphosphine-Au(111) system studied.

### 6.3 Conclusions

Previously, we postulated that Au islands in the TMP/Au(111) system originated solely from the excess atoms in the herringbone reconstruction, as evidenced by the lack of etch pit formation. Indeed, our measurements of the Au



islands revealed that island coverage never exceeded 4.5% across all molecular coverages examined. The interaction between TMP and the Au surface was strong enough that the molecules adsorbed and lifted the herringbone reconstruction, but was not so strong as to eject additional atoms and create etch pits. This observation is in direct contrast with that observed when thiol molecules self-assemble on Au, which requires excess atoms to be removed from the surface and participate in adatom mediated bonding of the molecules.<sup>41,57</sup>

To summarize, altering the headgroup element of a self-assembled monolayer can drastically affect Au surface restructuring upon adsorption. Upon TMP adsorption and subsequent annealing, the extra 4.5% Au atoms were forced out of the surface and the herringbone reconstruction disappeared as the surface atoms reorganized, ultimately adopting a  $(1 \times 1)$  configuration. Subtle changes in the surface binding strength of SAMs affected by either changing the anchoring group (as in this work) or by chemically altering the thiol head group through alkyl chain functionality (as with Azure A) may offer new routes to more defect-free monolayers.

## 6.4 Additional Experimental Details

Trimethylphosphine, 99% purity, was purchased from Sigma Aldrich and used without further purification. TMP was deposited on the sample by a collimated molecular doser while the tip was scanning and was always dosed with the metal sample at 78 K and subsequently annealed as noted. The TMP-Au systems could not be stably imaged as dosed at 78 K, and annealing the sample yielded more static systems. This observation indicates a mobile precursor state, such as that observed for benzene on Si,<sup>227</sup> and suggests that the system requires extra energy (*i.e.*, heat) in

order for the molecules to equilibrate to their preferred adsorbed state. Molecular coverage values were calculated from molecularly resolved STM images and one monolayer (ML) refers to the TMP coverage of a full close-packed ( $\sqrt{7} \times \sqrt{7}$ )R19° layer. Finally, island coverage measurements are reported for images in which both islands and herringbones are present, surveying  $> 17,000 \text{ nm}^2$  in each such system. For systems in which no herringbones remain, island coverage measurements were made using several images surveying  $> 47,000 \text{ nm}^2$  for each data point.

## 7 Effect of Head Group Chemistry on Surface-Mediated Molecular Self-Assembly

### 7.1 Introduction

In this chapter the interaction of a Au(111) surface with four chemical species – dimethyl sulfide, dibutyl sulfide, dibutyl selenide and trimethylphosphine – will be examined. Some of the information covered here has previously been presented in earlier chapters, but is repeated here for completeness. The chemical structures of these compounds are shown in Figure 7.1. The behavior of molecules on metal surfaces is often difficult to predict and can lead to unexpected self-assembled structures and surface restructuring. These molecules were carefully chosen in order to explore how changing the tail or head groups affect the dynamics of molecular adsorption, self-assembly and thermal stability in a systematic manner.

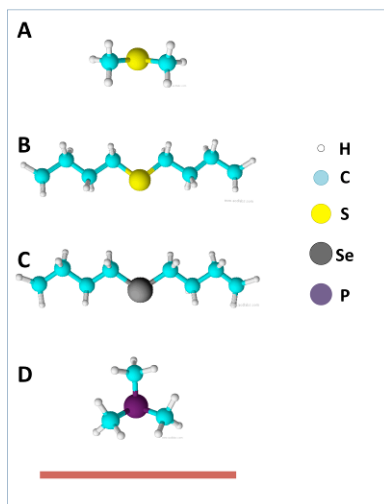


**Figure 7.1 Four Species for Comparison:** Scaled drawings of the four species under investigation: (A) dimethyl sulfide, (B) dibutyl sulfide, (C) dibutyl selenide and (D) trimethylphosphine. In the schematics the atoms are color coded as follows: white = hydrogen, blue = carbon, yellow = sulfur, grey = selenium and purple = phosphorous. Scale bar = 1 nm.

I have examined each system as a function of molecular coverage and annealing temperature, and have been able to uncover subtle differences in adsorption behavior. Within this subset of molecules I make the following direct comparisons: (1) dimethyl sulfide to dibutyl sulfide, (2) dibutyl sulfide to dibutyl selenide and (3) dimethyl sulfide to trimethylphosphine. In comparison (1), the length of the alkyl tails has a marked effect on the overlayer structure and system stability, with layers formed from the longer molecule exhibiting increased stability due to van der Waals interactions between the tails. In comparisons (2) and (3), the sulfides exhibited weaker interactions with the gold surface than either the selenide or phosphine, which can be related to the periodic trends described by the Hard and Soft Acids and Bases (HSAB) Principle.<sup>228,229</sup> This information should be useful, for example, in the field of nanoscale chemical patterning based on soft and hybrid nanolithographies, in which multiple species are patterned on a surface by virtue of their different assembly properties. Microdisplacement printing of multi-component SAMs, as described by Weiss and co-workers,<sup>80</sup> utilizes several different molecules with different interaction strengths. More labile molecules are preassembled on a surface and then displaced in regions defined by the stamp by a chemical species that assembles in a more dense fashion. This work offers new design options for such systems, as it addresses two key factors at play; molecule-substrate and molecule-molecule interactions.

## 7.2 Results and Discussion

### 7.2.1 Head Group Chemistry and Alkyl Tail Length Effect on Molecular Self-Assembly

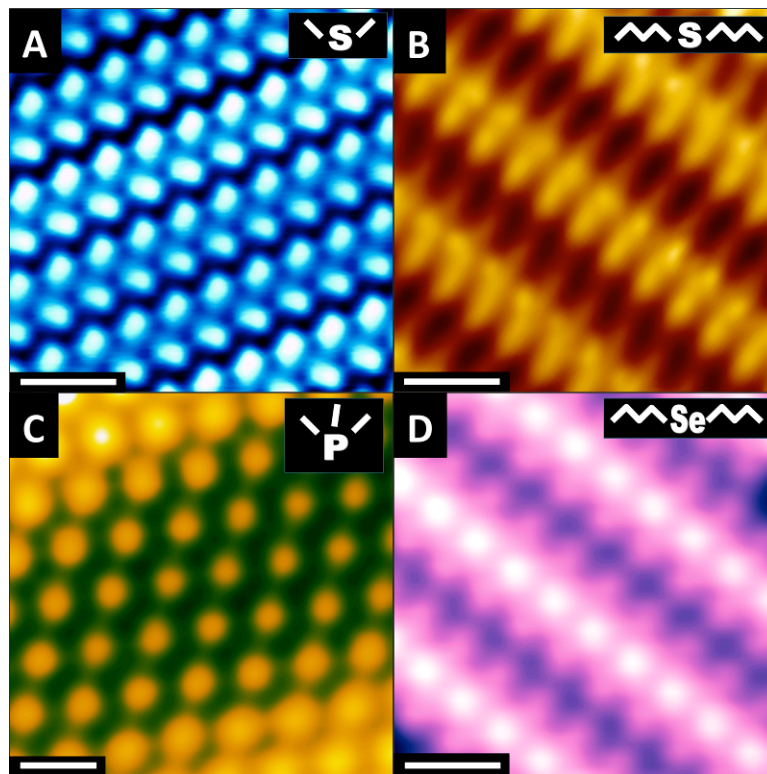


**Figure 7.2 Monolayer Assemblies for Four Species on Au:** STM images showing the full monolayer coverage molecular packing structures for (A) dimethyl sulfide, (B) dibutyl sulfide, (C) trimethylphosphine and (D) dibutyl selenide all on Au(111). Scale bars = 1 nm. Image conditions: (A) 5 K, 50 pA, 50 mV; (B) 78 K, 30 pA, -30 mV; (C) 78 K, 300 pA, 200 mV; and (D) 78 K, 25 pA, 100 mV.

The STM images in Figure 7.2 show the monolayer coverage packing structure on Au(111) for each species under investigation, including (A) dimethyl sulfide, (B) dibutyl sulfide, (C) trimethylphosphine and (D) dibutyl selenide. There are clear similarities and differences in the packing structures, which are dictated by the chemical composition of the molecules that comprise the adsorbed layers. The geometry of each ordered array will be discussed in detail below before drawing comparisons between each arrangement and explaining the head group effects.

Coverage for each compound was calculated from molecularly resolved STM images, and the 1 monolayer (ML) coverage of each species refers to the highest density ordered structure observed. The unit cells quoted describe the ML coverage arrangement for each compound relative to the atomic lattice of the underlying surface. All unit cell spacings and rotations are defined with respect to the close-packed  $[0\bar{1}1]$  atomic direction.

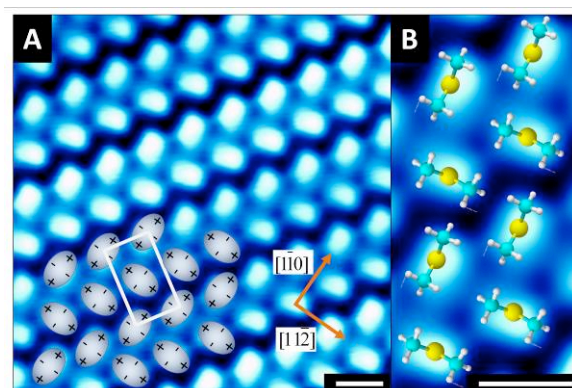


**Figure 7.3 Dimethyl Sulfide Assembly Structure on Au:** STM image showing the full monolayer molecular packing structure for dimethyl sulfide on Au(111). The molecules in the system exhibit a  $(\sqrt{3} \times 3)$  unit cell packing structure as indicated by the white rectangle. The red arrows in (A) show the underlying atomic lattice vectors. Each molecule behaves as a localized quadrupole as shown by the grey ovals in (A). The ovals in (A) and the scaled drawings of dimethyl sulfide in (B) demonstrate how the molecules alternate their orientations on the surface in order to maximize favorable electrostatic interactions between adjacent quadrupoles. Scale bars = 0.5 nm. Image conditions: 5 K, 50 pA, 50 mV.

The monolayer packing structure of dimethyl sulfide on Au(111) is explored in detail in Figure 7.3. The molecules appear in STM images as bright protrusions and exhibit a quasi-hexagonal arrangement with an average separation of  $0.48 \pm 0.04$  nm. The alternating shapes of the protrusions suggest that molecules in neighboring rows adopt opposing orientations. Figure 7.3(B) shows a zoomed-in image of the dimethyl sulfide layer with scaled molecular schematics. High-resolution images like the ones shown in Figure 7.3 allow us to assign a  $(\sqrt{3} \times 3)$  unit cell for dimethyl sulfide on Au(111). On Cu(111), dimethyl sulfide molecules adopt a unique “herringbone”

packing structure.<sup>32</sup> It is important to note that a herringbone packing structure refers to the end-to-middle type arrangement commonly adopted by quadrupolar molecules on surfaces and is not to be confused with the herringbone reconstruction of Au(111).<sup>230–235</sup> Dimethyl sulfide appears to exhibit a similar quadrupolar behavior on Au(111), as indicated in the molecular schematics and quadrupole overlayer in Figure 7.3. Neighboring dimethyl sulfide molecules self-assembled such that electrostatic interactions between the electronegative sulfur atoms and the electropositive methyl groups were maximized. The packing structure for dimethyl sulfide on gold differs from that on copper, however, in the molecular row spacing and arrangement. These differences likely arise due to variations in the electronic nature and lattice spacing between the two substrates. On Au(111), dimethyl sulfide molecules in alternating rows appear to move toward one another, presumably to maximize favorable electrostatic interactions. By alternating which molecular rows are compressed, the globally ideal molecular separation is maintained for the system. This type of rearrangement of molecular locations is somewhat analogous to a Peierls distortion in which a system's global energy is lowered by a doubling of the period.<sup>236,237</sup> Peierls distortion has been used to explain conformational geometries observed for species such as polyacetylene.<sup>238</sup>

Figure 7.4 shows the self-assembled overlayers of dibutyl sulfide and dibutyl selenide on Au(111). Both species exhibit similar monolayer coverage packing structures that are markedly different from that of dimethyl sulfide. In the dibutyl sulfide/Au(111) system, the molecules adsorb intact through one of the lone pairs on the central sulfur atom with the alkyl tails oriented nearly parallel to the surface.<sup>81,83,170,208</sup> In STM images, the sulfur atoms appear as a bright protrusion, while

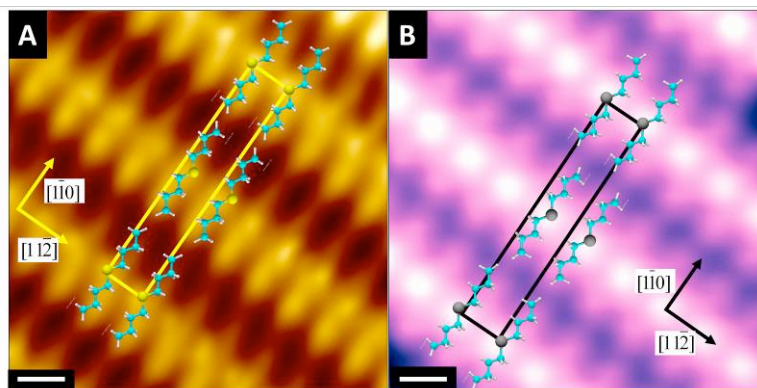


**Figure 7.4 Dibutyl Sulfide and Dibutyl Selenide Assembly Structures on Au:** STM images showing the molecular packing structures of (A) dibutyl sulfide and (B) dibutyl selenide on Au(111). Both molecules exhibit a  $(\sqrt{3} \times 10)$  unit cell packing structure as indicated by the yellow and black rectangles. Yellow and black arrows in (A) and (B), respectively, show the underlying atomic lattice vectors. Neighboring molecules align along the central sulfur (or selenium) atoms with their alkyl tails parallel to one another due to van der Waals interactions, as indicated with scaled drawings of molecules in both (A) and (B). Scale bars = 0.5 nm. Image conditions: (A) 78 K, 30 pA, -30 mV; and (B) 78 K, 25 pA, 100 mV.

the alkyl tails appear as less intense protrusions. At 0.3 ML coverage and above, the molecules form chains with alkyl tails parallel to one another due to van der Waals interactions. High-resolution images reveal that molecules in neighboring rows align with their tails in opposite directions, as shown with schematics in Figure 7.4(A), resulting in a  $(\sqrt{3} \times 10)$  unit cell. Dibutyl selenide also adsorbs intact on Au(111) and the selenium atom appears as a bright protrusion in STM images. The molecules pack in an arrangement similar to dibutyl sulfide, as shown with schematics in Figure 7.4(B), where molecules in adjacent rows assemble with their alkyl tails rotated  $180^\circ$  with respect to one another. Images such as the ones shown in Figure 7.4(B) allowed for precise molecular spacing measurements. The short axis spacing was  $0.48 \pm 0.06$  nm and the long axis spacing was  $1.39 \pm 0.08$  nm. In determining the overlayer structure, the long axis spacing is doubled to account for the alternating orientation of the alkyl tails within the monolayer, yielding a  $(\sqrt{3} \times 10)$  unit cell. Thus, in terms



of the geometrical packing of the molecules, the dibutyl sulfide and dibutyl selenide systems are indistinguishable from one another. I illustrate later in this chapter how the different head group chemistry of the two compounds influences substrate reconstruction and monolayer stability.

The comparison of dimethyl sulfide and dibutyl sulfide emphasizes the importance of the alkyl tails in determining the molecular packing structure. Dimethyl sulfide, with its short alkyl tails, adopts a “herringbone” arrangement, which maximizes quadrupole-quadrupole interactions. The longer alkyl chains of dibutyl sulfide and dibutyl selenide drive the molecules to arrange in a linear fashion so that van der Waals interactions are maximized.

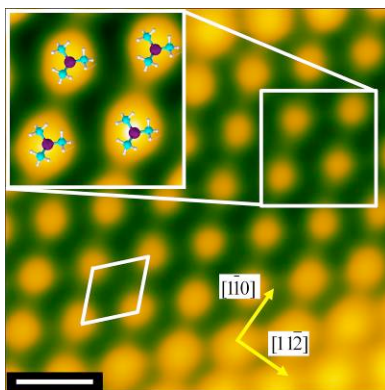


**Figure 7.5 Trimethylphosphine Assembly Structure on Au:** STM image showing the molecular packing structure for trimethylphosphine on Au(111). The monolayer exhibits a  $(\sqrt{7} \times \sqrt{7})R19^\circ$  unit cell as indicated by the white parallelogram. The blue arrows show the underlying atomic lattice vectors. The inset shows scaled drawings of trimethylphosphine superimposed onto the image. Scale bar = 1 nm. Image conditions: 78 K, 300 pA, 200 mV.

I also examined the adsorption of trimethylphosphine on Au(111). Previous macro-scale explorations of tertiary phosphines on Au(111) have determined that they adsorb intact through the lone pair on the phosphorus atoms with the alkyl substituents pointing away from the surface.<sup>214,219–222</sup> Here we show that trimethylphosphine molecules, indeed, adsorb intact and appear as a bright

protrusion in STM images. At low and medium coverage ( $<0.9$  ML), the molecules do not aggregate in ordered structures; however, at high coverage ( $>0.9$  ML) the molecules form a dense hexagonally-packed layer with an average spacing of  $0.76 \pm 0.06$  nm. The low coverage packing structure will be discussed in the next section. High-resolution images such as the one shown in Figure 7.5 allowed us to assign a  $(\sqrt{7} \times \sqrt{7})R19^\circ$  unit cell. The circular appearance of the molecules does not allow for the absolute assignment of sub-molecular orientation as for the other three compounds in this study, and the schematics in the inset of Figure 7.5 are provided to establish the geometric position of the molecules within the monolayer rather than their absolute orientation.

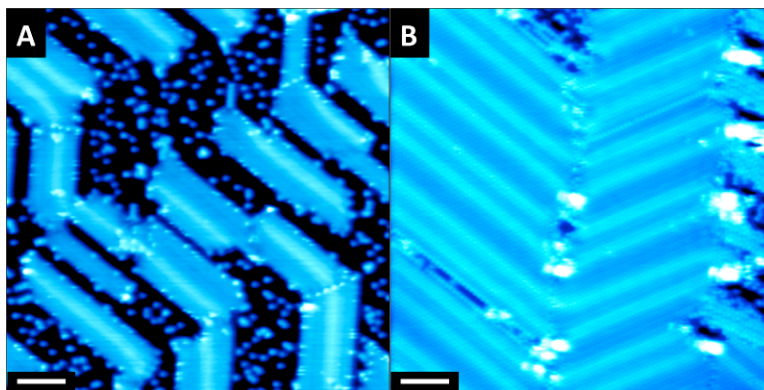
Trimethylphosphine, like ammonia, adopts an “umbrella” shape.<sup>142,239,240</sup> As such, the molecules pack very differently from dimethyl sulfide when adsorbed on Au(111). Furthermore, the bonding scheme for trimethylphosphine on gold is different from that of the other three compounds, with the latter complicated by the presence of an additional lone pair of electrons on the sulfur (selenium) atom that leads to the alkyl groups being tilted over onto the surface.<sup>82</sup>

### 7.2.2 *Effect of Molecular Identity on Au(111) $22 \times \sqrt{3}$ Surface Restructuring*

Figure 1.3 shows an STM image of clean Au(111) in which the native  $(22 \times \sqrt{3})$  “herringbone” reconstruction is clearly visible. In this chapter, the spacing of the herringbone reconstruction is used as a sensitive measure of the interaction strength between gold and the four aforementioned molecules. The herringbone separation was measured at various coverage and temperature treatments with the premise that a larger herringbone separation at similar conditions is indicative of a stronger

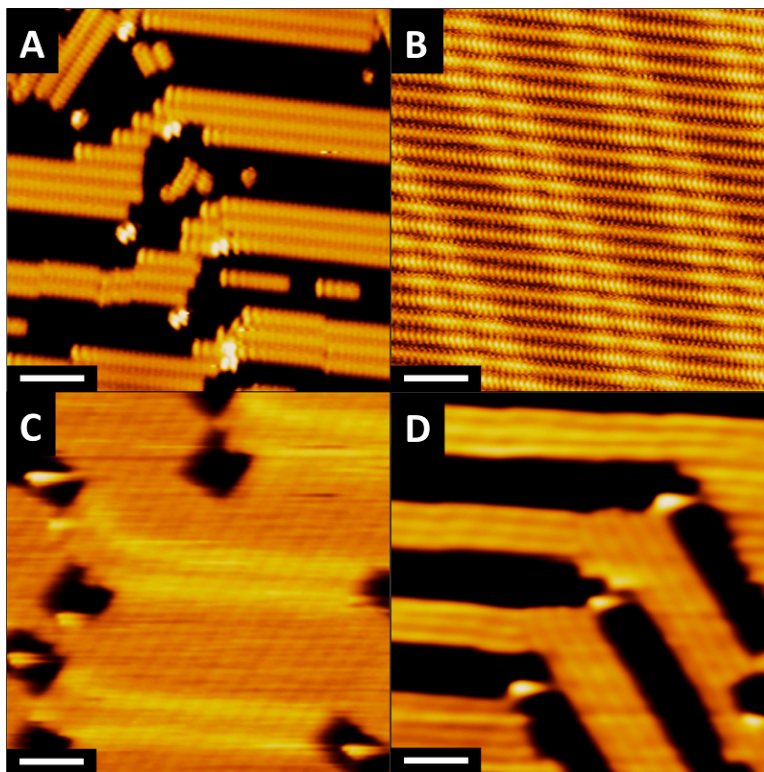
interaction of the molecule with the surface. As herringbone spacing can be easily and precisely measured from STM images, this approach provides an accurate measure of the interaction strength of adsorbates as a function of coverage and molecular chemistry. Enthalpy data for the adsorption of dibutyl sulfide on Au(111) has been previously determined using temperature programmed desorption to be  $\sim 90$  kJ/mol,<sup>5</sup> and the adsorption of dibutyl sulfide causes gold's native herringbone reconstruction to be *partially* lifted, even at temperatures as low as 120 K.<sup>208</sup> However, to the best of my knowledge there is no accurate adsorption enthalpy data available for monolayers of the other three molecules. Using STM images to measure herringbone separations provides a somewhat straightforward method to uncover subtle molecule-surface interaction differences between the four systems and relate that to both head group and alkyl tail functionality.

Figure 7.6 shows STM images of dimethyl sulfide at (A) 0.65 ML and (B) 0.90 ML coverage; these images were recorded at 5 K. Well ordered layers were not formed when dimethyl sulfide was deposited on the sample at 78 K because most of the molecules desorbed even at this low temperature. The data reveal that when deposited at 5 K and gently annealed, dimethyl sulfide forms well-ordered overlayers. The average herringbone spacing in the high coverage system is  $6.5 \pm 0.4$  nm, which is not significantly different to that of native gold, indicating either that the reconstruction is not lifted upon the adsorption of dimethyl sulfide or that the temperature was not high enough to allow restructuring to occur in the small and low temperature range over which the molecules remain on the surface.



**Figure 7.6 Dimethyl Sulfide as a Function of Coverage and Anneal Temperature:** STM images showing (A) 0.65 ML and (B) 0.90 ML dimethyl sulfide on Au(111). The systems were annealed to 50 K and 70 K, respectively. The herringbone reconstruction of the gold surface is clearly visible under the ordered molecular layer. The herringbone spacing is not affected by the adsorption of dimethyl sulfide. Scale bars = 5 nm. Image conditions: (A) 5 K, 200 pA, 200 mV and (B) 5 K, 50 pA, 50 mV.

Figure 7.7 shows STM images of the systems resulting from the sequential adsorption of (A) 0.60 ML and (B) 1.0 ML dibutyl sulfide on Au(111); both systems were annealed to 120 K to promote ordering. Figure 7.7(C) and (D) show the molecular layers that result from sequential anneals of the 1.0 ML system in Figure 7.7(B) to 300 K and >500 K, respectively. At low coverage, after a 120 K anneal, the molecules form well-ordered rows, which preferentially reside in the *fcc*-regions of the surface. In this system the average herringbone spacing is  $6.6 \pm 0.7$  nm, which is statistically no different to that of native gold (6.34 nm), suggesting that no reconstruction has taken place. At full coverage, after a 120 K anneal, the reconstruction is only partially lifted and exhibits an average herringbone spacing of  $7.6 \pm 0.5$  nm. The room temperature anneal promotes a significant reorganization of the surface structure, and the herringbone separation increases to  $11 \pm 1$  nm, almost twice that of native gold. A final annealing to >500 K leads to molecular desorption, and the resulting 0.65 ML overlayer contains molecules primarily in the *fcc*-regions of the herringbone reconstruction. In this system, the average herringbone separation is



**Figure 7.7 Dibutyl Sulfide as a Function of Coverage and Anneal Temperature:** STM images showing the evolution of the Au(111) herringbone reconstruction as a function of dibutyl sulfide coverage and annealing temperature. (A) 0.60 ML after anneal to 120 K. (B) 1.0 ML after anneal to 120 K. (C) 1.0 ML after anneal to 300 K. (D) 0.65 ML after annealing to >500 K. Scale bars = 5 nm. Image conditions: (A) 78 K, 30 pA, -80 mV; (B) 78 K, 30 pA, -30 mV; (C) 78 K, 5 pA, -200 mV; and (D) 78 K, 5 pA, -200 mV.

$9.8 \pm 0.6$  nm, foreshadowing the eventual return of the native reconstruction once all of the molecules are desorbed. These results indicate that the lifting of the herringbone reconstruction is an activated process, which requires thermal energy to occur.

Comparing the dimethyl sulfide and dibutyl sulfide systems at this larger scale emphasizes the differences between them in terms of their molecule-surface interaction. As previously mentioned dimethyl sulfide forms well ordered islands at  $T < 78$  K and desorbs at low temperature. Conversely, dibutyl sulfide requires warming to 120 K for the long-range order to emerge and does not fully desorb until >500 K.

The high temperature required for desorbing the dibutyl sulfide molecules suggests that the longer alkyl tails increase the stability of the system. This added stability likely arises due to increased van der Waals interactions between the tails in neighboring molecules and between the tails and the substrate itself.<sup>218</sup> We also suggest that because the butyl tails have stronger electron donating properties than the methyl tails, the central sulfur atom will form a stronger bond with the gold surface in the case of dibutyl sulfide.<sup>82</sup>

Figure 7.8 shows a similar set of experiments for dibutyl selenide on Au(111). The medium and high coverage molecular layers shown in Figure 7.8(A) and (B), respectively, were annealed to 160 K to promote ordering. The effect of temperature on the full coverage system from Figure 7.8(B) was studied by subsequently annealing the sample to (C) 300 K and (D) >500 K. Figure 7.8(A) shows 0.58 ML coverage dibutyl selenide annealed to 160 K. Here, the herringbones display an average separation of  $7.6 \pm 0.6$  nm, greater than that of native gold. Upon further deposition and an additional anneal to 160 K, the coverage increases to 1.0 ML, and the average herringbone separation increases to  $9.9 \pm 0.8$  nm. When the 1.0 ML coverage system is annealed to room temperature ( $\sim 300$  K), the molecular layer remains intact and well-ordered. However, the underlying surface is restructured even further and displays an average herringbone separation of  $16 \pm 3$  nm. When the system from Figure 7.8(C) is annealed to >500 K, the molecular coverage drops to 0.45 ML and the herringbones begin to return to their native spacing with an average separation of  $9 \pm 1$  nm. These results, again, point to the conclusion that the lifting of the herringbone reconstruction is an activated process that is aided by the addition of heat to the system.

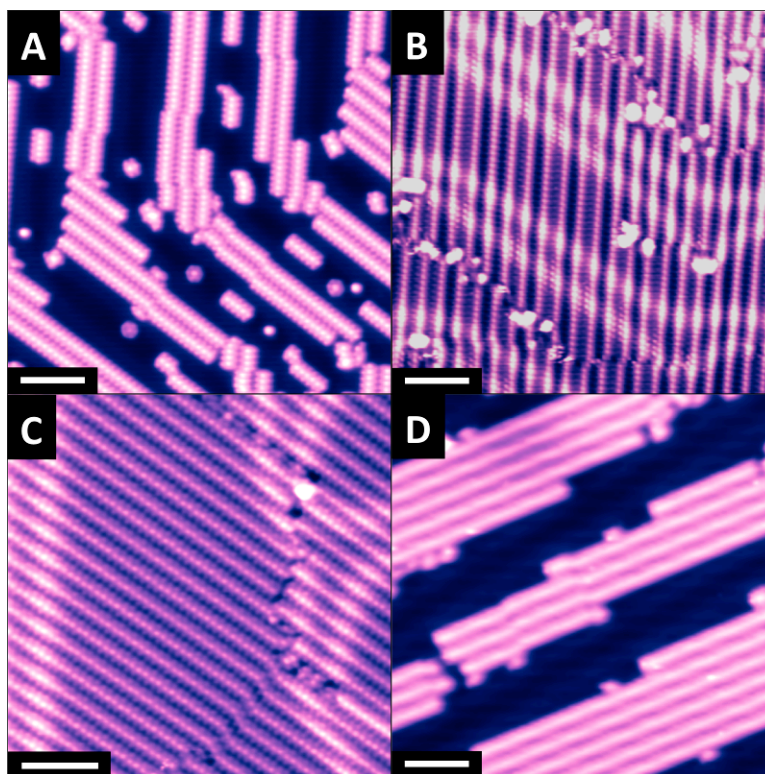


**Figure 7.8 Dibutyl Selenide as a Function of Coverage and Anneal Temperature:** STM images showing the evolution of the Au(111) herringbone reconstruction as a function of dibutyl selenide coverage and temperature treatment. (A) 0.60 ML after anneal to 160 K. (B) 1.0 ML after anneal to 160 K. (C) 1.0 ML after anneal to 300 K. (D) 0.45 ML after anneal to >500 K. Scale bars = 5 nm. Imaging conditions: (A) 78 K, 300 pA, -300 mV; (B) 78 K, 300 pA, 300 mV; (C) 78 K, 5 pA, -200 mV; and (D) 78 K, 300 pA, 300 mV.

The similarities between the dibutyl sulfide and dibutyl selenide systems are evident not only from their molecular packing structures, as previously discussed, but also in how they interact with the gold substrate. However, by measuring the herringbone separation as a function of molecular coverage and temperature treatment, it is clear that dibutyl selenide promotes a slightly greater degree of surface restructuring than its sulfur analogue. Furthermore, dibutyl sulfide requires heating to 120 K to form an ordered layer; while dibutyl selenide requires heating to 160 K. This higher temperature suggests a higher diffusion barrier for the selenide and hence a stronger adsorption strength on the gold surface. According to the HSAB



Principle, selenium-containing compounds are chemically softer than their sulfur containing counterparts.<sup>228</sup> The HSAB Principle predicts that the softer of the two species, dibutyl selenide, should exhibit a stronger chemical interaction with gold, which is itself a soft species.<sup>228</sup> Related studies comparing self-assembled monolayers of different but related thiols and selenols further support our finding that selenium species interact more strongly with gold than sulfur-containing analogs.<sup>241–249</sup>

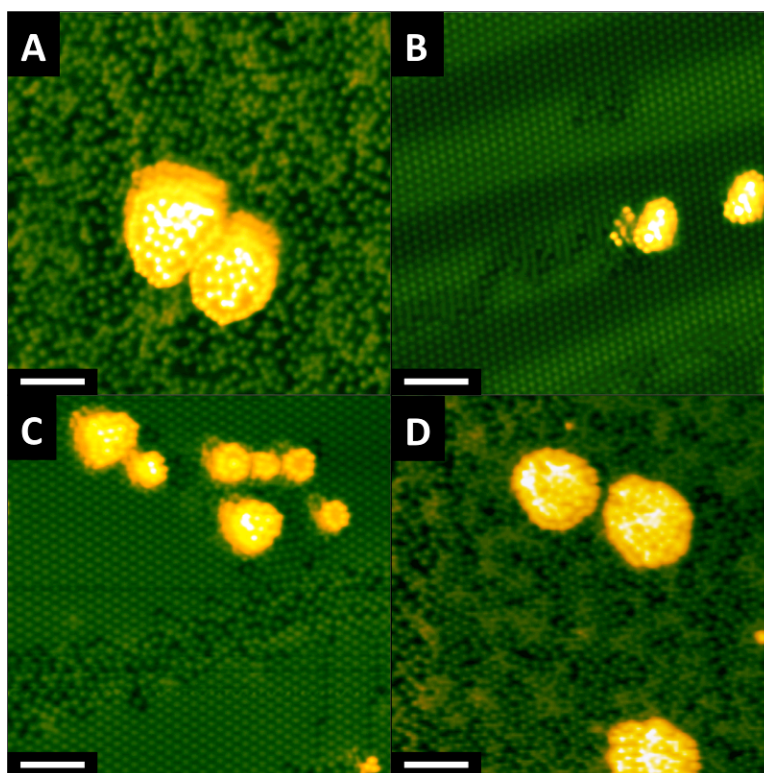


**Figure 7.9 Trimethylphosphine as a Function of Coverage and Anneal Temperature:** STM images showing the evolution of the Au(111) herringbone reconstruction as a function of trimethylphosphine coverage and temperature treatment. (A) 0.65 ML annealed to 220 K. The herringbone reconstruction is completely lifted and the ejected gold atoms form monolayer high islands on the surface. (B) 1.0 ML of trimethylphosphine annealed to 220 K. (C) 0.90 ML annealed to 300 K. (D) 0.85 ML annealed to 350 K. Scale bars = 5 nm. Image conditions: (A) 78 K, 500 pA, 200 mV; (B) 78 K, 300 pA, 200 mV; (C) 78 K, 300 pA, 200 mV; and (D) 78 K, 300 pA, 200 mV.

Figure 7.9(A) and (B) show the trimethylphosphine/Au(111) system at an initial molecular coverage of 0.62 ML and 1.0 ML, respectively. Both systems were



annealed to 220 K to promote ordering. The figure also illustrates how the system in (B) evolves when annealed to (C) 300 K and (D) 350 K, resulting in 0.90 ML and 0.88 ML coverage, respectively. There is some important information that can be gained, again, by simply comparing the temperature required to (1) achieve an ordered layer and (2) desorb the molecules in the trimethylphosphine system. The relatively high temperature (220 K) required for order to emerge suggests a higher diffusion barrier for trimethylphosphine than for the three other species examined in this chapter. The low desorption temperature (300-350 K) indicates that the molecular layer itself is not particularly stable. The lower stability is expected based on the aforementioned results where the short length of the alkyl tails does not offer the opportunity for van der Waals interactions between neighboring molecules on the surface.

A key observation of the trimethylphosphine systems suggests that there are very different molecule-molecule and molecule-surface interactions as compared to the sulfides and selenide. For example, the herringbone reconstruction is completely lifted for some of the conditions examined. Differences also arise in the molecular packing as a function of coverage. In the low coverage/low temperature system, trimethylphosphine does not tend to aggregate into localized islands separated by areas of bare metal as seen with their sulfur analogues. Trialkylphosphines are good electron donors,<sup>219,221,222,250</sup> and it is likely that some charge is transferred from the molecule to the surface upon adsorption. This leads to an induced dipole at the surface, which could lead to a short-range repulsion between adjacent molecules and account for the observed molecular arrangement at medium coverage.<sup>251-253</sup> This effect has been seen for molecules like tetrathiafulvalene and Sn-phthalocyanine and

is commonly attributed to dipole-dipole repulsion outweighing the nearest neighbor attraction seen for the thio- and selenoethers. When the coverage is very high (*i.e.*, > 0.90 ML), as is the case for the systems observed in Figure 7.9(B) and (C), the trimethylphosphine overlayer displays the dense packing structure previously described in Figure 7.5. Finally, when molecules are desorbed *via* higher temperature annealing treatments, the overlayer once again adopts the low density arrangement as seen in Figure 7.9(D) where molecules are separated from one another. This illustrates that the molecule-molecule separations observed in the lower coverage/temperature system is indeed an equilibrium effect. As the temperature of the ordered high coverage system is raised, molecular desorption occurs first from the *hcp* region of the herringbone reconstruction indicating preferred binding to *fcc* areas as observed for dibutyl sulfide and selenide. The strong region specificity is likely due to the regional variations in electron density or packing geometry of gold's herringbone reconstruction, and the order of stability (*fcc* > *hcp* > *sol*) suggests a preference for adsorption in areas of low electron binding energy.<sup>134,171,172,210</sup>

Another interesting characteristic of the trimethylphosphine/Au(111) scheme lies in the evolution of the herringbone separation. Figure 7.9 reveals that the herringbone is completely lifted in the medium coverage/low density systems, but is only partially lifted in the high coverage/high density arrangements. The 1.0 ML coverage system in Figure 7.9(B) was annealed to 220 K and has an average herringbone separation of  $11.2 \pm 0.9$  nm. When annealed to 300 K, a small percentage of the molecules desorbed, as shown in Figure 7.9(C), which displays an average herringbone separation of  $20 \pm 5$  nm – more than three times that of native gold. Further annealing to 350 K promotes more molecules to desorb and the

herringbones completely disappear. These results illustrate that the lifting of the herringbone reconstruction is a kinetically-limited process that requires vacant surface sites.<sup>214</sup> The interaction between trimethylphosphine and the gold substrate is strong enough to promote the complete lifting of the herringbone reconstruction. However, the high coverage systems do not offer the vacant sites for gold adatoms being pushed out of the surface. It is not until some molecules are desorbed *via* annealing treatments that gold adatoms can be ejected as the surface rearranges.<sup>214</sup> Further annealing to 470 K resulted in complete desorption of the molecules and return of the Au surface's native herringbone reconstruction.

The relative strengths of the molecule-surface interactions for dibutyl sulfide, dibutyl selenide and trimethylphosphine, as monitored by the degree to which the gold surface's herringbone reconstruction is lifted, are summarized in Figure 7.10. The subtle differences between the dibutyl sulfide and dibutyl selenide systems mentioned previously are readily apparent in the plot. The trialkylphosphine species clearly has the strongest interaction with the gold substrate, as indicated by the high degree of surface reorganization observed at each coverage and temperature examined. The HSAB Principle places trialkylphosphine species on the list of soft bases along with thioethers and selenoethers. Furthermore, the fact that trialkylphosphine shows the largest perturbation of gold's reconstruction is expected given the periodic trend whereby, for a given period, the group 15 species are softer than their group 16 counterparts. Hence, one would expect  $\text{PR}_3$  to interact more strongly with gold than  $\text{SR}_2$  or  $\text{SeR}_2$ . By the same logic, the larger size of Se relative to S would suggest that the Au–Se interaction should be stronger than the Au–S interaction, as evidenced by the data shown in Figure 7.10.

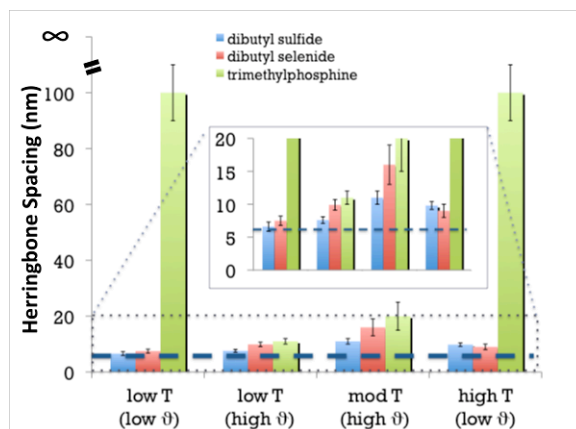


**Figure 7.10 Herringbone Separation as a Function of Species, Coverage and Anneal Temperature:** Plot comparing the molecule-surface binding strength (indicated by the Au(111) surface’s herringbone reconstruction separation) as a function of molecular coverage ( $\theta$ ) and temperature treatment (T) for dibutyl sulfide (blue), dibutyl selenide (red) and trimethylphosphine (green). The data presented reveals the relative order of the molecule/gold interaction strength: trimethylphosphine > dibutyl selenide > dibutyl sulfide.

A final important point to discuss is that a molecule’s adsorption enthalpy ( $\Delta H_{\text{ads}}$ ), which provides a clue to how strongly it will adsorb and perturb the surface structure, does not tell the whole story. For example, octanethiol<sup>5</sup> and trimethylphosphine<sup>219</sup> both have an adsorption enthalpy of  $\sim 130$  kJ/mol. However, thiol adsorption leads to the removal of substrate atoms and the creation of etch pits whereas the phosphine stops restructuring the gold surface once the herringbone reconstruction has been lifted and does not lead to the formation of etch pits. This phenomenon can be explained by considering how many molecules are adsorbed per unit area and hence how many strong bonds are made to the surface. In Table 7.1, I introduce a second descriptor  $\Delta H_{\text{ads}}^a$  that corrects for the size of a molecule’s “footprint” and is measured in J/m<sup>2</sup>. Despite the strong adsorption of C<sub>60</sub>, its lower  $\Delta H_{\text{ads}}^a$  can be used to explain why the gold surface herringbone reconstruction is lifted, but no etch pits are formed.

**Table 7.1 Herringbone Disruption as a Function of Adsorption Energy and Footprint**

Overview of adsorption enthalpy, adsorption energy “footprint” and the restructuring effect on the gold surface reconstruction of several relevant molecules. Energy per unit area ( $\Delta H_{\text{ads}}^a$ ) was calculated based on the unit cell for full monolayer coverage of each species. For data in which an energy range is reported, energy per unit area was calculated based on the lesser value.

Chemical Species	$\Delta H_{\text{ads}}$ (kJ/mol)	$\Delta H_{\text{ads}}^a$ (J/m <sup>2</sup> )	Herringbone Lifted?	Reference
<b>Thiols (RSH)</b>	130-170	1.0	Yes(etch pits formed)	5,40,41,59,78,79
<b>Trimethylphosphine</b>	130[a]	0.4	Yes	214,219 and this work.
<b>Fullerenes (C60)</b>	200-250	0.4	Yes	64,254,255
<b>Thioethers</b>	90	0.2	partially	5,208,218 and this work
<b>Benzene</b>	60	0.2	no	65,68

[a] The enthalpy of adsorption for trimethylphosphine was estimated based on trends observed in temperature programmed desorption experiments performed on dimethylphenylphosphine, diphenylmethylphosphine and triphenylphosphine.<sup>219,222</sup>

### 7.3 Conclusions

The work described in this chapter shows that it is possible to use gold surface’s native herringbone reconstruction as a sensitive readout of molecule-surface interaction strength to correlate head group chemistry with self-assembled monolayer properties. The hard/soft rules of inorganic chemistry effectively rationalize the measured molecular interaction strengths of self-assembled monolayers formed from molecules with different head groups and the soft gold surface (P > Se > S). Careful consideration of the “electronic” topography of the molecule in terms of whether dipolar, quadrupolar or van der Waals interactions between neighboring species dominate allows for an understanding of the molecular arrangements. We postulate that an *a priori* knowledge of the charge landscape within a molecule and an estimate of charge transfer to/from the surface from theory

would provide a good first estimate of an unknown molecule's self-assembly geometry. As this study directly compares one element with another in simple self-assembled surface systems, it may serve as a guide for the design of self-assembled monolayers with novel structures and properties.

#### 7.4 Additional Experimental Details

Dibutyl selenide was prepared by collaborators at the University of North Carolina at Charlotte as previously reported.<sup>256,257</sup> The product was further purified by ~10 cycles of freeze/pump/thaw. Dimethyl sulfide (anhydrous, >99.0%) and dibutyl sulfide (>96%) were purchased from Sigma Aldrich and were further purified by ~10 cycles of freeze/pump/thaw. Trimethylphosphine (>99%) purchased from Sigma Aldrich was used without further purification.

## 8 Molecular-Scale Surface Chemistry of a Common Metal Nanoparticle Capping Agent: Triphenylphosphine on Au(111)

### 8.1 Introduction

The unique catalytic properties of Au have been the focus of extensive investigations over the past two decades, yet the origin of its catalytic activity is still not fully understood.<sup>258–261</sup> It is well established that Au nanoparticles can be catalytically active for a range of reactions if the particle size falls below a certain size.<sup>259–263</sup> Interestingly, very small Au particles derived from Au<sub>55</sub> clusters supported on inert materials are effective catalysts for selective oxidation reactions.<sup>264–266</sup> Thus, appreciable effort has been directed towards synthesizing small Au nanoparticles with narrow size distributions by a variety of preparation methods.<sup>2,260,261,267,268</sup> Synthetic protocols often involve colloidal methods that result in well-defined particles of uniform size distribution. The nanoparticles are stabilized in solution by surfactants or ligand molecules, which ensure that they cannot coalesce.<sup>267,269</sup>

Phosphine-stabilized Au clusters, first described by Schmid *et al.* more than 30 years ago,<sup>270,271</sup> have been extensively studied for their unique structural, optical and electronic properties, and as model catalysts.<sup>267,272–277</sup> Au<sub>55</sub> clusters are particularly interesting due to their ideal cuboctahedral structure.<sup>271</sup> These materials are also often used as “seed” particles in the synthesis of larger functionalized nanoparticles.<sup>278,279</sup> In addition, triphenylphosphine (PPh<sub>3</sub>) is widely used in organic synthesis<sup>280,281</sup> and in organometallic compounds.<sup>282,283</sup> The relatively labile Au–PPh<sub>3</sub> bond can be used for exchange reactions with ligands that contain a thiol group that forms stable Au–S bonds, resulting in various Au<sub>55</sub> derivatives. Depending on the nature of the

exchanged ligand, the cluster can be tuned from hydrophilic to hydrophobic. It has been recently shown that such exchange reactions strongly depend on the thiol ligand used<sup>284</sup> and the size of the Au cluster, with the exchange rates being faster for larger clusters.<sup>285</sup>

Despite the number of studies on the electronic properties, stability, and catalytic behavior of PPh<sub>3</sub> stabilized Au clusters, our knowledge of the interaction of PPh<sub>3</sub> with flat Au surfaces, in the absence of solvents, is rather limited.<sup>219,222,223,286</sup> Steiner *et al.* were among the first to study surface-bound PPh<sub>3</sub>.<sup>223</sup> Using ellipsometry and infrared reflection-absorption spectroscopy (IRAS) they determined that PPh<sub>3</sub> adsorbed as a monolayer onto Au films when deposited from ethanolic solution. Westermarck *et al.* used IRAS to examine a series of tertiary phosphines deposited from solution onto Au films; the study included dimethylphenylphosphine (PMe<sub>2</sub>Ph), diphenylmethylphosphine (PMePh<sub>2</sub>) and PPh<sub>3</sub>.<sup>222</sup> Their work revealed that PPh<sub>3</sub> adsorbed intact through the lone-pair on the phosphorous atom with the phenyl groups oriented away from the surface. Critically, this bonding behavior is in direct contrast to thiol and dithiol adsorption on Au, which requires cleavage of the S-H or S-S bond, respectively.<sup>241</sup> The strength of chemisorption for these phosphines was found to decrease as the number of phenyl rings increased within the series. The effect was attributed to the increased number of phenyl groups, which decrease the electron-pair donor properties of the phosphorus due of the electron withdrawing effect of the phenyl moities.<sup>222</sup> In Chapter 6 trimethylphosphine (PMe<sub>3</sub>) was found to interact strongly enough with the Au(111) surface to cause the reorganization of Au's native surface structure.<sup>211,214</sup>



Our knowledge regarding the interaction of Au surfaces with  $\text{PPh}_3$  at the atomic scale is limited. Mautes *et al.* using scanning tunneling microscopy (STM) and scanning tunneling spectroscopy (STS) studied the adsorption of  $\text{PPh}_3$  deposition onto Au(111) by spin-coating from dichloromethane solution but did not observe any ordered structure within the monolayer.<sup>286</sup> More recently Xu *et al.* reported on the self-assembly of calix[4]arene dimelamine derivatives on Au(111).<sup>287</sup> These molecules consist of a central head formed from a calix[4]arene moiety, which is connected to two identical arms, starting at a melamine unit and terminating in a  $\text{PPh}_3$  group. The phenyl group can coordinately bind a Au(I) atom, which was found to have a stabilizing effect against fragmentation of this large organic molecule when adsorbed on a Au(111) surface.

In this chapter, the adsorption of  $\text{PPh}_3$  on Au(111) is investigated in UHV using STM. Au(111), through its surface reconstruction and the presence of both *hcp*- and *fcc*- stacking regions, provides an excellent test bed for examining the ordering, stability and mobility dependence of  $\text{PPh}_3$  as a function of surface structure. The  $\text{PPh}_3$ /Au(111) system appears to be significantly different to other commonly used self-assembly reagents like alkanethiols, thioethers and fullerenes. In clear contrast to earlier reports,<sup>286</sup>  $\text{PPh}_3$  self-assembles to form two highly ordered surface structures. More importantly the adsorption of  $\text{PPh}_3$  causes the partial lifting of Au's native reconstruction *via* the ejection of Au atoms, which become kinetically-trapped in the form of pure, monolayer-high Au(111) ( $1 \times 1$ ) islands, which remain stable up to high temperatures. Adsorbed  $\text{PPh}_3$  molecules effectively trap these newly formed Au structures in two dimensions, thus limiting their mobility.

## 8.2 Results and Discussion

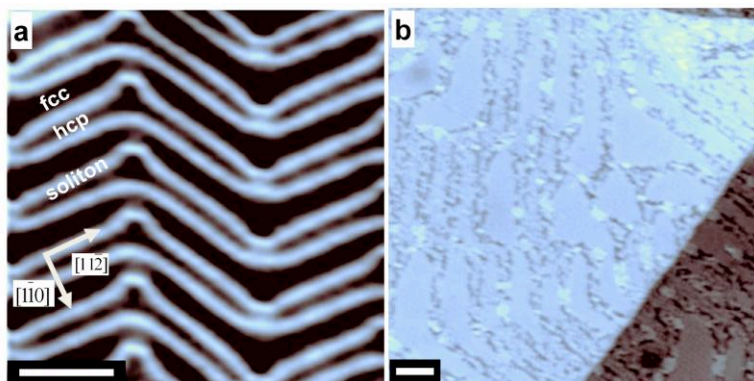


**Figure 8.1 Triphenylphosphine on Au:** STM images of (a) clean Au(111) and (b) high coverage PPh<sub>3</sub> on Au(111) after the system was annealed to 220 K. (a) The *fcc*-, *hcp*- and soliton-regions of the surface are indicated, as are the surface lattice vectors. (b) The large scale image shows that PPh<sub>3</sub> forms molecular domains confined by the soliton walls of the herringbone reconstruction. Scale bars = 10 nm.

The molecular density and packing arrangement of PPh<sub>3</sub> was found to be highly sensitive to the details of the surface reconstruction of the Au(111) sample (Figure 8.1a). Figure 8.1b shows an STM image after exposing clean Au(111) to a saturation coverage of PPh<sub>3</sub> at 78 K followed by annealing to 220 K. PPh<sub>3</sub> forms long range domains confined by the soliton walls of the herringbone reconstruction. High-resolution images (Figure 8.2a-c) indicate that the ordered structures reside primarily in the *fcc*-regions of the surface. The density of PPh<sub>3</sub> in *hcp*-regions is significantly lower, and the molecules do not form any ordered structures there. The smaller scale, molecularly-resolved images in Figure 8.2a-c reveal the packing arrangements of PPh<sub>3</sub> on the surface. The dominant structure, highlighted in yellow (Figure 8.2a and b) is a high density arrangement (1.15 molecules/nm<sup>2</sup>); the overlayer's vectors are separated by 60° and measured  $1.03 \pm 0.05$  nm and  $1.02 \pm 0.07$  nm experimentally, yielding a rhombic  $(2\sqrt{3} \times 2\sqrt{3})R30^\circ$  unit cell. In addition, a minority packing structure is observed, characterized by a rectangular  $(6 \times 4\sqrt{3})$  unit cell. This

structure, highlighted in red in Figure 8.2a and c, has perpendicular vectors experimentally measured as  $1.73 \pm 0.05$  nm and  $2.02 \pm 0.05$ . STM images suggest that this unit cell contains two molecules and is lower in density ( $0.58$  molecules/nm<sup>2</sup>) than the  $(2\sqrt{3} \times 2\sqrt{3})R30^\circ$  arrangement. Both packing arrangements are observed within the same local area of the surface; however globally the  $(2\sqrt{3} \times 2\sqrt{3})R30^\circ$  packing structure is favored  $\sim 3:1$ . The fact that we observe these structures co-existing on the surface after a number of different annealing treatments indicates that the two arrangements are similar in energy. When PMe<sub>3</sub> was adsorbed on the surface under identical conditions, a dense structure ( $2.0$  molecules/nm<sup>2</sup>) characterized by a  $(\sqrt{7} \times \sqrt{7})R19^\circ$  unit cell was observed.<sup>214</sup> The lower density of PPh<sub>3</sub> compared to PMe<sub>3</sub> can be understood in terms of the bulkiness of the two molecules, as the phenyl groups are expected to occupy more space than the methyl groups.<sup>288</sup>

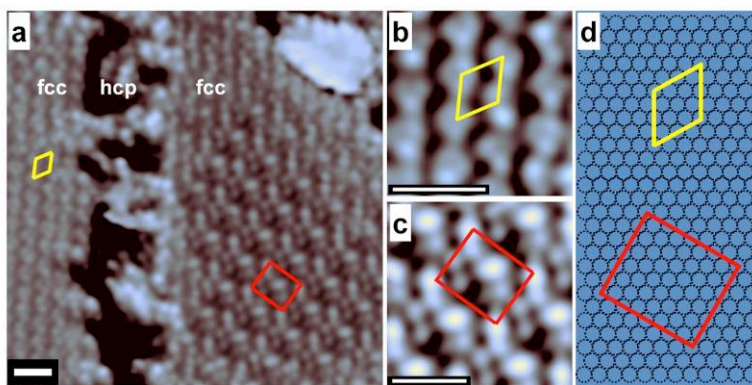


**Figure 8.2 Triphenylphosphine Assembly Structures on Au:** (a-c) Smaller scale, molecularly-resolved STM images of PPh<sub>3</sub> on Au(111) following a 220 K anneal show two distinct packing structures described by the unit cells  $(2\sqrt{3} \times 2\sqrt{3})R30^\circ$  (yellow) and  $(6 \times 4\sqrt{3})$  (red). The *fcc* and *hcp* areas of the Au surface are marked in (a). The schematic in (d) shows the two observed unit cell dimensions with respect to the underlying atomic lattice. Scale bars = 2 nm.

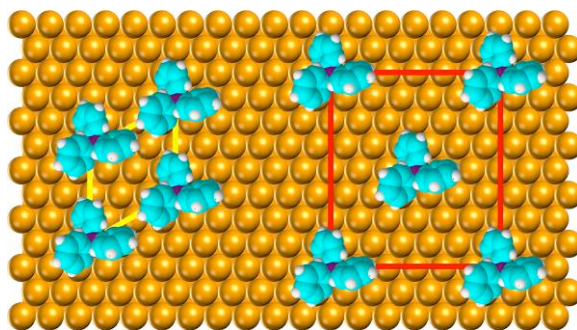


**Figure 8.3 Schematic of Triphenylphosphine Arrangements:** Schematic of the proposed molecular packing arrangement for PPh<sub>3</sub> on Au(111). The rhombic ( $2\sqrt{3} \times 2\sqrt{3}$ )R30° unit cell is shown in yellow (left), and the rectangular ( $6 \times 4\sqrt{3}$ ) unit cell is shown in red (right).

The proposed molecular arrangements for PPh<sub>3</sub> are depicted schematically in Figure 8.3. For the models shown I have assumed that PPh<sub>3</sub> maintains its umbrella configuration upon adsorption and assembly and that the phenyl groups maintain their pinwheel type arrangement.<sup>289</sup> However, I have not ruled out the possibility that one or more of the rings are reoriented upon adsorption in order to maximize the  $\pi$ -system overlap with the Au surface. This effect may be at play in the two types of unit cell. For example, in the common ( $2\sqrt{3} \times 2\sqrt{3}$ )R30° structure, high-resolution images (Figure 8.4a) reveal that each molecule appears as three lobes with equivalent apparent height, indicating that the molecules are upright. However, in the minority ( $6 \times 4\sqrt{3}$ ) arrangement each molecule appears as a single protrusion and a series of smaller lobes (Figure 8.4b), which suggests that the molecules are tilted on the surface, presenting predominantly one phenyl group. Finally, it is important to note that, although the schematics indicate atop adsorption for PPh<sub>3</sub>, I cannot assign an absolute adsorption site with the data available.

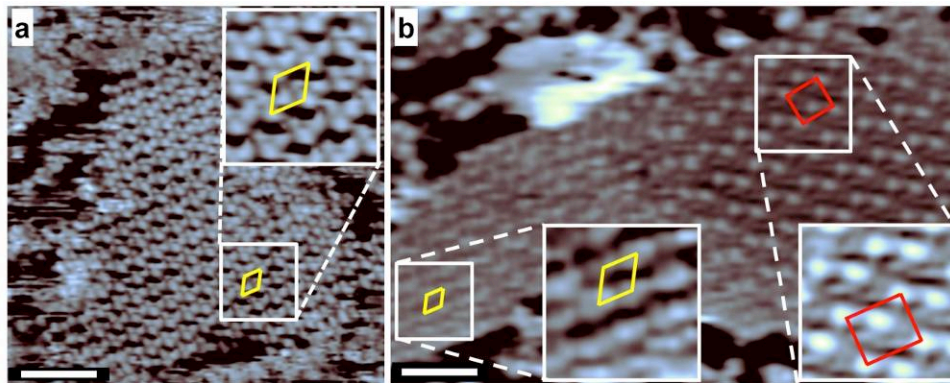


**Figure 8.4 Triphenylphosphine on Au Following Thermal Anneals:** STM images of PPh<sub>3</sub> on Au(111) after the system has been annealed to (a) 400 K and (b) 475 K. Molecularly resolved insets reveal that the packing motifs observed after the 220 K anneal are still present after the higher temperature anneals. Scale bars = 4 nm.

From Figure 8.1b it is evident that the periodicity of the soliton walls, and hence the arrangement of the *hcp*- and *fcc*-regions of the surface, is disrupted upon PPh<sub>3</sub> adsorption. After the 220 K anneal, the average separation of the herringbone was measured to be  $9 \pm 1$  nm; a 50% increase compared to the clean surface, indicating that the native reconstruction of Au was indeed perturbed. A number of well-resolved, topographically higher features are also observed in the STM images of PPh<sub>3</sub> on Au(111) (Figure 8.1b). These features are exclusively observed in *hcp* areas and, for reasons we will detail below, we assign them as Au clusters formed from the extra atoms ejected during the partial lifting of the herringbone reconstruction. Ejection of Au atoms results in a partial lifting of the herringbone reconstruction and

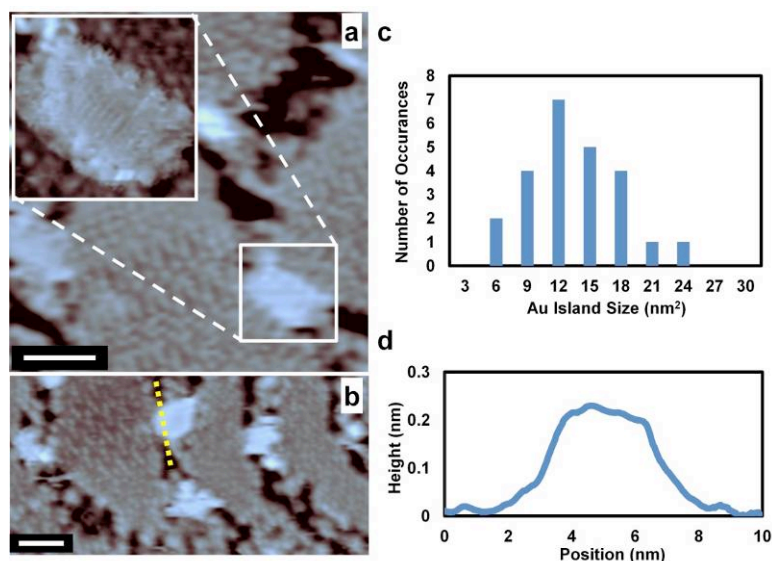


**Figure 8.5 Au Islands Trapped within Triphenylphosphine Monolayer:** (a) STM image of PPh<sub>3</sub> on Au(111), in which a clean Au (1 × 1) island is clearly observed, as shown in the atomically resolved inset. (b) Larger scale STM image in which many Au islands are visible. Scale bars = 2 nm, (c) Histogram showing the areas of several Au islands, which globally have an average area of 12 ± 4 nm<sup>2</sup>. (d) Topography along line scan (yellow dotted line) in panel (b) showing the Au island height to be ~0.23 nm.

the relative expansion of the *fcc* regions. These extra Au atoms are kinetically trapped in the form of two-dimensional islands by PPh<sub>3</sub> molecules. The shapes of the Au islands are irregular and defined by the shape of the *hcp*-regions where they form (Figure 8.5a). The histogram and the line scan depicted in Figure 8.5c and d, respectively, show that the average Au cluster area is  $12 \pm 4 \text{ nm}^2$  and that they are ~0.23 nm high, consistent with the expected monatomic step height of Au. The atomically resolved image in Figure 8.5a shows the top of an island where the (111) facet is clearly visible. The atomic spacing was measured to be  $0.30 \pm 0.04 \text{ nm}$ , which compares well to the bulk Au-Au spacing of 0.288 nm. This finding is important in terms of phosphine-stabilized Au clusters, as x-ray diffraction studies indicate that when a cluster exceeds a certain size ( $>\text{Au}_{39}$ ) its core transitions from cuboctahedral to a bulk-like, close-packed structure.<sup>290</sup> Thus, in terms of structure, the extended



Au(111) surface, which exposes both *fcc* and *hcp* terminations, is highly relevant to phosphine-stabilized nanoparticles. Furthermore our results indicate that the Au islands are compositionally homogeneous – *i.e.*, their surface and interior are comprised exclusively of Au atoms. However, only the perimeter of the islands are capped by phosphine molecules.

The observed PPh<sub>3</sub> self-assembled monolayer (SAM) appears to be thermally stable up to 475 K. Figure 8.4a and b show STM images after annealing the sample to 400 K and 475 K, respectively. The proposed  $(2\sqrt{3} \times 2\sqrt{3})R30^\circ$  and  $(6 \times 4\sqrt{3})$  unit cells are still clearly resolved following the 475 K anneal. The herringbone spacing after a 400 K anneal is found to be  $9 \pm 1$  nm and, after the 475 K anneal, is further increased to  $14 \pm 3$  nm. The herringbone spacing can be correlated to the number Au atoms ejected from the surface reconstruction according to the following equation:

$$N = N_o \left(1 - \frac{d_o}{d}\right)$$

where  $d_o$  and  $d$  are the native and observed herringbone separation, respectively,  $N_o$  is the maximum % island coverage possible if all excess Au atoms are ejected from the native reconstruction (*i.e.*, 4.5%) and  $N$  is the observed % island coverage.<sup>73</sup> The global island coverage in the PPh<sub>3</sub>/Au system was measured at  $2.5 \pm 0.7\%$  from images such as those shown in Figure 8.1, Figure 8.4 and Figure 8.5; according to the above equation, this island coverage should yield an average herringbone separation in the range of 10 to 22 nm, which is in good agreement with our observed herringbone separations. Increasing the annealing temperature above 500 K yields a

system in which molecules cannot be easily resolved, suggesting either molecular disorder or decomposition of the adsorbed species.

The adsorption and thermal stability of  $\text{PPh}_3$  on Au(111) appears to be drastically different when compared to other Au-based systems. It is generally observed that, depending on the adsorption enthalpy of the interacting species, a complete or partial lifting of the native surface structure may occur *via* various pathways. Alkanethiols, for instance, have been extensively studied on flat Au surfaces<sup>2,3,5,291</sup> and metal nanoparticles<sup>242,292–294</sup> due to potential applications in sensing, nanolithography and catalysis.<sup>2</sup> These molecules interact strongly with the Au surface, often leading to complete lifting of the herringbone reconstruction.<sup>56,59,78,79,295</sup> Although the precise mechanism is still widely debated, Maksymovych *et al.* have suggested that the binding of alkanethiolate species to Au is an adatom-mediated process in which single Au atoms are removed from the surface layer, and each is bound to two thiolate species.<sup>41</sup> Similarly, it has been reported that when octanethiol self-assembles on Au(111), Au atoms are incorporated into alkanethiol monolayers with a 1:2 Au adatom/alkanethiol ratio.<sup>78</sup> Thioethers (RSR') have also been studied extensively due to their potential applications in nanotechnology and surface patterning.<sup>5,35,36,208,218</sup> The weak interaction of thioethers as compared to thiols leads to only a partial lifting of the herringbone reconstruction. The rearrangement of Au's surface structure upon thioether adsorption is a thermally activated process that is completely reversible upon molecular desorption.<sup>208,218</sup> Notable extension of the herringbone reconstruction has also been observed when naphtho[2,3a]-pyrene (NP) was adsorbed on Au(111) followed by a room temperature anneal.<sup>73</sup> Critically, the formation of the molecular overlayers for thioethers and NP favored adsorption in



the *fcc*-regions of the surface, similar to what is seen for PPh<sub>3</sub>. In the case of the thioether and NP systems, ejected Au atoms were free to diffuse in the bare *hcp* channels on the surface and ultimately coalesce with nearby step edges. This theory is supported by the observation of scalloping at the step edges, which is indicative of rapid step growth. The fact that the Au islands remain in the PPh<sub>3</sub>/Au system despite the presence of nearly bare *hcp* channels suggests that these molecules have a stabilizing effect on the Au islands.

The formation of etch pits or vacancies, as commonly observed on other Au(111) SAM systems including alkanethiols,<sup>60,63,78</sup> cysteine,<sup>205</sup> and fullerenes,<sup>64,254</sup> are not observed in the PPh<sub>3</sub>/Au SAMs. The difference between PPh<sub>3</sub> and alkanethiols can be rationalized by the relatively weaker binding of the former with the Au surface. However, the adsorption enthalpy, which reflects the adsorption strength, and thus to what extent the molecule will perturb the surface structure, is not the only factor at play in determining overall system characteristics. Octanethiol and PMe<sub>3</sub> have similar adsorption enthalpies on Au (~130 kJ/mol), and both completely lift the herringbone reconstruction; however, only the thiol SAM formation is accompanied by etch pit formation. This can be explained by also taking into account the molecular densities of the two species (*i.e.*, how many molecules are adsorbed per unit area), and hence how many strong bonds are made to the surface. As discussed in Chapter 7, if an adsorbed molecule's "footprint" is accounted for in this manner, thiols have an adsorption energy ( $\Delta H_{\text{ads}}^{\text{a}}$ ) of 1.0 J/m<sup>2</sup> versus PMe<sub>3</sub> at 0.4 J/m<sup>2</sup>. Thus, it is clear that despite the strong adsorption of PMe<sub>3</sub>, its lower  $\Delta H_{\text{ads}}^{\text{a}}$  can explain why the Au surface herringbone is lifted, but no etch pits are created. The

lack of vacancy formation in the PPh<sub>3</sub>/Au system indicates that the energy per unit area of the PPh<sub>3</sub> monolayer is well below that of the other systems in which etch pits are observed. Assuming that PPh<sub>3</sub> has a similar binding energy to Au as PMe<sub>3</sub> (~130 kJ/mol), we can estimate  $\Delta H_{\text{ads}}^{\text{a}} \approx 0.2 \text{ J/m}^2$ . It is interesting to compare the degree to which PMe<sub>3</sub> and PPh<sub>3</sub> restructure the Au surface; the former ( $\Delta H_{\text{ads}}^{\text{a}} = 0.4 \text{ J/m}^2$ ) yields a maximum herringbone separation of >100 nm in contrast to the maximum of 14 nm seen for PPh<sub>3</sub> on Au ( $\Delta H_{\text{ads}}^{\text{a}} = 0.2 \text{ J/m}^2$ ). These calculations further support the assertion that PPh<sub>3</sub> has a relatively weak interaction with the Au(111) surface.

The stronger surface bonding of thiols as compared to phosphines is also utilized in the liquid phase chemistry of ligand stabilized Au clusters. The weakly coordinated monodentate PPh<sub>3</sub> ligand can be easily exchanged by sulfonated derivatives or other ligands with thiol groups that form stable Au-S bonds.<sup>284</sup> Interestingly, the exchange process depends on the size and the structure of the Au cluster, with the exchange rates being faster for larger clusters.<sup>285</sup> The structure of phosphine-capped Au clusters has been the focus of many theoretical and experimental investigations over the past three decades. A major drawback in experimental investigations is that phosphine-capped Au clusters are difficult to crystallize, and therefore a single-crystal X-ray analysis is not possible.<sup>271</sup> It has been shown that the structure of small Au clusters deviates significantly from the *fcc* structure observed for bulk Au and Au nanocrystals. Full-shell phosphine-stabilized Au clusters (*e.g.* Au<sub>13</sub>) can be described by icosahedral or cuboctahedral arrangements of the Au atoms.<sup>271,276,296</sup> Larger structures like the phosphine-stabilized Au<sub>55</sub> cluster,

can be described by a closed packed arrangement of the Au atoms.<sup>290</sup> In the present study the stacking fault domain structure of the Au(111) surface<sup>43</sup> allowed us to follow the adsorption of PPh<sub>3</sub> on both *fcc* and *hcp* Au regions. The bulk-like *fcc* regions favor the self-assembly of PPh<sub>3</sub> molecules, while formation of metastable Au structures occurs exclusively in *hcp* areas. In other words, the data suggest that bulk-like *fcc* Au would be less effective for ligand exchange reactions, as PPh<sub>3</sub> is relatively stable on these sites due to the formation of thermodynamically stable SAMs. The metastable Au structures nucleating in the *hcp* domains of the surface are effectively stabilized by adsorbed PPh<sub>3</sub> molecules. The STM images in Figure 8.4 indicate that the Au islands remain intact despite (i) the high anneal temperature and (ii) the presence of bare channels on the surface, which could act as diffusion pathways for ejected Au atoms to join step edges. The observation that Au islands exist even at high temperatures is attributed to capping of the perimeter of the islands by the PPh<sub>3</sub> molecules, as the top facets always appear free of molecules.

### 8.3 Conclusions

The behavior of PPh<sub>3</sub> on Au(111) after a variety of annealing treatments was examined using STM. The UHV experimental approach offers a relatively straightforward, accurate and highly reproducible sample preparation method, leading to a better understanding of the monolayer structure of PPh<sub>3</sub>, unknown up to now. The results reveal the complex self-assembly behavior of PPh<sub>3</sub>, a common ligand in organic, organometallic, and metal nanoparticle synthesis on Au(111). In contrast to other popular capping agents like thiols, the surface chemistry of this important species has to date gone almost completely unexamined.<sup>219,222,223,286</sup> The PPh<sub>3</sub> adsorption perturbs the Au(111) surface's native herringbone reconstruction

but stops short of etch pit formation commonly seen with thiol SAMs on Au. The packing was highly ordered and high-resolution STM imaging shows sub-molecular resolution indicating that, in the most common packing arrangement, the molecules are upright and all three phenyl groups are imaged with the same intensity. This result supports the current view that binding to the surface occurs *via* the P atom lone pair leading to very symmetric adsorption geometry. The dense packing of the molecular layer is evidenced by the trapping of Au atoms resulting from molecule-induced lifting of the Au surface's reconstruction. These ejected Au atoms coalesce into small islands that are stabilized by PPh<sub>3</sub> and are present even after annealing to well above room temperature. These results indicate the effect of PPh<sub>3</sub>'s intermediate binding strength in restructuring the Au substrate and reveal that the packing structure is in fact highly ordered, thermally stable and rather dense. This study should serve as a useful guide for the use of PPh<sub>3</sub> in Au nanoparticle synthesis.

#### 8.4 Additional Experimental Details

PPh<sub>3</sub> (99%) was purchased from Sigma Aldrich. The crystalline solid was transferred to a sealed vacuum tube which was heated to ~480 K, and the PPh<sub>3</sub> was deposited onto the cold sample *via* a heated gas line and precision leak valve. Data were recorded at 78 K with a sample bias range of -1.0 to +1.0 V and tunneling current range of 10 to 50 pA.

## 9 Magic Electret Clusters of 4-Fluorostyrene on Metal Surfaces

### 9.1 Introduction

The self-assembly of organic molecules on flat metal surfaces represents the 2D analog to the well-known solution-based supramolecular chemistry.<sup>2,3,80,198,297–299</sup> Substrates may set limits to the mobility of molecular adsorbates,<sup>300</sup> and interactions across the organic/inorganic interface may perturb the electronic structure of the molecules and the substrate considerably.<sup>301</sup> As a result, surface-supported organics can exhibit unique structural features and other properties that may not exist naturally in the respective crystalline phase, such as chirality and spontaneous electric polarization. A consequence of practical importance is that device-relevant properties of surfaces and interfaces, such as interface dipoles and transport barriers for charge and spin, can conveniently be engineered by exploiting interactions at organic/inorganic interfaces.<sup>302–305</sup> In this chapter I show how crystalline surfaces expand the paradigm of magic clusters. Magic clusters are particularly stable configurations of atoms or molecules, which are easily identified in a mass spectrum at a given cluster temperature because of their substantially increased abundance compared to other configurations. The underlying physics of magic clusters is related to geometric/electronic shell filling,<sup>306–308</sup> as well as details of entropic contributions to the Gibbs free energy.<sup>309</sup>

Although the magic cluster concept was initially established for free inorganic clusters in the gas phase, magic clusters have been recently reported for surface-supported organic clusters. Examples are the magic hexamers of  $\pi$ -conjugated hydrocarbons,<sup>310</sup> methanol hexamers,<sup>311</sup> and 1-nitronaphthalene decamers.<sup>7</sup> Unlike in

free clusters, interaction of clusters of atoms and molecules with a supporting substrate often results in electronic level rearrangement, hybridization and charge transfer at the interface.<sup>302</sup> Hence, any discussion of magic surface-supported clusters must include mechanisms besides structural and electronic shell filling alone. It has been proposed by Li *et al.* that the epitaxial relationship of the molecular cluster to the metal surface can be key to magic numbers for surface-supported molecular clusters.<sup>310</sup> In this chapter, the assembly of the styrene analog 4-fluorostyrene (4-FS) on two metal surfaces, Cu(111) and Au(111), is presented where epitaxial fit does indeed play a role in the cluster stability. However, using both experiment and theory we suggest that the dominant effect comes from the charge transfer across the interface, which is different for Cu and Au and yields different magic cluster configurations. A spontaneous parallel alignment of the intrinsic dipole moments of the 4-FS molecules in the clusters along the surface normal is observed. An electret is defined as a dielectric material with a permanent or semipermanent polarized electric field, similar to the magnetic field of a permanent magnet; thus 4-FS forms electrets of strong electric polarization with defined sizes that depend on the nature of the underlying surface.

## 9.2 Results and Discussion

Figure 9.1 shows scanning tunneling microscopy (STM) images of 4-FS on Cu(111) and Au(111) at 5 K following a 0.2 Langmuir (L,  $1 \times 10^{-6}$  torr s) dose and a thermal anneal to equilibrate the assemblies. From these images it is clear that 4-FS forms clusters on both surfaces; however, the dominant cluster size varies between substrates, as shown in the accompanying histograms (Figure 9.1C and D). On Cu, trimers are preferred 4:1 over all other cluster sizes observed (80% abundance);

however, cluster size is more variable on Au, with tetramers favored 1.3:1 over all other cluster sizes (58% abundance). It is obvious from the size distribution that the observed predominance of 4-FS trimers on Cu(111) and tetramers on Au(111) is distinctively different from cluster size distributions observed in typical growth experiments.<sup>312</sup> Doubling the molecular coverage did not alter the average cluster size, and only changed the number of trimers/tetramers, in other words trimers/tetramers remained the most abundant species. Hence, the present clusters are considered to have an energetically favorable configuration that makes them magic and most abundant. Most interestingly, this magic size is critically dependent on the nature of the underlying substrate.

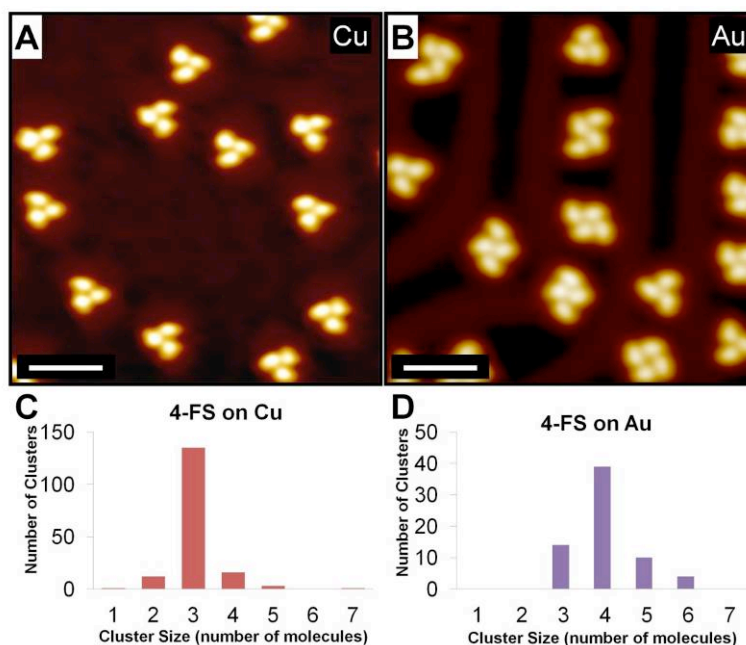


**Figure 9.1 4-Fluorostyrene Clusters on Cu and Au:** STM images of 4-FS on Cu(111) (A) and Au(111) (B) surfaces. Histograms in (C) and (D) show the distribution of cluster sizes on Cu and Au, respectively. Scale bars = 30 Å.

High-resolution imaging with STM (Figure 9.2) reveals how the 4-FS clusters are arranged with respect to the underlying metal lattice. The trimers follow two

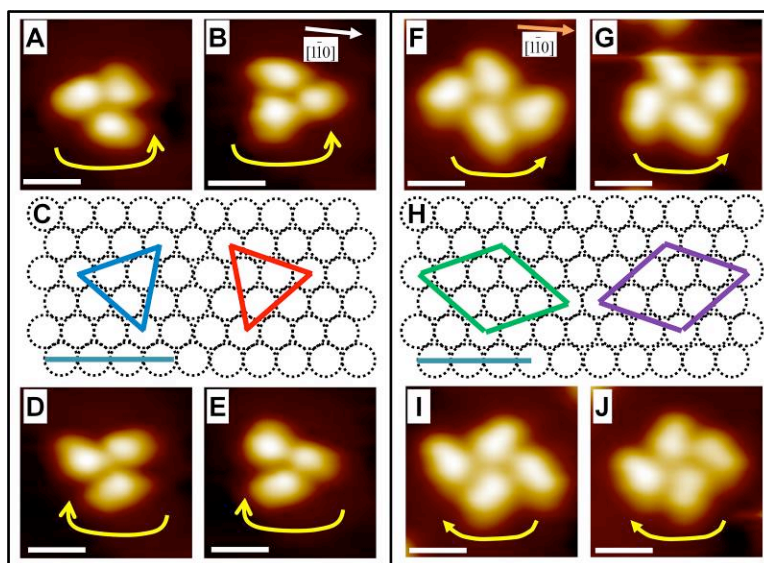


**Figure 9.2 4-Fluorostyrene Cluster Arrangements on Cu and Au:** (A-E) STM images and schematic showing the trimer cluster configurations for 4-FS on Cu(111). In (C) the blue triangle is rotated by  $-19^\circ$  from the close-packed direction (indicated by a white arrow in the STM image B) and the red triangle is rotated by  $+19^\circ$ . All trimers adopt a chiral pinwheel arrangement; anti-clockwise pinwheels are shown in (A) and (B) and clockwise pinwheels are shown in (D) and (E). (F-J) STM images and schematic showing the tetramer cluster arrangements for 4-FS on Au(111). In (H) the green parallelogram is rotated by  $-19^\circ$  from the close-packed direction (orange arrow in STM image in F), and the purple parallelogram is rotated by  $+19^\circ$ . The 4-FS molecules adopt an overall anti-clockwise (F and G) or clockwise (I and J) arrangement within the tetramers as seen in the STM images. Scale bars = 10 Å.

complementary arrangements on the Cu(111) substrate, as depicted in Figure 9.2A-E. In the schematic in Figure 9.2C, the center of each molecule lies at one of the equilateral triangle's three vertices, which are experimentally measured at  $(6.6 \pm 0.3)$  Å apart, or  $\sqrt{7}d_{Cu}$  (diameter  $d_{Cu} = 2.56$  Å). The triangles are rotated  $-19^\circ$  (blue) or  $+19^\circ$  (red) from the close-packed direction of the Cu lattice. Closer inspection of the STM images in Figure 9.2A-E reveals the chiral nature of the 4-FS trimers. The rotation off of a high-symmetry lattice direction results in a chiral molecular arrangement; also, depending on how the molecules arrange within the trimer cluster, we observe both clockwise and anti-clockwise pinwheel shapes. Thus, there are four degenerate 4-FS trimer structures on the Cu(111) surface. Figure 9.2F-J shows high-



resolution images of 4-FS tetramers on Au(111) and a schematic illustrating a proposed molecular arrangements with respect to the underlying surface atoms. In this structure (Figure 9.2H), the center of each molecule lies at one of the parallelogram's vertices. The center-to-center dimensions within the tetramer structures were experimentally measured to be  $(7.6 \pm 0.5) \text{ \AA}$ , or  $\sqrt{7}d_{Au}$  ( $d_{Au} = 2.88 \text{ \AA}$ ). The parallelograms are rotated  $-19^\circ$  (green) or  $+19^\circ$  (purple) from the close-packed direction of the Au lattice. Like the trimers on Cu, the 4-FS molecules aggregate within the tetramers such that all four appear to point clockwise or anti-clockwise. Thus, these chiral tetramers on Au have twelve degenerate molecular arrangements that were observed with equal probability, four of which are shown in Figure 9.2. Based on STM images, we are not able to assign the absolute adsorption site for 4-FS on Cu or Au, as simultaneous atomic and molecular resolution was not possible to obtain.

First principles calculations based upon dispersion corrected Density Functional Theory (DFT-D3) were performed in order to better understand the molecule-adsorbate interaction and to uncover the effects leading to the formation of different cluster types on the two metal surfaces. The optimized geometries for a single adsorbed 4-FS molecule on both Cu(111) and Au(111) reveal that the distance between the fluorinated end of the molecule and the surface is  $\sim 0.6 \text{ \AA}$  larger than for the ethenyl group (see Appendix). The 4-FS molecule interacts more strongly with the copper compared to the gold surface as evidenced by the binding energies, which were found to be 1.65 and 1.35 eV, respectively. In both systems, there is a net transfer of electron density from the 4-FS molecule to the surface, and the magnitude of the charge transfer is higher for Cu, as summarized in Table 9.1.

**Table 9.1 The Charge on a 4-Fluorostyrene Molecule Adsorbed on the Cu(111) and Au(111) Surface**

Surface [a]	Charge $Q_M$ (e)	Charge $Q_H$ (e)	Charge $Q_V$ (e)
Cu (111)	0.31	0.32	0.33
Au (111)	0.16	0.26	0.27

[a] Values were obtained using a Mulliken (QM), Hirshfeld (QH), and Voronoi (QV) charge analysis. The charge on the surface is equal and opposite to that on the adsorbate.

To clarify the nature of the bonding between the 4-FS molecule and the Cu and Au surfaces, a fragment orbital analysis, which yields the composition of the molecular orbitals (MOs) in terms of occupied and unoccupied MOs of the adsorbate and the metal cluster, was performed.<sup>313</sup> The bonding can be explained by taking into consideration the relative difference in energy of the Fermi level and the frontier orbitals of the adsorbate, along with their overlap with the surface bands.<sup>314</sup> As shown in Figure 9.3A and B, for both surfaces we find charge donation from the highest occupied molecular orbital (HOMO) of the adsorbate into the metal bands, and back donation from the surface into the lowest unoccupied molecular orbital (LUMO) of the 4-FS molecule – described by the Dewar, Chatt and Duncanson model.<sup>315,316</sup> Despite the similarity in the bonding mechanism, there are slight but important differences which become evident when visualizing how the charge density changes upon molecular adsorption, see Figure 9.3C and D. The binding energy, charge transfer, charge density difference plots and molecule-surface distances indicate a stronger interaction between 4-FS and Cu(111) than with Au(111), correlating with the well known trends of chemical reactivity in going from Cu to Ag to Au.<sup>317</sup>

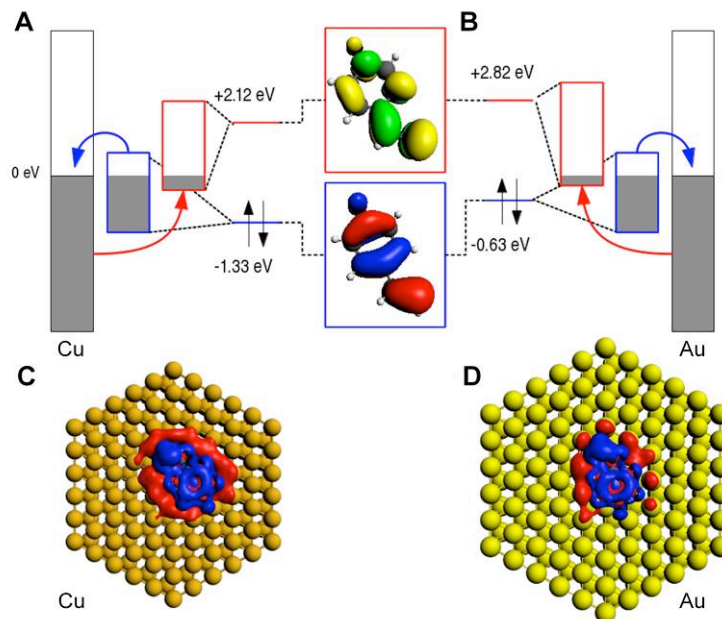


**Figure 9.3 Fragment Orbital Analysis and Charge Transfer Calculations for 4-Fluorostyrene on Cu and Au:** A schematic interaction diagram between 4-FS with (A) the Cu(111) surface and (B) the Au(111) surface. The central panel illustrates the HOMO (red/blue) and the LUMO (yellow/green), isovalue  $\pm 0.03$  a.u. The red/blue rectangles provide the approximate width of the bands resulting from the hybridization between the LUMO/HOMO of the adsorbate with the metal surface MOs. The Fermi-level of each surface has been adjusted to 0 eV. Charge Density Difference (CDD) isovalue plots ( $\pm 0.0003$  a.u.) for 4-FS on Cu(111) and Au(111) are shown in panels C and D respectively. The colors in C and D indicate the accumulation (red) and loss (blue) of charge upon molecular adsorption, respectively.

**Table 9.2 The dipole moment vector components for 4-FS adsorbed on Cu(111) and Au (111) in Debye**

Dipole Moment <sup>b</sup>	Cu				Au			
	X	Y	Z	MAG	X	Y	Z	MAG
4-FS	-0.56	1.06	-0.16	1.21	-0.14	1.21	-0.14	1.23
Metal Cluster	0.00	0.00	-0.41	0.41	0.03	-0.03	-0.47	0.47
(4-FS)+ Cluster	0.52	0.30	2.99	3.05	0.24	0.12	2.34	2.36

The axis employed is illustrated in Figure 4. The first and second rows provide values for the non-interacting molecule and metal cluster, but using the optimized geometry of the 4-FS adsorbed to the surface. The third row employs this same geometry, but allows the molecule and surface electron densities to interact.

The dipole moment of the free molecule in the gas phase was calculated to be 1.31 Debye (D,  $3.336 \times 10^{-30}$  C m). As a result of the charge transfer between the molecule and the surface, the dipole was found to decrease drastically in the plane of the surface, while increasing in the plane perpendicular to the surface. The dipole moment components are given in Table 9.2, where the first two rows are for the non-interacting molecule and metal cluster (but using the optimized geometry of the adsorbed system), and the last row is for the interacting system. Remarkably, on both surfaces the electric dipole moment of the molecule-surface complex, illustrated in Figure 9.4, is approximately double that of the gas phase dipole and shifted orientation almost  $90^\circ$  from in plane to surface normal. This result illustrates that one cannot assume dipolar molecules will retain the magnitude and direction of the dipole when adsorbed on metals and that theory must be employed to quantify the charge transfer and subsequent reorientation of the molecular dipole.

The molecular arrangement within the clusters was also explored. DFT-D3 calculations have been performed to elucidate the most stable trimers and tetramers of neutral 4-FS molecules in the gas phase. The calculated structures that best agreed with STM images are shown in Figure 9.5 (see Appendix for the ten most stable trimer/tetramer geometries). The global minimum configuration for the trimer was found to be a chiral configuration with  $C_{3h}$  symmetry and an overall dipole moment of 0 D, where the center to center distance between the 4-FS molecules measured 6.925 Å; which matches well with the proposed trimer aggregate on Cu(111) in Figure 9.2a. This preferred arrangement is attributed to both C-H $\cdots$ F hydrogen bonding and attractive dispersion interactions (see the Supporting Information). The first and second nearest neighbor H-F distances we find *via* DFT-D3, 2.36 Å and

2.55 Å, are somewhat shorter than the sum of the van der Waals radii of H and F (2.76 Å) as well as those computed at the MP2/6-31+G(d,p) level of theory for fluorocarbon dimers.<sup>318</sup>

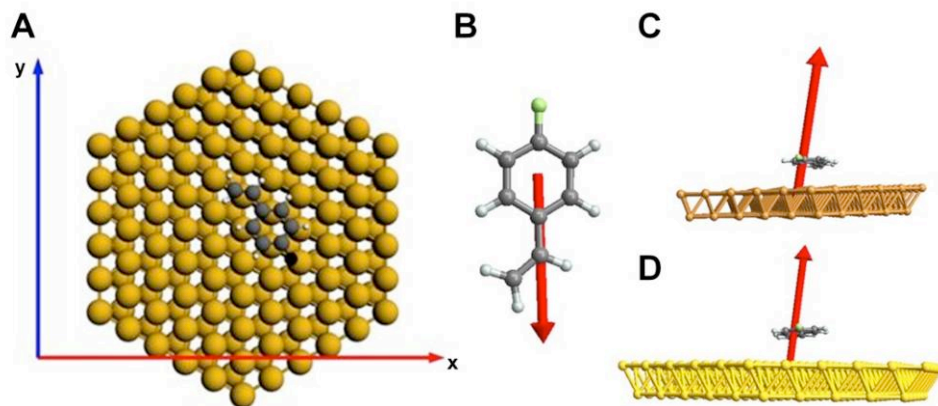


**Figure 9.4 Dipole Moment Illustrations for Gas-Phase and Adsorbed 4-Fluorostyrene:** (A) Schematic illustration of the dipole moment axis of the 4-FS/metal system; the “z” component is out of the plane of the page. Electric dipole moment vectors of (B) the free gas phase 4-FS, (C) 4-FS on Cu(111), and (D) 4-FS on Au(111). We employ the convention where the dipole moment vector points in the direction of positive charge.

The most favorable tetramer arrangement appeared to be derived from the trimer, but with an extra 4-FS molecule outside of the triangle (see Appendix). As this geometry does not match the observed tetramer geometry, a closely related parallelogram-shaped tetramer (see Appendix) with  $C_{2h}$  symmetry and center-to-center distances between the 4-FS molecules measuring 6.543 and 7.775 Å was constructed and its energy was minimized, (Figure 9.5c). This user-input geometry was higher in energy than the global minimum by only 15.6 meV. Attempts to construct and optimize a gas phase 4-FS parallelogram with sides of equal length always resulted in asymmetric relaxation as seen in the Appendix.

As previously stated, there is a transfer of charge from the 4-FS molecules to the surface upon adsorption; thus, the relative stabilities of *charged* trimers and tetramers are very relevant to this study and were therefore also modeled. Each 4-FS molecule

was given a charge of +0.05e to +0.35e, and the aforementioned trimer and tetramer structures were allowed to relax while maintaining the symmetry of the molecular complex; the results are summarized in Table 9.3. For all scenarios investigated, similar cluster structures as for the neutral species were obtained; however, differences arose in the relative cluster stabilities. At the lower charge regime (charge/molecule <0.12 e<sup>-</sup>) the difference in energy between the two motifs was minimal, but the trimer was favored at higher positive charges (charge/molecule >0.20 e<sup>-</sup>). Calculations performed on charged molecules indicate that the symmetric trimer geometry (Figure 9.5A) becomes progressively preferred over the tetramer (Figure 9.5C) as the charge on the 4-FS becomes more positive. This result is consistent with trimers being found on Cu and tetramers on Au as the charge transfer to Cu is higher than to Au (Table 9.1), and the tetramers are only rarely observed on Cu.

**Table 9.3 Trimer versus Tetramer Stability as a Function of Molecular Charge**

charge/molecule (e <sup>-</sup> )	difference (meV/molecule) <sup>a</sup>	charge/molecule (e <sup>-</sup> )	difference (meV/molecule) <sup>a</sup>
0.00	-2.6	0.14	-15.2
0.05	-3.9	0.15	-16.9
0.10	-9.1	0.20	-28.2
0.11	-10.4	0.25	-42.5
0.12	-11.7	0.30	-61.1
0.13	-13.4	0.35	-79.3

<sup>a</sup> The energies are reported in meV/molecule. The difference in energy is taken as the trimer energy minus the tetramer energy, with a negative value indicating that the trimer motif is more stable than the tetramer structure at the given charge.

Thus, through calculations that compare 4-FS adsorption on Cu and Au it is clear that several factors dictate selective growth of well-defined, nearly monodisperse clusters. Firstly, the stabilizing C-H $\cdots$ F interaction between adjacent molecules drives the formation of clusters. The minimum size of the cluster in which each molecule has its maximum complement of two of these directional bonds is a trimer. By comparison, a dimer molecular geometry dictates that only one C-H $\cdots$ F interaction can occur. In the absence of repulsive interactions, van der Waals attraction in concert with C-H $\cdots$ F would drive the formation of large ordered arrays. However, calculations show a significant charge transfer from the molecule to the surface that yields a large out of plane dipole and results in dipole-dipole repulsion between adjacent molecules and adjacent clusters.<sup>251,253</sup> The tendency of adjacent clusters to separate from one another on the surface rather than aggregate into large islands is clearly seen in Figure 9.1. Therefore, there is a cutoff size of three molecules for Cu and four for Au that yields maximum stability. This difference can be explained by considering the relative energies of charged trimers and tetramers given the greater charge transfer to Cu.

One must also note that the surface lattice constants of Cu and Au are different.<sup>310</sup> The calculated distances between the ring centers of the trimer and tetramer are reported in Figure 9.5E and F, respectively. The relaxed trimer and tetramer structures match well, but not exactly, with the metal substrates. However, measurements based on STM images suggest highly regular cluster arrangements (*i.e.*, standard deviation within  $\pm 0.5$  Å). It was determined that the Cu lattice better matched the molecule-molecule spacings observed in the relaxed trimers and tetramers ( $< 1$  meV/molecule), and that the fit on Au was slightly less favorable

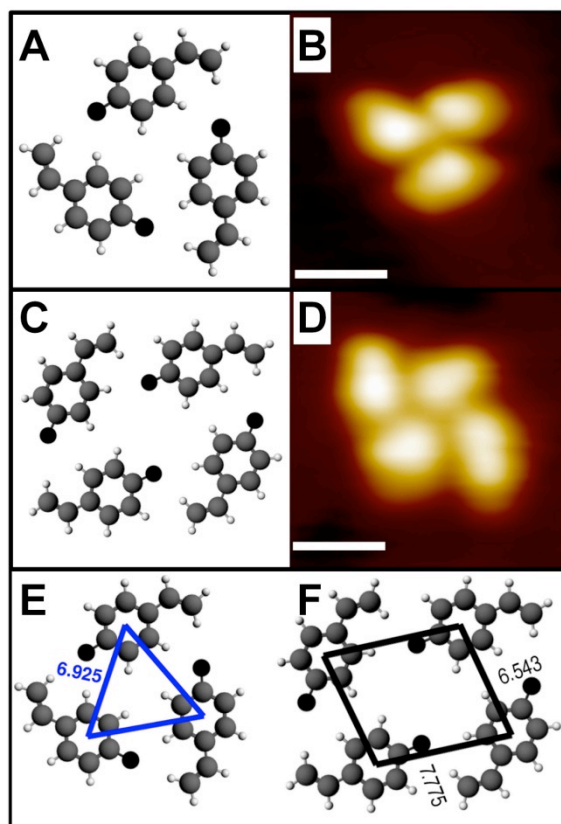


**Figure 9.5 Relaxed 4-Fluorostyrene Trimer and Tetramer Arrangements:** The lowest energy structures for the 4-FS (A) trimer and (C) tetramer compared to STM images in (B) and (D), respectively. The calculated distances (in Å) between the centers of the benzene rings on each 4-FS molecule within the trimers and tetramers are shown in (E) and (F), respectively.

(< 55 meV/molecule). These measurements assumed that the center of the benzene ring rested over a Cu or Au atom for each binding site. If the geometry of the molecules was restricted in our DFT-D3 calculations to match the Cu lattice, the calculated difference in energy was negligible (< 0.2 meV/molecule), and confining the molecules to fit on the Au lattice, the difference in energy was much larger (25-53 meV/molecule). These findings suggest that the epitaxial orientation of the molecules on the substrate may also play a role in determining the molecular arrangement. However, given the larger mismatch with Au one would expect smaller clusters on Au due to the poorer epitaxy in contrast to what is observed. Also, the



typical adsorption energy differences between the most and least favorable sites for benzene on Cu ( $\sim 25$  meV<sup>319</sup>) and the fact that 4-FS can reorient both laterally and internally with little energy penalty, suggest that the adsorption induced charging of the clusters on the two metals plays a larger role in determining the magic sizes of 4-FS on Cu and Au than differences in lattice parameters.

### 9.3 Conclusions

In this chapter, 4-FS, a simple dipolar organic molecule, assembles in a highly regular fashion to form predominantly trimers on Cu and tetramers on Au surfaces. This is the first work I know of illustrating how the preferred size of magic number of clusters can be changed by substrate choice. This effect is explained based on theory in terms of interfacial charge transfer. Interestingly, the electronic interaction between the molecules and the substrates is such that level hybridization causes a substrate-mediated charge transfer from the HOMO to the LUMO of the molecules, which concomitantly modifies the molecule's dipole. The dipole moments of the molecule-metal systems are aligned along the surface normal, which creates significant electric polarization of the surface-adsorbed clusters perpendicular to the surface. This dipole is rotated by  $\sim 90^\circ$  to what is predicted from knowledge of the only molecule's gas-phase dipole moment, and opposite to the surface dipole of bare metal surfaces, illustrating the importance of theory in understanding these surface-supported structures. The magic size of the clusters can be understood in terms of interplay between attractive interactions in the form of directional C-H $\cdots$ F bonds and van der Waals interactions, as well as Columbic repulsion between charged molecules. The change in magic number from Cu to Au likely derives from the different charge transfer to the two surfaces, which shifts the delicate balance

between attractive interactions and repulsive dipolar forces. This investigation could be extended to other surface facets or metals, and a range of sizes of magic clusters could be grown by controlling the interfacial charge transfer. The well-defined molecular clusters described here are both dipolar and chiral and offer exciting opportunities for the study of the interaction of electron spin with chiral entities as well as the possibility to probe the effect of spin filtering at the molecular scale.<sup>320</sup>

## 9.4 Additional Experimental Details

**Experimental Methods:** 4-Fluorostyrene (97+%, Sigma Aldrich) was purified by freeze/pump/thaw, and was introduced to the cold sample *via* a collimated molecular doser attached to a precision leak valve. The samples were annealed post-deposition by placing the cold sample into a room-temperature holder at the side of the STM stage until the temperature reached ( $\sim 40$  K, 30 s). Data were recorded at 5 K with a sample bias range of -500 to 300 mV and tunneling current range of 10 to 500 pA.

**Computational Methods:** The computations were performed by collaborators at State University of New York at Buffalo using the ADF software package,<sup>313,321</sup> the revPBE generalized gradient density functional,<sup>322</sup> and Grimme's dispersion correction (DFT-D3).<sup>323</sup> The basis functions on all of the atoms consisted of a triple- $\zeta$  Slater-type basis set with polarization functions (TZP) from the ADF basis set library. The core shells of the 1s level for C, and F, 3p for Cu and 4f for Au were kept frozen. For the gold surface, scalar relativistic effects were included by using the zeroth-order regular approximation (ZORA) Hamiltonian,<sup>324</sup> and ZORA basis sets. The metal surfaces were modeled using a finite cluster comprised of 166 atoms and 2

layers were employed. In the calculations the coordinates of the metal cluster were frozen at the experimental lattice parameters of 3.614 and 4.078 Å, while the molecule was free to relax. The Counterpoise method has been employed to calculate the basis set superposition corrected binding energies of the 4-FS molecules to the metal clusters. The dispersion correction used here is known to overestimate the binding energies of organic molecules to surfaces, however it is able to reproduce the correct trends for the different metal surfaces.<sup>323</sup>

In order to determine the most stable arrangement of 4-FS trimers and tetramers, RandomDock, a stochastic docking program, was employed. RandomDock has been written as an extension to the Avogadro molecular editor,<sup>325</sup> and is freely available under the Gnu Public License (GPL) as part of the XtalOpt source code.<sup>326</sup> For a user-specified number of matrix and substrate molecule(s), RandomDock generates random conformers and configurations (subject to user defined interatomic distance constraints) which are sent out for optimization by an external, first-principles program. For the purposes of this study, the randomly generated configurations were constrained so that all of the molecules lay in the same plane (*i.e.*, they were not displaced in the z-direction). RandomDock simulations were carried out for the neutral and charged 4-FS molecules; in total ~4000 geometries were optimized for the neutral species, and 2000/3000 for the charged tetramers/trimers.

## 10 Palladium Atom Geometries in the 1-10% Pd/Cu(111) Surface Alloy System

### 10.1 Introduction

Chapter 11 describes the assembly and diffusion of H and D atoms on a Cu(111) surface. The dissociative adsorption of H<sub>2</sub> on Cu(111) is an activated process with a barrier on the order of 0.4 eV;<sup>327</sup> however, when small amounts (~1%) of the active metal Pd is dispersed within the Cu lattice, the barrier to H<sub>2</sub> activation is reduced to 0.02 eV. Figure 10.1 shows STM images of monatomic steps on the clean Pd/Cu(111) surface (A) and one that is populated with H adatoms (C), with a schematic representation of the process of H<sub>2</sub> dissociation at a Pd site shown in B. In the 1% Pd coverage system, the majority (>99.9%) of the Pd exists as isolated entities surrounded by inert Cu atoms.<sup>85,86,89</sup> Thus, we have shown that single Pd atoms can perform the function of splitting the H-H bond, and that the resulting H can spillover onto the Cu surface where it is weakly bound. Using Temperature Programmed Reaction (TPR) we have also shown that this H is available to participate in low-temperature hydrogenation reactions.<sup>85</sup>

There are many examples in the field of heterogeneous catalysis and surface science in which the local geometry of the active site plays an important role in reactivity.<sup>328,329</sup> The dissociation of H<sub>2</sub> requires isolated Pd monomers; however, as work with the Pd/Cu(111) alloy surface continues and reactivity is explored, it will be useful to know how the alloy geometry changes as a function of Pd coverage. In this chapter I explore the structure of the Pd/Cu(111) alloy as a function of Pd coverage, from 1% to 10%. Specifically, I examine the relative abundances of Pd

monomers, dimers and trimers; the characterization is performed using STM images in which Pd species are clearly resolved in the Cu surface.

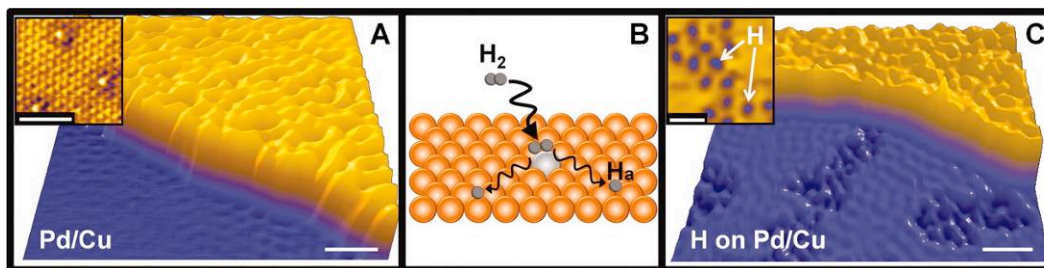


**Figure 10.1 Pd/Cu(111) Alloy and Hydrogen Activation:** (A) Pd atoms preferentially reside above step edges in the Cu(111) surface, as evidenced by the rumpled appearance of the upper terrace. The inset shows an atomically resolved image taken from the upper terrace in which the bright Pd atoms are clearly seen within the Cu host. (B) Schematic showing the process of H<sub>2</sub> dissociation at active Pd sites within the Cu host. (C) STM image following H<sub>2</sub> dissociation and H atom spillover onto the Cu terrace below the step. H atoms appear as dark depression in the image, as indicated it inset. Scale bars = 5 nm (inset scale bars = 2 nm) Reproduced from Kyriakou *et al.*<sup>85</sup>

## 10.2 Results and Discussion

The process whereby Pd alloys into the Cu(111) surface has been described in detail elsewhere.<sup>85–90,330,331</sup> Briefly, when Pd is deposited onto the clean Cu(111) surface, the Pd atoms skate across a terrace until they come to an ascending step where alloying occurs. Thus, Pd is localized at the brim of ascending steps on the Cu surface. The sample temperature during Pd deposition will have an effect on the location of the Pd atoms within the Cu host.<sup>86,88</sup> The systems described here were prepared with the sample temperature held at ~450 K; thus the majority of the Pd resides in surface sites, with a small percentage occupying subsurface sites. If the sample temperature is increased beyond ~500 K during or following Pd deposition, subsurface Pd will dominate.<sup>86,88</sup> The structure of the Pd/Cu(001) surface alloy exhibits similar temperature dependent behavior, emphasizing the importance of balancing sample preparation conditions when working with PdCu alloys.<sup>332–335</sup>

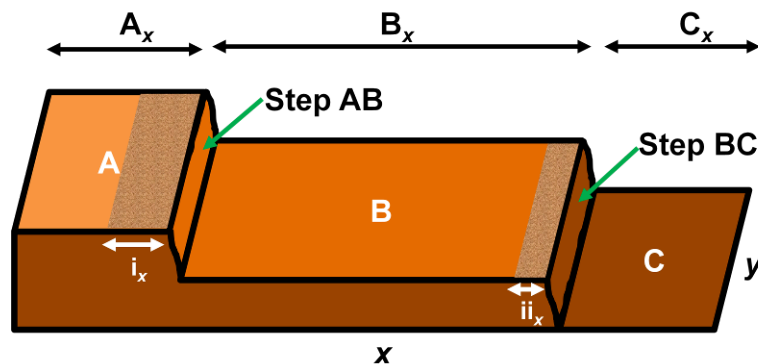


**Figure 10.2 Pd/Cu(111) Alloy Formation:** Schematic Model for the alloy formation in the Pd/Cu(111) system. Pd atoms diffuse to ascending step-edges, where alloying occurs. The width of the Pd brims (i and ii) is determined by the width of the lower terrace (B and C, respectively).

There is some variation in local terrace widths in the Pd/Cu(111) surface alloy, and the apparent width of a resulting Pd brim is dictated by the width of the lower terrace, or “catchment” area. Figure 10.2 shows a schematic of three Cu terraces – **A**, **B**, and **C** – separated by two steps, **AB** and **BC**. The EFM3 used to deposit Pd produces a collimated atomized beam, the diameter of which is three times that of our Cu sample. The number of Pd atoms that impinge upon the surface per unit area is relatively constant over the majority of crystal, with local variation negligible. As such, for the situation depicted in Figure 10.2, if terrace **B** is much wider than terrace **C**, the number of atoms landing on **B** would be proportionally larger than the number landing on **C**, and the resulting Pd brim **i** would be wider than brim **ii**. Furthermore, the number of Pd atoms in the Pd brim can be counted from atomically resolved STM images, such as those shown in Figure 10.3. Pd atoms appear as bright protrusions within the darker Cu host. The Pd coverage can then be accurately calculated if the width of the lower terrace is also known. For example, the Pd atoms in brim **i** are atoms that landed on catchment area/terrace **B** and alloyed at step **AB**; and coverage ( $\theta$ ) can be calculated by the equation:

$$\theta = \left( \frac{\alpha_i}{\beta_B} \right) \times 100$$

where  $\alpha_i$  is the number of Pd atoms in an area defined by  $\mathbf{i}$ 's width ( $x_i$ ) and a given length interrogated along the brim ( $y$ ), and  $\beta_B$  is the number of Cu atoms in an area defined by  $\mathbf{B}$ 's width ( $x_B$ ) and  $y$ . Here, the relative abundance of Pd monomers, dimers and trimers are investigated as a function of  $\theta$ .

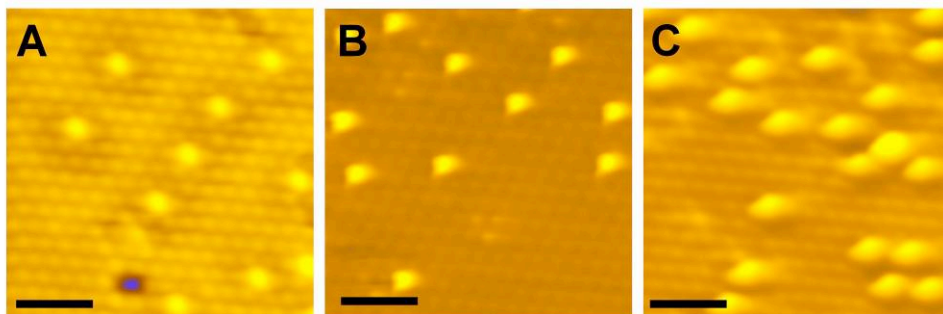


**Figure 10.3 The Pd/Cu(111) Alloy:** Atomically resolved images of the Pd/Cu(111) alloy in which the bright Pd atoms are clearly seen within the darker Cu host. Scale bars = 1 nm; image conditions: (A) 50 mV, 60 pA; (B) 1 mV, 20 nA ; (C) 10 mV, 10 nA.

Our findings regarding the mechanism of Pd/Cu(111) alloy formation is in good agreement with previous reports.<sup>86</sup> Aaen *et al.* examined the growth of sub-monolayer amounts of Pd on Cu(111) using STM. In their images, Pd appeared as bright protrusions within the Cu host, as it does in this work. Through pair correlation analysis, in which the populations of various  $n^{\text{th}}$  neighbor sites are compared, they determined that the distribution of Pd atoms in the surface was random. Surprisingly, their pair correlation analysis revealed a distinct lack of Pd-Pd nearest neighbors. In other words, Pd dimer and trimer populations were not observed. Aaen *et al.* used a surface energy based argument to describe a short-range order (SRO) that excludes the population of nearest neighbor surface sites. Thus, for a random alloy at a Pd concentration of 33%, the ordered  $(\sqrt{3} \times \sqrt{3})$ -Cu<sub>2</sub>Pd would

emerge. They further concluded that, in the absence of this SRO interaction there is practically no energy difference between an ordered and disordered Pd/Cu phase. Their discussion primarily focused on the high coverage system (*i.e.*,  $\theta > 15\%$ ); however, one can infer from their conclusions that in the low coverage regime, the populations of dimers and trimers are expected to be negligible.

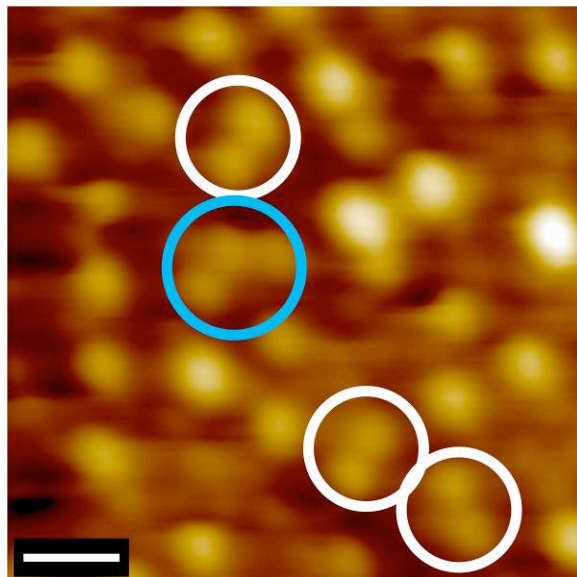


**Figure 10.4 Pd Geometries in the Pd/Cu(111) Alloy:** Atomically resolved STM image of the 10% Pd/Cu(111) alloy. The Pd atoms are clearly resolved as bright atoms within the darker Cu host. Pd dimers and a trimer are indicated by the white and blue circles, respectively. Scale bar = 0.5 nm, 50 mV, 60 pA.

Recent work with the Pd/Cu(111) surface alloy in the Sykes Lab has prompted an investigation into the exact nature of Pd sites within the low coverage system. Three different alloy systems were prepared with the goal of producing varying Pd concentrations from 1-10%. The number and type of Pd atom assemblies were investigated for each system using atomically resolved images such as those shown in Figure 10.3 and Figure 10.4. For each Pd brim, the width of the lower terrace was also determined from large scale STM images, and  $\theta$  was calculated using the equation above. The prepared systems were 2%, 7% and 10% Pd (all values are +/-



1%). Figure 10.4 shows an STM image of a Pd rich brim in which Pd dimers and a trimer are clearly imaged, as indicated by the white and blue circles, respectively.

The plot in Figure 10.5 shows the relative abundance of Pd monomers (blue), dimers (red) and trimers (green) as a function of Pd coverage. From these data it is clear that, while monomers dominate at every coverage examined, the percentage of dimers and trimers increases with increasing Pd coverage. As  $\theta$  is increased from 2 to 7%, the ratio of monomers to dimers increases by an order of magnitude; a similar increase in the monomer to dimer ratio is observed when  $\theta$  increased to 10%. Pd trimers are observed only in the 10% system, at a monomer:dimer:trimer ratio of 47:5:1.

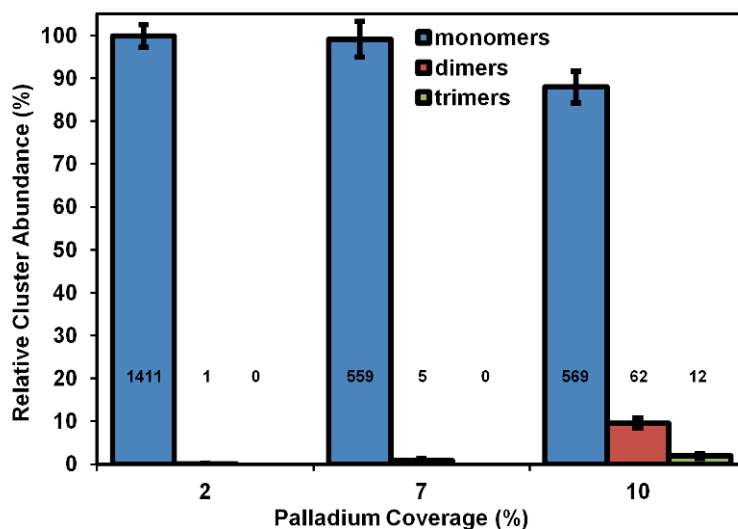


**Figure 10.5 Pd Geometries as a Function of Coverage:** Plot showing the relative abundance (in %) of Pd monomers, dimers and trimers as a function of  $\theta$ . The number of species counted is indicated by the integer value above/on each bar.

There are three possible trimer configurations, as outlined in

Figure 10.6. Trimer (A) has all three Pd atoms arranged in a triangular pattern, where their nearest neighbors consist of two Pd atoms and four Cu atoms. Trimers

B and C are arranged such that only the central Pd atom is surrounded by this 1:2 Pd:Cu ratio, and the remaining two Pd atoms' nearest neighbors consist of one Pd atom and five Cu atoms. Of these trimer configurations, B forms the majority structure, representing 50% of the observed trimers in the  $\theta = 10\%$  system. Trimers A and C were observed with equal probability.

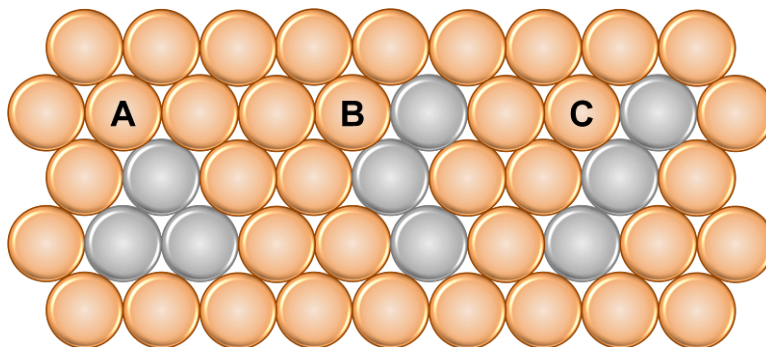


**Figure 10.6 Pd Trimer Configurations:** Schematic showing the three possible Pd trimer configurations. Cu and Pd atoms are represented by orange and silver circles, respectively. In trimer A, all Pd atoms have two nearest-neighbor Pd atoms. Trimers B and C are arranged such that only the central Pd atom has two nearest-neighbor Pd atoms; the other two Pd atoms in trimers B and C have one Pd nearest neighbor and are otherwise surrounded by Cu atoms.

### 10.3 Conclusions

A detailed investigation of Pd geometries in the Pd/Cu(111) alloy has been presented for Pd coverage in the 1-10% range. At the lower extreme, isolated Pd monomers are preferred over larger clusters (dimers and trimers) by an overwhelming (1000:1) majority. However, when Pd coverage increases by as little as five percentage points, the ratio of monomers to dimers is seen to decrease by an order of magnitude to 100:1, and further decreases to 10:1 at 10% Pd coverage. The overall structure of our Pd/Cu(111) alloy is in good agreement with what has been described previously by Aaen *et al.* However, their assertion that the occurrence of nearest neighbor Pd geometries is “negligible” is perhaps misleading; as I show here,

these types of clusters are present in statistically relevant populations at Pd coverage as low as 10%. The information presented here may be important in future model catalytic studies with the Pd/Cu(111) alloy where the geometry of the active site (Pd) potentially plays a role in reactant binding and subsequent product formation.

#### 10.4 Additional Experimental Details

Alloy preparation was performed using the Focus EFM3 metal deposition source from Omicron NanoTechnology; this doser and its operation have been described in detail in Chapter 2. The active metal was deposited by physical vapor deposition onto the clean Cu(111) sample using the EFM3, as described in Chapter 2. Changing the total time for each deposition varied the total Pd coverage. The details for each Pd deposition are included in Table 10.1. From these data it is determined that a flux ( $I_F$ ) = 10.4 nA yields a Pd coverage of 5% per minute, or ~0.05 monolayers/min.

**Table 10.1 Pd Deposition Parameters**

<b>Pd Coverage (%)<sup>a</sup></b>	<b>Flux (nA)</b>	<b>Deposition Time (s)</b>	<b>T<sub>s</sub> at Start (K)</b>	<b>T<sub>s</sub> at End (K)</b>
2	10.4	12	440	435
7	10.4	60	440	425
10	10.4	125	440	413

T<sub>s</sub> refers to the temperature of the Cu sample and are reported +/- 10 K.

<sup>a</sup>Coverage reported within 1% error.

Special thanks go to Michael Mattera for his help counting well over two thousand Pd atoms.

## 11 Self-Assembly of Hydrogen Atoms on Cu(111) *via* Quantum Tunneling

### 11.1 Introduction

During the past several decades the self-assembly of chemical species on metal and semiconductor surfaces has been a topic of great interest to the scientific community. Self-assembled monolayers (SAMs) offer a relatively straightforward route for surface modification and tailored chemical functionality, and SAMs have widespread applications in a variety of fields, including the electronics and medical industries. The organization of atoms and molecules adsorbed on a surface is dependent on a variety of factors pertaining to interactions with the surface and between the adsorbates themselves;<sup>198,297,299,303</sup> some aspects to consider include the adsorbate-substrate binding energy, substrate-mediated and direct lateral interactions, and charge transfer between adsorbates and the surface.

Surface diffusion, or thermal mobility, is also a key driving force in SAM formation, and knowledge of how adsorbates move on a surface is a topic of great importance. For instance, thiol SAMs on Au are by far the most widely studied system in molecular assembly.<sup>2,3,160,291</sup> Overlayers are often formed in solution at room temperature, resulting in structures with small domains sizes and high defect densities.<sup>2</sup> These defects result in facile degradation of the SAM; however, it has been shown that thermal annealing treatments lead to domain fusion and defect “healing,”<sup>28,336</sup> which is a direct effect of an increased rate of lateral diffusion on the surface and improves SAM stability. In a different study, Kern and co-workers examined the behavior of O on Pt using scanning tunneling microscopy (STM).<sup>337</sup>

They showed that at low coverage and 160 K, chemisorbed O-atoms exist as randomly distributed pairs; yet, at lower temperatures (*i.e.*, <140 K) the O-pairs form clusters and interconnected, one-dimensional chains on the surface. These observations elucidated the role of already chemisorbed O as the active site for the dissociation of O<sub>2</sub>: the mobile O<sub>2</sub> molecules adsorb in a mobile precursor state, diffuse to the active site where O-O bond splitting occurs, and became frozen in place as the chemisorbed O species.<sup>337</sup> Thus, thermally activated adsorbate diffusion can play an important role in our understanding of surface-based phenomena.

The quantum-mechanical-tunneling-driven diffusion of adsorbates has previously been observed in various surface systems by field emission microscopy,<sup>338–342</sup> optical diffraction,<sup>343–346</sup> and scanning tunneling microscopy (STM).<sup>158,347,348</sup> Typically, scanning probe investigations of diffusing species have focused on individual, isolated atoms and molecules;<sup>158,347–350</sup> however, the interaction and assembly of atoms are also of great interest. In this chapter we report an experimental and theoretical study of the assembly of H and D adatoms on a Cu(111) surface. The use of a Pd/Cu single atom alloy allows us to uptake a significant amount of H(D) onto the Cu as compared to the single atoms studies performed previously by Ho and co-workers.<sup>158</sup> Combining low-temperature STM with Density Functional Theory (DFT) calculations, we find further support for the quantum tunneling diffusion of H(D) adatoms. We discuss the influence of short and longer-range interactions that lead to fairly complex assemblies of H atoms. We show that the short-range interactions result in a stabilization of dimers on the 0.3 nm scale; this phenomenon is especially apparent in the case of D. However, the tunneling rate of H is orders of magnitude faster than D, allowing H to form large

islands due to a weaker long-range interaction between small clusters, which, as we show in the case of D, are dominantly dimers. The experiments described herein were performed at 5 K, well below the temperature regime for activated diffusion, and all of the diffusion and assembly observed is quantum tunneling mediated. Differences in rates of motion of H(D) monomers can be explained, not in terms of the barrier height (*i.e.*, as in classical, thermally driven diffusion), but in terms of tunneling probability, which depends on the barrier height and width, as well as particle mass. Also, the relative positions of the initial and final state energy levels will have an effect on the tunneling efficiency.<sup>347,351–353</sup>

## 11.2 Results and Discussion

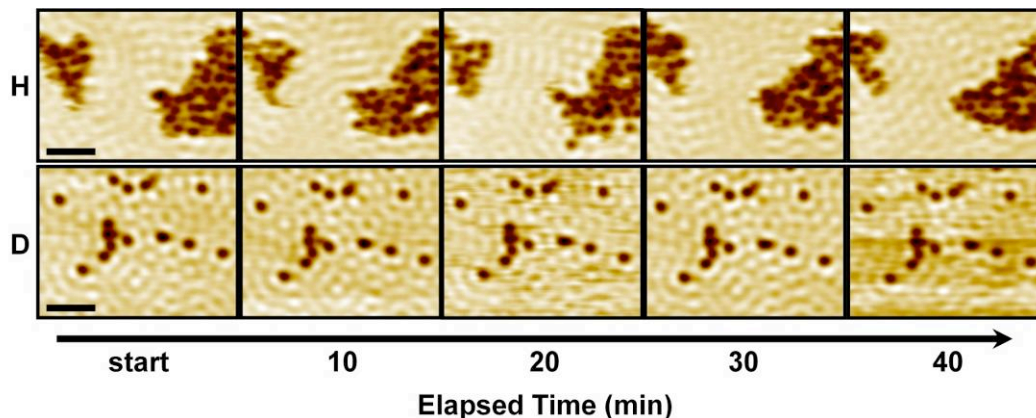


**Figure 11.1 Hydrogen and Deuterium on Cu(111):** Time-lapse STM images of H (top) and D (bottom) on Cu(111). Time between images is 10 minutes. Scale bars = 5 nm.

The dissociative adsorption of  $H_2$  on Cu is known to be an activated process, with a barrier on the order of 400 meV;<sup>327</sup> however, we have recently shown that this barrier can be overcome in the presence of single, isolated atoms of Pd in the Cu(111) metal lattice.<sup>85,89</sup> Using this alloy system with a Pd coverage of 0.1 monolayers (ML), we populated a Cu surface with H(D) adatoms, as shown in Figure 11.1. H(D) atoms appear in STM images as shallow ( $\sim 10$  pm) depressions on the Cu

surface due to the lower electron tunneling probability through the atom-metal complex as compared to the bare metal at energies close to the Fermi level (typically  $<100$  meV).<sup>158,354</sup>

Low-temperature STM imaging offers an advantage in that processes that are normally quite rapid at room temperature are significantly slowed; thus, at 5 K we are able to follow adsorbate diffusion by repeated imaging of the same area. The time-lapse sequence of images in Figure 11.1 depicts the result of adatom diffusion for H (top row) and D (bottom row). These images were taken from STM movies recorded over several hours with continuous scanning at 30 mV and 50 pA, where each image took  $\sim 1$  min. to acquire; the systems are shown at 10-min. intervals. The complete H(D) diffusion STM movies are available in the Appendix. The non-perturbative scanning conditions are in line with those previously used by Ho and co-workers for H(D) on Cu(001).<sup>158</sup> In the case of H, we note that there is clear evidence for diffusion in the center and along the edges of both islands, and we note that the island perimeters vary significantly over time. Conversely, there is little diffusion of the D features over a similar 40-min. interval. These data suggest that under identical scanning conditions and surface temperature the diffusion rate of H is much faster than that of D.

The H islands shown in Figure 11.2A were disrupted with the STM tip using perturbative scanning conditions at a gap voltage of 150 mV. In this manner, the H atoms within the islands were dispersed on the Cu terrace as shown in Figure 11.2B. Scanning was continued under normal conditions (30 mV, 50 pA), and the motion of the H was monitored. Figure 11.2C-E shows a sequence of time-lapse STM images, recorded in 10-min. intervals, in which the re-formation of H island assemblies is

observed. A STM movie showing H assembly is available in the Appendix. These data clearly demonstrate that there is an attractive interaction between H species, and further characterization, described below, shows that the depressions seen in STM images are not exclusively monomers, but H monomers and clusters.

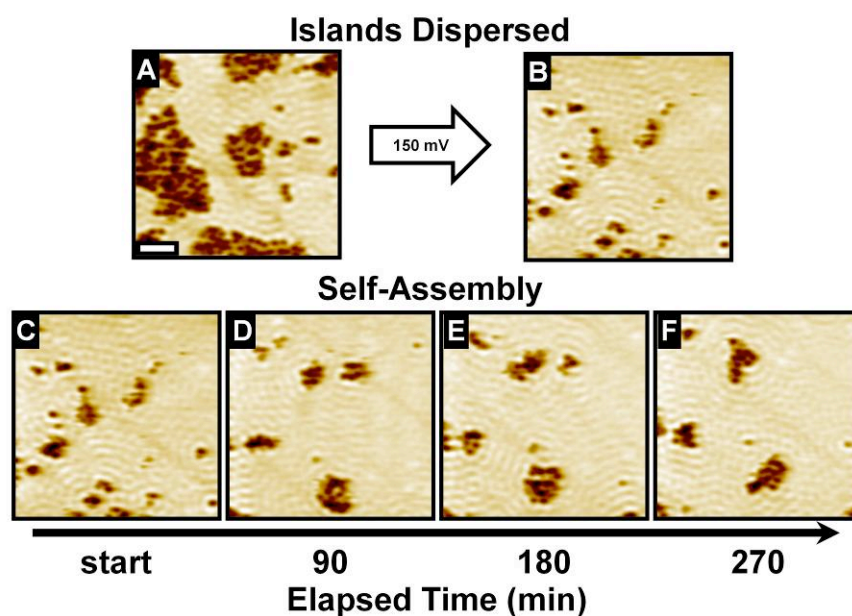


**Figure 11.2 Hydrogen Assembly at 5 K:** (A) STM image of H islands on Cu(111); the islands were dispersed by scanning at 150 mV resulting in the system in (B). (C-E) Time-lapse STM images showing the re-assembly of H islands over 270 min at 5 K. Scale bar = 5 nm.

Figure 11.3 shows STM images of H on Cu(111) in which H atoms form small clusters that appear as depressions and congregate into islands. In this system (Figure 11.3A), large islands of H clusters with well-defined boundaries are present. Occasionally, smaller features corresponding to H monomers appeared at the island edges (Figure 11.3C), typically as a result of cluster splitting; however, these H monomers were transient and diffused away by the next image (Figure 11.3D). Absolute cluster sizes were not easily determined in the H system due to rapid diffusion of H monomers during cluster splitting.



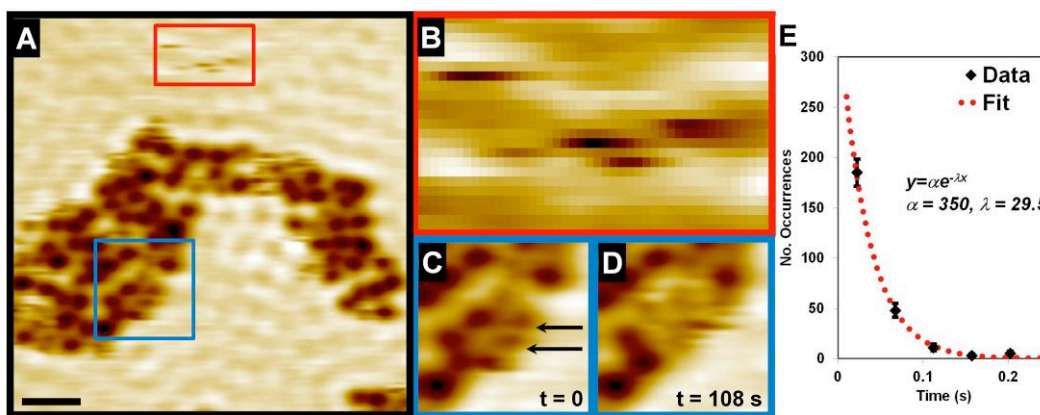


**Figure 11.3 Hydrogen Diffusion on Cu(111) at 5 K:** (A) STM image showing H clustering and islanding on the Cu surface. The red inset (B) shows the streaky H monomer, which is diffusing much faster than STM imaging. The blue insets show two H monomers (indicated with black arrows) at the edge of an island both (C) before and (D) after diffusing away (time elapsed between C and D is 108 s). (E) Plot showing residence time data for H monomers; the rate of monomer diffusion can be estimated based on the exponential fit to the data.

The identities of D clusters were easier to investigate due to the slower motion in that system. Figure 11.4A and B show the D system before and after a cluster was split to monomers using a 100 meV voltage pulse from the STM tip. From these images it is clear the D monomers and dimers appear differently on the Cu surface. Topographic line scans of a dimer pre- and post-separation and that of an intact dimer (confirmed with voltage pulse after the image was recorded) are shown in Figure 11.4C; from the data we see that D monomers appear  $\sim$ two-thirds as deep as the dimers, and both are approximately the same width (full width at half maximum). Because we could split each D feature into individual monomers with voltage pulses, we have a reliable and straightforward way of determining D cluster size (*i.e.*, number of atoms). An interrogation of 400 D features revealed that the majority of these species were monomers (37%) and dimers (49%), with larger clusters being less common. A histogram showing the relative abundances of D cluster sizes is shown in Figure 11.4D.

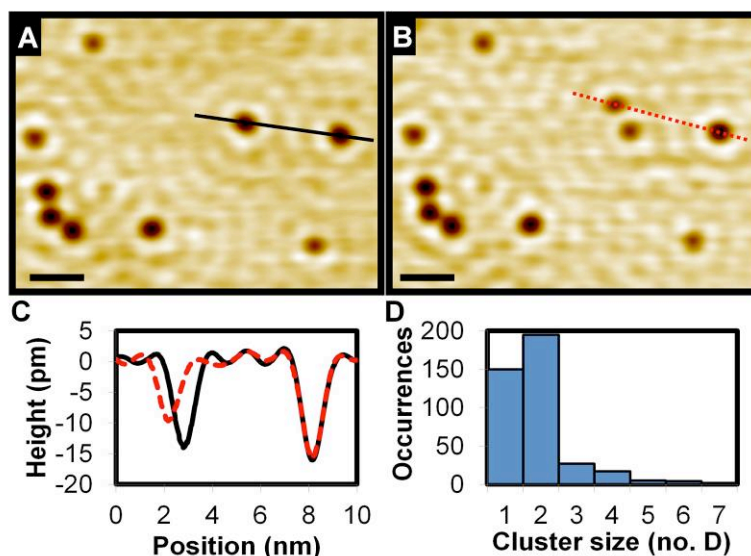


**Figure 11.4 Deuterium Clustering on Cu(111):** STM images showing D monomers and clusters on a Cu surface both (A) before and (B) after a dimer split into two monomers as the result of a low-energy voltage pulse with the STM tip. Scale bars = 3 nm. (C) Topographic profiles for the lines shown in A (solid black) and B (dashed red) reveal that the monomer and dimer also differ in their apparent height. (D) Histogram showing the relative abundance of D cluster types found on an unperturbed surface.

Using DFT we have modeled the interactions between H atoms on Cu(111) and calculated the differential binding energy as a function of coverage for 0.1 – 0.8 monolayer (Figure 11.5). Consistent with previous reports, the most stable adsorption site for H is in a three-fold hollow site.<sup>355</sup> Others groups have independently determined that the *fcc*-hollow is favored slightly over the *hcp*-hollow by as much as 10 meV.<sup>356,357</sup> The most stable 2H configuration has the H atoms arranged so that the second H atom is in the third nearest neighbor (3NN) position at a separation of 0.295 nm. This finding of an attractive 3NN interaction is consistent with previous calculations for H on Ni(111).<sup>345,358,359</sup> With the two H atoms arranged in this manner, one will occupy an *fcc* site, while the other is forced into the less favored *hcp* site. If the second H atom is frozen in the second nearest

neighbor ( $2NN$ ) position, the energy penalty is  $\sim 40$  meV (Figure 11.6). Thus, the atom-atom repulsion at this closer separation is larger the difference in binding

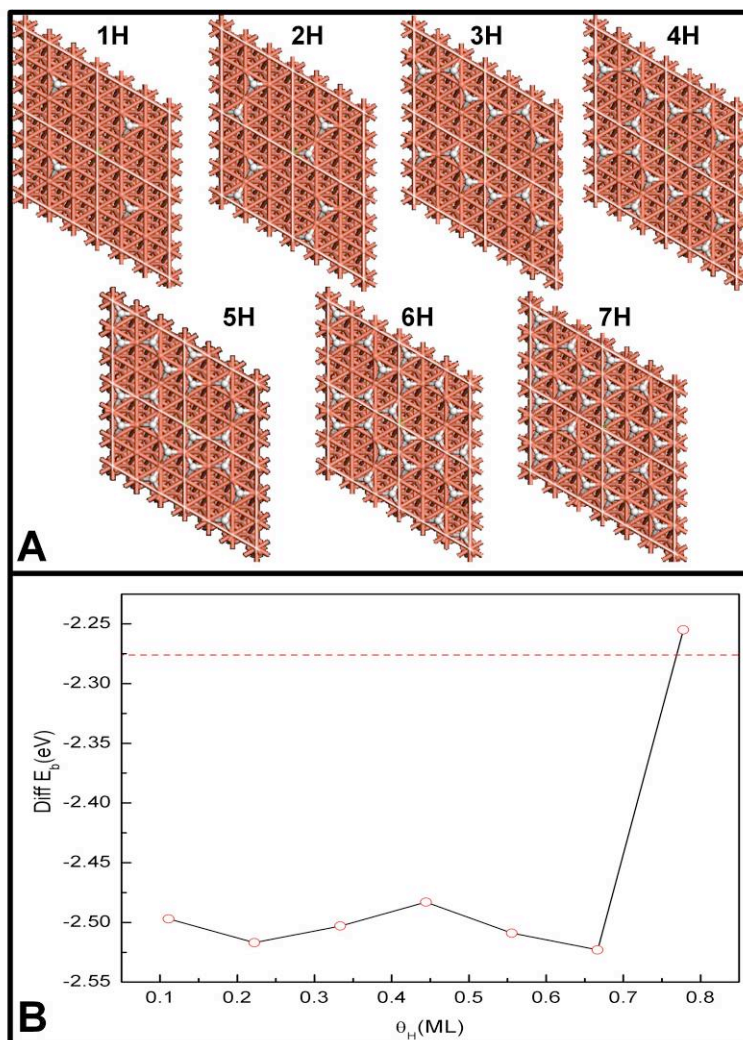


**Figure 11.5 Hydrogen Stability on Cu(111) as a Function of Coverage:** Schematics showing (A) the lowest energy configurations for H on Cu(111) from 0.1 to 0.8 monolayer and (B) the differential binding energy as a function of coverage ( $\theta$ ) in monolayers (ML) for H on Cu(111). The red dashed line indicates relative binding energy for  $H_2(g)$ .

energy between the two three-fold hollow sites. This finding is in direct contrast to experimental and theoretical findings for Cu-dimers on Cu(111), where the  $2NN$  arrangement is preferred and having both Cu atoms in neighboring *fcc* sites is favored over having both in neighboring *hcp* sites.<sup>360</sup> Finally, this paired (2H) configuration is

more stable than the isolated atom (1H) by 20 mV and is the most stable low coverage ( $<0.5$  ML) geometry examined. This result explains why we observe both H and D in the form of clusters consisting predominantly of two atoms.

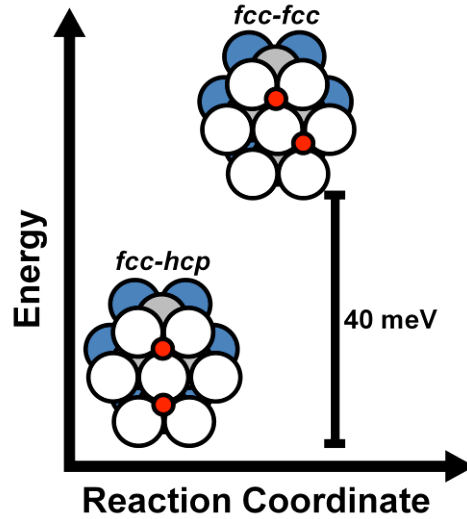


**Figure 11.6 Hydrogen Pairing Geometry and Stability:** Reaction coordinate showing the calculated difference in stability for 2H in the 3NN *vs* 2NN configuration. Cu atoms in the 1<sup>st</sup>, 2<sup>nd</sup> and 3<sup>rd</sup> layers are represented by white, grey and blue spheres, respectively, and H is represented by red spheres.

We have also investigated the stabilizing effect of clustering for both H and D by examining the relative barriers to diffusion for isolated and paired H and D atoms using DFT. The overall rate of diffusion ( $R$ ) for H(D) monomers in these systems can be described by combining the rates of activated thermal diffusion ( $R_A$ ) and diffusion due to tunneling ( $R_T$ ):  $R = R_A + R_T$ . In the activated diffusion regime,  $R_A$  can be described by:  $R_A = R_0 \exp(-E_d/k_B T)$ , where  $R_0$  is  $\sim 10^{13}$  Hz and corresponds to a typical frustrated translation frequency,<sup>158</sup>  $E_d$  is the barrier height,  $T$  is temperature, and  $k_B$  is the Boltzmann constant. The shortest hop distance for H(D) on Cu(111) is between neighboring three-fold hollow sites, 0.148 nm, and the lowest energy pathway for this transition is over a bridge site. Based on SC-HTST calculations,  $E_d$

$\approx 0.134$  eV; thus at 5 K, the temperature at which diffusion data were collected,  $R_A$  can be ignored as it is diminishingly small (*i.e.*  $\sim 10^{-123}$  Hz). Also, it has previously been established with energy electron loss spectroscopy (EELS)<sup>361</sup> and inelastic electron tunneling spectroscopy (STM-IETS)<sup>158</sup> that the H-Cu(D-Cu) vibrational stretch lies at 70(51) mV. The experiments here were performed at 30 meV, below the vibrational excitation energy, in an effort to negate the tip's influence on the diffusion rate. Thus, we can conclude with reasonable certainty that all observed diffusion arises from quantum tunneling of the adsorbates. A comparison of the DFT-derived tunneling probability for H and D suggests that the relative diffusion rates for the two species would be  $R_T(D) \approx R_T(H)/145$ .

From high-resolution STM movies taken over several hours, the diffusion of H(D) monomers on Cu(111) could be followed and the rate quantified. Figure 11.3 shows STM images in which H monomers are visible. H monomers diffuse rapidly even at 5 K and are much faster than the time resolution of STM under normal scanning conditions, where each image requires 54 s to capture (imaging rate of 0.18 Hz per line). Thus, H monomers appear as streaks of different thickness, as shown in Figure 11.3A and B. The residence time of H atoms was measured, and the data were fit to an exponential plot with the formula  $y = \alpha \exp(-\lambda t)$ , where  $\lambda$  gives the hop rate (Figure 11.3E) and  $\alpha$  depends on the number of events recorded and the time bin. From 252 H hop events, we calculate  $R(H) \geq 29$  Hz; due to the time-resolution of our instrument, in which the fastest scan speed to yield reliable data is 0.015 Hz per line, this value represents the lower limit for  $R(H)$ . Unlike H monomers, D monomers diffused slowly enough that these short-range diffusion events were easily

captured, and  $R(D)$  was measured to be  $3.2 \pm 0.5$  mHz, well below  $R(H)$ . The rate of D dimer (2D) diffusion was measured to be  $0.5 \pm 0.4$  mHz; these events included motion of the entire 2D species, as well as 2D splitting into monomers. The large error results from the low event frequency, which is an order of magnitude lower than for D monomers.

We performed DFT calculations in order to elucidate the possible mechanism for dimer diffusion. We first considered local motion in the form of dimer rotation around the central atom; the starting and ending 2H(2D) configurations were identical with one atom in an *fcc* site and the other in the 3NN, *hcp* site (low energy arrangement in Figure 11.6). In the case where both atoms move simultaneously, we calculate  $E_d \approx 0.31$  eV, more than twice what was calculated for monomer diffusion. In the case where the atoms move consecutively, the first motion results in the higher energy arrangement described in Figure 11.6 with  $E_d \approx 0.16$  eV, and the second motion returns the system to the lower energy arrangement from Figure 11.6 with  $E_d \approx 0.12$  eV. Based on these calculations, we propose that dimer diffusion follows the consecutive pathway, as the barrier for concerted motion is quite high. We also examined dimer separation (splitting) in which one atom moves from the 3NN *hcp* site to the fourth nearest neighbor (4N) *fcc* site. Calculations show that this separation results in a configuration that is less stable than the 3NN arrangement by  $\sim 0.04$  eV and has a barrier of  $\sim 0.16$  eV. Finally, the difference in the measured tunneling rates for D *vs* 2D is consistent with DFT calculations of tunneling probability for these two arrangements where  $R_T(D) \approx 150 \times R_T(2D)$ .

We characterized the distance moved for 106 D monomer hop events, where only the six nearest neighbor three-fold hollow sites were considered; the data are

summarized in Figure 11.7A. The histogram in Figure 11.7A shows the surprising result that hops to the 2NN site are favored 2:1 over hops to the first nearest neighbor (NN) and 3NN sites. This finding further supports that there is an energetic difference for H(D) adsorbed at a *fcc* vs *hcp* three-fold hollow sites on Cu(111), as we have predicted by theory (Figure 11.7B).<sup>356,357</sup> To our knowledge, this work is the first experimental evidence of this phenomenon. As such, while hops to *N* are expected to be the most abundant, the difference in adsorption site energy ( $\sim 10$  meV) means that the hop to *NN* is comparatively slow as the particle has to effectively tunnel uphill in energy. Once at the higher energy *hcp*-*NN* site, the atom is subject to fast tunneling motion back to the original *fcc* site or to the *fcc*-2NN site, as both of these events involve tunneling downhill in energy, which is expected to be much faster than the original *fcc* to *hcp* tunneling event.

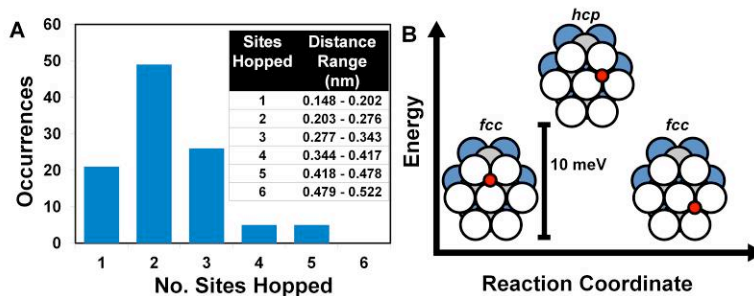


**Figure 11.7 Deuterium Hop Distance and Adsorption Site Stability on Cu(111):** (A) Histogram showing the number of sites hopped for 106 D monomer hop events. The table details the distance ranges (in nm) utilized in the histogram, which correspond to hopping events between three-fold hollow sites. (B) Reaction coordinate diagram showing the proposed difference in binding energy for H in *fcc* vs *hcp* three-fold hollow sites. Cu atoms in the 1<sup>st</sup>, 2<sup>nd</sup> and 3<sup>rd</sup> layers are represented by white, grey and blue spheres, respectively, and H is represented by red spheres.

Lauhon and Ho noted weakly temperature dependent diffusion behavior within the tunneling diffusion temperature regime for H on Cu(001). Due to lattice vibrations, the ground state levels of the occupied and nearest neighbor sites were

brought into resonance, resulting in a phonon-assisted tunneling process with a low activation barrier on the order of  $\sim 3$  meV. The D/Cu(111) system examined here also exhibits weakly temperature dependent diffusion behavior, which was observed as the instrument was allowed to warm following complete evaporation of the liquid He coolant. The diffusion of D monomers was characterized as a function of temperature over the 5-9 K range. The instrument warmed rapidly, and it was not possible to stringently determine an exact rate of diffusion *per se*; thus, the probability of diffusion over three consecutive images was measured. An Arrhenius plot relating the probability of diffusion to temperature is shown in Figure 11.8; from the slope of a linear fit we calculate  $E_d \approx 2$  meV. This measured energy barrier is much lower than what is calculated for the activated diffusion regime (134 meV). Thus, we have evidence for phonon-assisted tunneling for D on Cu(111).

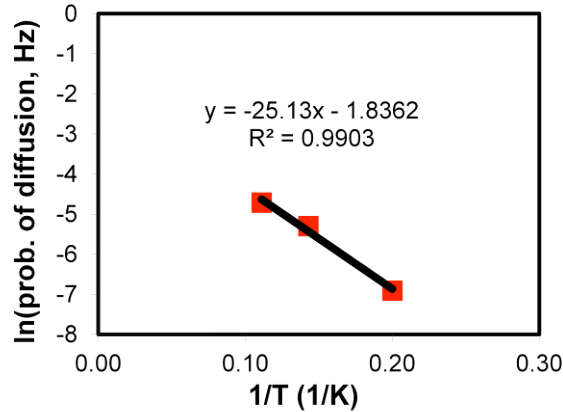


**Figure 11.8 Temperature Dependent Behavior for Dueterium on Cu(111):** Arrhenius plot for the diffusion of D on Cu(111) over the 5-9 K temperature range. The activation barrier ( $E_d$ ) can be determined from the liner-fit slope.

The Si-diode used for temperature readout in the LT-STM is currently non-functioning, so it is not possible to get an accurate readout of temperature, nor is it



possible to heat the sample in a controlled manner. Thus, more detailed studies of this system are warranted once temperature control has been restored.

### 11.3 Conclusions

The diffusion of H and D on Cu(111) has been explored using STM at 5 K and DFT. In agreement with previous investigations of H(D) on metal surfaces, we show that diffusion at low temperature is driven primarily by quantum tunneling diffusion (*i.e.*, under-barrier tunneling). We also show the tunneling driven assembly of H(D) atoms, which can be explained in terms of pairwise interactions between atoms that leads to cluster stabilization. This stabilization also results in a slower rate of diffusion, as explicitly shown in the case of D. To our knowledge, this study represents the first atomic-scale, visual evidence for the self-assembly of H(D) on a metal surface. Furthermore, the behavior of H(D) atoms on a surface may have implications, for example, in the field of catalysis where adsorbed species often interact to form desired products.

### 11.4 Additional Experimental Details

Hydrogen and deuterium were introduced to the clean sample at 5 K followed by a thermal anneal to 80 K. The sample was again cooled down to 5 K for imaging. STM images were recorded at a sample bias range of 30-50 mV and a tunneling current range of 30-90 pA.

### 11.5 Computational Details

Density Functional Theory (DFT) calculations were performed using the VASP code<sup>362,363</sup> and the projector augmented wave (PAW) potentials.<sup>364,365</sup> The Cu(111) surface was modeled with a five-layer slab; a Cu(111)-(3 × 3) surface unit

cell was employed. The adsorbates and top three Cu layers were allowed to relax, while the bottom two layers were fixed at bulk positions using the Cu-Cu experimental (111) spacing of 2.56 Å. Exchange and correlation parameters were performed using the GGA-PW91 exchange-correlation functional,<sup>366</sup> and an energy cut-off of 400 eV was used. The diffusion barriers were determined with the climbing image nudged elastic band method (CI-NEB),<sup>367</sup> and estimated tunneling rates were calculated using semiclassically corrected harmonic transition state theory (SC-HTST).<sup>368,369</sup>

## 12 Appendices

### 12.1 Appendix to Chapter 4

Several STM movies which show the dynamics of self-assembly of dibutyl sulfide on Au(111) are provided. Descriptions of the movies and detailed scanning conditions are provided below. Each frame took  $\sim 2$  minutes to acquire, and all movies were recorded at 78 K. Schematics of molecular orientation are shown along with each STM movie frame; in the schematics sulfur atoms are blue, carbon is yellow, hydrogen is white and gold is grey. Movies can be viewed on the Sykes Lab website (<http://ase.tufts.edu/chemistry/sykes/index.html>) under the Links tab.

#### **Movie A1 Molecular Rotation and Translation**

Two dibutyl sulfide molecules adsorbed on Au(111) rotate about the central sulfur-Au bond. The molecules rotate much faster than the scan speed, but translate (or diffuse) along the surface at  $< 0.1$  Hz. Image Conditions:  $\sim 4.0$  nm  $\times$  4.0 nm, 10 pA, 0.1 V.

#### **Movie A2 Dimers Rearranging**

Several pairs, or “dimers”, of dibutyl sulfide molecules can be seen rearranging and changing orientation with respect to the underlying Au lattice. Image Conditions:  $\sim 7.5$  nm  $\times$  3.5 nm, 10 pA, 0.1 V.

#### **Movie A3 Trimer Formation**

A single rotating dibutyl sulfide molecule approaches a dimer; the three molecules interact then form a trimer. Image Conditions:  $\sim 5.5$  nm  $\times$  4.8 nm, 10 pA, 0.1 V.

#### **Movie A4 Trimer Rearrangement**

A short chain of three dibutyl sulfide molecules rearranges and changes orientation with respect to the underlying Au lattice. Both the initial and the final chain orientations lay along one of the  $\sqrt{3}$  axes of the Au surface. Image Conditions:  $\sim 3.0$  nm  $\times$  3.0 nm, 10 pA, 0.1 V.

#### **Movie A5 Single Molecule Interacting with Molecular Chain**

A single dibutyl sulfide molecule moves along a short chain of five molecules. This sixth molecule appears to induce motion of molecules along the chain. Image Conditions:  $\sim 4.5$  nm  $\times$  2.4 nm, 10 pA, 0.1 V.

## 12.2 Appendix to Chapter 5

Several STM movies showing the dynamics of self-assembly of butyl methyl sulfide on Au(111) are provided. Each frame took  $\sim 2$  minutes to acquire, and the movies were recorded at 78 K. Schematics of molecular orientation are shown along with each STM movie frame; in the schematics sulfur atoms are blue, carbon is yellow, hydrogen is white and gold is grey. Movies can be viewed on the Sykes Lab website (<http://ase.tufts.edu/chemistry/sykes/index.html>) under the Links tab.

### **Movie A6 Enantiospecific Assembly of Butyl Methyl Sulfide Trimer**

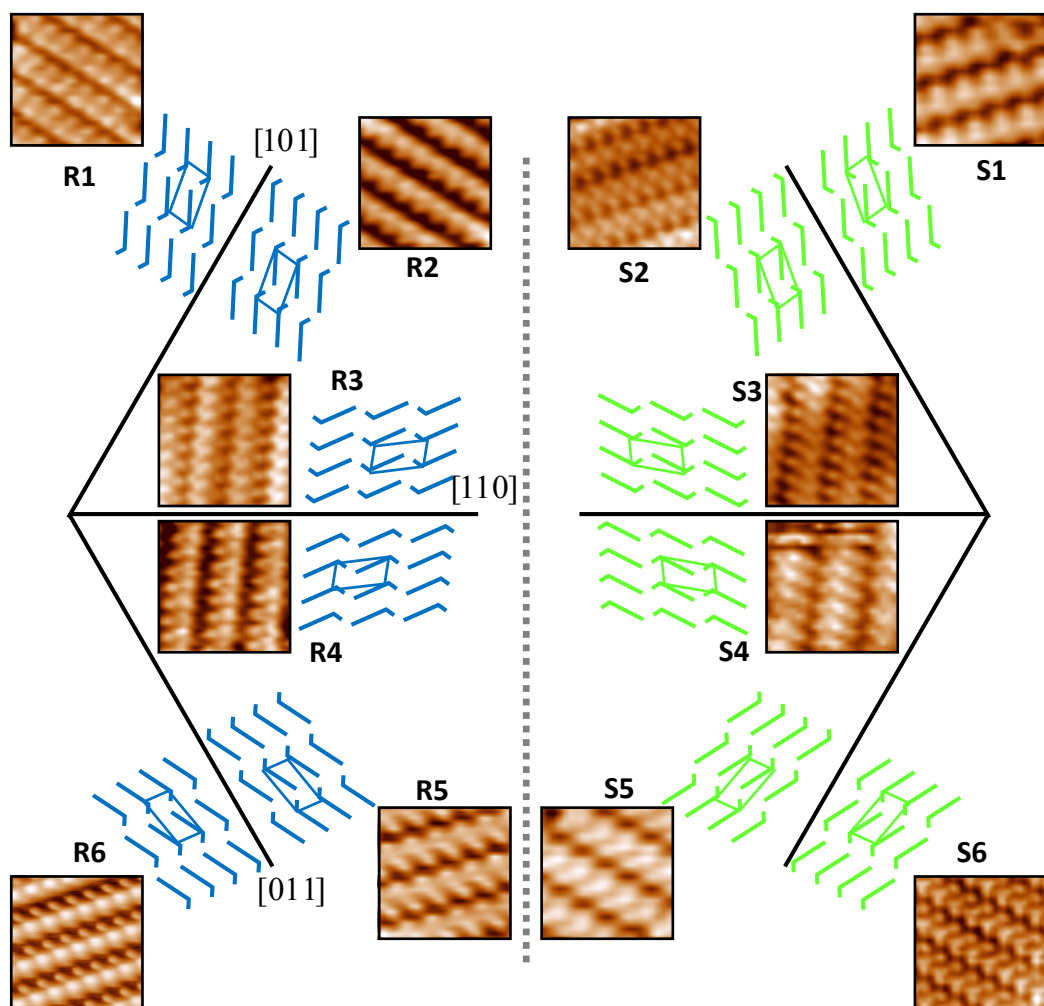
A spinning S-type molecule approaches two nested R-type molecules. The three interact to form a nested trimer with all molecules R-type. Three inversion events occur during the movie, which was taken over 80 min. This inversion rate agrees well with the expected rate of 0.2 mHz at 78 K, given the calculated inversion barrier for butyl methyl sulfide on Au of 0.24 eV.<sup>82</sup> Image Conditions: 2 nm  $\times$  5 nm, 250 pA, -1 V.

### **Movie A7 Enantiospecific Assembly of Butyl Methyl Sulfide Tetramer**

Focusing on the four left-most molecules, three nested R-type molecules are next to an S-type molecule. The S molecule approaches the trimer and the four form a nested tetramer where all molecules are R-type. Several inversion events occur during the movie, as expected given the calculated rate of inversion at this temperature. Image Conditions: 2 nm  $\times$  7 nm, 250 pA, -1 V.

### **Movie A8 Butyl Methyl Sulfide Cluster to Chain Rearrangement**

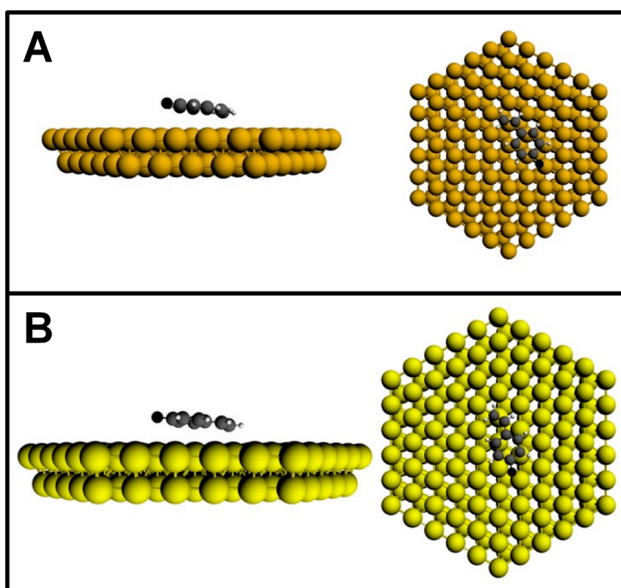
Five butyl methyl sulfide molecules rearrange into a beautifully nested pentamer. There is no cartoon schematic associated with this video. Image Conditions:  $\sim 7$  nm  $\times$  6 nm, 500 pA, -400 mV.



**Appendix Figure 1 Twelve Degenerate Domains of Butyl Methyl Sulfide on Au:** STM images and schematics showing the twelve molecular packing structures for butyl methyl sulfide on Au(111). Six of the orientations arise for each of the molecule's two enantiomers due to the three-fold symmetry of the (111) surface lattice. All twelve structures are related by either rotational or mirror symmetry. S/R labels refer to the different rotational domains for the packing structure of the two enantiomers. All image dimensions are approximately  $4 \text{ nm} \times 4 \text{ nm}$ . Imaging Conditions: 78 K, 10-500 pA,  $\pm(10-600) \text{ mV}$ .

### 12.3 Appendix to Chapter 9

Here we illustrate the optimized geometries of the 4-FS molecules on the clusters employed to model the Cu(111) and Au(111) surfaces, the ten most stable trimer and tetramer 4-FS aggregates obtained from our RandomDock calculations, trimer geometries obtained without dispersion corrections, and provide structural coordinates and energies of these as obtained in our DFT-D3 calculations.

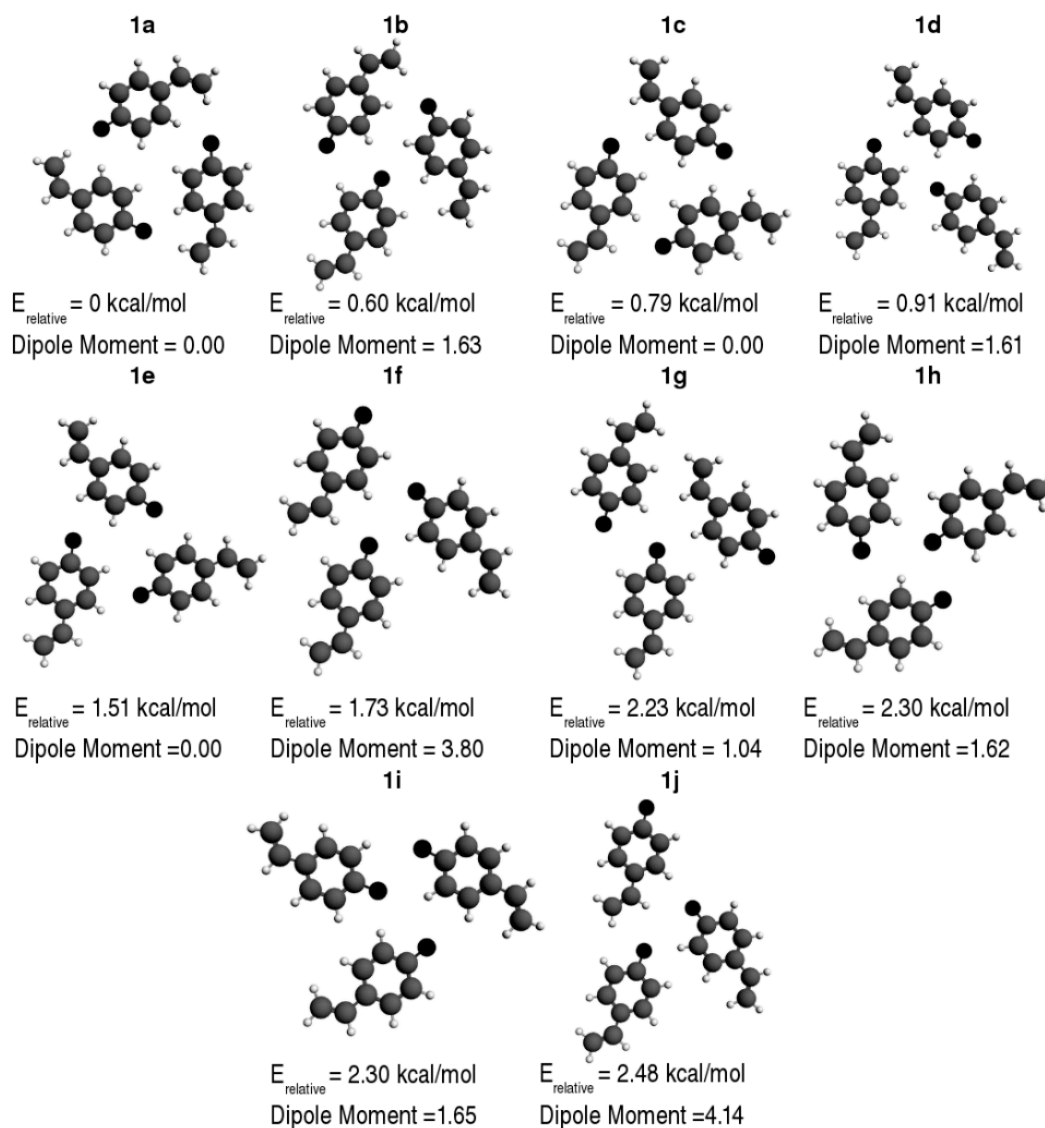


**Appendix Figure 2 DFT Optimized Geometries for 4-Fluorostyrene on Cu(111) and Au(111):** 4-FS on (A) Cu and (B) Au.

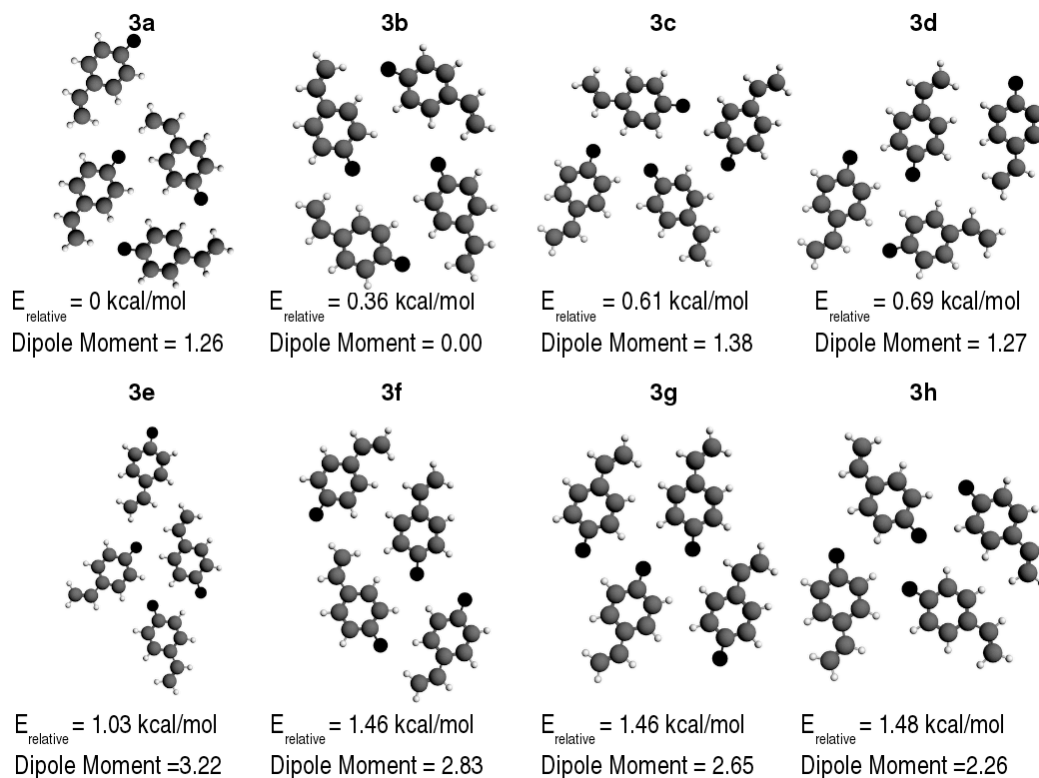
**Table A.1 Distance Calculations for 4-Fluorostyrene on Cu and Au**

System	$D_C$ (Å)	$D_{\text{Benzene}}$ (Å)	$D_F$ (Å)
Cu	2.53	2.78	3.18
Au	2.75	2.98	3.35

Surface to adsorbate distances in Angstrom.  $D_C$  is the distance of the carbon on the vinyl substituent that is closest to the metal surface.  $D_{\text{Benzene}}$  is the distance of the carbon in the central benzene ring that is closest to the metal surface.  $D_F$  is the distance of the fluorine atom to the metal surface.

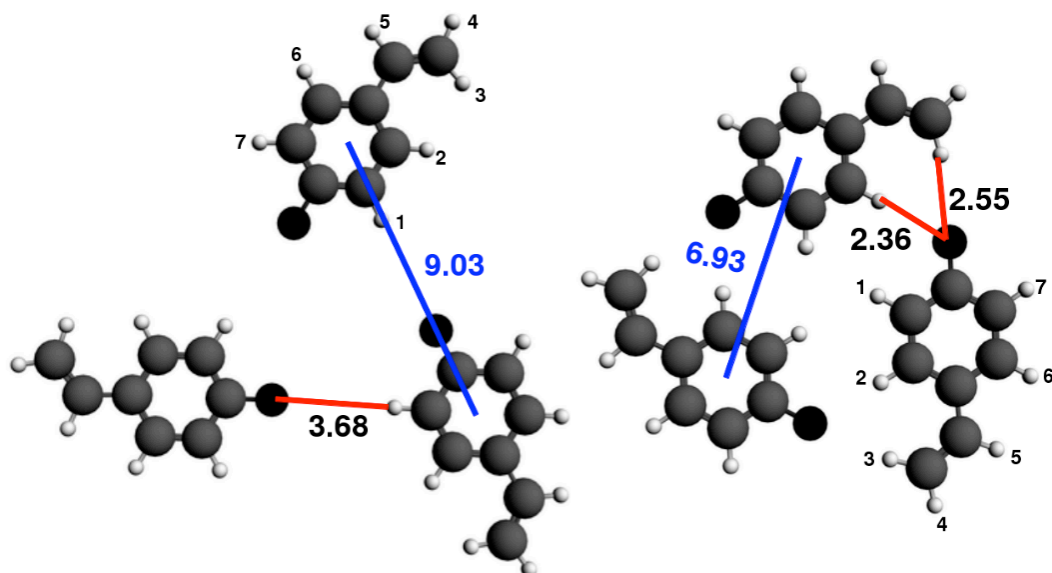


**Appendix Figure 3 Relaxed Structures for 4-Fluorostyrene Trimers:** The ten structures lowest in energy for trimers of 4-FS as obtained from our RandomDock calculations and their dipole moments in Debye. The energies are given relative to the most stable configuration, 1a, which is chiral, with  $C_{3h}$  symmetry, and has a net dipole moment of 0 D.



**Appendix Figure 4 Relaxed Structures for 4-Fluorostyrene Tetramers:** The seven structures lowest in energy for tetramers of 4-FS as obtained from our RandomDock calculations and their dipole moments in Debye. The energies are given relative to the most stable configuration, 3a, which is similar to the most stable trimer, but with an excess 4-FS outside the chiral ring. Structure 3b was not obtained from the RandomDock simulations, but constructed by hand.





**Appendix Figure 5 DFT Geometries for Neutral 4-Fluorostyrene Trimers with and without Dispersion Corrections:** Optimized geometries of the neutral 4-FS trimer obtained (left) at the revPBE/TZP level of theory, and (right) with dispersion corrections (DFT-D3). The center-to-center distances, and the nearest neighbor H-F distances are provided. The Hirschfeld charges on the hydrogen atoms of a single 4-FS molecule were calculated as being: 0.054, 0.049, 0.040, 0.041, 0.042, 0.048 and 0.054 for H1-H7, respectively. In the left panel the nearest neighbor H-F contact is with the hydrogen which has the most positive charge. Comparison of the left and right panels illustrates that dispersion interactions are important in decreasing the center-to-center and H-F distance between molecules.

## 12.4 Appendix to Chapter 11

Several STM movies which show the dynamics of hydrogen and deuterium on Cu(111) are provided. Descriptions of the movies and detailed scanning conditions are provided below. Each frame took  $\sim 2$  minutes to acquire, and all movies were recorded at 5 K. Movies can be viewed on the Sykes Lab website (<http://ase.tufts.edu/chemistry/sykes/index.html>) under the Links tab.

### **Movie A9 Hydrogen Diffusion on Cu(111)**

STM movie recorded over  $\sim 1$  hour in which the diffusion of H atoms on Cu is seen. H forms small clusters that appear as depressions and congregate into islands. The H clusters within the island rearrange often, and clusters on the island perimeters diffuse rapidly. Image Conditions:  $40\text{ nm} \times 40\text{ nm}$ , 30 mV, 50 pA.

### **Movie A10 Deuterium Diffusion on Cu(111)**

STM movie recorded over  $\sim 1$  hour in which the diffusion of D atoms on Cu is seen. D forms small clusters that appear as depressions. The D clusters diffuse very slowly relative to H diffusion seen in Movie A8. Image Conditions:  $40\text{ nm} \times 40\text{ nm}$ , 30 mV, 90 pA.

### **Movie A11 Hydrogen Self-Assembly on Cu(111)**

STM movie recorded over  $\sim 1$  hour in which the self-assembly of H atoms on Cu is seen. H forms small clusters that appear as depressions and congregate into islands. As isolated H atoms approach one another they form clusters and islands. The small islands are shown to disappear as the H atoms on their perimeters migrate to larger islands, which as a result get larger. Image Conditions:  $40\text{ nm} \times 35\text{ nm}$ , 30 mV, 50 pA.

### 13 Bibliography

- (1) Binnig, G.; Rohrer, H.; Gerber, C.; Weibel, E. Tunneling Through a Controllable Vacuum Gap. *Applied Physics Letters* **1982**, *40*, 178–180.
- (2) Love, J. C.; Estroff, L. A.; Kriebel, J. K.; Nuzzo, R. G.; Whitesides, G. M. Self-Assembled Monolayers of Thiolates on Metals As a Form of Nanotechnology. *Chemical Reviews* **2005**, *105*, 1103–1169.
- (3) Smith, R. K.; Lewis, P. A.; Weiss, P. S. Patterning Self-Assembled Monolayers. *Progress in Surface Science* **2004**, *75*, 1–68.
- (4) Eciya, D.; Seufert, K.; Heim, D.; Auwarter, W.; Aurisicchio, C.; Fabbro, C.; Bonifazi, D.; Barth, J. V. Hierarchic Self-Assembly of Nanoporous Chiral Networks with Conformationally Flexible Porphyrins. *ACS Nano* **2010**, *4*, 4936–4942.
- (5) Lavrich, D. J.; Wetterer, S. M.; Bernasek, S. L.; Scoles, G. Physisorption and Chemisorption of Alkanethiols and Alkyl Sulfides on Au(111). *Journal of Physical Chemistry B* **1998**, *102*, 3456–3465.
- (6) Driver, S. M.; Zhang, T. F.; King, D. A. Massively Cooperative Adsorbate-Induced Surface Restructuring and Nanocluster Formation. *Angewandte Chemie International Edition* **2007**, *46*, 700–703.
- (7) Bohringer, M.; Morgenstern, K.; Schneider, W. D.; Berndt, R.; Mauri, F.; De Vita, A.; Car, R. Two-Dimensional Self-Assembly of Supramolecular Clusters and Chains. *Physical Review Letters* **1999**, *83*, 324–327.
- (8) Rojas, G.; Chen, X.; Bravo, C.; Kim, J.-H.; Kim, J.-S.; Xiao, J.; Dowben, P. a.; Gao, Y.; Zeng, X. C.; Choe, W.; Enders, A. Self-Assembly and Properties of Nonmetalated Tetraphenyl-Porphyrin on Metal Substrates. *Journal of Physical Chemistry C* **2010**, *114*, 9408–9415.
- (9) Cimatu, K.; Moore, H. J.; Barriet, D.; Chinwangso, P.; Lee, T. R.; Baldelli, S. Sum Frequency Generation Imaging Microscopy of Patterned Self-Assembled Monolayers with Terminal –CH<sub>3</sub>, –OCH<sub>3</sub>, –CF<sub>2</sub>CF<sub>3</sub>, –C≡C, –Phenyl, and –Cyclopropyl Groups. *Journal of Physical Chemistry C* **2008**, *112*, 14529–14537.
- (10) Voigt, N. V.; Tørring, T.; Rotaru, A.; Jacobsen, M. F.; Ravnsbaek, J. B.; Subramani, R.; Mamdouh, W.; Kjems, J.; Mokhir, A.; Besenbacher, F.;

- Gothelf, K. V. Single-Molecule Chemical Reactions on DNA Origami. *Nature Nanotechnology* **2010**, *5*, 200–203.
- (11) Clayden, J.; Greeves, N.; Warren, S.; Wothers, P. *Organic Chemistry*; Oxford University Press: Oxford, 2001.
  - (12) Gispert, J. R. *Coordination Chemistry*; Wiley-VCH: Weinheim, 2008.
  - (13) Dameron, A. A.; Hampton, J. R.; Smith, R. K.; Mullen, T. J.; Gillmor, S. D.; Weiss, P. S. Microdisplacement Printing. *Nano Letters* **2005**, *5*, 1834–1837.
  - (14) Donhauser, Z. J.; Mantoosh, B. A.; Kelly, K. F.; Bumm, L. A.; Monnell, J. D.; Stapleton, J. J.; Price, D. W.; Rawlett, A. M.; Allara, D. L.; Tour, J. M.; Weiss, P. S. Conductance Switching in Single Molecules Through Conformational Changes. *Science* **2001**, *292*, 2303–2307.
  - (15) Flink, S.; van Veggel, F. C. J. M.; Reinhoudt, D. N. Sensor Functionalities in Self-Assembled Monolayers. *Advanced Materials* **2000**, *12*, 1315–1328.
  - (16) Hatzor, A.; Weiss, P. S. Molecular Rulers for Scaling Down Nanostructures. *Science* **2001**, *291*, 1019–1020.
  - (17) Patton, S. T.; Voevodin, A. A.; Vaia, R. A.; Pender, M.; Dianianti, S. J.; Phillips, B. Nanoparticle Liquids for Surface Modification and Lubrication of MEMS Switch Contacts. *Journal of Microelectromechanical Systems* **2008**, *17*, 741–746.
  - (18) Stuart, D. A.; Yuen, J. M.; Lyandres, N. S. O.; Yonzon, C. R.; Glucksberg, M. R.; Walsh, J. T.; Van Duyne, R. P. *in vivo* Glucose Measurement by Surface-Enhanced Raman Spectroscopy. *Analytical Chemistry* **2006**, *78*, 7211–7215.
  - (19) Zhang, Q.; Archer, L. A. Interfacial Friction of Surfaces Grafted with One-And Two-Component Self-Assembled Monolayers. *Langmuir* **2005**, *21*, 5405–5413.
  - (20) Jian, H.; Tour, J. M. en route to Surface-Bound Electric Field-Driven Molecular Motors. *Journal of Organic Chemistry* **2003**, *68*, 5091–5103.
  - (21) Xia, Y. N.; Whitesides, G. M. Soft Lithography. *Angewandte Chemie International Edition* **1998**, *37*, 550–575.
  - (22) Rao, B. V.; Kwon, K. Y.; Zhang, J.; Liu, A. W.; Bartels, L. Low-Temperature Mobility and Structure Formation of a Prochiral Aromatic thiol (2,5-dichlorothiophenol) on Cu(111). *Langmuir* **2004**, *20*, 4406–4412.

- (23) Ron, H.; Cohen, H.; Matlis, S.; Rappaport, M.; Rubinstein, I. Self-Assembled Monolayers on Oxidized Metals. 4. Superior n -Alkanethiol Monolayers on Copper. *Journal of Physical Chemistry B* **1998**, *102*, 9861–9869.
- (24) Laibinis, P. E.; Whitesides, G. M.; Allara, D. L.; Tao, Y. T.; Parikh, A. N.; Nuzzo, R. G. Comparison of the Structures and Wetting Properties of Self-Assembled Monolayers of n-Alkanethiols on the Coinage Metal Surfaces, Copper, Silver, and Gold. *Journal of the American Chemical Society* **1991**, *113*, 7152–7167.
- (25) Schreiber, F. Structure and Growth of Self-Assembling Monolayers. *Progress in Surface Science* **2000**, *65*, 151–257.
- (26) Rieley, H.; Kendall, G. K. X-ray Studies of Self-Assembled Monolayers on Coinage Metals. 3. Angularly Resolved Near Edge X-ray Absorption Fine Structure Determination of the Orientation in 1-Octanethiol SAMs on Ag(111) and Cu(111). *Langmuir* **1999**, *15*, 8867–8875.
- (27) Rieley, H.; Kendall, G. K.; Jones, R. G.; Woodruff, D. P. X-ray Studies of Self-Assembled Monolayers on Coinage Metals. 2. Surface Adsorption Structures in 1-Octanethiol on Cu(111) and Ag(111) and Their Determination by the Normal Incidence X-ray Standing Wave Technique. *Langmuir* **1999**, *15*, 8856–8866.
- (28) Bucher, J.-P.; Santesson, L.; Kern, K. Thermal Healing of Self-Assembled Organic Monolayers: Hexane- and Octadecanethiol on Au(111) and Ag(111). *Langmuir* **1994**, *10*, 979–983.
- (29) Li, Z.; Chang, S.-C.; Williams, R. S. Self-Assembly of Alkanethiol Molecules onto Platinum and Platinum Oxide Surfaces. *Langmuir* **2003**, *19*, 6744–6749.
- (30) Love, J. C.; Wolfe, D. B.; Haasch, R.; Chabinyc, M. L.; Paul, K. E.; Whitesides, G. M.; Nuzzo, R. G. Formation and Structure of Self-Assembled Monolayers of Alkanethiolates on Palladium. *Journal of the American Chemical Society* **2003**, *125*, 2597–2609.
- (31) Jensen, S. C.; Baber, A. E.; Tierney, H. L.; Sykes, E. C. H. Adsorption, Interaction, and Manipulation of Dibutyl Sulfide on Cu{111}. *ACS Nano* **2007**, *1*, 22–29.
- (32) Jensen, S. C.; Baber, A. E.; Tierney, H. L.; Sykes, E. C. Dimethyl Sulfide on Cu{111}: Molecular Self-Assembly and Submolecular Resolution Imaging. *ACS Nano* **2007**, *1*, 423–428.

- (33) Troughton, E. B.; Bain, C. D.; Whitesides, G. M.; Nuzzo, R. G.; Allara, D. L.; Porter, M. D. Monolayer Films Prepared by the Spontaneous Self-Assembly of Symmetrical and Unsymmetrical Dialkyl Sulfides from Solution onto Gold Substrates - Structure, Properties, and Reactivity of Constituent Functional-Groups. *Langmuir* **1988**, *4*, 365–385.
- (34) Beulen, M. W. J.; Huisman, B.-H.; van der Heijden, P. A.; van Veggel, F. C. J. M.; Simons, M. G.; Biemond, E. M. E. F.; de Lange, P. J.; Reinhoudt, D. N. Evidence for Nondestructive Adsorption of Dialkyl Sulfides on Gold. *Langmuir* **1996**, *12*, 6170–6172.
- (35) Noh, J.; Murase, T.; Nakajima, K.; Lee, H.; Hara, M. Nanoscopic Investigation of the Self-Assembly Processes of Dialkyl Disulfides and Dialkyl Sulfides on Au(111). *Journal of Physical Chemistry B* **2000**, *104*, 7411–7416.
- (36) Noh, J.; Nakamura, F.; Kim, J.; Lee, H.; Hara, M. Structural Study of Dialkyl Sulfide Self-Assembled Monolayers on Au(111). *Molecular Crystals and Liquid Crystals* **2002**, *377*, 165–168.
- (37) Liu, W.; Howarth, M.; Greytak, A. B.; Zheng, Y.; Nocera, D. G.; Ting, A. Y.; Bawendi, M. G. Compact Biocompatible Quantum Dots Functionalized for Cellular Imaging. *Journal of the American Chemical Society* **2008**, *130*, 1274–1284.
- (38) Norsten, T. B.; Frankamp, B. L.; Rotello, V. M. Metal Directed Assembly of Terpyridine-Functionalized Gold Nanoparticles. *Nano Letters* **2002**, *2*, 1345–1348.
- (39) Pierrat, S.; Zins, I.; Breivogel, A.; Sonnichsen, C. Self-assembly of Small Gold Colloids with Functionalized Gold Nanorods. *Nano Letters* **2007**, *7*, 259–263.
- (40) Li, F. S.; Zhou, W. C.; Guo, Q. M. Uncovering the Hidden Gold Atoms in a Self-Assembled Monolayer of Alkanethiol Molecules on Au(111). *Physical Review B* **2009**, *79*, 113412.
- (41) Maksymovych, P.; Sorescu, D. C.; Yates, J. T. Gold-Adatom-Mediated Bonding in Self-Assembled Short-Chain Alkanethiolate Species on the Au(111) Surface. *Physical Review Letters* **2006**, *97*, 146103.
- (42) Singh, A.; Dahanayaka, D. H.; Biswas, A.; Bumm, L. a; Halterman, R. L. Molecularly Ordered Decanethiolate Self-Assembled Monolayers on Au(111) from *in situ* Cleaved Decanethioacetate: An NMR and STM Study of the Efficacy of Reagents for Thioacetate Cleavage. *Langmuir* **2010**, *26*, 13221–6.

- (43) Barth, J. V. V.; Brune, H.; Ertl, G.; Behm, R. J. Scanning Tunneling Microscopy Observations on the Reconstructed Au(111) Surface: Atomic Structure, Long-Range Substructure, Rotational Domains, and Surface Defects. *Physical Review B* **1990**, *42*, 9307–9318.
- (44) Min, B. K.; Alemozafar, A. R.; Biener, M. M.; Biener, J.; Friend, C. M. Reaction of Au(111) with Sulfur and Oxygen: Scanning Tunneling Microscopic Study. *Topics in Catalysis* **2005**, *36*, 77–90.
- (45) Schaff, O.; Schmid, A. K.; Bartelt, N. C.; de la Figuera, J.; Hwang, R. Q. In-situ STM Studies of Strain-Stabilized Thin-Film Dislocation Networks Under Applied Stress. *Materials Science and Engineering A* **2001**, *319*, 914–918.
- (46) Woll, C.; Chiang, S.; Wilson, R. J.; Lippel, P. H. Determination of Atom Positions at Stacking-Fault Dislocations on Au(111) by Scanning Tunneling Microscopy. *Physical Review B* **1989**, *39*, 7988–7991.
- (47) Voigtlander, B.; Meyer, G.; Amer, N. M. Epitaxial-growth of Thin Magnetic Cobalt Films on Au(111) Studied by Scanning Tunneling Microscopy. *Physical Review B* **1991**, *44*, 10354–10357.
- (48) Huang, K.; Gibbs, D.; Zehner, D.; Sandy, A.; Mochrie, S. Phase Behavior of the Au(111) Surface: Discommensurations and Kinks. *Physical Review Letters* **1990**, *65*, 3313–3316.
- (49) Cho, J.; Levy, N.; Kirakosian, A.; Comstock, M. J.; Lauterwasser, F.; Fréchet, J. M. J.; Crommie, M. F. Surface Anchoring and Dynamics of Thiolated Azobenzene Molecules on Au(111). *Journal of Chemical Physics* **2009**, *131*, 034707.
- (50) Bach, C. E.; Giesen, M.; Ibach, H.; Einstein, T. L. Stress Relief in Reconstruction. *Physical Review Letters* **1997**, *78*, 4225–4228.
- (51) Stroscio, J. A.; Eigler, D. M. Atomic and Molecular Manipulation with the Scanning Tunneling Microscope. *Science* **1991**, *254*, 1319–1326.
- (52) Chambliss, D. D.; Wilson, R. J.; Chiang, S. Ordered Nucleation of Ni and Au Islands on Au(111) Studied by Scanning Tunneling Microscopy. *Journal of Vacuum Science & Technology B* **1991**, *9*, 933–937.
- (53) Yin, F.; Palmer, R.; Guo, Q. Nanoscale Surface Recrystallization Driven by Localized Electric Field. *Physical Review B* **2006**, *73*, 073405.

- (54) Tartaglino, U.; Tosatti, E.; Passerone, D.; Ercolessi, F. Bending Strain-Driven Modification of Surface Reconstructions: Au(111). *Physical Review B* **2002**, *65*, 241406.
- (55) Kowalczyk, P. High Temperature STM/STS Investigations of Resonant Image States on Au(111). *Applied Surface Science* **2007**, *253*, 4036–4040.
- (56) Li, F.; Tang, L.; Zhou, W.; Guo, Q. Adsorption Site Determination for Au-Octanethiolate on Au(111). *Langmuir* **2010**, *26*, 9484–9490.
- (57) Maksymovych, P.; Dougherty, D. B. Molecular Self-Assembly Guided by Surface Reconstruction: CH<sub>3</sub>SH Monolayer on the Au(111) Surface. *Surface Science* **2008**, *602*, 2017–2024.
- (58) Maksymovych, P.; Sorescu, D. C.; Dougherty, D.; Yates, J. T. Surface Bonding and Dynamical Behavior of the CH<sub>3</sub>SH Molecule on Au(111). *Journal of Physical Chemistry B* **2005**, *109*, 22463–22468.
- (59) Nenchev, G.; Diaconescu, B.; Hagelberg, F.; Pohl, K. Self-Assembly of Methanethiol on the Reconstructed Au(111) Surface. *Physical Review B* **2009**, *80*, 81401.
- (60) Voznyy, O.; Dubowski, J. J.; Yates, J. T.; Maksymovych, P. The Role of Gold Adatoms and Stereochemistry in Self-Assembly of Methylthiolate on Au(111). *Journal of the American Chemical Society* **2009**, *131*, 12989–12993.
- (61) Baker, T. A.; Kaxiras, E.; Friend, C. M. Insights from Theory on the Relationship Between Surface Reactivity and Gold Atom Release. *Topics in Catalysis* **2010**, *53*, 365–377.
- (62) Biener, M. M.; Biener, J.; Friend, C. M. Sulfur-Induced Mobilization of Au Surface Atoms on Au(111) Studied by Real-Time STM. *Surface Science* **2007**, *601*, 1659–1667.
- (63) Biener, M. M.; Biener, J.; Friend, C. M. Revisiting the S-Au(111) Interaction: Static or Dynamic? *Langmuir* **2005**, *21*, 1668–1671.
- (64) Zhang, X.; Yin, F.; Palmer, R. E.; Guo, Q. The C<sub>60</sub>/Au(111) Interface at Room Temperature: A Scanning Tunnelling Microscopy Study. *Surface Science* **2008**, *602*, 885–892.
- (65) Baber, A. E.; Jensen, S. C.; Iski, E. V.; Sykes, E. C. H. Extraordinary Atomic Mobility of Au{111} at 80 Kelvin: Effect of Styrene Adsorption. *Journal of the American Chemical Society* **2006**, *128*, 15384–15385.



- (66) Baber, A. E.; Jensen, S. C.; Sykes, E. C. H. Dipole-Driven Ferroelectric Assembly of Styrene on Au{111}. *Journal of the American Chemical Society* **2007**, *129*, 6368–6369.
- (67) Syomin, D.; Kim, J.; Koel, B. E.; Ellison, G. B. Identification of Adsorbed Phenyl (C<sub>6</sub>H<sub>5</sub>) Groups on Metal Surfaces: Electron-Induced Dissociation of Benzene on Au(111). *Journal of Physical Chemistry B* **2001**, *105*, 8387–8394.
- (68) Han, P.; Mantooth, B. A.; Sykes, E. C. H.; Donhauser, Z. J.; Weiss, P. S. Benzene on Au[111] at 4 K: Monolayer Growth and Tip-Induced Molecular Cascades. *Journal of the American Chemical Society* **2004**, *126*, 10787–10793.
- (69) Gong, J.; Flaherty, D. W.; Ojifinni, R. A.; White, J. M.; Mullins, C. B. Surface Chemistry of Methanol on Clean and Atomic Oxygen Pre-Covered Au(111). *Journal of Physical Chemistry C* **2008**, *112*, 5501–5509.
- (70) Baber, A. E.; Lawton, T. J.; Sykes, E. C. H. Hydrogen-Bonded Networks in Surface-Bound Methanol. *Journal of Physical Chemistry C* **2011**, *115*, 9157–9163.
- (71) Rossel, F.; Brodard, P.; Patthey, F.; Richardson, N. V.; Schneider, W. D. Modified Herringbone Reconstruction on Au(111) Induced by Self-Assembled Azure A Islands. *Surface Science* **2008**, *602*, L115–L117.
- (72) Iski, E. V.; Jewell, A. D.; Tierney, H. L.; Kyriakou, G.; Sykes, E. C. H. Organic Thin Film Induced Substrate Restructuring: An STM Study of the Interaction of naphtho[2,3-a]pyrene with Au(111). *Journal of Vacuum Science & Technology A* **2011**, *29*, 40601.
- (73) Iski, E. V.; Jewell, A. D.; Tierney, H. L.; Kyriakou, G.; Sykes, E. C. H. Controllable Restructuring of a Metal Substrate: Tuning the Surface Morphology of Gold. *Surface Science* **2012**, *606*, 536–541.
- (74) Yu, M.; Bovet, N.; Satterley, C. J.; Bengio, S.; Lovelock, K. R. J.; Milligan, P. K.; Jones, R. G.; Woodruff, D. P.; Dhanak, V. True Nature of an Archetypal Self-Assembly System: Mobile Au-Thiolate Species on Au(111). *Physical Review Letters* **2006**, *97*, 166102.
- (75) Gronbeck, H. Thiolate Induced Reconstruction of Au(111) and Cu(111) Investigated by Density Functional Theory Calculations. *Journal of Physical Chemistry C* **2010**, *ASAP*, DOI 10.1021/jp100278.
- (76) Nagoya, A.; Morikawa, Y. Adsorption States of Methylthiolate on the Au(111) Surface. *Journal of Physics-Condensed Matter* **2007**, *19*, 365245.

- (77) Mazzarello, R.; Cossaro, A.; Verdini, A.; Rousseau, R.; Casalis, L.; Danisman, M. F.; Floreano, L.; Scandolo, S.; Morgante, A.; Scoles, G. Structure of a CH<sub>3</sub>S Monolayer on Au(111) Solved by the Interplay Between Molecular Dynamics Calculations and Diffraction Measurements. *Physical Review Letters* **2007**, *98*, 16102.
- (78) Kautz, N. A.; Kandel, S. A. Alkanethiol/Au(111) Self-Assembled Monolayers Contain Gold Adatoms: Scanning Tunneling Microscopy Before and After Reaction with Atomic Hydrogen. *Journal of the American Chemical Society* **2008**, *130*, 6908–6909.
- (79) Kautz, N. A.; Kandel, S. A. Alkanethiol Monolayers Contain Gold Adatoms, and Adatom Coverage is Independent of Chain Length. *Journal of Physical Chemistry C* **2009**, *113*, 19286–19291.
- (80) Srinivasan, C.; Mullen, T. J.; Hohman, J. N.; Anderson, M. E.; Dameron, A. A.; Andrews, A. M.; Dickey, E. C.; Horn, M. W.; Weiss, P. S. Scanning Electron Microscopy of Nanoscale Chemical Patterns. *ACS Nano* **2007**, *1*, 191–201.
- (81) Baber, A. E.; Tierney, H. L.; Sykes, E. C. H. A Quantitative Single-Molecule Study of Thioether Molecular Rotors. *ACS Nano* **2008**, *2*, 2385–2391.
- (82) Tierney, H. L.; Han, J. W.; Jewell, A. D.; Baber, A. E.; Iski, E. V.; Sholl, D. S.; Sykes, E. C. H. Chirality and Rotation of Asymmetric Surface-Bound Thioethers. *Journal of Physical Chemistry C* **2011**, *115*, 897–901.
- (83) Tierney, H. L.; Baber, A. E.; Jewell, A. D.; Iski, E. V.; Boucher, M. B.; Sykes, E. C. H. Mode-Selective Electrical Excitation of a Molecular Rotor. *Chemistry - A European Journal* **2009**, *15*, 9678–9680.
- (84) Tierney, H. L.; Calderon, C. E.; Baber, A. E.; Sykes, E. C. H.; Wang, F. Understanding the Rotational Mechanism of a Single Molecule: STM and DFT Investigations of Dimethyl Sulfide Molecular Rotors on Au(111). *Journal of Physical Chemistry C* **2010**, *114*, 3152–3155.
- (85) Kyriakou, G.; Boucher, M. B.; Jewell, A. D.; Lewis, E. A.; Lawton, T. J.; Baber, A. E.; Tierney, H. L.; Flytzani-Stephanopoulos, M.; Sykes, E. C. H. Isolated Metal Atom Geometries as a Strategy for Selective Heterogeneous Hydrogenations. *Science* **2012**, *335*, 1209–1212.
- (86) Aaen, A. B.; Lægsgaard, E.; Ruban, A. V.; Stensgaard, I. Submonolayer Growth of Pd on Cu(111) Studied by Scanning Tunneling Microscopy. *Surface Science* **1998**, *408*, 43–56.

- (87) Bellisario, D. O.; Han, J. W.; Tierney, H. L.; Baber, A. E.; Sholl, D. S.; Sykes, E. C. H. Importance of Kinetics in Surface Alloying: A Comparison of the Diffusion Pathways of Pd and Ag Atoms on Cu(111). *Journal of Physical Chemistry C* **2009**, *113*, 12863–12869.
- (88) Tierney, H. L.; Baber, A. E.; Sykes, E. C. H. Atomic-Scale Imaging and Electronic Structure Determination of Catalytic Sites on Pd/Cu Near Surface Alloys. *Journal of Physical Chemistry C* **2009**, *113*, 7246–7250.
- (89) Tierney, H. L.; Baber, A. E.; Kitchin, J. R.; Sykes, E. C. H. Hydrogen Dissociation and Spillover on Individual Isolated Palladium Atoms. *Physical Review Letters* **2009**, *103*, 246102.
- (90) Baber, A. E.; Tierney, H. L.; Lawton, T. J.; Sykes, E. C. H. An Atomic-Scale View of Palladium Alloys and their Ability to Dissociate Molecular Hydrogen. *ChemCatChem* **2011**, *3*, 607–614.
- (91) Becker, T.; Hövel, H.; Tschudy, M.; Reihl, B. Applications with a New Low-Temperature UHV STM at 5 K. *Applied Physics A* **1998**, *66*, S27–S30.
- (92) Iski, E. V. Assembly, Chirality, and Polymorphism of Large Molecules on Metal Surfaces, Tufts University, 2011.
- (93) Cavallini, M.; Biscarini, F. Electrochemically Etched Nickel Tips for Spin Polarized Scanning Tunneling Microscopy. *Review of Scientific Instruments* **2000**, *71*, 4457–4460.
- (94) Baber, A. E. Nanoscale Studies of Molecules, Metals and Alloys, Tufts University, 2011.
- (95) EFM 3 <http://www.omicron.de/en/products/efm-3-/instrument-concept> (accessed Jul 23, 2012).
- (96) Tierney, H. L.; Murphy, C. J.; Jewell, A. D.; Baber, A. E.; Iski, E. V.; Khodaverdian, H. Y.; McGuire, A. F.; Klebanov, N.; Sykes, E. C. H. Experimental Demonstration of a Single-Molecule Electric Motor. *Nature Nanotechnology* **2011**, *6*, 625–629.
- (97) Somorjai, G. A. *Introduction to Surface Chemistry and Catalysis*; Wiley: New York City, 1994; p. 694.
- (98) Besenbacher, F.; Lægsgaard, E.; Stensgaard, I. Fast-Scanning STM Studies. *Materials Today* **2005**, *8*, 26–30.

- (99) Laegsgaard, E.; Österlund, L.; Thostrup, P.; Rasmussen, P. B.; Stensgaard, I.; Besenbacher, F. A High-Pressure Scanning Tunneling Microscope. *Review of Scientific Instruments* **2001**, *72*, 3537–3542.
- (100) Rost, M. J.; Crama, L.; Schakel, P.; van Tol, E.; van Velzen-Williams, G. B. E. M.; Overgaw, C. F.; ter Horst, H.; Dekker, H.; Okhuijsen, B.; Seynen, M.; Vijftigschild, A.; Han, P.; Katan, A. J.; Schoots, K.; Schumm, R.; van Loo, W.; Oosterkamp, T. H.; Frenken, J. W. M. Scanning probe Microscopes Go Video Rate and Beyond. *Review of Scientific Instruments* **2005**, *76*, 053710.
- (101) Winterlin, J.; Trost, J.; Renisch, S.; Schuster, R.; Zambelli, T.; Ertl, G. Real-Time STM Observations of Atomic Equilibrium Fluctuations in an Adsorbate System: O/Ru(0001). *Surface Science* **1997**, *394*, 159–169.
- (102) Gaudioso, J.; Ho, W. Steric Turnoff of Vibrationally Mediated Negative Differential Resistance in a Single Molecule. *Angewandte Chemie International Edition* **2001**, *40*, 4080–4082.
- (103) Gaudioso, J.; Lee, H. J.; Ho, W. Vibrational Analysis of Single Molecule Chemistry: Ethylene Dehydrogenation on Ni(110). *Journal of the American Chemical Society* **1999**, *121*, 8479–8485.
- (104) Gimzewski, J. K. Nanoscale Science of Single Molecules Using Local Probes. *Science* **1999**, *283*, 1683–1688.
- (105) Harikumar, K. R.; Polanyi, J. C.; Sloan, P. A.; Ayissi, S.; Hofer, W. A. Electronic Switching of Single Silicon Atoms by Molecular Field Effects. *Journal of the American Chemical Society* **2006**, *128*, 16791–16797.
- (106) Hata, K.; Sainoo, Y.; Shigekawa, H. Atomically Resolved Local Variation of the Barrier Height of the Flip-Flop Motion of Single Buckled Dimers of Si(100). *Physical Review Letters* **2001**, *86*, 3084–3087.
- (107) Krause, S.; Berbil-Bautista, L.; Herzog, G.; Bode, M.; Wiesendanger, R. Current-Induced Magnetization Switching with a Spin-Polarized Scanning Tunneling Microscope. *Science* **2007**, *317*, 1537–1540.
- (108) Lauhon, L. J.; Ho, W. Single Molecule Thermal Rotation and Diffusion: Acetylene on Cu(001). *Journal of Chemical Physics* **1999**, *111*, 5633.
- (109) Lozano, M. L.; Tringides, M. C. Surface Diffusion Measurements from STM Tunneling Current Fluctuations. *Europhysics Letters* **1995**, *30*, 537–542.

- (110) Moore, A. M.; Mantooth, B. A.; Donhauser, Z. J.; Yao, Y.; Tour, J. M.; Weiss, P. S. Real-Time Measurements of Conductance Switching and Motion of Single oligo(phenylene ethynylene) Molecules. *Journal of the American Chemical Society* **2007**, *129*, 10352–10353.
- (111) Parschau, M.; Passerone, D.; Rieder, K.-H.; Hug, H. J.; Ernst, K.-H. Switching the Chirality of Single Adsorbate Complexes. *Angewandte Chemie International Edition* **2009**, *48*, 4065–4068.
- (112) Ronci, F.; Colonna, S.; Thorpe, S. D.; Cricenti, A. Direct Observation of Sn Adatoms Dynamical Fluctuations at the Sn/Ge(111) Surface. *Physical Review Letters* **2005**, *95*, 156101.
- (113) Ronci, F.; Colonna, S.; Thorpe, S. D.; Cricenti, A.; Le Lay, G. Low Temperature Scanning Tunneling Microscopy and Scanning Tunneling Spectroscopy Study at the  $\alpha$ -Sn/Ge(111) Surface. *Japanese Journal of Applied Physics* **2006**, *45*, 2180–2183.
- (114) Saedi, A.; Poelsema, B.; Zandvliet, H. J. W. Hydrogen Adsorption Configurations on Ge(001) Probed with STM. *Physical Review B* **2009**, *79*, 153402.
- (115) Saedi, A.; van Houselt, A.; van Gastel, R.; Poelsema, B.; Zandvliet, H. J. W. Playing Pinball with Atoms. *Nano Letters* **2009**, *9*, 1733–1736.
- (116) Stipe, B. C.; Rezaei, M. A.; Ho, W. Inducing and Viewing the Rotational Motion of a Single Molecule. *Science* **1998**, *279*, 1907–1909.
- (117) Stipe, B. C.; Rezaei, M. A.; Ho, W. Single-Molecule Vibrational Spectroscopy and Microscopy. *Science* **1998**, *280*, 1732–1735.
- (118) Stipe, B. C.; Rezaei, M. A.; Ho, W. Coupling of Vibrational Excitation to the Rotational Motion of a Single Adsorbed Molecule. *Physical Review Letters* **1998**, *81*, 1263–1266.
- (119) Wang, K.; Zhang, C.; Loy, M.; Xiao, X. Time-Dependent Tunneling Spectroscopy for Studying Surface Diffusion Confined in Nanostructures. *Physical Review Letters* **2005**, *94*, 036103.
- (120) Mugarza, A.; Shimizu, T. K.; Frank Ogletree, D.; Salmeron, M. Chemical Reactions of Water Molecules on Ru(0001) Induced by Selective Excitation of Vibrational Modes. *Surface Science* **2009**, *603*, 2030–2036.
- (121) Schliwa, M.; Woehlke, G. Molecular Motors. *Nature* **2003**, *422*, 759–765.

- (122) Kottas, G. S.; Clarke, L. I.; Horinek, D.; Michl, J. Artificial Molecular Rotors. *Chemical Reviews* **2005**, *105*, 1281–1376.
- (123) Michl, J.; Sykes, E. C. H. Molecular Rotors and Motors: Recent Advances and Future Challenges. *ACS Nano* **2009**, *3*, 1042–1048.
- (124) Kay, E. R.; Leigh, D. A.; Zerbetto, F. Synthetic Molecular Motors and Mechanical Machines. *Angewandte Chemie International Edition* **2007**, *46*, 72–191.
- (125) Haidekker, M. A.; Brady, T.; Wen, K.; Okada, C.; Stevens, H. Y.; Snell, J. M.; Frangos, J. A.; Theodorakis, E. A. Phospholipid-Bound Molecular Rotors: Synthesis and Characterization. *Bioorganic & Medicinal Chemistry* **2002**, *10*, 3627–3636.
- (126) Haidekker, M. A.; Theodorakis, E. A. Molecular Rotors--Fluorescent Biosensors for Viscosity and Flow. *Organic & Biomolecular Chemistry* **2007**, *5*, 1669–1678.
- (127) Haidekker, M. A.; Brady, T. P.; Chalian, S. H.; Akers, W.; Lichlyter, D.; Theodorakis, E. A. Hydrophilic Molecular Rotor Derivatives-Synthesis and Characterization. *Bioorganic Chemistry* **2004**, *32*, 274–289.
- (128) Schoevaars, A. M.; Kruizinga, W.; Zijlstra, R. W. J.; Veldman, N.; Spek, A. L.; Feringa, B. L. Toward a Switchable Molecular Rotor. Unexpected Dynamic Behavior of Functionalized Overcrowded Alkenes. *Journal of Organic Chemistry* **1997**, *62*, 4943–4948.
- (129) Bellisario, D. O.; Baber, A. E.; Tierney, H. L.; Sykes, E. C. H. Engineering Dislocation Networks for the Directed Assembly of Two-Dimensional Rotor Arrays. *Journal of Physical Chemistry C* **2009**, *113*, 5895–5898.
- (130) Tierney, H. L.; Baber, A. E.; Sykes, E. C. H.; Akimov, A.; Kolomeisky, A. B. Dynamics of Thioether Molecular Rotors: Effects of Surface Interactions and Chain Flexibility. *Journal of Physical Chemistry C* **2009**, *113*, 10913–10920.
- (131) Rao, B. V.; Kwon, K. Y.; Liu, A. W.; Bartels, L. Measurement of a Linear Free Energy Relationship One Molecule at a Time. *Proceedings of the National Academy of Sciences of the United States of America* **2004**, *101*, 17920–17923.
- (132) Astumian, R. D. Thermodynamics and Kinetics of a Brownian Motor. *Science* **1997**, *276*, 917–922.

- (133) Bohringer, M.; Morgenstern, K.; Schneider, W. D.; Wuhn, M.; Woll, C.; Berndt, R. Self-assembly of 1-nitronaphthalene on Au(111). *Surface Science* **2000**, *444*, 199–210.
- (134) Sykes, E. C. H.; Mantooth, B. A.; Han, P.; Donhauser, Z. J.; Weiss, P. S. Substrate-Mediated Intermolecular Interactions: A Quantitative Single Molecule Analysis. *Journal of the American Chemical Society* **2005**, *127*, 7255–7260.
- (135) Grönbeck, H.; Curioni, A.; Andreoni, W. Thiols and Disulfides on the Au(111) Surface: The Headgroup–Gold Interaction. *Journal of the American Chemical Society* **2000**, *122*, 3839–3842.
- (136) Gawronski, H.; Mehlhorn, M.; Morgenstern, K. Imaging Phonon Excitation with Atomic Resolution. *Science* **2008**, *319*, 930–933.
- (137) Barth, J.; Brune, H.; Fischer, B.; Weckesser, J.; Kern, K. Dynamics of Surface Migration in the Weak Corrugation Regime. *Physical Review Letters* **2000**, *84*, 1732–1735.
- (138) Chung, C. H.; Jung, W. J.; Lyo, I. W. Trapping-Mediated Chemisorption of Ethylene on Si(001)-c(4 x 2). *Physical Review Letters* **2006**, *97*, 116102.
- (139) Wahl, M.; Stöhr, M.; Spillmann, H.; Jung, T. A.; Gade, L. H. Rotation-Libration in a Hierarchic Supramolecular Rotor-Stator System: Arrhenius Activation and Retardation by Local Interaction. *Chemical Communications* **2007**, 1349–1351.
- (140) Komeda, T.; Kim, Y.; Kawai, M.; Persson, B. N. J.; Ueba, H. Lateral Hopping of Molecules Induced by Excitation of Internal Vibration Mode. *Science* **2002**, *295*, 2055–2058.
- (141) Ohara, M.; Kim, Y.; Yanagisawa, S.; Morikawa, Y.; Kawai, M. Role of Molecular Orbitals Near the Fermi Level in the Excitation of Vibrational Modes of a Single Molecule at a Scanning Tunneling Microscope Junction. *Physical Review Letters* **2008**, *100*.
- (142) Pascual, J. I.; Lorente, N.; Song, Z.; Conrad, H.; Rust, H. P. Selectivity in Vibrationally Mediated Single-Molecule Chemistry. *Nature* **2003**, *423*, 525–528.
- (143) Sainoo, Y.; Kim, Y.; Okawa, T.; Komeda, T.; Shigekawa, H.; Kawai, M. Excitation of Molecular Vibrational Modes with Inelastic Scanning Tunneling Microscopy Processes: Examination through Action Spectra of cis-2-butene on Pd(110). *Physical Review Letters* **2005**, *95*.

- (144) Wintjes, N.; Bonifazi, D.; Cheng, F. Y.; Kiebele, A.; Stohr, M.; Jung, T.; Spillmann, H.; Diederich, F. A Supramolecular Multiposition Rotary Device. *Angewandte Chemie International Edition* **2007**, *46*, 4089–4092.
- (145) Simic-Milosevic, V.; Meyer, J.; Morgenstern, K. Chirality Change of Chloronitrobenzene on Au(111) Induced by Inelastic Electron Tunneling. *Angewandte Chemie International Edition* **2009**, *48*, 4061–4064.
- (146) Chiaravalloti, F.; Gross, L.; Rieder, K. H.; Stojkovic, S. M.; Gourdon, A.; Joachim, C.; Moresco, F. A Rack-and-Pinion Device at the Molecular Scale. *Nature Materials* **2007**, *6*, 30–33.
- (147) Vaughan, O. P. H.; Williams, F. J.; Bampos, N.; Lambert, R. M. A Chemically Switchable Molecular Pinwheel. *Angewandte Chemie International Edition* **2006**, *45*, 3779–3781.
- (148) Stöhr, M.; Wagner, T.; Gabriel, M.; Weyers, B.; Möller, R. Direct Observation of Hindered Eccentric Rotation of an Individual Molecule: Cu-Phthalocyanine On C{60}. *Physical Review B* **2001**, *65*, 33404.
- (149) Astumian, R. D.; Hanggi, P. Brownian Motors. *Physics Today* **2002**, *55*, 33–39.
- (150) Ohara, M.; Kim, Y.; Kawai, M. Electric Field Response of a Vibrationally Excited Molecule in an STM Junction. *Physical Review B* **2008**, *78*.
- (151) Komeda, T.; Kim, Y.; Fujita, Y.; Sainoo, Y.; Kawai, M. Local Chemical Reaction of Benzene on Cu(110) *via* STM-Induced Excitation. *Journal of Chemical Physics* **2004**, *120*, 5347–5352.
- (152) Vacek, J.; Michl, J. Artificial Surface-Mounted Molecular Rotors: Molecular Dynamics Simulations. *Advanced Functional Materials* **2007**, *17*, 730–739.
- (153) Zhong, D.; Wedeking, K.; Chi, L.; Erker, G.; Fuchs, H. Surface-Mounted Molecular Rotors with Variable Functional Groups and Rotation Radii. *Nano Letters* **2009**, *9*, 4387–4391.
- (154) Joachim, C.; Gimzewski, J. K. Single Molecular Rotor at the Nanoscale. In *Molecular Machines and Motors*; Springer-Verlag Berlin: Berlin, 2001; Vol. 99, pp. 1–18.
- (155) Gao, L.; Liu, Q.; Zhang, Y. Y.; Jiang, N.; Zhang, H. G.; Cheng, Z. H.; Qiu, W. F.; Du, S. X.; Liu, Y. Q.; Hofer, W. A.; Gao, H. J. Constructing an Array of Anchored Single-Molecule Rotors on Gold Surfaces. *Physical Review Letters* **2008**, *101*.



- (156) Gimzewski, J. K.; Joachim, C.; Schlittler, R. R.; Langlais, V.; Tang, H.; Johannsen, I. Rotation of a Single Molecule within a Supramolecular Bearing. *Science* **1998**, *281*, 531–533.
- (157) Kawai, M.; Komeda, T.; Kim, Y.; Sainoo, Y.; Katano, S. Single-Molecule Reactions and Spectroscopy via Vibrational Excitation. *Philosophical Transactions of the Royal Society of London Series A* **2004**, *362*, 1163–1171.
- (158) Lauhon, L. J.; Ho, W. Direct Observation of the Quantum Tunneling of Single Hydrogen Atoms with a Scanning Tunneling Microscope. *Physical Review Letters* **2000**, *85*, 4566–4569.
- (159) Sainoo, Y.; Kim, Y.; Komeda, T.; Kawai, M. Inelastic Tunneling Spectroscopy Using Scanning Tunneling Microscopy on trans-2-butene Molecule: Spectroscopy and Mapping of Vibrational Feature. *Journal of Chemical Physics* **2004**, *120*, 7249–7251.
- (160) Poirier, G. E.; Pylant, E. D. The Self-Assembly Mechanism of Alkanethiols on Au(111). *Science* **1996**, *272*, 1145–1148.
- (161) Noh, J.; Jeong, Y.; Ito, E.; Hara, M. Formation and Domain Structure of Self-Assembled Monolayers by Adsorption of Tetrahydrothiophene on Au(111). *Journal of Physical Chemistry C* **2007**, *111*, 2691–2695.
- (162) Zhong, C. J.; Porter, M. D. Evidence for Carbon Sulfur Bond-Cleavage in Spontaneously Adsorbed Organosulfide-Based Monolayers at Gold. *Journal of the American Chemical Society* **1994**, *116*, 11616–11617.
- (163) Zhong, C. J.; Brush, R. C.; Andereg, J.; Porter, M. D. Organosulfur Monolayers at Gold Surfaces: Reexamination of the Case for Sulfide Adsorption and Implications to the Formation of Monolayers from Thiols and Disulfides. *Langmuir* **1999**, *15*, 518–525.
- (164) Weidner, T.; Kramer, A.; Bruhn, C.; Zharnikov, M.; Shaporenko, A.; Siemeling, U.; Trager, F. Novel Tripod Ligands for Prickly Self-Assembled Monolayers. *Dalton Transactions* **2006**, 2767–2777.
- (165) Bain, C. D.; Biebuyck, H. A.; Whitesides, G. M. Comparison of Self-Assembled Monolayers on Gold - Coadsorption of Thiols and Disulfides. *Langmuir* **1989**, *5*, 723–727.
- (166) Rubinstein, I.; Steinberg, S.; Tor, Y.; Shanzer, A.; Sagiv, J. Ionic Recognition and Selective Response in Self-Assembling Monolayer Membranes on Electrodes. *Nature* **1988**, *332*, 426–429.

- (167) Padowitz, D. F.; Messmore, B. W. STM Observations of Exchange Dynamics at the Solid-Liquid Interface Using a Molecular Tracer. *Journal of Physical Chemistry B* **2000**, *104*, 9943–9946.
- (168) Padowitz, D. F.; Sada, D. M.; Kemer, E. L.; Dougan, M. L.; Xue, W. A. Molecular Tracer Dynamics in Crystalline Organic Films at the Solid-Liquid Interface. *Journal of Physical Chemistry B* **2002**, *106*, 593–598.
- (169) Schonherr, H.; Vancso, G. J. Lattice Structure of Self-Assembled Monolayers of Dialkyl Sulfides and calix[4]arene Sulfide Adsorbates on Au(111) Revealed by Atomic Force Microscopy. *Langmuir* **1999**, *15*, 5541–5546.
- (170) Jewell, A.; Tierney, H. L.; Baber, A. E.; Iski, E. V.; Laha, M. M.; Sykes, E. C. H. Time-Resolved Studies of Individual Molecular Rotors. *Journal of Physics: Condensed Matter* **2010**, *22*, 264006.
- (171) Bürgi, L.; Brune, H.; Kern, K.; Burgi, L. Imaging of Electron Potential Landscapes on Au(111). *Physical Review Letters* **2002**, *89*, 176801.
- (172) Rzeznicka, I. I.; Lee, J. S.; Maksymovych, P.; Yates, J. T.; Rzeznicka, I. I. Nondissociative Chemisorption of Short Chain Alkanethiols on Au(111). *Journal of Physical Chemistry B* **2005**, *109*, 15992–15996.
- (173) Pasteur, L. *Annales de Chimie et de Physique* **1848**, *24*, 442–459.
- (174) Haq, S.; Liu, N.; Humblot, V.; Jansen, A. P. J.; Raval, R. Drastic Symmetry Breaking in Supramolecular Organization of Enantiomerically Unbalanced Monolayers at Surfaces. *Nature Chemistry* **2009**, *1*, 409–414.
- (175) Lorenzo, M. O.; Baddeley, C. J.; Muryn, C.; Raval, R. Extended Surface Chirality from Supramolecular Assemblies of Adsorbed Chiral Molecules. *Nature* **2000**, *404*, 376–379.
- (176) Lorenzo, M. O.; Haq, S.; Bertrams, T.; Murray, P.; Raval, R.; Baddeley, C. J. Creating Chiral Surfaces for Enantioselective Heterogeneous Catalysis: R,R-tartaric Acid on Cu(110). *Journal of Physical Chemistry B* **1999**, *103*, 10661–10669.
- (177) Lorenzo, M.; Humblot, V.; Murray, P.; Raval, R.; Baddeley, C. J. Chemical Transformations, Molecular Transport, and Kinetic Barriers in Creating the Chiral Phase of (R, R)-Tartaric Acid on Cu(110). *Journal of Catalysis* **2002**, *205*, 123–134.
- (178) Barbosa, L. A. M. M.; Sautet, P. Stability of Chiral Domains Produced by Adsorption of Tartaric Acid Isomers on the Cu(110) Surface: A Periodic

Density Functional Theory Study. *Journal of the American Chemical Society* **2001**, *123*, 6639–6648.

- (179) Hermse, C. G. M.; van Bavel, A. P.; Jansen, A. P. J.; Barbosa, L. A. M. M.; Sautet, P.; van Santen, R. A. Formation of Chiral Domains for Tartaric Acid on Cu(110): A Combined DFT and Kinetic Monte Carlo Study. *Journal of Physical Chemistry B* **2004**, *108*, 11035–11043.
- (180) Fasel, R.; Wider, J.; Quitmann, C.; Ernst, K.-H.; Greber, T. Determination of the Absolute Chirality of Adsorbed Molecules. *Angewandte Chemie International Edition* **2004**, *43*, 2853–2856.
- (181) Parschau, M.; Romer, S.; Ernst, K.-H. Induction of Homochirality in Achiral Enantiomorphous Monolayers. *Journal of the American Chemical Society* **2004**, *126*, 15398–9.
- (182) Parschau, M.; Kampen, T.; Ernst, K.-H. Homochirality in Monolayers of Achiral Meso Tartaric Acid. *Chemical Physics Letters* **2005**, *407*, 433–437.
- (183) Kacprzak, K.; Gawronski, J. Cinchona Alkaloids and Their Derivatives: Versatile Catalysts and Ligands in Asymmetric Synthesis. *Synthesis-Stuttgart* **2001**, 961–998.
- (184) France, S.; Guerin, D. J.; Miller, S. J.; Lectka, T. Nucleophilic Chiral Amines as Catalysts in Asymmetric Synthesis. *Chemical Reviews* **2003**, *103*, 2985–3012.
- (185) Zaera, F. Chiral Modification of Solid Surfaces: A Molecular View. *Journal of Physical Chemistry C* **2008**, *112*, 16196–16203.
- (186) Fasel, R.; Parschau, M.; Ernst, K. H. Amplification of Chirality in Two-Dimensional Enantiomorphous Lattices. *Nature* **2006**, *439*, 449–452.
- (187) Fasel, R.; Parschau, M.; Ernst, K. H. Chirality Transfer from Single Molecules into Self-Assembled Monolayers. *Angewandte Chemie International Edition* **2003**, *42*, 5178–5181.
- (188) Ernst, K. H.; Kuster, Y.; Fasel, R.; McFadden, C. F.; Ellerbeck, U. Adsorption of Helical Aromatic Molecules: Heptahelicene on Ni(111). *Surface Science* **2003**, *530*, 195–202.
- (189) Stacchiola, D.; Burkholder, L.; Tysoe, W. T. Enantioselective Chemisorption on a Chirally Modified Surface in Ultrahigh Vacuum: Adsorption of Propylene Oxide on 2-Butoxide-Covered Palladium(111). *Journal of the American Chemical Society* **2002**, *124*, 8984–8989.

- (190) Lee, I.; Zaera, F. Enantioselectivity of Adsorption Sites Created by Chiral 2-butanol Adsorbed on Pt(111) single-crystal surfaces. *Journal of Physical Chemistry B* **2005**, *109*, 12920–6.
- (191) Gao, F.; Wang, Y. L.; Li, Z. J.; Furlong, O.; Tysoe, W. T. Enantioselective Reactions on a Au/Pd(111) Surface Alloy With Coadsorbed Chiral 2-Butanol And Propylene Oxide. *Journal of Physical Chemistry C* **2008**, *112*, 3362–3372.
- (192) Lee, I.; Zaera, F. Chiral templating of surfaces: Adsorption of (S)-2-Methylbutanoic Acid on Pt(111) Single-Crystal Surfaces. *Journal of the American Chemical Society* **2006**, *128*, 8890–8898.
- (193) Weidner, T.; Ballav, N.; Siemeling, U.; Troegel, D.; Walter, T.; Tacke, R.; Castner, D. G.; Zharnikov, M. Tripodal Binding Units for Self-Assembled Monolayers on Gold: A Comparison of Thiol and Thioether Headgroups. *Journal of Physical Chemistry C* **2009**, *113*, 19609–19617.
- (194) Santagata, N. M.; Lakhani, A. M.; Davis, B. F.; Luo, P. S.; Nardelli, M. B.; Pearl, T. P. Chiral Steering of Molecular Organization in the Limit of Weak Adsorbate-Substrate Interactions: Enantiopure and Racemic Tartaric Acid Domains on Ag(111). *Journal of Physical Chemistry C* **2010**, *114*, 8917–8925.
- (195) Lakhani, A. M.; DeWitt, D. J.; Sant'Agata, N. M.; Pearl, T. P. Persistence of chirality for a weakly bound adsorbate: (R,R)- and (S,S)-tartaric acid/Ag(111). *Journal of Physical Chemistry C* **2007**, *111*, 5750–5755.
- (196) Xiao, W. D.; Jiang, Y. H.; Aiet-Mansour, K.; Ruffieux, P.; Gao, H. J.; Fasel, R. Chiral Biphenyldicarboxylic Acid Networks Stabilized by Hydrogen Bonding. *Journal of Physical Chemistry C* **2010**, *114*, 6646–6649.
- (197) Bombis, C.; Weigelt, S.; Knudsen, M. M.; Norgaard, M.; Busse, C.; Laegsgaard, E.; Besenbacher, F.; Gothelf, K. V.; Linderth, T. R. Steering Organizational and Conformational Surface Chirality by Controlling Molecular Chemical Functionality. *ACS Nano* **2010**, *4*, 297–311.
- (198) Bartels, L. Tailoring Molecular Layers at Metal Surfaces. *Nature Chemistry* **2010**, *2*, 87–95.
- (199) Barth, J. V.; Weckesser, J.; Trimarchi, G.; Vladimirova, M.; De Vita, A.; Cai, C. Z.; Brune, H.; Gunter, P.; Kern, K. Stereochemical Effects in Supramolecular Self-Assembly at Surfaces: 1-D versus 2-D Enantiomorphic Ordering for PVBA and PEBA on Ag(111). *Journal of the American Chemical Society* **2002**, *124*, 7991–8000.

- (200) Bohringer, M.; Schneider, W. D.; Berndt, R. Real Space Observation of a Chiral Phase Transition in a Two-Dimensional Organic Layer. *Angewandte Chemie International Edition* **2000**, *39*, 792.
- (201) De Feyter, S.; Gesquiere, A.; Wurst, K.; Amabilino, D. B.; Veciana, J.; De Schryver, F. C. Homo- and Heterochiral Supramolecular Tapes from Achiral, Enantiopure, and Racemic Promesogenic Formamides: Expression of Molecular Chirality in Two and Three Dimensions. *Angewandte Chemie International Edition* **2001**, *40*, 3217.
- (202) Cortes, R.; Mascaraque, A.; Schmidt-Weber, P.; Dil, H.; Kampen, T. U.; Horn, K. Coexistence of Racemic and Homochiral Two-Dimensional Lattices Formed by a Prochiral Molecule: Dicarboxystilbene, on Cu(110). *Nano Letters* **2008**, *8*, 4162–4167.
- (203) Chen, Q.; Richardson, N. V. Enantiomeric Interactions between Nucleic Acid Bases and Amino Acids on Solid Surfaces. *Nature Materials* **2003**, *2*, 324–328.
- (204) Forster, M.; Dyer, M. S.; Persson, M.; Raval, R. 2D Random Organization of Racemic Amino Acid Mono layers Driven by Nanoscale Adsorption Footprints: Pro line on Cu(110). *Angewandte Chemie International Edition* **2010**, *49*, 2344–2348.
- (205) Kuhnle, A.; Linderoth, T. R.; Hammer, B.; Besenbacher, F. Chiral Recognition in Dimerization of Adsorbed Cysteine Observed by Scanning Tunnelling Microscopy. *Nature* **2002**, *415*, 891–893.
- (206) Patole, S. N.; Baddeley, C. J.; Schuler, A.; O'Hagan, D.; Richardson, N. V. Driving Forces Underlying the Formation of Chiral Domains of Fluorinated Diacids on Graphite. *Langmuir* **2009**, *25*, 1412–1416.
- (207) Mark, A. G.; Forster, M.; Raval, R. Direct visualization of chirality in two dimensions. *Tetrahedron - Asymmetry* **2010**, *21*, 1125–1134.
- (208) Bellisario, D. O.; Jewell, A. D.; Tierney, H. L.; Baber, A. E.; Sykes, E. C. H. Adsorption, Assembly, and Dynamics of Dibutyl Sulfide on Au{111}. *Journal of Physical Chemistry C* **2010**, *114*, 14583–14589.
- (209) Noh, J.; Ito, E.; Nakajima, K.; Kim, J.; Lee, H.; Hara, M. High-Resolution STM And XPS Studies of Thiophene Self-Assembled Monolayers on Au(111). *Journal of Physical Chemistry B* **2002**, *106*, 7139–7141.
- (210) Bohringer, M.; Morgenstern, K.; Schneider, W. D.; Berndt, R. Reversed Surface Corrugation in STM Images on Au(111) by Field-Induced Lateral Motion of Adsorbed Molecules. *Surface Science* **2000**, *457*, 37–50.

- (211) Jewell, A. D.; Kryan, S. J.; Rabinovich, D.; Sykes, E. C. H. Effect of Head Group Chemistry on Surface-Mediated Molecular Self-Assembly. *Chemistry - A European Journal* in press.
- (212) Müller, U. *Inorganic Structural Chemistry*; John Wiley & Sons: West Sussex, 1993.
- (213) Tierney, H. L.; Jewell, A.; Baber, A.; Iski, E. V.; Sykes, E. C. H. Dynamics of Molecular Adsorption and Rotation on Nonequilibrium Sites. *Langmuir* **2010**, *26*, 15350–5.
- (214) Jewell, A.; Tierney, H.; Sykes, E. C. H. Gently Lifting Gold's Herringbone Reconstruction: Trimethylphosphine on Au(111). *Physical Review B* **2010**, *82*, 205401.
- (215) Taylor, R.; Torr, N.; Huang, Z.; Li, F. S.; Guo, Q. M. A Scanning Tunnelling Microscopy Investigation of Gold Island Formation from an Octanethiol Self-Assembled Monolayer on Au(111). *Surface Science* **2010**, *604*, 165–170.
- (216) Meyer, J. A.; Baikie, I. D.; Kopatzki, E.; Behm, R. J. Preferential Island Nucleation at the Elbows of the Au(111) Herringbone Reconstruction Through Place Exchange. *Surface Science* **1996**, *365*, L647–L651.
- (217) Guo, Q. M.; Yin, F.; Palmer, R. E. Beyond the Herringbone Reconstruction: Magic Gold Fingers. *Small* **2005**, *1*, 76–79.
- (218) Jewell, A. D.; Tierney, H. L.; Zenasni, O.; Lee, T. R.; Sykes, E. C. H. Asymmetric Thioethers as Building Blocks for Chiral Monolayers. *Topics in Catalysis* **2011**, *54*, 1357–1367.
- (219) Kariis, H.; Westermarck, G.; Persson, I.; Liedberg, B. Infrared Spectroscopic and Temperature-Programmed Desorption Studies of Dimethylphenylphosphine Adsorbed on the Coinage Metals. *Langmuir* **1998**, *14*, 2736–2743.
- (220) Uvdal, K.; Persson, I.; Liedberg, B. Tricyclohexylphosphine Adsorbed on Gold. *Langmuir* **1995**, *11*, 1252–1256.
- (221) Westermarck, G.; Persson, I. Chemisorption of Tertiary Phosphines on Coinage and Platinum Group Metal Powders - An Infrared Reflectance Absorption Spectroscopic, Enhanced Raman Spectroscopic and Surface Coverage Study. *Colloids and Surfaces A* **1998**, *144*, 149–166.

- (222) Westermarck, G.; Kariis, H.; Persson, I.; Liedberg, B. An Infrared Study on the Chemisorption of Tertiary Phosphines on Coinage and Platinum Group Metal Surfaces. *Colloids and Surfaces A* **1999**, *150*, 31–43.
- (223) Steiner, U. B.; Neuenschwander, P.; Caseri, W. R.; Suter, U. W.; Stucki, F. Adsorption of  $\text{NPh}_3$ ,  $\text{PPh}_3$ ,  $\text{AsPh}_3$ ,  $\text{SbPh}_3$  and  $\text{BiPh}_3$  on Gold and Copper. *Langmuir* **1992**, *8*, 90–94.
- (224) Methot, J. L.; Roush, W. R. Nucleophilic Phosphine Organocatalysis. *Advanced Synthesis & Catalysis* **2004**, *346*, 1035–1050.
- (225) Trindade, T.; O'Brien, P.; Zhang, X. M. Synthesis of CdS and CdSe Nanocrystallites Using a Novel Single-Molecule Precursors Approach. *Chemistry of Materials* **1997**, *9*, 523–530.
- (226) de la Figuera, J.; Pohl, K.; de la Fuente, O. R.; Schmid, A. K.; Bartelt, N. C.; Carter, C. B.; Hwang, R. Q. Direct Observation of Misfit Dislocation Glide on Surfaces. *Physical Review Letters* **2001**, *86*, 3819–3822.
- (227) Brown, D. E.; Moffatt, D. J.; Wolkow, R. A. Isolation of an Intrinsic Precursor to Molecular Chemisorption. *Science* **1998**, *279*, 542–544.
- (228) Pearson, R. G. *Chemical Hardness: Applications From Molecules to Solids*; Wiley-VCH: Weinheim, Germany, 1997.
- (229) Ho, T.-L. Hard Soft Acids Bases (HSAB) Principle and Organic Chemistry. *Chemical Reviews* **1975**, *75*, 1–20.
- (230) Terlain, A.; Larher, Y.; Angerand, F.; Parette, G.; Lauter, H.; Bassignana, I. C. Neutron Diffraction Study of the Structure of the Crystal Monolayer of  $\text{C}_2\text{N}_2$  Adsorbed on Graphite (0001). *Molecular Physics* **1986**, *58*, 799–813.
- (231) Han, P.; Sykes, E. C. H.; Pearl, T. P.; Mantooth, B. A.; Donhauser, Z. J.; Weiss, P. S. A Comparative Scanning Tunneling Microscopy Study of Physisorbed Linear Quadrupolar Molecules:  $\text{C}_2\text{N}_2$  and  $\text{CS}_2$  on  $\text{Au}\{111\}$  at 4 K. *Journal of Physical Chemistry A* **2003**, *126*, 8124–8129.
- (232) Dagg, I. R.; Anderson, A.; Yan, S.; Smith, W.; Joslin, C. G.; Read, L. A. A. The Quadrupole-Moment of Cyanogen - A Comparative-Study of Collision-Induced Absorption in Gaseous  $\text{C}_2\text{N}_2$ ,  $\text{CO}_2$ , and Mixtures with Argon. *Canadian Journal of Physics* **1986**, *64*, 1475–1481.
- (233) Coriani, S.; Halkier, A.; Rizzo, A.; Ruud, K. On the Molecular Electric Quadrupole Moment and the Electric-Field-Gradient-Induced

Birefringence of CO<sub>2</sub> and CS<sub>2</sub>. *Chemical Physics Letters* **2000**, 326, 269–276.

- (234) Jiang, P.; Deng, K.; Fichou, D.; Xie, S. S.; Nion, A.; Wang, C. STM Imaging ortho- and para-Fluorothiophenol Self-Assembled Monolayers on Au(111). *Langmuir* **2009**, 25, 5012–5017.
- (235) Ludwig, C.; Gompf, B.; Petersen, J.; Strohmaier, R.; Eisenmenger, W. STM Investigations of PTCDA and PTCDI on Graphite and MoS<sub>2</sub>. A Systematic Study of Epitaxy and STM Image Contrast. *Zeitschrift Physik B Condensed Matter* **1994**, 93, 365–373.
- (236) Peierls, R. *Surprises in Theoretical Physics*; Princeton University Press: Princeton, 1979.
- (237) Peierls, R. *Quantum Theory of Solids*; Oxford University Press: Oxford, 1955.
- (238) Garcia-Bach, M. A.; Blaise, P.; Malrieu, J. P. Dimerization of Polyacetylene Treated as a Spin-Peierls Distortion of the Heisenberg Hamiltonian. *Physical Review B* **1992**, 46, 15645–15651.
- (239) Bleeker, J. R.; Hays, M. K. Pentadienyl-Metal-Phosphine Chemistry. 9. The 2,4-dimethylpentadienyl-iron-trimethylphosphine Reaction System. *Organometallics* **1987**, 6, 486–491.
- (240) Miessler, G. L.; Tarr, D. A. *Inorganic Chemistry*; 3rd ed.; Prentice Hall: Upper Saddle River, 2003.
- (241) Dishner, M. H.; Hemminger, J. C.; Feher, F. J. Scanning Tunneling Microscopy Characterization of Organoselenium Monolayers on Au(111). *Langmuir* **1997**, 13, 4788–4790.
- (242) Yee, C. K.; Ulman, A.; Ruiz, J. D.; Parikh, A.; White, H.; Rafailovich, M. Alkyl Selenide- and Alkyl Thiolate-Functionalized Gold Nanoparticles: Chain Packing and Bond Nature. *Langmuir* **2003**, 19, 9450–9458.
- (243) Shaporenko, A.; Ulman, A.; Terfort, A.; Zharnikov, M. Self-assembled Monolayers of Alkaneselenolates on (111) Gold and Silver. *Journal of Physical Chemistry B* **2005**, 109, 3898–906.
- (244) Monnell, J. D.; Stapleton, J. J.; Dirk, S. M.; Reinerth, W. A.; Tour, J. M.; Allara, D. L.; Weiss, P. S. Relative Conductances of Alkaneselenolate and Alkanethiolate Monolayers on Au{111}. *Journal of Physical Chemistry B* **2005**, 109, 20343–9.



- (245) Monnell, J. D.; Stapleton, J. J.; Jackiw, J. J.; Dunbar, T.; Reinerth, W. A.; Dirk, S. M.; Tour, J. M.; Allara, D. L.; Weiss, P. S. Ordered Local Domain Structures of Decaneselenolate and Dodecaneselenolate Monolayers on Au{111}. *Journal of Physical Chemistry B* **2004**, *108*, 9834–9841.
- (246) de la Llave, E.; Scherlis, D. A. Selenium-Based Self-Assembled Monolayers: The Nature of Adsorbate-Surface Interactions. *Langmuir* **2010**, *26*, 173–178.
- (247) Nakano, K.; Sato, T.; Tazaki, M.; Takagi, M. Self-Assembled Monolayer Formation from Decaneselenol on Polycrystalline Gold As Characterized by Electrochemical Measurements, Quartz-Crystal Microbalance, XPS, and IR Spectroscopy. *Langmuir* **2000**, *16*, 2225–2229.
- (248) Shaporenko, A.; Cyganik, P.; Buck, M.; Ulman, A.; Zharnikov, M. Self-Assembled Monolayers of Semifluorinated Alkaneselenolates on Noble Metal Substrates. *Langmuir* **2005**, *21*, 8204–13.
- (249) Han, S. W.; Lee, S. J.; Kim, K. Self-Assembled Monolayers of Aromatic Thiol and Selenol on Silver: Comparative Study of Adsorptivity and Stability. *Langmuir* **2001**, *17*, 6981–6987.
- (250) Uvdal, K.; Kariis, H.; Westermarck, G.; Wirde, M.; Gelius, U.; Persson, I.; Liedberg, B. Tricyclohexylphosphine Adsorbed on Rhodium. *Langmuir* **1998**, *14*, 7189–7196.
- (251) Stadler, C.; Hansen, S.; Kroger, I.; Kumpf, C.; Umbach, E. Tuning Intermolecular Interaction in Long-Range-Ordered Submonolayer Organic Films. *Nature Physics* **2009**, *5*, 153–158.
- (252) Nanayakkara, S. U.; Sykes, E. C. H.; Fernandez-Torres, L. C.; Blake, M. M.; Weiss, P. S. Long-Range Electronic Interactions at a High Temperature: Bromine Adatom Islands on Cu(111). *Physical Review Letters* **2007**, *98*, 206108.
- (253) Fernandez-Torrente, I.; Monturet, S.; Franke, K. J.; Fraxedas, J.; Lorente, N.; Pascual, J. I. Long-Range Repulsive Interaction Between Molecules on a Metal Surface Induced by Charge Transfer. *Physical Review Letters* **2007**, *99*, 176103.
- (254) Altman, E. I.; Colton, R. J. The Interaction of C60 with Noble Metal Surfaces. *Surface Science* **1993**, *295*, 13–33.
- (255) Sanchez, L.; Otero, R.; Gallego, J. M.; Miranda, R.; Martián, N. Ordering Fullerenes at the Nanometer Scale on Solid Surfaces. *Chemical Reviews* **2009**, *109*, 2081–2091.

- (256) Krief, A.; Trabelsi, M.; Dumont, W.; Derock, M. Conditions-Driven Selective Synthesis of Selenides and Selenols from Elemental Selenium. *Synlett* **2004**, 1751–1754.
- (257) Krief, A.; Dumont, W.; Gillina, F. Reactivity of Alkyl Aryl Selenides Towards Butyllithiums: Synthesis and Alkylation of Aryllithiums; a New Synthetic Route to Aryl Alkanes. *Arkivoc* **2007**, 51–64.
- (258) Min, B. K.; Friend, C. M. Heterogeneous Gold-Based Catalysis for Green Chemistry: Low-Temperature CO Oxidation and Propene Oxidation. *Chemical Reviews* **2007**, *107*, 2709–2724.
- (259) Rodriguez, J. A. Gold-Based Catalysts for the Water–Gas Shift Reaction: Active Sites and Reaction Mechanism. *Catalysis Today* **2011**, *160*, 3–10.
- (260) Hashmi, A. S. K.; Hutchings, G. J. Gold Catalysis. *Angewandte Chemie International Edition* **2006**, *45*, 7896–7936.
- (261) Haruta, M. Spiers Memorial Lecture: Role of Perimeter Interfaces in Catalysis by Gold Nanoparticles. *Faraday Discussions* **2011**, *152*, 11–32.
- (262) Valden, M.; Lai, X.; Goodman, D. W. Onset of Catalytic Activity of Gold Clusters on Titania with the Appearance of Nonmetallic Properties. *Science* **1998**, *281*, 1647–1650.
- (263) Herzing, A. A.; Kiely, C. J.; Carley, A. F.; Landon, P.; Hutchings, G. J. Identification of Active Gold Nanoclusters on Iron Oxide Supports for CO Oxidation. *Science* **2008**, *321*, 1331–1335.
- (264) Turner, M.; Golovko, V. B.; Vaughan, O. P. H.; Abdulkin, P.; Berenguer-Murcia, A.; Tikhov, M. S.; Johnson, B. F. G.; Lambert, R. M. Selective Oxidation with Dioxygen by Gold Nanoparticle Catalysts Derived from 55-Atom Clusters. *Nature* **2008**, *454*, 981–983.
- (265) Guzman, J.; Gates, B. C. Catalysis by Supported Gold: Correlation Between Catalytic Activity for CO Oxidation and Oxidation States of Gold. *Journal of the American Chemical Society* **2004**, *126*, 2672–3.
- (266) Barton, D. G.; Podkolzin, S. G. Kinetic Study of a Direct Water Synthesis Over Silica-Supported Gold Nanoparticles. *Journal of Physical Chemistry B* **2005**, *109*, 2262–74.
- (267) Daniel, M.-C.; Astruc, D. Gold Nanoparticles: Assembly, Supramolecular Chemistry, Quantum-Size-Related Properties, and Applications Toward Biology, Catalysis, and Nanotechnology. *Chemical Reviews* **2004**, *104*, 293–346.

- (268) Yeh, Y.-C.; Creran, B.; Rotello, V. M. Gold Nanoparticles: Preparation, Properties, and Applications in Bionanotechnology. *Nanoscale* **2012**, *4*, 1871–1880.
- (269) Lopez-Sanchez, J. A.; Dimitratos, N.; Hammond, C.; Brett, G. L.; Kesavan, L.; White, S.; Miedziak, P.; Tiruvalam, R.; Jenkins, R. L.; Carley, A. F.; Knight, D.; Kiely, C. J.; Hutchings, G. J. Facile Removal of Stabilizer-Ligands from Supported Gold Nanoparticles. *Nature Chemistry* **2011**, *3*, 551–556.
- (270) Schmid, G.; Pfeil, R.; Boese, R.; Bandermann, F.; Meyer, S.; Calis, G. H. M.; van der Velden, J. W. A. Au<sub>55</sub>[P(C<sub>6</sub>H<sub>5</sub>)<sub>3</sub>]<sub>12</sub>Cl<sub>6</sub> - Ein Goldcluster Ungewöhnlicher Größe. *Chemische Berichte* **1981**, *114*, 3634–3642.
- (271) Schmid, G. The Relevance of Shape and Size of Au<sub>55</sub> Clusters. *Chemical Society Reviews* **2008**, *37*, 1909–1930.
- (272) Schmid, G. Large Clusters and Colloids: Metals in the Embryonic State. *Chemical Reviews* **1992**, *92*, 1709–1727.
- (273) Smith, R. K.; Nanayakkara, S. U.; Woehrle, G. H.; Pearl, T. P.; Blake, M. M.; Hutchison, J. E.; Weiss, P. S. Spectral Diffusion in the Tunneling Spectra of Ligand-Stabilized Undecagold Clusters. *Journal of the American Chemical Society* **2006**, *128*, 9266–9267.
- (274) Zhang, H.; Schmid, G.; Hartmann, U. Reduced Metallic Properties of Ligand-Stabilized Small Metal Clusters. *Nano Letters* **2003**, *3*, 305–307.
- (275) Chusuei, C. C.; Lai, X.; Davis, K. A.; Bowers, E. K.; Fackler, J. P.; Goodman, D. W. A Nanoscale Model Catalyst Preparation: Solution Deposition of Phosphine-Stabilized Gold Clusters Onto a Planar TiO<sub>2</sub> (110) Support. *Langmuir* **2001**, *17*, 4113–4117.
- (276) Jin, R.; Zhu, Y.; Qian, H. Quantum-Sized Gold Nanoclusters: Bridging the Gap Between Organometallics and Nanocrystals. *Chemistry - A European Journal* **2011**, *17*, 6584–93.
- (277) Shem, P. M.; Sardar, R.; Shumaker-Parry, J. S. One-Step Synthesis of Phosphine-Stabilized Gold Nanoparticles Using the Mild Reducing Agent 9-BBN. *Langmuir* **2009**, *25*, 13279–13283.
- (278) Hutchison, J. E.; Foster, E. W.; Warner, M. G.; Reed, S. M.; Weare, W. W.; Buhro, W.; Yu, H. Triphenylphosphine-Stabilized Gold Nanoparticles. In *Inorganic Syntheses*; Shapley, J. R., Ed.; John Wiley & Sons Inc: New York, 2004; pp. 228–232.

- (279) Sharma, R.; Holland, G. P.; Solomon, V. C.; Zimmermann, H.; Schiffenhaus, S.; Amin, S. A.; Buttry, D. A.; Yarger, J. L. NMR Characterization of Ligand Binding and Exchange Dynamics in Triphenylphosphine-Capped Gold Nanoparticles. *Journal of Physical Chemistry C* **2009**, *113*, 16387–16393.
- (280) Ramazani, A.; Kazemizadeh, A. R.; Ahmadi, E.; Noshiranzadeh, N.; Souldozi, A. Synthesis and Reactions of Stabilized Phosphorus Ylides. *Current Organic Chemistry* **2008**, *12*, 59–82.
- (281) Du, Y.; Lu, X.; Zhang, C. A Catalytic Carbon-Phosphorus Ylide Reaction: Phosphane-Catalyzed Annulation of Allylic Compounds with Electron-Deficient Alkenes. *Angewandte Chemie International Edition* **2003**, *42*, 1035–1037.
- (282) Sun, W.-H.; Zhang, W.; Gao, T.; Tang, X.; Chen, L.; Li, Y.; Jin, X. Synthesis and Characterization of n-(2-pyridyl)benzamide-Based Nickel Complexes and Their Activity for Ethylene Oligomerization. *Journal of Organometallic Chemistry* **2004**, *689*, 917–929.
- (283) Cohen, C. T.; Chu, T.; Coates, G. W. Cobalt Catalysts for the Alternating Copolymerization of Propylene Oxide and Carbon Dioxide: Combining High Activity and Selectivity. *Journal of the American Chemical Society* **2005**, *127*, 10869–10878.
- (284) Woehrle, G. H.; Brown, L. O.; Hutchison, J. E. Thiol-Functionalized, 1.5-nm Gold Nanoparticles Through Ligand Exchange Reactions: Scope and Mechanism of Ligand Exchange. *Journal of the American Chemical Society* **2005**, *127*, 2172–83.
- (285) Petroski, J.; Chou, M. H.; Creutz, C. Rapid Phosphine Exchange on 1.5-nm Gold Nanoparticles. *Inorganic chemistry* **2004**, *43*, 1597–9.
- (286) Mautes, D.; Zhang, H.; Hartmann, U. Symmetry-Break-Induced Variation of Energy-Level Degeneracy Observed on Individual Molecules by Low-Temperature STM. In *AIP Conference Proceedings*; AIP, 2003; Vol. 696, pp. 979–984.
- (287) Xu, W.; Dong, M.; Vázquez-Campos, S.; Gersen, H.; Laegsgaard, E.; Stensgaard, I.; Crego-Calama, M.; Reinhoudt, D. N.; Linderoth, T. R.; Besenbacher, F. Enhanced Stability of Large Molecules Vacuum-Sublimated Onto Au(111) Achieved by Incorporation of Coordinated Au-Atoms. *Journal of the American Chemical Society* **2007**, *129*, 10624–10625.

- (288) Tolman, C. A. Steric Effects of Phosphorous Ligands in Organometallic Chemistry and Homogeneous Catalysis. *Chemical Reviews* **1977**, *77*, 313–348.
- (289) Dance, I.; Scudder, M. Intramolecular and Supramolecular Geometry of Coordinated PPh<sub>3</sub>. *Dalton Transactions* **2000**, 1579–1585.
- (290) Schmid, G.; Corain, B. Nanoparticulated Gold: Syntheses, Structures, Electronics, and Reactivities. *European Journal of Inorganic Chemistry* **2003**, *2003*, 3081–3098.
- (291) Nuzzo, R. G.; Allara, D. L. Adsorption of Bifunctional Organic Disulfides on Gold Surfaces. *Journal of the American Chemical Society* **1983**, *105*, 4481–4483.
- (292) Giangregorio, M. M.; Losurdo, M.; Bianco, G. V.; Operamolla, A.; Dilonardo, E.; Sacchetti, A.; Capezzuto, P.; Babudri, F.; Bruno, G. Insight into Gold Nanoparticles-Hydrogen Interaction: A Way to Tailor Nanoparticles Surface Charge and SAMs Chemisorption. *Journal of Physical Chemistry C* **2011**, *115*, 19520–19528.
- (293) Jadzinsky, P. D.; Calero, G.; Ackerson, C. J.; Bushnell, D. A.; Kornberg, R. D. Structure of a Thiol Monolayer-Protected Gold Nanoparticle at 1.1 Å Resolution. *Science* **2007**, *318*, 430–433.
- (294) Wessels, J. M.; Nothofer, H.-G.; Ford, W. E.; von Wrochem, F.; Scholz, F.; Vossmeier, T.; Schroedter, A.; Weller, H.; Yasuda, A. Optical and Electrical Properties of Three-Dimensional Interlinked Gold Nanoparticle Assemblies. *Journal of the American Chemical Society* **2004**, *126*, 3349–3356.
- (295) Maksymovych, P.; Sorescu, D. C.; Yates, J. T. Methanethiolate Adsorption Site on Au(111): A Combined STM/DFT Study at the Single-Molecule Level. *Journal of Physical Chemistry B* **2006**, *110*, 21161–21167.
- (296) Pei, Y.; Shao, N.; Gao, Y.; Zeng, X. C. Investigating Active Site of Gold Nanoparticle Au<sub>55</sub>(PPh<sub>3</sub>)<sub>12</sub>Cl<sub>6</sub> in Selective Oxidation. *ACS Nano* **2010**, *4*, 2009–20.
- (297) Sykes, E. C. H.; Han, P.; Kandel, S. A.; Kelly, K. F.; McCarty, G. S.; Weiss, P. S. Substrate-Mediated Interactions and Intermolecular Forces Between Molecules Adsorbed on Surfaces. *Accounts of Chemical Research* **2003**, *36*, 945–953.
- (298) Barth, J. V.; Costantini, G.; Kern, K. Engineering Atomic and Molecular Nanostructures at Surfaces. *Nature* **2005**, *437*, 671–679.

- (299) Barth, J. V. Molecular Architectonic on Metal Surfaces. *Annual Review of Physical Chemistry* **2007**, *58*, 375–407.
- (300) Rojas, G.; Chen, X.; Kunkel, D.; Bode, M.; Enders, A. Temperature Dependence of Metal-Organic Heteroepitaxy. *Langmuir* **2011**, *27*, 14267–14271.
- (301) Rojas, G.; Simpson, S.; Chen, X.; Kunkel, D. A.; Nitz, J.; Xiao, J.; Dowben, P. A.; Zurek, E.; Enders, A. Surface State Engineering of Molecule-Molecule Interactions. *Physical Chemistry Chemical Physics* **2012**, *14*, 4971–4976.
- (302) Ishii, H.; Sugiyama, K.; Ito, E.; Seki, K. Energy Level Alignment and Interfacial Electronic Structures at Organic/Metal and Organic/Organic Interfaces. *Advanced Materials* **1999**, *11*, 605–625.
- (303) Han, P.; Weiss, P. S. Electronic Substrate-Mediated Interactions. *Surface Science Reports* **2012**, *67*, 19–81.
- (304) Yuan, Y.; Reece, T. J.; Sharma, P.; Poddar, S.; Ducharme, S.; Gruverman, A.; Yang, Y.; Huang, J. Efficiency Enhancement in Organic Solar Cells with Ferroelectric Polymers. *Nature Materials* **2011**, *10*, 296–302.
- (305) Vaughan, O. P. H.; Alavi, A.; Williams, F. J.; Lambert, R. M. Dipole Amplification: A Principle for the Self-Assembly of Asymmetric Monomers on Metal Surfaces. *Angewandte Chemie International Edition* **2008**, *47*, 2422–2426.
- (306) Cleveland, C. L.; Landman, U. The Energetics and Structure of Nickel Clusters: Size Dependence. *The Journal of Chemical Physics* **1991**, *94*, 7376–7396.
- (307) Martin, T.; P. Shells of Atoms. *Physics Reports* **1996**, *273*, 199–241.
- (308) de Heer, W. The Physics of Simple Metal Clusters: Experimental Aspects and Simple Models. *Reviews of Modern Physics* **1993**, *65*, 611–676.
- (309) Enders, A.; Malinowski, N.; Ievlev, D.; Zurek, E.; Autschbach, J.; Kern, K. Magic Alkali-Fullerene Compound Clusters of Extreme Thermal Stability. *Journal of Chemical Physics* **2006**, *125*, 191102.
- (310) Li, Q.; Han, C.; Horton, S. R.; Fuentes-Cabrera, M.; Sumpter, B. G.; Lu, W.; Bernholc, J.; Maksymovych, P.; Pan, M. Supramolecular Self-Assembly of  $\pi$ -Conjugated Hydrocarbons via 2D Cooperative CH/ $\pi$  Interaction. *ACS Nano* **2012**, *6*, 566–572.

- (311) Lawton, T.; Carrasco, J.; Baber, A.; Michaelides, A.; Sykes, E. C. Visualization of Hydrogen Bonding and Associated Chirality in Methanol Hexamers. *Physical Review Letters* **2011**, *107*, 256101.
- (312) Brune, H.; Röder, H.; Boragno, C.; Kern, K. Microscopic View of Nucleation on Surfaces. *Physical Review Letters* **1994**, *73*, 1955–1958.
- (313) te Velde, G.; Bickelhaupt, F. M.; Baerends, E. J.; Fonseca Guerra, C.; van Gisbergen, S. J. A.; Snijders, J. G.; Ziegler, T. Chemistry with ADF. *Journal of Computational Chemistry* **2001**, *22*, 931–967.
- (314) Hoffmann, R. A Chemical and Theoretical Way to Look at Bonding on Surfaces. *Reviews of Modern Physics* **1988**, *60*, 601–628.
- (315) Dewar, M. J. A review of  $\pi$  Complex Theory. *Bulletin de la Societe Chimique de France* **1951**, C71–C79.
- (316) Chatt, J.; Duncanson, L. A. 586. Olefin Co-Ordination Compounds. Part III. Infra-Red Spectra and Structure: Attempted Preparation of Acetylene Complexes. *Journal of the Chemical Society* **1953**, 2939–2947.
- (317) Hammer, B.; Norskov, J. K. Why Gold Is the Noblest of All the Metals. *Nature* **1995**, *376*, 238–240.
- (318) Kryachko, E.; Scheiner, S. CH $\cdots$ F Hydrogen Bonds. Dimers of Fluoromethanes. *The Journal of Physical Chemistry A* **2004**, *108*, 2527–2535.
- (319) Berland, K.; Einstein, T. L.; Hyldgaard, P. Rings Sliding on a Honeycomb Network: Adsorption Contours, Interactions, and Assembly of Benzene on Cu(111). *Physical Review B* **2009**, *80*, 155431.
- (320) Göhler, B.; Hamelbeck, V.; Markus, T. Z.; Kettner, M.; Hanne, G. F.; Vager, Z.; Naaman, R.; Zacharias, H. Spin Selectivity in Electron Transmission Through Self-Assembled Monolayers of Double-Stranded DNA. *Science* **2011**, *331*, 894–897.
- (321) ADF®: Amsterdam Density Functional Software <http://www.scm.com> (accessed Apr 27, 2012).
- (322) Perdew, J.; Burke, K.; Wang, Y. Generalized Gradient Approximation for the Exchange-Correlation Hole of a Many-Electron System. *Physical Review B* **1996**, *54*, 16533–16539.
- (323) Grimme, S.; Antony, J.; Ehrlich, S.; Krieg, H. A Consistent and Accurate *ab initio* Parametrization of Density Functional Dispersion Correction

- (DFT-D) for the 94 Elements H-Pu. *Journal of Chemical Physics* **2010**, *132*, 154104.
- (324) Lenthe, E. van; Baerends, E. J.; Snijders, J. G. Relativistic Regular Two-Component Hamiltonians. *Journal of Chemical Physics* **1993**, *99*, 4597–4620.
- (325) Avogadro <http://avogadro.openmolecules.net> (accessed Apr 27, 2012).
- (326) Lonie, D. C.; Zurek, E. XtalOpt Version R7: An Open-Source Evolutionary Algorithm for Crystal Structure Prediction. *Computer Physics Communications* **2011**, *182*, 2305–2306.
- (327) Kammler, T.; Küppers, J. Interaction of H atoms with Cu(111) Surfaces: Adsorption, Absorption, and Abstraction. *Journal of Chemical Physics* **1999**, *111*, 8115–8123.
- (328) Besenbacher, F.; Lauritsen, J. V.; Linderöth, T. R.; Lægsgaard, E.; Vang, R. T.; Wendt, S. Atomic-Scale Surface Science Phenomena Studied by Scanning Tunneling Microscopy. *Surface Science* **2009**, *603*, 1315–1327.
- (329) Chopra, I. S.; Chaudhuri, S.; Veyan, J. F.; Chabal, Y. J. Turning Aluminium into a Noble-Metal-Like Catalyst for Low-Temperature Activation of Molecular Hydrogen. *Nature Materials* **2011**, *10*, 1–6.
- (330) Canzian, A.; Mosca, H. O.; Bozzolo, G. Surface Alloying of Pd on Cu(111). *Surface Science* **2004**, *551*, 9–22.
- (331) Paniago, R.; de Siervo, A.; Soares, E. A.; Pfannes, H.-D.; Landers, R. Pd Growth on Cu(111): Stress Relaxation Through Surface Alloying? *Surface Science* **2004**, *560*, 27–34.
- (332) Sun, J.; Hannon, J.; Kellogg, G.; Pohl, K. Local Structural And Compositional Determination via Electron Scattering: Heterogeneous Cu(001)-Pd Surface Alloy. *Physical Review B* **2007**, *76*, 205414.
- (333) Hannon, J.; Sun, J.; Pohl, K.; Kellogg, G. Origins of Nanoscale Heterogeneity in Ultrathin Films. *Physical Review Letters* **2006**, *96*, 246103.
- (334) Koymen, A.; Lee, K.; Yang, G.; Jensen, K.; Weiss, A. Temperature-Dependent Top-Layer Composition of Ultrathin Pd Films on Cu(100). *Physical Review B* **1993**, *48*, 2020–2023.
- (335) Murray, P. W.; Stensgaard, I.; Lægsgaard, E.; Besenbacher, F. Growth and Structure of Pd alloys on Cu(100). *Surface Science* **1996**, *365*, 591–601.



- (336) Delamarche, E.; Michel, B.; Kang, H.; Gerber, C. Thermal Stability of Self-Assembled Monolayers. *Langmuir* **1994**, *10*, 4103–4108.
- (337) Zambelli, T.; Barth, J. V.; Wintterlin, J.; Ertl, G. Complex Pathways in Dissociative Adsorption of Oxygen on Platinum. *Nature* **1997**, *390*, 495–497.
- (338) Lin, T.-S.; Gomer, R. Diffusion of 1H and 2H on the Ni(111) and (100) Planes. *Surface Science* **1991**, *255*, 41–60.
- (339) DiFoggio, R.; Gomer, R. Diffusion of Hydrogen and Deuterium on the (110) Plane of Tungsten. *Physical Review B* **1982**, *25*, 3490–3511.
- (340) Dharmadhikari, C.; Gomer, R. Diffusion of Hydrogen and Deuterium on the (111) Plane of Tungsten. *Surface Science* **1984**, *143*, 223–242.
- (341) Wang, S. C.; Gomer, R. Diffusion of Hydrogen, Deuterium, and Tritium on the (110) Plane of Tungsten. *Journal of Chemical Physics* **1985**, *83*, 4193–4209.
- (342) Daniels, E. A.; Lin, J. C.; Gomer, R. Diffusion Anisotropy of Hydrogen and Deuterium on the Tungsten (211) Plane. *Surface Science* **1988**, *204*, 129–146.
- (343) Lee, A.; Zhu, X. D.; Deng, L.; Linke, U. Observation of a Transition from Over-Barrier Hopping to Activated Tunneling Diffusion: H and D on Ni(100). *Physical Review B* **1992**, *46*, 472–476.
- (344) Lee, A.; Zhu, X. D.; Wong, A.; Deng, L.; Linke, U. Observation of Diffusion of H and D on Ni(111) from Over-Barrier Hopping to Nonactivated Tunneling. *Physical Review B* **1993**, *48*, 256–259.
- (345) Wong, A.; Lee, A.; Zhu, X. D. Coverage Dependence of Quantum Tunneling Diffusion of Hydrogen and Deuterium on Ni(111). *Physical Review B* **1995**, *51*, 4418–4425.
- (346) Wang, X.; Fei, Y. Y.; Zhu, X. D. Classical and Quantum Diffusion of Hydrogen Atoms on Cu(111). *Chemical Physics Letters* **2009**, *481*, 58–61.
- (347) Kua, J.; Lauhon, L. J.; Ho, W.; Goddard, W. A. Direct Comparisons of Rates for Low Temperature Diffusion of Hydrogen and Deuterium on Cu(001) from Quantum Mechanical Calculations and Scanning Tunneling Microscopy Experiments. *Journal of Chemical Physics* **2001**, *115*, 5620.
- (348) Heinrich, A. J.; Lutz, C. P.; Gupta, J. A.; Eigler, D. M. Molecule Cascades. *Science* **2002**, *298*, 1381–1387.

- (349) Stroschio, J. A.; Tavazza, F.; Crain, J. N.; Celotta, R. J.; Chaka, A. M. Electronically Induced Atom Motion Engineered CoCu<sub>n</sub> Nanostructures. *Science* **2006**, *313*, 948–951.
- (350) Pawin, G.; Wong, K. L.; Kwon, K.-Y.; Frisbee, R. J.; Rahman, T. S.; Bartels, L. Surface Diffusive Motion in a Periodic and Asymmetric Potential. *Journal of the American Chemical Society* **2008**, *130*, 15244–15245.
- (351) Mattsson, T.; Wahnström, G. Isotope Effect in Hydrogen Surface Diffusion. *Physical Review B* **1997**, *56*, 14944–14947.
- (352) Mattsson, T.; Engberg, U.; Wahnström, G. H Diffusion on Ni(100): A Quantum Monte Carlo Simulation. *Physical Review Letters* **1993**, *71*, 2615–2618.
- (353) Chen, L.; Ying, S. Theory of Surface Diffusion: Crossover from Classical to Quantum Regime. *Physical Review Letters* **1994**, *73*, 700–703.
- (354) Mitsui, T.; Rose, M. K.; Fomin, E.; Ogletree, D. F.; Salmeron, M. Dissociative Hydrogen Adsorption on Palladium Requires Aggregates of Three or More Vacancies. *Nature* **2003**, *422*, 705–707.
- (355) Luo, M. F.; Hu, G. R.; Lee, M. H. Surface Structures of Atomic Hydrogen Adsorbed on Cu(111) Surface Studied by Density-Functional-Theory Calculations. *Surface Science* **2007**, *601*, 1461–1466.
- (356) Pang, X.-Y.; Xue, L.-Q.; Wang, G.-C. Adsorption of Atoms on Cu Surfaces: A Density Functional Theory Study. *Langmuir* **2007**, *23*, 4910–4917.
- (357) Nie, J. L.; Xiao, H. Y.; Zu, X. T. First-Principles Study of H Adsorption on and Absorption in Cu(111) Surface. *Chemical Physics* **2006**, *321*, 48–54.
- (358) Domany, E.; Schick, M.; Walker, J. S. Proposed Structure of Hydrogen on Ni(111). *Solid State Communications* **1979**, *30*, 331–332.
- (359) Walker, J.; Schick, M. Order-Disorder Transitions to  $2 \times 2$  Structures. *Physical Review B* **1979**, *20*, 2088–2096.
- (360) Repp, J.; Meyer, G.; Rieder, K.-H.; Hyldgaard, P. Site Determination and Thermally Assisted Tunneling in Homogenous Nucleation. *Physical Review Letters* **2003**, *91*, 206102.
- (361) Chorkendorff, I.; Rasmussen, P. B. Reconstruction of Cu(100) by Adsorption of Atomic Hydrogen. *Surface Science* **1991**, *248*, 35–44.

- (362) Kresse, G.; Furthmüller, J. Efficiency of *ab-initio* Total Energy Calculations for Metals and Semiconductors Using a Plane-Wave Basis Set. *Computational Materials Science* **1996**, *6*, 15–50.
- (363) Kresse, G. Efficient Iterative Schemes For *ab initio* Total-Energy Calculations Using a Plane-Wave Basis Set. *Physical Review B* **1996**, *54*, 11169–11186.
- (364) Kresse, G. From Ultrasoft Pseudopotentials to the Projector Augmented-Wave Method. *Physical Review B* **1999**, *59*, 1758–1775.
- (365) Blöchl, P. E. Projector Augmented-Wave Method. *Physical Review B* **1994**, *50*, 17953–17979.
- (366) Perdew, J. P.; Wang, Y. Accurate and Simple Analytic Representation of the Electron-Gas Correlation Energy. *Physical Review B* **1992**, *45*, 13244–13249.
- (367) Henkelman, G.; Uberuaga, B. P.; Jónsson, H. A Climbing Image Nudged Elastic Band Method for Finding Saddle Points and Minimum Energy Paths. *Journal of Chemical Physics* **2000**, *113*, 9901–9904.
- (368) Fermann, J. T.; Auerbach, S. Modeling Proton Mobility in Acidic Zeolite Clusters: II. Room Temperature Tunneling Effects from Semiclassical Rate Theory. *The Journal of Chemical Physics* **2000**, *112*, 6787–6794.
- (369) Bhatia, B.; Sholl, D. Quantitative Assessment of Hydrogen Diffusion by Activated Hopping and Quantum Tunneling in Ordered Intermetallics. *Physical Review B* **2005**, *72*.